DEPARTMENT OF PHYSICS
UNIVERSITY OF JYVÄSKYLÄ
RESEARCH REPORT No. 9/2013

A SPECTROSCOPIC STUDY OF LOW-LYING STATES IN NEUTRON-DEFICIENT ASTATINE AND FRANCIUM NUCLEI

by
Ulrika Jakobsson

Academic Dissertation
for the Degree of
Doctor of Philosophy

To be presented, by permission of the
Faculty of Mathematics and Natural Sciences
of the University of Jyväskylä,
for public examination in Auditorium FYS1 of the
University of Jyväskylä on November 20th, 2013
at 12 o'clock noon

Jyväskylä, Finland
November 2013

Abstract

Jakobsson, Ulrika
A spectroscopic study of low-lying states in neutron-deficient astatine and francium nuclei
Jyväskylä: University of Jyväskylä 2013, 131 p.
Department of Physics Research Report No. 9/2013
ISSN: 0075-465X
ISBN: 978-951-39-5418-5 (paper version)
ISBN: 978-951-39-5419-2 (electronic version)
Diss.

This thesis investigates the evolution of nuclear structure in the neutron-deficient astatine and francium nuclei by concentrating on the four nuclei ^{197}At, ^{199}At, ^{203}Fr and ^{205}Fr. The studies have been performed through prompt and delayed spectroscopy and by using the recoil-decay tagging technique. The results suggest that while the ground states in ^{199}At and ^{197}At, having $I^{\pi} = 9/2^{-}$, are still dominated by spherical structures, the coupling of the $h_{9/2}/f_{7/2}$ proton to the polonium core increases in ^{197}At as the unfavoured signature partner in the ground-state band has been observed. It is further suggested that both in ^{203}Fr and ^{205}Fr the ground state is still dominated by spherical structures and, moreover, no strengthening of the coupling of the $h_{9/2}/f_{7/2}$ proton to the radon core has been observed. The systematics of the intruder $1/2^{+}$ state is extended by the observation of this state in the nuclei ^{199}At, ^{203}Fr and ^{205}Fr. The isomeric $13/2^{+}$ state is reported for the first time in the neutron-deficient odd-mass francium nuclei, as it has been observed in the present study in ^{203}Fr and ^{205}Fr. In the nuclei ^{197}At, ^{199}At and ^{205}Fr a rotational band has been observed to be built on this state and in ^{203}Fr the start of a band has been observed. These results suggest that the isomeric $13/2^{+}$ state is oblate deformed in the four nuclei studied. The results from the thesis work are compared with systematics in this region, and based on the results the intruder picture is suggested to prevail at low excitation energy to the francium nuclei that lie five protons away from the $Z = 82$ shell closure.

Keywords: Nuclear spectroscopy, nuclear structure, recoil-decay tagging, neutron-deficient nuclei, nuclear deformation.

Author's address: Ulrika Jakobsson
Department of Physics
University of Jyväskylä
Finland

Supervisors: Dr. Juha Uusitalo
Department of Physics
University of Jyväskylä
Finland

Dr. Sakari Juutinen
Department of Physics
University of Jyväskylä
Finland

Reviewers: Prof. Andrei Andreyev
Department of Physics
University of York
U.K.

Dr. Filip Kondev
Nuclear Engineering Division
Argonne National Laboratory
U.S.A.

Opponent: Prof. Piet Van Duppen
Instituut voor Kern- en Stralingsfysica
Departement Natuurkunde en Sterrenkunde
KU Leuven
Belgium

Preface

This work has been carried out between the years 2007-2013 at the Accelerator laboratory of the Physics Department of the University of Jyväskylä. I want to acknowledge the financial support from the University of Jyväskylä, The Finnish Academy of Science and Letters: Vilho, Yrjö ja Kalle Väisälä Foundation, the Emil Aaltonen Foundation, the Graduate School for Nuclear and Particle Physics and the Academy of Finland; Finnish Centre of Excellence Programmes 2006–2011 and 2012-2017.

I would like to express my gratitude to Prof. Matti Leino for employing me as a summer student in the RITU group in 2005, and later as a PhD student in 2007, and thereby for giving me the opportunity to study nuclear physics. Thank you for keeping an eye on the progress of my thesis project and for all of your help and advice during these years. My very deepest thanks go to my supervisor Dr. Juha Uusitalo. Throughout all these years you have shown so much patience and you always have time for my questions, even though sometimes the question could turn into a long discussion. I greatly appreciate all your guidance and support! I want to thank my second supervisor Dr. Sakari Juutinen for showing great interest in my thesis project. All your help and all the knowledge you have shared during these years have been very valuable. A great thankyou goes to Prof. Rauno Julin for teaching me a lot about nuclear physics. I would also like to acknowledge the help of Dr. Päivi Nieminen and Dr. Karl Hauschild who were of great help when producing the papers. The valuable comments on this thesis provided by the reviewers Prof. Andrei Andreyev and Dr. Filip Kondev are greatly appreciated.

I have had the privilege to work as a member of the RITU-Gamma group. I would like to thank all past and present cool members of the group for a fun and relaxed working atmosphere. You have all contributed to this work and I have really enjoyed these years working with you! A special thankyou goes to Dr. Cath Scholey and Dr. Jan Sarén for all your support and advice throughout these years and for all the fun times working at the focal plane. Not to forget all my past and present fellow juniors for all the fruitful discussions we have had, I have learned a lot from you. Appreciations go to Mr. Taneli Kalvas who has shared an office with me and therefore has had to witness all the ups and downs of the writing of this thesis.

Ett stort huaa går till la famiglia: tack pappa, mamma, Klister och Schnilli för ert stöd under alla dessa år jag har tillbringat här uppe i “vildmarken”. Sist men inte minst vill jag tacka min kära Pauli. Jag vet att utan dig och ditt stöd skulle de här orden inte ha blivit skrivna, tack för alla dessa gemensamma år.

Ulrika Jakobsson,
Jyväskylä, November 2013

Contents

Chapter 1

Introduction

The atomic nucleus consists of protons and neutrons, the nucleons, closely packed together. The interaction between the nucleons, that holds the nucleus together, is known as the strong force. It is one of the four basic interactions known to exist in nature. As the strong force, which is understood to have a complex nature, is associated with the interaction between the nucleons, the study of its properties quickly becomes a very complicated many-body problem. Consequently, its exact nature is not known and the field of nuclear physics does not have an overall model explaining all nuclear phenomena. This fact in itself indicates the fundamental importance of basic nuclear physics research today and in the future. Although an all-encompassing model of the strong force does not exist, several phenomenology-based models dealing with different nuclear properties have been developed with great success. Interestingly some of these models, such as the spherical shell model, have their origin in other fields of physics and have successfully been adapted into nuclear physics.

Some observations of the properties of the strong force can already be made based solely on early experimental results (see for example [Casten00]). For instance the mere existence of heavy nuclei implies that the strong force is attractive. The saturation of the nuclear binding energy per nucleon, starting close to $A \sim 20$, indicates that the force must be of short range. Its near charge-independence has been observed through the similarity of certain properties of mirror nuclei next to the $N = Z$ line. To test the applicability of nuclear models on a large scale, say from the lightest to the heaviest of atomic nuclei, a large amount of experimental data is needed. This information is provided by a variety of fields such as those of mass spectrometry, laser spectroscopy and nuclear spectroscopy, which take on a large number of nuclear physics problems that puzzle experimentalists today. Of these, nuclear spectroscopy concentrates on the analysis of radiation emitted by the nucleus. As a result, information on the nuclear states that disintegrate, generating the radiation, is obtained. As a subfield of nuclear spectroscopy, gamma-ray spectroscopy deals with the radiation emitted from excited states of the nucleus, with the aim to study the properties of nuclear states at very high

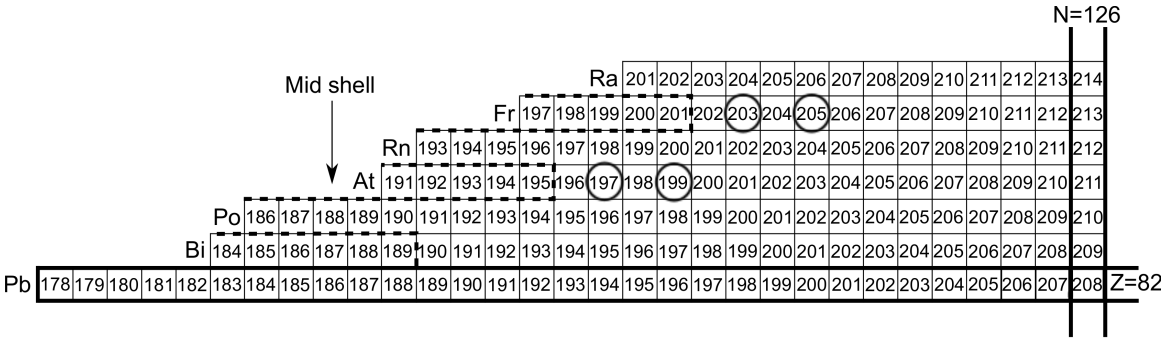

Figure 1.1: Section of the nuclear chart relevant for the thesis work. The nuclei are labelled according to their mass number A, which is the sum of the atomic number Z (the number of protons) and the number of neutrons N. The atomic number increases when moving upward in the scheme and the neutron number when moving to the right. Nuclei with the same Z are called isotopes of an element, the ones with the same N are called isotones and the ones sharing the same A are known as isobars. The proton and neutron shell closures are indicated with thicker lines and the proton drip-line by dashed lines. The neutron mid-shell, that is the middle point between adjacent neutron shell closures, is indicated by an arrow. The nuclei studied in the present work are encircled.

spin at best. Contemporary in-beam gamma-ray spectroscopy involves the utilisation of large germanium-detector arrays consisting of increasingly complicated detector configurations in combination with elaborate data-acquisition techniques. These arrays are usually operated in conjunction with a particle accelerator and they may even move between accelerator laboratories. The study of low-spin and ground-state properties of nuclei involves, besides gamma-ray spectroscopy, charged-particle spectroscopy such as alpha-particle and conversion-electron spectroscopy. Often spectrometers for this purpose are mounted at the focal plane of a recoil separator and include a combination of different types of detectors operating together. Such spectrometers are used for a variety of applications of which a prominent example is the identification of new atomic elements. When combining these spectroscopic techniques, a powerful tool for the study of nuclear structure is obtained.

New phenomena in nuclear physics are often searched for at the extremes of nuclear existence. Such areas are for instance nuclei at the proton or neutron drip-line, very heavy nuclei or nuclear states at very high spin. The nuclei studied in the present work, see figure 1.1, belong to the lightest among those atomic elements that are heavier than lead, and that have no known stable isotopes. The elements in this region, such as astatine or francium, are the very rarest ones known on earth and they are only observed in nature in the decay chains of heavy elements. To be more precise, the nuclei that the present work concentrates on are situated close to the proton drip-line; the extreme boundary behind which the nuclei are proton-unbound in their ground state. The high relative number of protons against the number of neutrons causes the nuclei in this region to be very unstable against fission even at moderate excitation energies. This makes the artificial production of these nuclei for in-beam

studies in the laboratory very difficult due to the high probability of the nucleus to fission immediately after it has been produced. Consequently the production yields are low which sets high demands on the experimental apparatus and makes the study of these nuclei, from an experimentalist's point of view, quite challenging.

The properties of the nuclei in this region are strongly affected by the proximity of the $Z = 82$ proton shell closure, see figure 1.1. For example intruder configurations (see for instance [Heyde11]) associated with nuclear deformation and the possible consequence shape coexistence are interesting topics to study in nuclei in this region. The intruder model describes particle-hole excitations across closed shells, such as the $Z = 82$ shell closure, forming configurations that can become favourable in energy, that is "intrude" down in energy as a function of neutron number with a systematically parabolic behaviour. By studying the evolution of these configurations, ultimately new information on the interactions that govern the changes in level energies may be obtained. Nuclear deformation and, furthermore, shape coexistence have been observed throughout the nuclear chart, and it has been suggested that the spherical structure of a nucleus is merely a special case in a large variety of deformations nuclei can exhibit [Heyde11]. A good example of deformed cases are the neutron-deficient lead nuclei, where states with oblate and prolate deformation have been observed alongside the spherical ground state. The deformed states are, moreover, associated with the intruder configurations (see for example the work by Julin *et al.* [Julin01] and references therein). A well-known case, which today is a classic example of shape coexistence, is the neutron mid-shell nucleus ^{186}Pb where both an oblate and a prolate shaped excited 0^+ state have been found to coexist with the spherical ground state [Andreyev00]. Similar oblate configurations as in the lead nuclei have also been reported to exist in neutron-deficient polonium nuclei [Oros99, Julin01]. Here the intruder configurations can even become strongly mixed with the spherical ones in the ground state [Van Duppen00] when approaching the neutron mid-shell. New results have recently been published for polonium nuclei. Laser-spectroscopic studies [Cocolios11, Seliverstov13] report the onset of ground-state deformation of polonium nuclei in ^{197,198}Po. These results show a change in the character of the ground states in polonium nuclei to that of the ground states in lead nuclei, which have by laser-spectroscopic studies been shown to remain spherical beyond the neutron mid-shell [De Witte07]. Figure 1.2 presents with filled symbols the excited 0^+ states based on the intruder configurations observed in neutron deficient lead and polonium nuclei. In the lightest lead nuclei the prolate intruder 0^+ state has been observed alongside the oblate one. In polonium nuclei the excited oblate 0^+ state has been observed and the lightest nucleus where this state has been reported is ^{196}Po [Van Duppen00]. Although the excited intruder 0^+ state itself is not known in the lighter polonium nuclei, information may be gained by studying the effects of the intruder configuration on other excited states in the nucleus. For example Grahn *et al.* [Grahn06] suggest, by studying the lifetimes of the excited 2^+ and 4^+ states, that the ground state in ^{194}Po is dominated by oblate structures. Moreover, the levelling off of the excitation energy of the

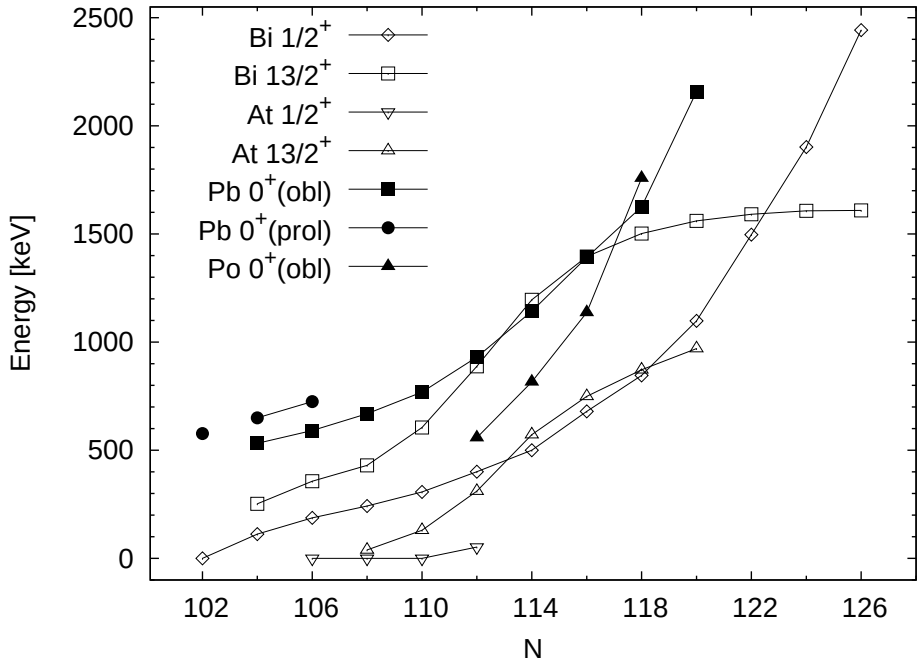

Figure 1.2: Systematics of the isomeric $13/2^+$ ($\pi i_{13/2}$) and intruder $1/2^+$ ($\pi(s_{1/2})^{-1}$) state in neutron-deficient bismuth and astatine nuclei together with the intruder 0^+ states in the lead and polonium isotones. The lead data are taken from the references [Van Duppen84, Kantele86, Van Duppen87, Le Coz99, Andreyev99, Van Duppen00, Andreyev00], the polonium data from the references [Bijnens98, Van Duppen00], the bismuth data from references [Alpsten69, Lönnroth82, Lönnroth86, Chapuran86, Braga86, Coenen86, Firestone96, Andreyev01, Hürstel02, Kettunen03a, Kettunen03b, Andreyev04a, Nieminen04] and the astatine data from references [Dybdal83, Davie84, Coenen86, Lach00, Kettunen03a, Kettunen03b, Andgren08, Nyman13].

yrast states in ^{192}Po indicates that the oblate intruder configuration has reached the ground state [Helariutta99]. When moving even further towards the neutron mid-shell, the prolate intruder structure is additionally reported to become yrast for the 4^+, 6^+ and 8^+ states in ^{190}Po [Van de Vel03, Wiseman07], based on the level energies of the three states. Moreover, results from alpha-decay studies suggest that the ground state in ^{189}Po and in lighter isotopes is prolate deformed [Van de Vel05, Andreyev06a]. The neutron-deficient radon nuclei are less well-known than the polonium nuclei, and the excited intruder 0^+ states have not been observed yet. The first signs of the intruder configurations have, however, been observed in the excited states of the light radon isotopes (see for example the work by Dobson *et al.* [Dobson02] and references therein). Moreover, the ground state is suggested to become deformed in ^{196}Rn [Kettunen01] and further to be prolate deformed in ^{193}Rn [Andreyev06b], based on results from alpha-decay studies.

When studying nuclei in this region, the question arises if similar configurations may be found in the odd-Z isotones of the lead and polonium nuclei and, moreover, if they

can be found further away from the proton shell closure such as in francium nuclei. Deformed states in odd-Z nuclei in this region may either originate from an intruder proton configuration itself or the odd proton may possibly be coupled to such a configuration in the even-even core. By studying the evolution of these low-lying states information can be gained concerning the properties of the intruder proton configuration, or a change in the properties of the core which the odd proton is coupled to may be observed. This information can be gained by investigating the deexcitation patterns of these states, and through the properties of possible rotational bands built on them. This thesis concentrates on the properties of the $9/2^-$ ($\pi h_{9/2}$), $1/2^+$ ($\pi(s_{1/2})^{-1}$) and $13/2^+$ ($\pi i_{13/2}$) states[1]. These three states are often related to shape coexistence and they are, furthermore, often associated with the intruder picture. The nuclei ^{197}At and ^{199}At lie in the region where oblate deformation of the ground state is expected to set in, based on the results from the studies of polonium nuclei. In the region above lead the intruder $1/2^+$ state in odd-Z nuclei is formed by a similar mechanism as the intruder configurations in their even-Z isotones. This state is well-known throughout the neutron-deficient bismuth nuclei and becomes the ground state in ^{185}Bi [Andreyev04a]. Systematics of the $1/2^+$ state in the neutron-deficient bismuth nuclei are included in figure 1.2. Note how similar the downward-sloping behaviour of this state is as compared with the oblate 0^+ state in the lead nuclei. The $1/2^+$ state is less well-known in the astatine nuclei, where it has been observed at low excitation energy through its alpha-decay branch [Coenen86, Kettunen03a, Kettunen03b]. An upward-sloping behaviour of the $1/2^+$ state, when moving towards heavier isotopes, has not yet been well established. In the neutron-deficient francium nuclei the state has previously been observed in ^{201}Fr and ^{203}Fr [Uusitalo05] at low excitation energy, however, the level energy in ^{203}Fr has not been determined. Very recent results suggest that the $1/2^+$ state becomes the ground state in ^{199}Fr [Kalaninová13, Uusitalo13]. Although conclusions on the configuration of the ground state have not been made, Uusitalo *et al.* suggest that the structure of the ground state changes from that of heavier francium isotopes, where the ground state is based on the $\pi h_{9/2}$ configuration. Similarly as for the $1/2^+$ state, the isomeric $13/2^+$ state is quite well-known in the neutron-deficient bismuth nuclei (see for example the work by Nieminen *et al.* [Nieminen04] and references therein). In the nuclei ^{191}Bi, ^{193}Bi and ^{195}Bi a rotational band has been observed to be built on this state [Nieminen04, Pai12], indicating that the nucleus is deformed in this state. Nieminen *et al.* suggest that this deformation originates from the coupling of the $i_{13/2}$ proton to the oblate intruder configuration of the lead core. A similar downward-sloping behaviour of this state, when moving towards the neutron mid-shell, has been observed in the corresponding astatine nuclei. Prior to this study, a rotational band built on this state in astatine nuclei had only been observed in ^{199}At [Styczeń99]. In the study by Andgren *et al.* [Andgren08] Total Routhian surface (TRS)-calculations were performed, suggesting a substantial oblate deformation for this state in ^{197}At. Thus the existence of a rotational band

[1]Here π denotes that the configuration is based on a proton orbital.

in this nucleus could be anticipated as well. In the neutron-deficient francium nuclei this state had not been observed prior to this study. The isomeric $13/2^+$ states in neutron-deficient bismuth and astatine nuclei have been added to figure 1.2 for comparison.

This thesis is a spectroscopic study of the neutron-deficient nuclei ^{197}At, ^{199}At, ^{203}Fr and ^{205}Fr. The aim of the study is to trace the evolution of low-lying excited states in neutron-deficient odd-mass nuclei in the region above lead. In more detail, an attempt is made to probe the intruder configurations in low-lying states of francium and astatine nuclei. New information on the properties of the ground state and the $13/2^+$ state for ^{197}At is presented. Discrepancies based on previous results are resolved in ^{199}At, and a higher-lying isomer and the $1/2^+$ state are observed for the first time. This thesis extends the knowledge of the excited states in the nuclei ^{203}Fr and ^{205}Fr that are less well-known than for example the corresponding states in ^{197}At and ^{199}At. In ^{203}Fr only the $1/2^+$ state has previously been observed besides the ground state [Uusitalo05] and in ^{205}Fr only states promptly feeding the ground state have been reported [Hartley08]. The $1/2^+$ state has now been observed for the first time in ^{205}Fr and the level energy of the state has been established in ^{203}Fr. This work includes first observations of the isomeric $13/2^+$ state in both ^{203}Fr and ^{205}Fr, and indeed therefore the first observation of this state in neutron-deficient francium nuclei altogether. Structures built on the $9/2^-$ state and the $13/2^+$ state have, moreover, been established in this work.

The collection of studies forming the basis of this thesis was performed during the years 2007-2013 at the accelerator laboratory of the University of Jyväskylä (JYFL-ACCLAB). The nuclei were produced through fusion-evaporation reactions, with a heavy-ion beam, provided by an ECR ion source (6.4 GHz or 14 GHz) and accelerated with the K-130 cyclotron, impinging on a thin target. The fusion-evaporation recoils were separated using the gas-filled recoil separator RITU [Leino95] and detected at the focal plane of RITU with the GREAT spectrometer [Page03]. The radiation emitted by the fusion-evaporation recoils was studied employing the GREAT spectrometer and the JUROGAM [Beausang92, Rossi Alvarez93] germanium-detector array at the target position. The measurements of ^{197}At and ^{199}At were performed in collaboration with the nuclear physics group at the Royal Institute of Technology (KTH) and the measurement of ^{203}Fr and ^{205}Fr were performed in-house. Altogether five experiments were performed within twenty days of beam time.

This thesis will start with a brief introduction to the physics background relevant for the work described in chapter two. Nuclear models will be introduced and nuclear disintegration will be discussed. Experimental techniques will be presented in chapter three together with the instrumentation used by the RITU-Gamma group for spectroscopic studies. Throughout this chapter and especially in the section for data-analysis methods, examples from the studies will be presented as an illustration. The experimental results will be summarised in chapter four and compared with systematics in

the region of nuclei in chapter five. Finally conclusions will be presented in chapter six together with future prospects.

The results presented in this thesis have been published in three scientific publications, where the author of the thesis has performed the analysis and has acted as the leading author in the writing process. The publications are listed below and they are attached as appendices A-C.

U. Jakobsson, J. Uusitalo, S. Juutinen, M. Leino, P. Nieminen, K. Andgren, B. Cederwall, P. T. Greenlees, B. Hadinia, P. Jones, R. Julin, S. Ketelhut, A. Khaplanov, M. Nyman, P. Peura, P. Rahkila, P. Ruotsalainen, M. Sandzelius, J. Sarén, C. Scholey, and J. Sorri
Prompt and delayed spectroscopy of ^{199}At
Phys. Rev. C **82**, 044302 (2010)

U. Jakobsson, J. Uusitalo, S. Juutinen, M. Leino, T. Enqvist, P. T. Greenlees, K. Hauschild, P. Jones, R. Julin, S. Ketelhut, P. Kuusiniemi, M. Nyman, P. Peura, P. Rahkila, P. Ruotsalainen, J. Sarén, C. Scholey, and J. Sorri
Recoil-decay tagging study of ^{205}Fr
Phys. Rev. C **85**, 014309 (2012)

U. Jakobsson, S. Juutinen, J. Uusitalo, M. Leino, K. Auranen, T. Enqvist, P. T. Greenlees, K. Hauschild, P. Jones, R. Julin, S. Ketelhut, P. Kuusiniemi, M. Nyman, P. Peura, P. Rahkila, P. Ruotsalainen, J. Sarén, C. Scholey, and J. Sorri
Spectroscopy of the proton drip-line nucleus ^{203}Fr
Phys. Rev. C **87**, 054320 (2013)

The following publications arose from the experimental data that also was the basis for the studies producing the first publication presented above. The author performed a parallel independent analysis of the data for the first publication and was involved in carrying out the experiments producing both publications.

K. Andgren, U. Jakobsson, B. Cederwall, J. Uusitalo, A. N. Andreyev, S. J. Freeman, P. T. Greenlees, B. Hadinia, A. Johnson, P. M. Jones, D. T. Joss, S. Juutinen, R. Julin, S. Ketelhut, A. Khaplanov, M. Leino, M. Nyman, R. D. Page, P. Rahkila, M. Sandzelius, P. Sapple, J. Sarén, C. Scholey, J. Simpson, J. Sorri, J. Thomson, and R. Wyss
Gamma-ray spectroscopy of ^{197}At
Phys. Rev. C **78**, 044328 (2008)

K. Andgren, B. Cederwall, J. Uusitalo, A. N. Andreyev, S. J. Freeman, P. T. Greenlees, B. Hadinia, U. Jakobsson, A. Johnson, P. M. Jones, D. T. Joss, S. Juutinen, R. Julin, S. Ketelhut, A. Khaplanov, M. Leino, M. Nyman, R. D. Page, P. Rahkila, M. Sandzelius, P. Sapple, J. Sarén, C. Scholey, J. Simpson, J. Sorri, J. Thomson, and R. Wyss
Excited states in the neutron-deficient nuclei $^{197,199,201}Rn$
Phys. Rev. C **77**, 054303 (2008)

Chapter 2

Theoretical background

This chapter provides a brief description of the theoretical background central for the present work. The spherical shell model and deformed shell model will be discussed, and collective effects will be touched upon with a concentration on nuclear rotation. Following that, radioactive decay and its different forms will be described. Emphasis will be given to alpha decay and gamma-ray emission together with internal conversion, all essential for the present work.

2.1 Nuclear models

The liquid-drop model, where the atomic nucleus is assumed to behave like a drop of liquid, is considered to be the simplest nuclear model. The applicability of this model is supported by the success of the compound-nucleus model and that of the description of nuclear fission, both describing large scale properties of the nucleus. The model was also helpful in the construction of the semi-empirical mass formula which predicts binding energies of nuclei quite successfully. The liquid-drop model, however, cannot describe nuclear properties that require finer detail. For instance nucleon separation energies do not have a monotonic behaviour with respect to nucleon number, but show drastic changes when crossing certain nucleon numbers, named magic numbers. A quantum-mechanical approach was therefore taken and a shell-like structure, familiar from atomic physics, of the nucleus was suggested to account for these observations. This model was, however, not satisfactory until the spin-orbit splitting was introduced by Mayer, Haxel, Jensen and Suess [Mayer49, Haxel49] in 1949, which proved to be a major breakthrough in understanding the behaviour of the nucleus at the magic numbers. The model, known as the spherical shell model, is a widely used model of the atomic nucleus.

The spherical shell model assumes that the protons and neutrons move independently

in a central potential that is created by their surrounding nucleons obeying the Pauli exclusion principle. The energy of the nucleon will be quantized according to the principal quantum number N, the orbital angular momentum quantum number l and the total angular momentum quantum number j. The l quantum number has the notation where the values $l = 0, 1, 2, 3, 4, 5, ...$ are named by the letters $s, p, d, f, g, h, ...$, respectively, adapted from atomic physics. The spin-orbit interaction couples the orbital angular momentum of the nucleon to its intrinsic spin ($s = 1/2$) to form two total angular momentum orbitals with $j = l \pm 1/2$. The two orbitals undergo spin-orbit splitting and the higher-j orbital lies lower in energy. Each j orbital holds a number of $2j + 1$ like nucleons. The orbitals are bunched together to form major shells separated by gaps called shell closures at the magic numbers. The parity quantum number $\pi = (-1)^l$ can be defined for each orbital based on the symmetry properties of the orbital angular momentum wave function. Positive parity $(+)$ is assigned for even-l orbitals and negative parity $(-)$ for the odd-l orbitals. Most of the orbitals in a major shell have the same parity, however, the spin-orbit splitting can push a $j = l + 1/2$ orbital from a higher-lying major shell down to a lower-lying one. This orbital will have a unique parity as compared with surrounding orbitals and is called a shell-model intruder orbital. Such an orbital is for example the $i_{13/2}$ orbital in figure 2.1. In the simplest approach the j orbitals are filled up by the nucleons to the Fermi level, with the orbital where the last valence nucleon lies determining the properties of the nucleus. Single-particle states can be generated by exciting the valence nucleon to higher orbitals, or by exciting a nucleon beneath the Fermi level to create a nucleon vacancy called a hole. The hole is treated in a similar manner as a particle.

The shell structure of the nuclei could be seen in the behaviour of the nuclear electric quadrupole moments across the nuclear chart, but the spherical shell model with the single particle could not explain the magnitude of the electric quadrupole moments observed in some nuclei. Rainwater then suggested that by allowing the nucleus to become deformed, the high quadrupole moments could be explained [Rainwater50]. This led to the requirement that the shell model needed to be refined for the cases where the nucleus is deformed. A j orbital of the spherical shell model consists of $2j + 1$ magnetic sub-states. Each sub-state is denoted by the quantum number m, associated with the projection of j onto a chosen axis, with values ranging from $-j$ to j. These states will be degenerate in a spherically symmetric potential. However, when the potential is stretched along one axis, called the axis of symmetry, this degeneracy is removed and the j orbital will split into twofold-degenerate orbitals each described by the projection of j onto the axis of symmetry. This splitting is illustrated, as a function of quadrupole deformation of the potential, in figure 2.1 for proton orbitals relevant to the present work. The model describing the evolution of the arising new orbitals is called the deformed shell model or the Nilsson model [Nilsson55] and the orbitals consequently Nilsson orbitals. As j is no longer a good quantum number, a new set of quantum numbers is required. The asymptotic quantum numbers $\Omega^\pi[Nn_r\Lambda]$ are generally used. Here N and π are familiar from the spherical shell model. The quantum

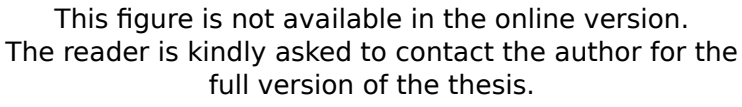

Figure 2.1: Nilsson diagram of proton orbitals, relevant for the present work, in a quadrupole deformed potential. The model reproduces the spherical orbitals when $\varepsilon_2 = 0$. The shapes drawn into the figure serve as a guide to the two areas of the Nilsson diagram, the eccentricities have been highly exaggerated. Note that $\varepsilon_2 \approx 0.95\beta_2$ [Firestone96], β_2 is used in the text. In producing the figure a hexadecapole deformation $\varepsilon_4 = \varepsilon_2^2/6$ has been applied. The figure is taken from Table of Isotopes [Firestone96] page H-15. Copyright Wiley-VCH Verlag GmbH & Co. KGaA. Reproduced with permission.

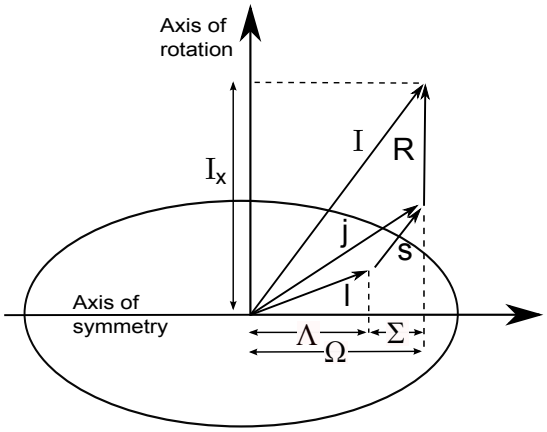

Figure 2.2: The asymptotic quantum numbers defined for the single particle in the deformed shell model together with quantum numbers related to nuclear rotation. The quantum numbers for the single particle arise from the projection of those of the spherical shell model onto the symmetry axis. R denotes the rotation of the nucleus.

numbers Ω and Λ are presented in figure 2.2 as the projections of l and j, respectively, onto the symmetry axis. Lastly the quantum number n_r describes the number of radial nodes. The magnitude of the quadrupole deformation in figure 2.1 is depicted on the horizontal axis and is described by the parameter ε_2. Most commonly, however, the quadrupole deformation parameter β_2 is used, with the subscript denoting the multipolarity of the deformation. Both ε_2 and β_2 are connected to the eccentricity of the nucleus. A negative β_2 value describes oblate (disc-like) deformation and a positive value prolate (cigar-like) deformation. These shapes have been drawn in figure 2.1. Alternatively the Lund convention (see for instance [Nilsson95]) may be used, where $\beta > 0$ and the deformation is described by the parameter γ, where $\gamma = -60°$ stands for collective oblate deformation and $\gamma = 0°$ for collective prolate deformation. Values of γ between those of oblate and prolate denote triaxial shapes. In these cases there is no axis of symmetry.

The single-particle approach describes the properties of the nucleus as being solely defined by the last valence particle. Although it is a very useful approximation, it is not always very realistic. Instead one may consider all valence particles outside closed shells to have a collective effect on the nuclear properties. Such an effect can be seen for example in the evolution of level energies of low-lying states in nuclei when adding more valence nucleons. The Grodzins rule indicates this by relating the $B(E2)$ value (to be discussed in section 2.2.2) of the transition from the first 2^+ state to the 0^+ ground state with the inverse of the level energy of the 2^+ state [Grodzins62]. Thus the gradual lowering in energy of the first 2^+ state indicates a smooth increase in collectivity. Other typical signs of collaboration between the nucleons are the collective motions in which a large number of the nucleons take part. Nuclear vibration is one of such motions, where the nuclear shape vibrates in a liquid-drop-like way around a spherical equilibrium shape. The vibration may take on different multipoles, all with their own characteristics, and nuclear states will emerge based on the vibrational quanta called phonons. As an example a distinct sign of quadrupole vibrational states is the level energy ratio $E(4_1^+)/E(2_1^+) = 2.0$ of a nucleus with an even number of

protons and of neutrons. Furthermore, when the equilibrium shape of the nucleus is deformed, nuclear rotation may be observed. The rotation manifests itself in a sequence of rotational states called a rotational band. For a rigid rotor with an even number of protons and of neutrons the inspection of the $E(4_1^+)/E(2_1^+)$ ratio gives the value 3.33 called the rigid rotor limit. In a typical "horizontal" inspection of the level energies the nuclei start at shell closures with the $E(4_1^+)/E(2_1^+)$ ratio of less than 2.0 and evolve into vibrational nuclei and further through a transitional region finally to rotational nuclei at the open shell. The change of the $E(4_1^+)/E(2_1^+)$ ratio is expected to be quite smooth in the transitional region. Similar energy-level inspections can be done for odd-mass nuclei [Bucurescu94]. Nuclear rotation will be discussed further in the following.

The rotation of the nucleus can be described by the moment of inertia $\mathscr{I}$, with an analogy to a classical description of a rotating body. The moment of inertia can therefore be associated with the response of the nucleons (forming the nucleus) to the rotation of the nucleus. The kinematic moment of inertia $\mathscr{I}^{(1)}$ can be derived from experimental data to study the behaviour of the rotating nucleus, and it is often plotted against the rotational frequency ω of the nucleus [Bohr75]

$$\mathscr{I}^{(1)} = \hbar \frac{I_x}{\omega(I_x)}, \tag{2.1}$$

where $\omega(I_x)$ is extracted from the level energies and spins of the $I+1$ and $I-1$ states through the following relation

$$\omega(I_x) = \frac{1}{\hbar} \frac{E_{I+1} - E_{I-1}}{(I+1)_x - (I-1)_x}, \tag{2.2}$$

and $I_x = \sqrt{I(I+1) - \Omega^2}$ is the projection of I onto the axis of rotation. The values for the nuclear moment of inertia generally lie between that of a rigid rotor and fluid-like behaviour, and they change smoothly as the rotational energy increases. Deviations from this smooth behaviour, such as an upward bend, may indicate structural changes inside the rotating body. The kinematic moment of inertia cannot explain the details of such a change. Often the aligned angular momentum $i(\omega)$ is used, where the angular momentum of the rotational band is plotted with respect to the rotational properties of a chosen reference band. A sudden upward bend in such a plot signals a sudden gain in angular momentum of the system. By a comparison with similar bands in close-lying nuclei, a common feature may be found. To further gain knowledge of the valence particles causing the change of the rotational properties, the cranked shell model [Inglis54] is employed, where a transfer into the coordinate system of the rotating nuclear core is made. The properties of the valence particles may then be studied. Changes in these properties can be attributed to effects caused by "fictitious"

forces due to the rotating coordinate system. At slow rotation these effects are small, but at faster rotation they can cause phenomena such as the alignment of the particle angular momentum with that of the rotational core, resulting in a gain in total aligned angular momentum. The effects are interpreted as having a classical analogy in the Coriolis force observed on the Earth.

The particle rotor model [Bohr53] describes the rotational properties of the deformed nucleus with a valence particle coupled to the rotation. An axis perpendicular to the symmetry axis is chosen and the nuclear core is set to rotate around it with the rotational quantum number R (see figure 2.2). The nuclear states with spin I will now include components of angular momenta from the odd particle and the rotating core, and the rotational states form a regular band-like structure on top of the band head with $I = \Omega$. The Nilsson orbital will split into two orbitals which are known as signatures and are denoted by the quantum number α (see for example reference [deVoigt83]). The quantum number α has the values $\pm 1/2$ for an odd-mass nucleus. Of these two values the one denoting the favoured signature can be determined by the relation $j \equiv \alpha \mod 2$. Moreover, the rotational states I belonging to either signature can be determined by the relation $I \equiv \alpha \mod 2$. Experimentally the rotational band of an odd-mass nucleus will consist of two parallel cascades consisting of stretched $E2$ transitions representing the two signatures. Transitions with $M1$ character are observed linking the two signatures together. In the strong-coupling scheme [Bohr53] the odd particle is strongly coupled to the motion of the core and is therefore able to feel the slow rotation of the core. This is observed by the state I of the favoured signature being halfway between the states $I-1$ and $I+1$ of the unfavoured signature. This is an ideal case and often a signature splitting of the band can be observed by the rising in energy of the unfavoured signature. This alters the feeding between the two signatures with every second $M1$ transition having a higher energy. A reason for the splitting can for example be the perturbative effect of the Coriolis force acting on the valence particle moving in the rotational frame of reference of the core [Stephens75]. The Coriolis force is pronounced in low-Ω Nilsson orbitals from high-j spherical orbitals and increases with increasing I of the nucleus. At worst the rotational spectrum may consequently be completely distorted. As a fingerprint a decoupled band, consisting solely of the stretched $E2$ transitions from the favoured signature, resembling that of the neighbouring even-even core is observed as the states of the unfavoured signature lie high in energy. For high-Ω states, such as the ones in this thesis work, the effect is moderate at best and a strong coupling is observed. In the region of nuclei above lead the odd particle having a high Ω quantum number is coupled to an oblate core and that of low Ω to a prolate core. The opposite holds, however, if the odd particle is a hole.

The average nuclear potential alone cannot describe such effects in nuclei as the ground state spin and parity of 0^+ of even-even nuclei or the differences in nucleon binding energy between odd-mass and even-mass nuclei. These effects have been attributed

to the pairing interaction; an attractive strong short-range residual force acting on like particles on identical orbitals, with angular momenta antialigned due to the Pauli exclusion principle (see for instance [Casten00]). This leads to the approach discussed above that all particles in even-even nuclei are paired in the ground state to a net spin and parity of 0^+ and that the spin of the odd-mass nucleus is by a good approximation determined by that of the odd particle. For the coupling of like particles in non-identical orbitals a longer range residual interaction is applied (see for instance [Casten00]). In this case for like particles the I_{MAX} or I_{MIN} coupled state comes lowest in energy. The case of a coupling between protons and neutrons is represented by the parabolic rule of Paar [Paar79], in which an I_{MIN} or I_{MAX} coupled state may be favoured and lowest in energy if the coupling is between two particles or two holes. If either the proton or the neutron is of hole type the parabola is reversed and an $I_{\mathrm{MAX}} - 1$ state can become favoured.

Besides single-particle features, the proton-neutron interaction is, furthermore, suggested to play a leading role in the deformation of nuclei (see for instance [Casten00]). Consequently the tendency of the nuclei to deform is associated with the number of valence nucleons of both kinds and hence singly magic nuclei are not deformed in their ground state whereas open-shell nuclei may exhibit substantial deformation as the proton-neutron interaction has reached its maximum effect. Particle-hole excitations across the shell gap do, however, create valence nucleons, such that singly magic nuclei may have low-lying excited states that are deformed. The states formed through such an excitation are known as intruder states. Nuclei near shell closures already include valence nucleons of both kinds, however, intruder excitations further increase the number of valence nucleons in these nuclei. Unlike intruder states in singly magic nuclei, the intruder states in nuclei near shell closures may become favoured and reach the ground state leading to a substantial ground-state deformation. Consequently a nucleus, at or near a shell closure, can be observed to exhibit different low-lying structures associated with different shapes. This phenomenon, expected to occur throughout the nuclear chart, is known as shape coexistence. Shape coexistence was first introduced in 1956 by Morinaga, who suggested that the nucleus ^{16}O has a highly deformed state resembling a structure of four alpha particles in a row [Morinaga56]. This state coexists in ^{16}O at a high excitation energy, with the spherical ground state. In the even-mass nuclei in the lead region the intruder configurations are associated with the particle-hole excitation of protons across the $Z = 82$ shell closure. By creating a $2p-2h$ excitation an excited 0^+ state is generated with oblate deformation. Moreover, the creation of a $4p-4h$ excitation across the proton shell closure generates a 0^+ intruder state with prolate deformation. In neighbouring odd-mass nuclei similar intruder characteristics are associated with a $1p-1h$ excitation with oblate deformation and a $3p-3h$ excitation with prolate deformation. In these two cases a $1/2^+$ state is generated in nuclei above lead. See for example reference [Heyde11] for more information on the intruder concept and shape coexistence. In the discussion above the particle-hole excitations are made based on the spherical

shell model. An alternative approach to intruder states can be made starting from the Nilsson model [Nilsson55] for a deformed nucleus. In this scheme the level energy of the intruder state originating from a quasiparticle excitation decreases when moving towards the neutron mid-shell together with the increasing nuclear deformation [Heyde89]. The resulting behaviour of the level energy of the intruder state is quite similar to that obtained from the spherical shell model approach. Moreover, Heyde *et al.* report that the two approaches presented above are, in fact, equivalent [Heyde89].

2.2 Radioactive decay

The ever increasing number of known nuclei is now estimated to be over 3300 [nndc13]. With the number of practically stable nuclei being 288 [Erler12], it is evident that most nuclei are unstable in their ground state and undergo radioactive decay to become a more tightly bound daughter nucleus. This process will go on, forming a decay chain, until a stable final nucleus is reached. The radioactive nuclei can be said to form two slopes around the so-called valley of stability on the nuclear chart, also known as the Segré chart, a grid where the known nuclei are mapped according to their proton and neutron number (see for instance [Magill06]).

Radioactive decay is a statistical process governed by the exponential distribution. The spontaneous decay of a nucleus is normally independent of the conditions of its surroundings and also of the decay of adjacent nuclei. The number of remaining nuclei $N(t)$ of a given type at a chosen point t in time in a sample can be predicted by the exponential law of radioactive decay (see for instance [Krane88])

$$N(t) = N(0)e^{-\lambda t}, \tag{2.3}$$

where $N(0)$ is the number of nuclei at time $t = 0$ and λ is the decay constant which is characteristic to the decaying nuclear state. The half-life $T_{1/2}$ of the activity describes the time in which half of the original activity has decayed, and it is related to the decay constant by the relation

$$T_{1/2} = \frac{\ln 2}{\lambda}. \tag{2.4}$$

A nuclear state may have decay branches to different final states. For each branch a partial decay constant can be defined and the total decay constant is the sum of all partial decay constants. Considering equation (2.4) a partial half-life can be defined for each branch and the inverse of the total half-life is the sum of the inverses of the

partial half-lives. Measurements always yield the total half-life and the partial half-life is merely useful when further studying the properties of the corresponding decay branch. The partial half-life $T^i_{1/2}$ for branch i can be expressed based on the total half-life and the branching ratio b_i in the following way

$$T^i_{1/2} = \frac{T_{1/2}}{b_i}. \tag{2.5}$$

The branching ratio is defined as the percentage of the total decay proceeding through the specific branch.

The most common decay mode of the nuclear ground state is beta decay which can be divided into three decay modes. In β^- decay a neutron is transformed into a proton resulting in the emission of an electron and an electron anti-neutrino. In β^+ decay the reverse occurs, that is a proton is transformed into a neutron and a positron is emitted together with an electron neutrino. Furthermore, electron capture by the nucleus competes with β^+ decay. All three beta-decay modes proceed via isobaric nuclear chains towards the valley of stability. In heavy (neutron-deficient) nuclei alpha decay starts to compete against beta decay, due to the Coulomb repulsion between the protons. Alpha decay proceeds by the emission of a ^{4}He nucleus called an alpha particle. When moving towards neutron-deficient nuclei and further across the proton drip-line, the nuclei become unbound in their ground states against proton emission and proton emission starts to compete as a decay mode. Similarly a neutron drip-line has been established in light neutron-rich nuclei, where neutron emission has been reported. In very heavy nuclei the ground state may decay, besides by particle emission, by spontaneous fission and more exotic decay modes such as that of ^{12}C emission have been observed as well. Besides the particle emission of the unstable ground state, nuclei in excited states may emit electromagnetic radiation when removing excitation energy on the path towards the energy minimum of the ground state. The transition energy is then released by the emission of a gamma-ray quantum. In the following sections, alpha decay and gamma-ray emission together with its competing mode internal conversion, will be discussed.

If the electromagnetic transition from an excited state requires a change of the intrinsic structure of the nucleus, the decay of the state may be slowed down to such an extent that the half-life of the state becomes measurable. Such an excited state is known as a nuclear isomer. It is worth noting, however, that the mere possibility of measuring the half-life of a nuclear state does not make the state an isomer, as the half-life of for instance short-lived collective states can be measured today. The structural change causing the isomerism could for example be a considerable difference in nuclear deformation, in the K-quantum number or in the nuclear spin between the initial and final state [Walker99]. The electromagnetic transition from an isomer can, furthermore, be slowed down to such an extent that particle emission may compete

with the electromagnetic transition. It may even dominate to such an extent that the ground state is completely bypassed. Isomeric states have also been called metastable states. From this stems the use of the superscript m when describing the particle emission of an isomeric state.

2.2.1 Alpha decay

When the Coulomb repulsion between the protons competes against the nuclear binding, an effective way to release energy is the emission of the tightly bound alpha particle. The alpha particle has a spin and parity of 0^+ and carries therefore only orbital angular momentum. As parity is conserved in alpha decay, the parity of the final state in the daughter nucleus will equal that of the parent nucleus if the angular momentum carried by the alpha particle is even and opposite if the angular momentum is odd.

For a nucleus to be unstable against alpha-particle emission, the energy release known as the decay Q-value must be positive

$$Q_\alpha = \big[m(A,Z) - m(A-4,Z-2) - m_\alpha\big]c^2 \; > \; 0, \tag{2.6}$$

where the masses of the parent and daughter nuclei and that of the alpha particle are given as nuclear masses. In many cases only the energy of the alpha particle is measured and the decay Q-value can be obtained using the following relation obtained from energy and momentum conservation

$$Q_\alpha = \Big[1 + \frac{m_\alpha}{m(A-4,Z-2)}\Big]E_\alpha. \tag{2.7}$$

In the one-body model for alpha decay, developed by Gamow, Condon and Gurney [Gamow28, Gurney28], the alpha particle is assumed to be preformed, that is to say it exists as a separate entity inside the parent nucleus. Alpha decay can consequently be regarded as a barrier-penetration problem. The rate of emission of the alpha particle λ is determined by the frequency f at which the particle "knocks" at the barrier, known as the knocking frequency, and by the probability P at which the particle penetrates through the classically forbidden area of the barrier (see for instance [Perlman57])

$$\lambda = fP. \tag{2.8}$$

The knocking frequency can be expressed in terms of the reduced alpha-emission width δ^2 [Perlman57], a quantity that contains the nuclear structure information of the decay. The rate of emission then gets the form

$$\lambda = \delta^2 \frac{P}{h}, \tag{2.9}$$

where h is Planck's constant. The barrier penetration probability P can be expressed as represented by Rasmussen [Rasmussen59]

$$\ln(P) = -2 \int_{R_i}^{R_o} \frac{(2M)^{1/2}}{\hbar} \Big[V(r) + \frac{1}{4\pi\varepsilon_0} \frac{2Ze^2}{r} + \frac{\hbar^2}{2mr^2} l(l+1) - Q_{\text{bare}} \Big]^{1/2} dr, \tag{2.10}$$

where M is the reduced mass of the alpha particle, Ze is the charge and m the reduced mass of the daughter nucleus and l is the orbital angular momentum carried by the alpha particle. The first term of the integrand $V(r)$ expresses the nuclear potential. Rasmussen used the potential presented by Igo [Igo58]. The second term is the Coulomb potential and the third term the centrifugal potential. Q_{bare} expresses the total decay energy exhibited by a bare nucleus, that is taking into account the screening effect of the atomic electrons on the alpha particle. The integral, also known as the Gamow factor [Krane88], is performed over the barrier radius r between the inner R_i and outer R_o turning points.

Equation (2.10) shows that even with the slightest change in the alpha-decay energy Q_{bare} the penetration probability P, and consequently the rate of emission λ, can change drastically. A linear relation between the logarithm of the alpha-particle range and the logarithm of the rate of emission was shown by Geiger and Nuttall as early as in 1911 [Geiger11], and the empirical Geiger-Nuttall rule has been named after their findings. This relationship was, however, not understood until the introduction of the quantum-mechanical one-body model. A modern version of the rule states a linear dependence between $\log(T_{1/2})$ and $1/\sqrt{Q_\alpha}$. This dependence holds strikingly well for half-lives from the order of microseconds to millions of years.

The hindrance factor of alpha decay is generally used when comparing the properties of different alpha decays. One way to express the hindrance factor of a decay is to normalise the δ^2 value of the decay to that of, for example, the ground-state to ground-state alpha decay of a close-lying even-even nucleus. A favoured decay has the factor $\lesssim 4$ and a higher factor indicates that the decay is hindered. The large hindrance of a decay is a sign of structural change between the initial and final state. This implies the great value of alpha decay as a spectroscopic tool when studying the structure of low-lying nuclear states.

2.2.2 Gamma-ray emission

If the nucleus is in an excited state, it can deexcite for instance by emitting electromagnetic radiation. In this case the nuclear charge distribution is assumed to interact

with the surrounding electromagnetic field and the energy is released to the field by the emission of a gamma quantum called a photon. The multipolarity L of the photon is determined by the coupling between the angular momentum of the initial state to the final state such that $|I_i - I_f| \leq L \leq I_i + I_f$, with the lowest multipole being the dominating one. The radiation can be of electric or magnetic character, depending on the possible change in parity between the initial and final state. If the parity of the initial state is equal to that of the final state, the radiation will be of odd magnetic or even electric multipolarity. The opposite holds if the parities are opposite. This rule is illustrated in table 2.1, displayed for the dominating multipole. Further rules read that no magnetic monopoles exist in nature and therefore no M0 transitions either. Finally, the photon carries an angular momentum of at least one unit, and therefore $E0$ transitions cannot proceed via the emission of a gamma ray.

Table 2.1: Illustration of the selection rule between electric (E) and magnetic (M) character of electromagnetic radiation for the lowest multipole depending on the parity of the initial and final states.

$\lvert I_i - I_f \rvert$	1	2	3	4	5	...
Parity equal	$M1$	$E2$	$M3$	$E4$	$M5$	...
Parity opposite	$E1$	$M2$	$E3$	$M4$	$E5$	...

Although the lowest multipole of the transition dominates, higher multipoles can contribute to the transition. However, the higher the multipole the lesser is the contribution. Magnetic transitions are, furthermore, more hindered than their electric counterparts of the same multipolarity. Consequently if the dominating transition is of electric character the next-multipole magnetic transition usually cannot compete, but if the dominating transition is magnetic the next-multipole electric transition may well compete.

The transition probability $T_{fi}(L)$ between the initial and final state [Weisskopf51] can be estimated using the formula

$$T_{fi}(L) = \frac{\ln 2}{T^i_{1/2}} = \left(\frac{2}{\epsilon_0 \hbar}\right) \frac{L+1}{L[(2L+1)!!]^2} \left(\frac{E_\gamma}{\hbar c}\right)^{2L+1} B_{fi}(L), \tag{2.11}$$

where $T^i_{1/2}$ denotes the partial gamma-ray half-life, L denotes the multipolarity of the transition, E_γ the energy of the transition and $B_{fi}(L)$ the reduced transition probability containing the nuclear information. The transition probabilities can be evaluated separately for transitions of electric and magnetic character by using the single-particle estimates proposed by Weisskopf [Weisskopf51] for the reduced transition probabilities. The resulting transition probabilities evaluated for each multipole in table 2.1 are presented in table 2.2. The strength of an observed transition can

be estimated by comparing the experimentally extracted transition probability with that given by table 2.2. The strength is expressed in Weisskopf units (W.u.). If the value exceeds that of one W.u., that is the observed transition rate is higher than the single-particle estimate, the transition is said to be enhanced. The opposite holds if the strength is lower than one W.u. in which case the transition is considered to be delayed.

Table 2.2: Transition probabilities for the first five electric and magnetic multipoles. The transition energies are given in units of MeV. The formulas are taken from reference [Suhonen07].

EL	$T[1/s]$	ML	$T[1/s]$
$E1$	$1.023 \times 10^{14} E^3 A^{2/3}$	$M1$	$3.184 \times 10^{13} E^3$
$E2$	$7.265 \times 10^{7} E^5 A^{4/3}$	$M2$	$2.262 \times 10^{7} E^5 A^{2/3}$
$E3$	$3.385 \times 10^{1} E^7 A^2$	$M3$	$1.054 \times 10^{1} E^7 A^{4/3}$
$E4$	$1.065 \times 10^{-5} E^9 A^{8/3}$	$M4$	$3.316 \times 10^{-6} E^9 A^2$
$E5$	$2.391 \times 10^{-12} E^{11} A^{10/3}$	$M5$	$7.422 \times 10^{-13} E^{11} A^{8/3}$

For strongly-coupled rotational bands, the two signatures can each be identified by a cascade of stretched $E2$ transitions. The signatures are, furthermore, linked together by $M1$ transitions. The ratio of the $M1$ transitions between the two signatures to the stretched $E2$ transitions depopulating each state provides useful information on the properties of the rotational band and the underlying band-head state. The $B(M1)/B(E2)$ ratio can be estimated by solving equation (2.11) for a $M1$ and an $E2$ transition and by applying equations (2.4) and (2.5)

$$\frac{B(M1)}{B(E2)} = 0.697 \frac{E_\gamma(E2)^5}{E_\gamma(M1)^3} \frac{I_\gamma(M1)}{I_\gamma(E2)(1+\delta^2)} \left[\frac{\mu_N^2}{(eb)^2}\right], \tag{2.12}$$

where δ, the mixing ratio (not to be confused with the reduced alpha-emission width), has been added as a non-stretched $E2$ transition can compete with the $M1$ transition between the signatures. For simplification the transitions have been assumed as pure in the present work.

Theoretical estimates for the $B(M1)/B(E2)$ ratios can be obtained with the semi-classical model by Dönau and Frauendorf [Dönau82, Dönau87], in which they propose to study the properties of rotational bands through the examination of magnetic moments. In the model the $M1$ radiation originates from the component of the magnetic moment μ that precesses around the spin vector I. This component is sensitive to the single-particle g-factor g_K, with the collective g-factor $g_R \approx Z/A$ subtracted, and to the quantum number Ω of the underlying band head. From the model the band head, on which the rotational band is built, can be predicted by comparing with the experimental results obtained with equation (2.12). The $B(E2)$ value is proportional to the

intrinsic quadrupole moment accounting for the collective behaviour of the band. See reference [Larabee84] for the equation used in the present work.

In the compound-nucleus reaction, to be discussed further in section 3.1, the beam particle brings in a high amount of angular momentum to the system. The reaction, furthermore, leaves the product nucleus in a highly aligned state with reference to the beam axis [Diamond66] and the alignment is not lost in the short time scale of the nuclear deexcitation. This property of the compound-nucleus reaction enables the study of angular distributions of the gamma rays emitted by the nucleus. The angular distribution $w(\theta)$ of multipole radiation is distinct to the multipole and it can be described by an expanded series of the Legendre polynomial $P_{2L}(\cos\theta)$ as a function of the angle θ [deGroot68]

$$w(\theta) = A_0 P_0(\cos\theta) + A_2 P_2(\cos\theta) + A_4 P_4(\cos\theta) + ..., \tag{2.13}$$

where the three first terms are $P_0(\cos\theta) = 1$, $P_2(\cos\theta) = 1/2(3\cos^2\theta - 1)$ and $P_4(\cos\theta) = 1/8(35\cos^4\theta - 30\cos^2\theta + 3)$ [Spiegel09]. The constants A are specific for the type of radiation with A_0 used for normalization purposes. The comparison is often made between stretched $E2$ transitions and stretched dipole transitions. For a stretched $E2$ transition A_2/A_0 is positive and for a stretched dipole transition negative [Diamond66, Yamazaki67]. In the present work A_4/A_0 is set as zero due to experimental limitations and equation (2.13) is simplified to the two first terms. Finally with the knowledge of the character of the A_2 coefficient, the multipolarity of the radiation may be obtained and, furthermore, the spin of the initial state may be assigned if the spin of the final state is known.

2.2.3 Internal conversion

When a transition proceeds between two states both having a spin and parity of 0^+, the transition cannot proceed via gamma-ray emission, but the transition itself is not forbidden. The transition having an $E0$ character proceeds solely by internal conversion. Furthermore, although higher-multipolarity transitions can proceed via gamma-ray emission, internal conversion can also be observed. Conversion acts in these cases as a competing deexcitation mode to gamma-ray emission. The strength of internal conversion against gamma-ray emission increases according to Z^3, and decreases with increasing transition energy. Consequently internal conversion may well dominate heavily over gamma-ray emission in low-energy transitions of heavy elements. The strength of internal conversion, furthermore, increases with increasing transition multipolarity and the strength is different between transitions of electric and magnetic character. This property enables the extraction of nuclear information

from a comparison of the gamma-ray data of a transition to that of the corresponding internal-conversion data.

In the process of internal conversion the transition energy is transferred to an inner-orbital atomic electron, which is promptly emitted. The energy E_e of the conversion electron is determined by that of the transition E_γ with the electron binding energy B_e subtracted

$$E_e = E_\gamma - B_e. \tag{2.14}$$

As a result the electron spectrum from internal conversion is a line spectrum and electrons associated with a certain transition and emitted from different atomic orbitals are observed at different energies in the line spectrum due to the difference in binding energies between the electron orbitals.

The competition between gamma-ray emission and internal conversion is expressed by the conversion coefficient α, which is defined as the ratio between the transition probabilities of internal conversion λ_e and of gamma-ray emission λ_γ

$$\alpha = \frac{\lambda_e}{\lambda_\gamma}. \tag{2.15}$$

The coefficient may take any value between zero and infinity. A small value indicates that internal conversion is negligible and a large value that it dominates. Based on this equation and the fact that gamma-ray emission and internal conversion together contribute to the total transition probability λ, the transition probability can be expressed with the help of the conversion coefficient in the following way,

$$\lambda = \lambda_e + \lambda_\gamma = \lambda_\gamma(1 + \alpha) = \lambda_e(1 + \alpha^{-1}). \tag{2.16}$$

The probability of electron emission varies depending on which atomic orbital the electron lies on. The total conversion coefficient may then be separately defined for each atomic orbital and the total conversion coefficient is additive

$$\alpha = \alpha_K + \alpha_L + \alpha_M + ... \tag{2.17}$$

Moreover, for the L, M and higher orbitals even a further subdivision can be made. If a transition is highly converted, the gamma rays may not be observed at all. In this case use may be found in comparing the internal conversion between different atomic orbitals such as for example the K and L orbitals, in which case the quantity of comparison is known as the K/L ratio. This ratio decreases with increasing multipolarity,

and may become very similar for high multipolarities, preventing a clear determination. For lower multipolarities the K/L ratio is, however, more widely spaced, which may enable a distinction between the multipolarities. See for example [Alburger57] for K/L ratios obtained for astatine nuclei.

Internal conversion always creates a vacancy on an inner electron orbital that will be rapidly filled by a less-bound electron from a higher-lying orbital. In this process energy is released by the emission of either an X-ray or an Auger electron. In the latter case the energy release is transferred to a less-bound electron that in turn is emitted. Via these processes the electron cloud can relax to a final state that is multiply ionised. The X-rays are named after the orbital of the vacancy, such that a K-X-ray is emitted when a K-orbital vacancy is filled. The competition between X-ray emission and Auger-electron emission depends on the Z of the nucleus and on the orbital in which the vacancy lies. In heavy nuclei the filling of the K-orbital vacancy is nearly always followed by the emission of an X-ray whereas Auger-electron emission may dominate in the filling of vacancies in higher-lying orbitals [Kantele95]. The energy of the X-ray is obtained from the difference of binding energy between the final and initial electron orbitals. It is a direct indication of the element in which the filled vacancy lies, as the electron binding energies are distinct for each element in the periodic table.

Chapter 3

Experimental techniques

This chapter will start with a brief introduction to the fusion-evaporation reaction, used to produce the nuclei studied. The experimental equipment will be presented, followed by a description of the data-processing techniques used in the present work. Throughout this chapter example spectra will be presented from the present data to demonstrate the effects of the analysis technique on the data or to merely introduce the spectra obtainable with the setup used in this thesis work.

3.1 The fusion-evaporation reaction

The nuclei studied were produced through the fusion-evaporation reaction (see for example [Fröbrich96]) by bombarding a stationary target with a beam of heavy ions. For the beam and target nucleus to fuse together they must overcome the Coulomb barrier. The resulting compound nucleus is formed in a highly excited state with a high angular momentum. The excitation energy is redistributed between the nucleons as they rearrange themselves, and the compound nucleus can be said to have "forgotten" its origin, that is to say, the entry channel that produced it. The nucleus has a high amount of excitation energy, it is "hot", and it spins rapidly. To remove this extra energy the compound nucleus evaporates particles such as protons, neutrons or even alpha particles in a stepwise process. In the region of neutron-deficient nuclei close to lead protons and neutrons remove approximately the same amount of excitation energy in the evaporation process. This is due to their binding energy and the Coulomb barrier, which the proton needs to overcome to escape the nucleus. The beam energy is adjusted in such a way that the evaporation process is optimized to favour a certain number of evaporation steps, to produce the desired final nucleus.

Fusion-evaporation cross sections are heavily reduced by the fission competition when producing nuclei in the region above lead. Indeed the channel-specific fusion-evapo-

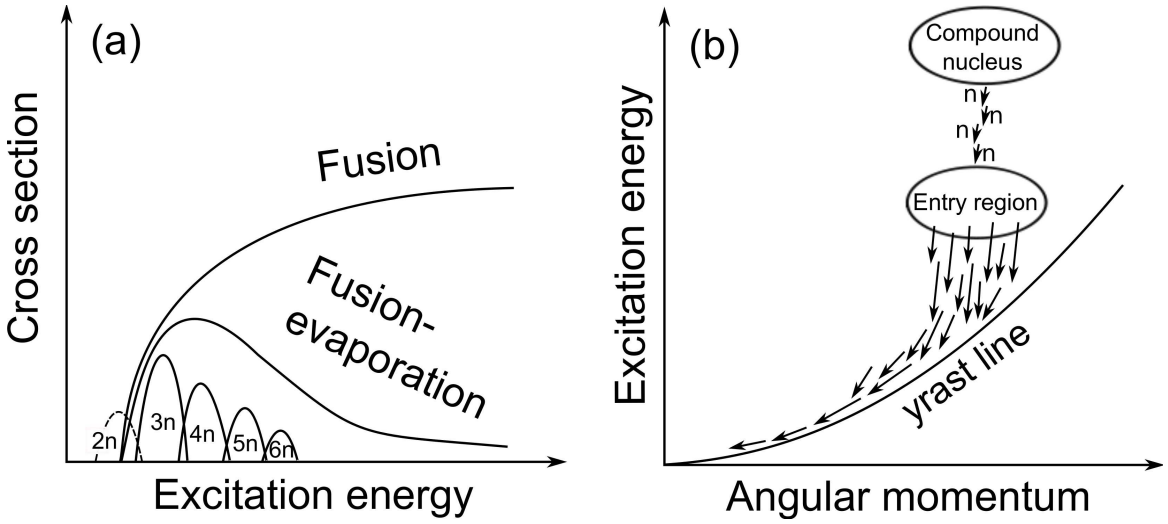

Figure 3.1: (a) Schematic illustration of the fusion-evaporation cross section with respect to excitation energy of the compound nucleus. The cross sections of fusion and fission rise with rising excitation energy, and fission cuts the fusion-evaporation cross section that starts to decrease. The 2n-channel is presented by a dashed line as the fusion barrier cuts this exit channel. The neutron-evaporation channels have been added to roughly present the ^{40}Ar + ^{165}Tm reaction used in the present work. (b) The deexcitation path of the final nucleus, produced in the entry region through the evaporation of neutrons from the compound nucleus, to the yrast line. The $4n$ evaporation channel has been drawn as an example and the arrows from the entry region downward denote emitted gamma rays.

ration cross section in this region decreases approximately by one order of magnitude with each evaporation step as fission competes with each particle evaporation. This effect can be seen in figure 3.1(a) that presents a sketch of the fusion-evaporation cross section with respect to the excitation energy of the compound nucleus. The sketch has been made to roughly describe the reaction that was used to produce the nuclei ^{203}Fr and ^{205}Fr in the thesis work. The total fusion cross section rises with rising beam energy, however, the fusion evaporation cross section decreases after a fast rise due to the fission competition. This effect can also be seen in the figure in the lowering of the cross section of the individual evaporation channels with the increasing number of evaporated neutrons. When the desired nucleus is reached through the evaporation steps, the excitation energy is not sufficient for any further particle evaporation. The final nucleus is, however, still formed in a highly excited state. This so called entry region has a high nuclear level density and the final nucleus removes its remaining excitation energy by promptly emitting statistical gamma rays until it reaches a region of low level density. In this region the nucleus has already cooled down and the remaining excitation energy is removed by gamma rays that are associated with the slowing down of the rotation of the nucleus. Finally the yrast line, describing the parabolic behaviour of the lowest-energy state for a certain spin value, is reached and the nucleus deexcites along this line to the ground state. The deexcitation path start-

ing from the compound nucleus is presented in figure 3.1(b). As can be seen from the figure, the region where the yrast line is reached is dependent on the position of the entry region determined by the fusion-evaporation reaction, with the statistical gamma rays removing little angular momentum. As the evaporated particles, moreover, remove little angular momentum, the position of the entry region is roughly defined by the entrance channel of the fusion-evaporation reaction. As an example, light projectiles induce a small amount of angular momentum to the compound nucleus, which can be useful when studying non-yrast states that have low angular momentum. The reactions used in the thesis work, with experimental details, are presented in Table 3.1.

Table 3.1: The reactions used in the present study with experimental details.

Reaction	Beam energy [MeV]	Beam intensity [pnA]	Target thickness [μg/cm^2]	Irradiation time [h]	Cross section [μb]
$^{118}_{50}$Sn($^{82}_{36}$Kr, $p2n$)$^{197}_{85}$At	362	13	500	178	1.3
$^{150}_{62}$Sm($^{52}_{24}$Cr, $p2n$)$^{199}_{85}$At	231	17	500	80	10
$^{120}_{50}$Sn($^{82}_{36}$Kr, $p2n$)$^{199}_{85}$At	355	10	500	60	15
$^{165}_{67}$Ho($^{40}_{18}$Ar, $6n$)$^{199}_{85}$At	200	6/40	340	30	700
$^{169}_{69}$Tm($^{40}_{18}$Ar, $4n$)$^{205}_{87}$Fr	180	14	410	60	130
$^{169}_{69}$Tm($^{40}_{18}$Ar, $6n$)$^{203}_{87}$Fr	205	13	410	60	4

3.2 Instrumentation

As the target is bombarded with beam particles, the target region is very hostile. A large portion of the beam passes through the target, target atoms are scattered by the beam, and various reactions such as Coulomb excitation, transfer reactions or fission occur. Most of the reaction products are forward-focused and only a fraction of them are the desired fusion-evaporation recoils. It is clear that the recoils need to be firstly separated from the other reaction products and the primary beam particles, and secondly to be moved away from the target area for study. An efficient tool for this is a recoil separator, such as the RITU gas-filled recoil separator, which is the main workhorse in the experimental setup used in the present work. A sensitive detector setup, consisting of an implantation detector combined with ancillary detectors, can be placed at the low-background focal plane of the separator to study the decays of the separated reaction products. This purpose is filled by the GREAT spectrometer located at the focal plane of the RITU separator. To investigate high-spin properties of the recoils, prompt gamma rays need to be measured at the target area. This is

Figure 3.2: Technical drawing of the experimental setup. The beam enters from the right, and impinges on the target in the middle of the JUROGAM array on the right. The fusion-evaporation products are separated from the beam and unwanted reaction products in RITU at the centre of the image and are transported to the GREAT spectrometer on the left. Figure courtesy of Dave Seddon (Liverpool NSG).

often performed using a germanium-detector array. The array consists of germanium detectors, placed in a spherical arrangement around the target chamber, covering a large solid angle for high detection efficiency. The germanium-detector array situated at JYFL is the JUROGAM array[1]. See figure 3.2 for a technical drawing of the experimental setup. The RITU separator, GREAT spectrometer and the JUROGAM array will be presented in closer detail in the following.

3.2.1 The RITU gas-filled recoil separator

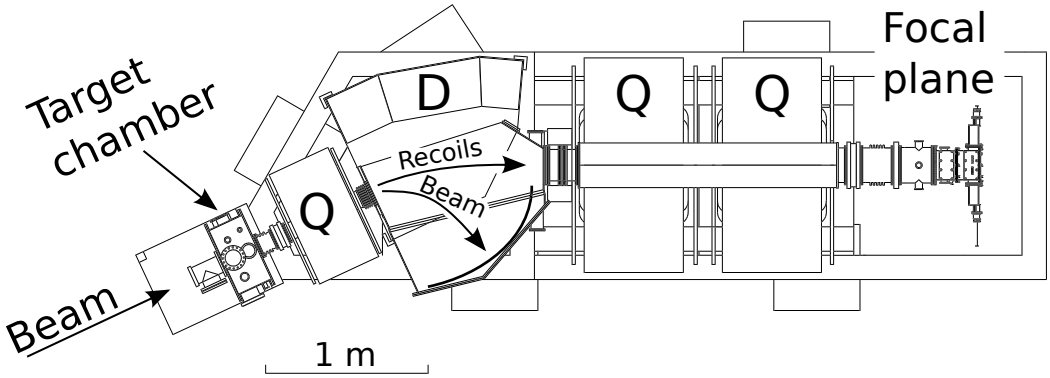

Figure 3.3: Technical drawing of the RITU separator. The magnetic dipole is denoted by the letter D and the quadrupoles by the letter Q. The fusion-evaporation recoils are separated from the beam particles in the dipole and transported to the focal plane. The target chamber and the focal-plane detector setup do not represent the ones that are in use today.

A recoil separator often consists of separating components and additional focusing components. The focusing components are usually magnetic quadrupoles (Q) and the separating components electric or/and magnetic dipoles (D). Electric dipoles are used in conjunction with magnetic dipoles in vacuum-mode separators, whereas gas-filled separators usually employ a single magnetic dipole. The RITU (Recoil Ion Transport Unit) gas-filled recoil separator [Leino95] is of QDQQ design, with the first quadrupole used to match the acceptance of the separator, and to enable the use of JUROGAM without losing acceptance. The two quadrupoles behind the magnetic dipole are used for vertical and horizontal focusing, respectively. See figure 3.3 for a technical drawing of the RITU separator.

The volume of the separator is filled with a constant flow of helium gas at a pressure of approximately 1 mbar. As the fusion-evaporation recoils emerge from the target they have obtained a large variety of charge states. As the recoils interact with the gas ions through charge-exchanging collisions, their tracks in the magnetic field are

[1] A recent upgrade has updated the detector setup to include clover-type detectors, and the data acquisition channels have been digitized. The upgraded array is called JUROGAM II. The thesis work has, however, been performed with the old JUROGAM array.

altered resulting in a net movement resembling that of a recoil with an average charge state. The beam particles will have a small bending radius and will end up in the beam dump, whereas the desired fusion-evaporation recoils will be transported to the focal plane of RITU with high efficiency.

3.2.2 The GREAT focal-plane spectrometer

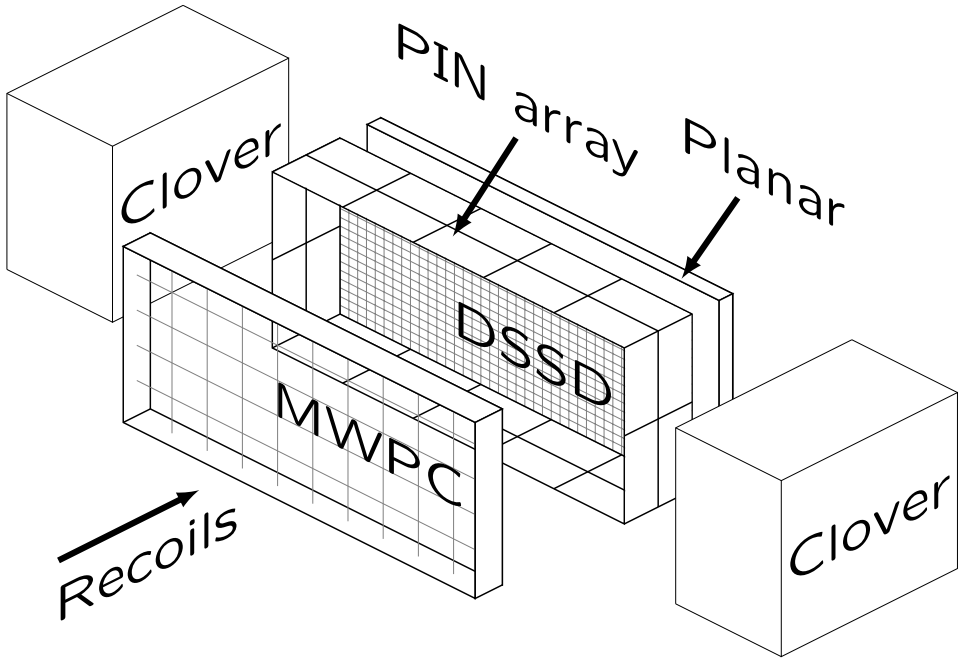

Figure 3.4: The GREAT spectrometer. The fusion-evaporation recoils pass through the MWPC and are implanted in the DSSD. The radiation emitted by the recoil is then detected with the DSSD or with the PIN array or the planar or clover germanium detectors. The top clover has been omitted for visual purposes.

The GREAT (Gamma Recoil Electron Alpha Time) spectrometer [Page03] consists of a multi-wire proportional counter (MWPC), an implantation detector, an array for detecting escaped particles and a set of germanium detectors. A schematic view of the detector setup is shown in figure 3.4.

The main instrument of the GREAT spectrometer is the double-sided silicon strip detector (DSSD). The detector is used for the implantation of the fusion evaporation recoils, arriving from RITU, and for the detection of their subsequent decays such as alpha decay or internal conversion. The thickness of the DSSD used in the present work was 300 μm. Although the DSSD is electronically mapped as one detector, it

consists physically of two detectors, each being 6 cm wide and 4 cm high, mounted side-by-side in the GREAT chamber. The DSSD is divided into 120 strips in the horizontal direction and 40 strips in the vertical direction. This results in a strip pitch of 1 mm and a total number of 4800 pixels. The alpha-particle detection efficiency of the DSSD is approximately 50% due to the shallow implantation depth of maximally 10 μm of the recoils. The DSSD detectors are mounted on an aluminium cooling block with ethanol circulation to improve the detector resolution by cooling it down to a temperature of –25 °C. Figure 3.5 presents as an example the MWPC-vetoed alpha-particle spectra obtained from the three reactions used to produce the nucleus ^{199}At, detected with the GREAT DSSD.

A MWPC is located upstream from the DSSD to measure the energy loss of, and to give a timing signal to, the reaction products passing through it to the DSSD. The MWPC is separated from the GREAT chamber volume by thin Mylar windows, and isobutane gas with a pressure of ∼3.5 mbar flows through the detector volume. The detector consists of horizontal and vertical wiring, for position sensitivity.

Due to the shallow implantation depth of the recoils in the DSSD, a part of the alpha particles or conversion electrons will escape the detector. To collect these escaped particles, an array of PIN silicon detectors is mounted on the inside of the cooling block in a box arrangement upstream from the DSSD. The array consists of 28 silicon detectors with a thickness of 500 μm. The simulated absolute efficiency of the PIN array is approximately 20 % for a 300-keV conversion electron [Andreyev04b].

Germanium detectors are used to detect delayed gamma rays and X-rays close to the DSSD. A planar Ge-detector, with 24 horizontal strips and 12 vertical strips, is mounted directly behind the DSSD inside the GREAT chamber to detect low-energy gamma rays and X-rays. A large clover Ge-detector is placed to face the GREAT chamber from above detecting higher-energy gamma rays. Additional Ge-detectors can be added to face the GREAT chamber from the sides.

The GREAT spectrometer is very versatile as different setups can be built around the existing one. The planar detector can for instance be replaced by a scintillator, or the DSSD by a second MWPC. This flexibility allows for very elegant operation in varied applications when studying the lightest to the heaviest of nuclei.

The linear amplifier signals for each silicon detector were mutually gain-matched for alpha-particle detection by using a source consisting of ^{239}Pu, ^{241}Am and ^{244}Cm, and for electron detection by using a ^{133}Ba source. The DSSD was further internally calibrated in order to account for the recoil effect of alpha decay, and to eliminate for instance the effect of the dead layer on the surface of the DSSD, which distorts the alpha-particle energy from the external source, using known activities. The germanium detectors were calibrated using a source consisting of ^{152}Eu and ^{133}Ba.

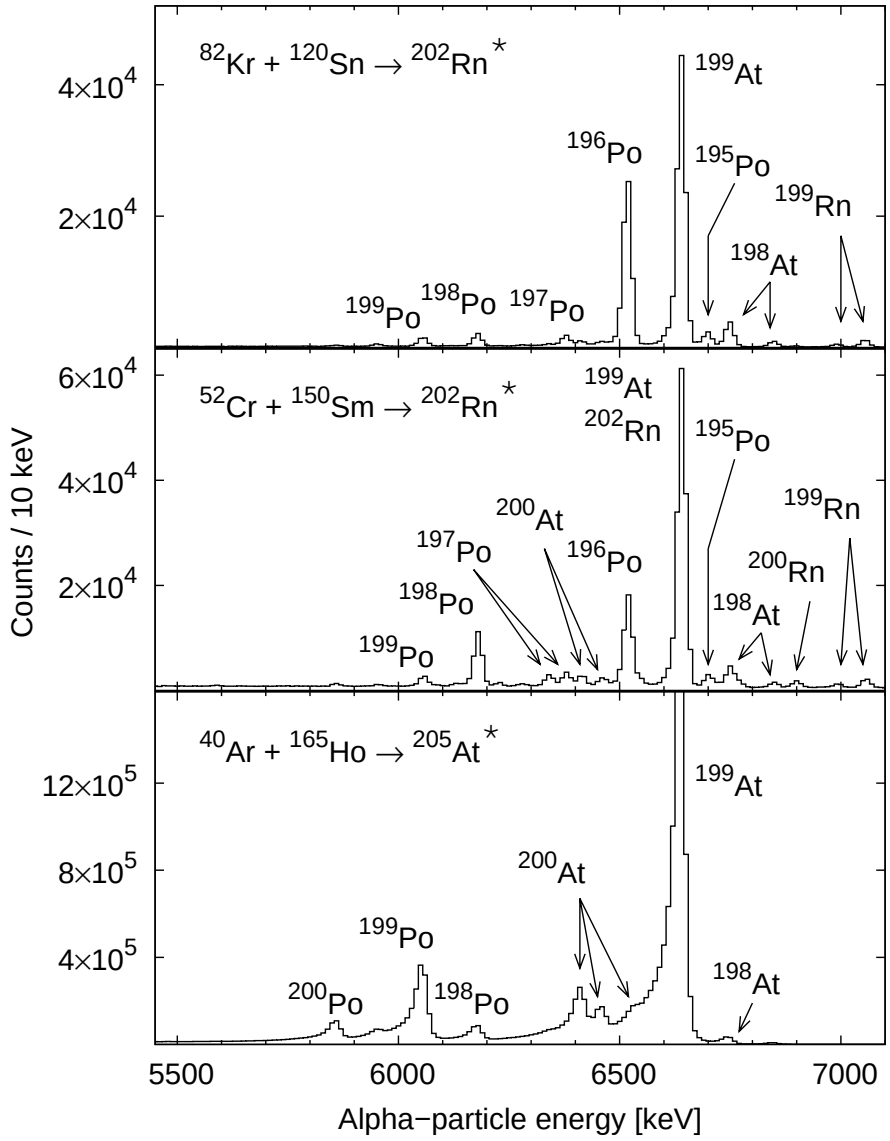

Figure 3.5: MWPC-vetoed alpha-particle spectra from the three reactions used to produce the nucleus ^{199}At. See table 3.1 for details on the reactions.

3.2.3 The JUROGAM germanium-detector array

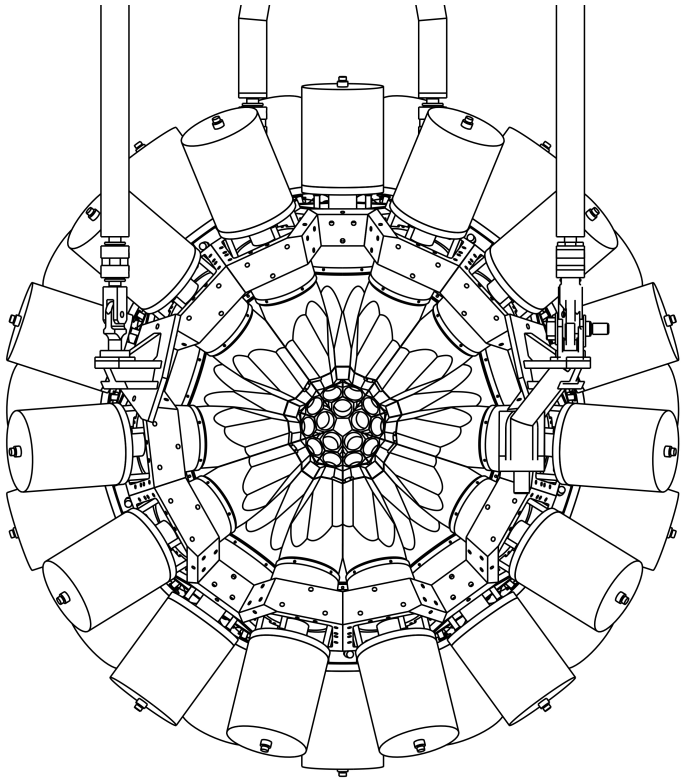

Figure 3.6: Technical drawing of the JUROGAM array as viewed upstream from RITU. The array hangs from the support structure (see figure 3.2) with the help of the four vertical bars and it is divided into a left and a right hemisphere that can be moved separately. Each detector is placed inside a BGO shield and the dewars for the liquid nitrogen remain visible. Figure courtesy of Dave Seddon (Liverpool NSG).

The JUROGAM array consists of 43 tapered High-Purity germanium detectors of GASP and Phase1 type [Beausang92, Rossi Alvarez93] placed in a spherical configuration around the target area. The detectors are cooled down using liquid nitrogen. The array has a photo peak efficiency of 4.2 % at a gamma-ray energy of 1332.5 keV [Pakarinen05]. See figure 3.6 for a technical drawing of the JUROGAM array.

The gamma ray interacts with the detector material mainly by photoelectric absorption, Compton scattering or, if the gamma-ray energy is high enough, through pair production. In the photoelectric absorption process, the entire energy of the gamma-ray is transferred to an inner atomic orbital electron of a detector-material atom, and thus the gamma ray is completely absorbed. In Compton scattering the gamma ray scatters from a nearly free electron, losing part of its energy but not being completely absorbed. The pair-production process occurs if the gamma-ray energy is sufficient to

produce an electron-positron pair, and in the process the entire gamma-ray energy is absorbed. Due to the finite size of the germanium crystals, part of the gamma rays will escape from the crystal after Compton scattering from the detector material. This worsens the peak-to-total ratio of the detector. To reduce the gamma-ray background caused by the Compton-scattered events, each detector is surrounded by a BGO scintillator detector. By discarding those events, detected with the germanium detector, that have a coincident event detected with the surrounding BGO detector, the latter can be used as an anti-Compton shield. The shield acts, furthermore, passively to reduce the number of events of background radiation from the surroundings that reach the detector. The opening of the BGO shield has a heavymet collimator mounted to reduce direct absorption of gamma rays into the shield from the target area. Thin absorbers are placed to cover the opening of the BGO shield to reduce the number of low-energy X-rays, produced in reactions other than the fusion-evaporation reaction, that reach the germanium detector.

The energy of a gamma ray, emitted by a moving nucleus, is Doppler-shifted when observed with a stationary detector. The magnitude of this shift varies with respect to the angle of detection, defined with respect to the direction of movement of the recoil, and with the velocity of the recoil. The shifted gamma-ray energy E'_γ can be approximated to the first order as [Kantele95]

$$E'_\gamma = E_\gamma\big(1 + \frac{v}{c}\cos\theta\big), \tag{3.1}$$

where E_γ is the unshifted gamma-ray energy and v is the velocity of the nucleus. As the fusion-evaporation recoils are strongly forward-focused, the detector angle θ is defined with respect to the beam direction. Another lesser consequence on the gamma-ray spectrum caused by the Doppler effect is the broadening of the gamma-ray peaks due to the opening angle of the detector. Although the peak shift is corrected for by implementing equation (3.1), the peak broadening can only be reduced by reducing the opening angle of the detector.

The detectors were calibrated, and the relative efficiencies were determined, using a source consisting of ^{152}Eu and ^{133}Ba.

3.2.4 Data processing

The signals from each detector are collected by a charge-sensitive preamplifier and fed through a linear amplifier to an analogue-to-digital converter (ADC). The timing signal is taken from the preamplifier through a timing-filter amplifier (TFA) and a constant-fraction discriminator (CFD) to the ADC. The digitized data are then fed through a collator, which time-orders the data from different ADCs. The data from different collators are further merged and sent to the event builder.

All data channels are read out synchronously using the total-data-readout system (TDR) [Lazarus01]. Dead-time limitations between the ADC channels are avoided in the system by giving each event an absolute time stamp. The time stamps are distributed by a 100 MHz metronome, providing a time interval of 10 ns. The DSSD is set as the triggering element in the system by using a software trigger. As the fusion-evaporation recoils are formed at the target position, the prompt gamma rays detected with the JUROGAM array will temporally precede the implantation of the triggering recoil in the DSSD. A trigger delay, based on the time of flight of the recoil through RITU, is therefore implemented in software in order to perform correlations between the DSSD and the JUROGAM array. Furthermore, a trigger width is set both to encompass the trigger delay and to extend temporally further over the delayed events that are detected with the PIN array or the germanium detectors in the GREAT spectrometer, and that are associated with the recoil. The trigger width is roughly adjusted based on the half-life of the studied delayed transitions, keeping in mind, however, that it has to extend over the trigger delay if prompt gamma rays detected with the JUROGAM array are to be included in the analysis. Only the events occurring inside the trigger width are chosen for further processing. As all events receive an absolute time stamp, they can be linked to the triggering fusion-evaporation recoil and, moreover, to each other by applying temporal conditions.

The triggers were applied and the data were processed using the GRAIN software package [Rahkila08] developed by Rahkila. The package allows the user to write their own sort program, using the java language, on top of a platform where the detector setup, triggers and events are implemented.

3.3 Data analysis methods

The fusion-evaporation recoils are distinguished from other reaction products reaching the GREAT spectrometer by their time of flight between the MWPC and the DSSD, and their energy deposit in the MWPC. Figure 3.7 presents the time of flight versus energy deposit matrix from the ^{40}Ar + ^{169}Tm reaction with a beam energy of 205 MeV. The fusion-evaporation recoils are situated at the centre. The remaining fast beam

particles, that were not successfully separated by RITU, on the right, together with the scattered target-like particles, are excluded from further data-analysis by applying a gate on the region depicting the fusion-evaporation recoils.

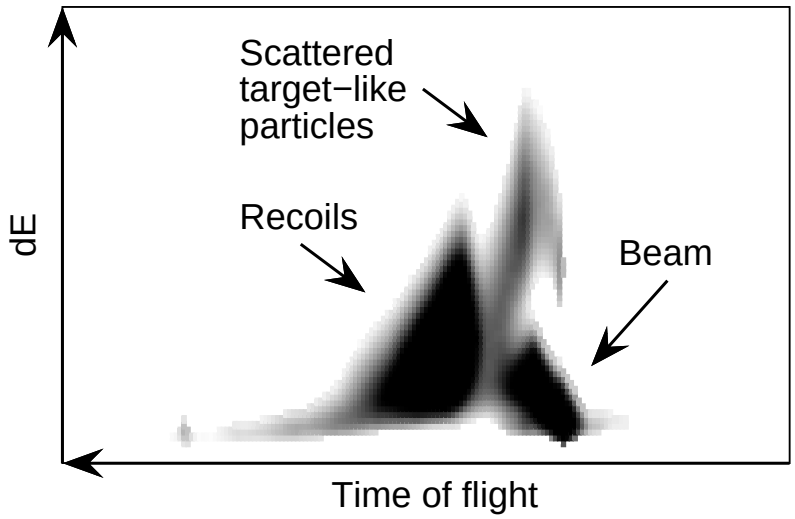

Figure 3.7: The energy deposit in the MWPC versus the time of flight of the reaction products between the MWPC and the DSSD, extracted from the ^{40}Ar + ^{169}Tm reaction with a beam energy of 205 MeV to produce the nucleus ^{203}Fr. Note that the values of time of flight grow to the left.

The recoils were further in the present work identified by their alpha decay observed subsequent to the recoil implantation within the same DSSD pixel. This was done by requiring the proper alpha-particle energy for the decay and by setting an appropriate maximum correlation time, based on the half-life of the alpha-decaying state, between the recoil implantation and the alpha decay. Longer decay chains, such as recoil-alpha-alpha chains, were similarly extracted by requiring a third event with the proper alpha-particle energy and being inside a maximum correlation time, subsequent to the parent alpha decay.

The recoil-decay tagging (RDT) technique [Schmidt86, Simon86, Paul95] was used in analysing the data in the present study. The technique is based on temporal correlations between events. It enables events such as those of gamma rays emitted by a certain recoil, which are a small fraction of all gamma-ray events detected with the detector setup, to be associated with the right recoil that emitted them. The RDT technique includes that of recoil gating, where events that are associated with any fusion-evaporation recoil detected with the DSSD are chosen. The recoil-alpha-tagging technique further produces a subgroup of the recoil-gated events, in which a certain species of recoil, identified by its subsequent alpha decay, has been required. The recoil-isomer tagging technique, where the recoil is identified based on its isomeric transition, is similar to the recoil-alpha tagging technique. A combination of

these techniques can be used as well.

3.3.1 Delayed spectroscopy with the GREAT spectrometer

The time of flight of a recoil through RITU is typically 500–1000 ns. Transitions from isomeric states that have a half-life of less than even a hundred nanoseconds can, however, be detected with the GREAT spectrometer if the yield of the isomeric state is sufficient. In these cases the gamma-ray transition is detected with the clover and the planar detector, and the PIN array is utilized for detecting the corresponding escaped conversion electrons[2].

The half-lives of the isomeric states are extracted by studying the distribution of time differences between the transition from the isomer and the preceding event. This preceding event could be an event in a recoil-decay chain, detected with the DSSD, or a transition from another isomer detected with the GREAT spectrometer. Depending on the amount of statistics obtained, the half-life was extracted in the present study by using a least-squares fit to the data with either a linear time scale or by using the logarithmic-time method [Schmidt00]. Although the two methods are equivalent from a technical aspect, the logarithmic-time method has the visual benefit of displaying the different components in the time distribution originating from different event groups. For low statistics the maximum-likelihood method [Schmidt84] was used. Furthermore, a rough estimate for the half-life could also be obtained by estimating the initial yield of the isomer and comparing it with the number of transitions from the isomer detected at the focal plane, knowing the time of flight of the recoil through RITU.

The internal conversion coefficient of the transition from an isomeric state was extracted by comparing the intensity of the gamma-ray peak from the events detected with the clover or the planar detector with the intensity of the corresponding electron peak from the events detected with the PIN array. Furthermore, the $K/(L+M+...)$ ratio of the conversion coefficients was obtained from the electron spectra detected with the PIN array.

An example of the extraction of the properties of a fast isomer from the present work is presented in figure 3.8 in the case of the deexcitation of the $13/2^+$ isomer to the

[2]Although the TDR system avoids dead-time limitations between the signal-processing channels, each channel has a processing time of roughly 10 μs. Therefore the detection of the internal conversion from the deexcitation of a fast isomer cannot be performed through the same ADC channel that has recorded the preceding recoil implantation. Now the shallow implantation of the recoil in the DSSD presents the opportunity for the fast conversion electrons to escape. The escaped electrons can then be detected with the PIN array. Hence not only does the PIN array contribute to enhance the alpha-particle detection efficiency by detecting alpha particles that have escaped from the DSSD, but it also serves independently to detect events, such as fast conversion electrons in cases where the DSSD cannot be utilized.

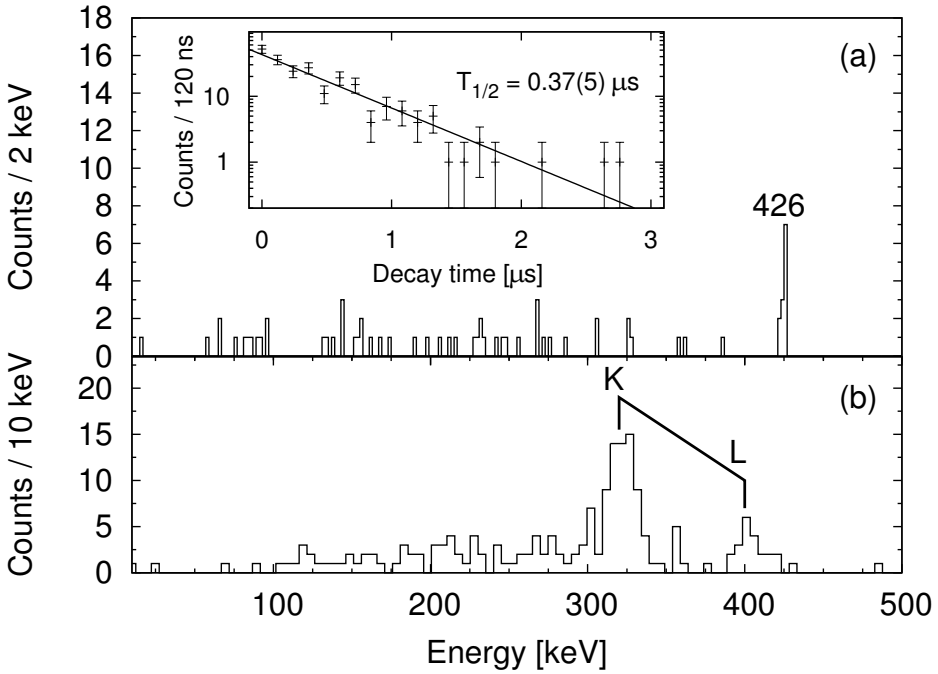

Figure 3.8: The deexcitation of the $13/2^+$ isomer in ^{203}Fr. Energy spectrum of (a) gamma-ray transitions detected with the GREAT clover detector and (b) electrons detected with the PIN array are shown. Both spectra were produced by tagging with the ground-state alpha decay of ^{203}Fr. The inset in panel (a) presents the distribution of time differences between the implantation of the recoil in the DSSD and the detection of the ^{203}Fr ground-state alpha-tagged electron with the PIN array within a maximum correlation time of 3 μs. The solid line represents a least-squares fit to the data.

$9/2^-$ ground state in ^{203}Fr. Panel (a) presents the energy spectrum of gamma-ray transitions, detected with the GREAT clover detector, and tagged with the ground-state alpha decay of ^{203}Fr. Panel (b) presents the energy spectrum of corresponding electrons detected with the PIN array. The indicated K- and L-conversion peaks are associated with the 426-keV transition. By comparing peak intensities in panel (a) and (b) a conversion coefficient can be determined. Alternatively the $K/(L+M+...)$ ratio can be determined with slightly better precision by studying the intensities of the peaks in panel (b). It is worth noting that although the higher-energy electron peak is denoted to consist of L-conversion electrons, the peak includes higher-shell conversion electrons due to the PIN array resolution. Therefore the higher shells are added to the K/L ratio. The inset presents the distribution of time differences between the recoil implantation and the detection of the ^{203}Fr ground-state alpha-tagged electron with the PIN array. The half-life can be extracted from this data by a least-squares fit. Based on such a fit a maximum correlation time of 1.2 μs, which is approximately three half-lives, was used to extract the gamma-ray and conversion-electron spectra presented in panels (a) and (b). From these results the character and, furthermore, the strength of the transition from the isomeric state can be determined. The results obtained from the data in figure 3.8 are presented in section 4.2.

3.3.2 Electron spectroscopy with the GREAT DSSD

The internal conversion of a transition from an isomeric state can be detected as a separate event in the DSSD pixel, subsequent to the implantation of the recoil in an isomeric state or an alpha decay to an isomeric state, if the half-life of the isomer is longer than the signal-processing time of roughly 10 μs. If the amplifier gain of the X-side of the DSSD is set to detect conversion electrons, then for example recoil-electron-alpha chains or recoil-alpha-electron chains can be extracted from the same pixel.

As the internal conversion occurs inside the DSSD, the relaxation of the atomic electron cloud, promptly following the emission of the conversion electron, is observed alongside the conversion electron. These atomic events consist of low-energy X-rays and Auger electrons emitted when filling vacancies in lower-lying electron orbitals. As the FWHM for the electron peaks in this work was close to 12 keV, conversion electrons from the $L+M+...$ orbitals will lie in the same peak. This peak should have an energy that is 12–13 keV lower than the transition energy due to the electron binding energies of the L and higher-lying orbitals. However, because the energy release in the relaxation of the electron cloud is detected with the DSSD, the resulting peak is shifted higher in energy. This shift is on average $\sim$10 keV and the resulting electron peak is consequently observed 2–3 keV below the transition energy. Considering the FWHM of the electron peaks, the energy of the resulting conversion-electron peak representing the $L + M + ...$ orbital conversion coincides with the transition energy.

Figure 3.9 shows this effect for known transitions in the alpha-decay chain of ^{204}Fr [Huyse92] produced alongside ^{205}Fr in the present study. The energies of the electron peaks representing the 231-keV $E3$ transition in ^{200}At, the 275-keV $E3$ transition in ^{204}Fr and the 158-keV $M3$ transition observed in ^{196}Bi, align with the respective transition energies. The existence of the 275-keV transition was earlier predicted by Huyse *et al.* [Huyse92] based on alpha-decay energies, and observed for the first time in the present work. The cases in figure 3.9 are fairly simple as the cascade consists of a single transition. A more complex scenario arises when the cascade consists of two or three prompt transitions. Each of the transitions may proceed through internal conversion or by gamma-ray emission. Furthermore, if the transition proceeds through internal conversion, the conversion electron may escape from the DSSD. If the conversion electron escapes, then only the relaxation of the electron cloud will be detected. These scenarios are, furthermore, combined with the competition between $K-$ and $L + M + ...$ shell conversion. The electron spectrum resulting from such a cascade is quite complex. However, an interesting property of this electron spectrum is that the "end-point" peak represents the level energy of the isomer. This peak originates from the scenario in which each of the transitions in the cascade proceeds by internal L-conversion and the conversion electrons are fully absorbed.

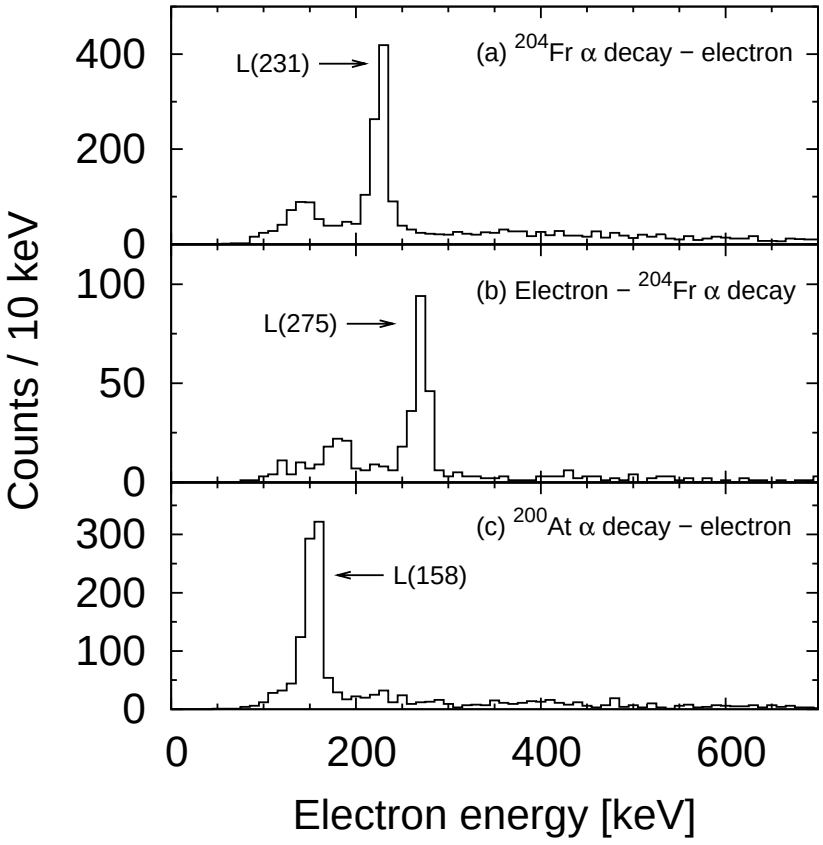

Figure 3.9: Energy spectra presenting L-conversion electrons in coincidence with the alpha decays in the decay chain of ^{204}Fr. (a) The 231-keV $E3$ transition from the 10^- state in ^{200}At, (b) the 275-keV $E3$ transition from the 10^- state in ^{204}Fr and (c) the 158-keV $M3$ transition from the 6^+ state in ^{196}Bi.

To unravel the properties of the cascade from the electron spectrum, the possible scenarios should be narrowed down to a few feasible ones based on systematics in the region of study. Furthermore, gamma-ray transitions in coincidence with the conversion electrons in the cascade can reveal the energy of part of the transitions. With this information and by studying the position of the electron peaks in the spectrum, some estimates of the transition energies can be made. Finally, simulations based on the rough initial estimates from the peak positions, provide a helpful tool in reproducing the electron spectrum. While this study presents a first analysis of electron spectra from internal conversion summing in the DSSD using the GREAT spectrometer, the idea itself is not new. Such studies were proposed for superheavy elements by Jones [Jones02] in 2002.

Example spectra of electrons detected with the DSSD, and tagged with the alpha decays of ^{203}Fr are presented in Figure 3.10. Panel (a) presents the electrons detected temporally between the recoil implantation and the ground-state alpha decay of ^{203}Fr.

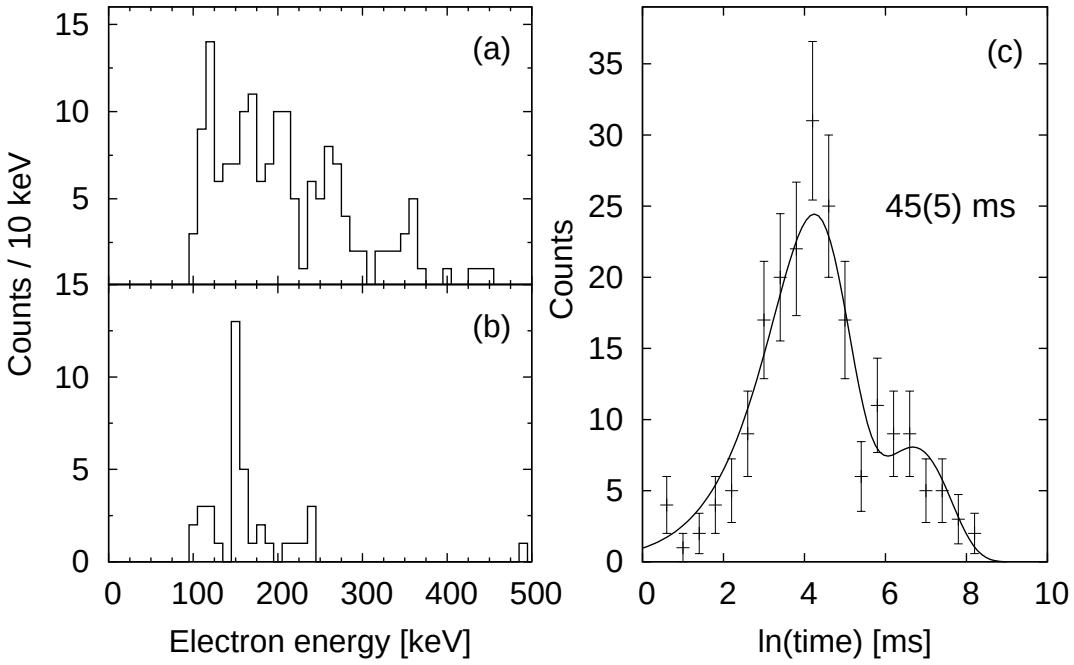

Figure 3.10: (a) Energy spectrum of electrons detected temporally between the implantation of the ^{203}Fr recoil in the DSSD and the detection of the ground-state alpha decay within a maximum correlation time of 150 ms between the recoil implantation and the subsequent electron. (b) Energy spectrum of electrons detected after the detection of the alpha decay of the $1/2^+$ isomer within a maximum correlation time of 900 ms between the alpha decay and the conversion electron. Panel (c) presents the distribution of time differences between the recoil implantation and the detection of a ^{203}Fr ground-state alpha-tagged electron. These events include the ones in panel (a). The solid line represents a two-component fit to the data based on the logarithmic-time method [Schmidt00]. The resulting half-life obtained for the studied activity is denoted in the figure.

The shape of the cascade differs from the one in panel (b) representing the electrons detected temporally after the alpha decay of the $1/2^+$ isomer in ^{203}Fr. The electron spectrum in panel (a) originates from a cascade including three transitions, a $M2$ transition followed by two $M1$ transitions. The complexity of this spectrum originates from the multiple ways the three-step cascade can deexcite, when including the possibility of a conversion electron to escape. This complexity increases if an $E3$ branch is assumed to compete with the $M2$ and first $M1$ transition. A simpler spectrum arises in the scenario where the cascade consists solely of an $E3$ transition followed by a $M1$ transition. Such a spectrum is the one presented in panel (b). In both spectra the position of the highest-energy peak represents the excitation energy of the isomer, as the energy of the whole cascade has been deposited. Panel (c) presents the distribution of time differences between the implantation of the recoil in the DSSD and the detection of the electron tagged with the ^{203}Fr ground-state alpha decay. These events include the ones presented in panel (a). The logarithmic-time method [Schmidt00] was used in the present study, and a two-component fit was made to the data. The component

originating from random correlations is visible to the right of the studied activity for which a half-life of 45(5) ms was determined from the fit. The half-life of the $1/2^+$ isomer can be extracted by a fit to this peak data, and based on the results a maximum correlation time of 150 ms is used to obtain the electron spectrum in panel (a). The results obtained from the analysis of these spectra will be discussed later in section 4.2, together with the constructed decay schemes.

3.3.3 Gamma-ray spectroscopy with the JUROGAM array

The prompt recoil-gated gamma-ray events detected with the JUROGAM array are chosen based on the time difference between the detection of the prompt gamma ray with the JUROGAM array and the subsequent implantation of the recoil in the DSSD. This time difference originates from the time of flight of the recoil through RITU. To further filter the gamma rays belonging to the studied nucleus, the recoil-alpha-tagging technique is used. Moreover, if statistics allows, the gamma rays preceding a certain isomeric state observed with the GREAT spectrometer can be filtered by further using the recoil-isomer-tagging technique on the alpha-tagged recoil.

The level schemes in the thesis work were built by using the RADWARE software package [Radford95b, Radford95a]. The assignment of the transitions and the consequent states was performed by applying gamma-gamma coincidences and energy-sum arguments. Between two transitions the one with the higher total intensity was placed lower in the level scheme. When the assignment remained uncertain, the transition and the consequent state was marked as tentative in the level scheme.

Figure 3.11 demonstrates the energy spectra of gamma-ray transitions detected with the JUROGAM array in the study of the nucleus ^{203}Fr produced in the ^{40}Ar + ^{169}Tm reaction. Panel (a) shows raw (BGO-vetoed) gamma-ray data. The events include the annihilation peak at 511 keV and gamma-ray events originating from inelastic reactions. The events in panel (b) have been recoil-gated. Still the transitions associated with ^{203}Fr are quite weakly visible, as the identity of the fusion-evaporation recoil is not specified, and therefore transitions belonging to the dominating reaction channels are pronounced. To extract the transitions belonging to ^{203}Fr, the recoil-alpha-tagging procedure was utilized using its ground-state alpha decay. The resulting spectrum is presented in panel (c). Events, indicated by open circles, associated with the ^{169}Tm [Baglin08] target recoils still leak through together with events from the $(n,n'\gamma)$ reaction occurring inside the germanium detector crystal, visible in the region close to 600 keV. The broadness of this peak is due to the Doppler correction performed for the gamma rays emitted by the moving fusion-evaporation recoil. However, the intense peaks in panel (b), belonging to the radon nuclei, are filtered out. Furthermore, to study the relationships between the gamma-ray transitions, gamma-gamma coincidences were examined. Panel (d) depicts a spectrum of gamma rays in coincidence

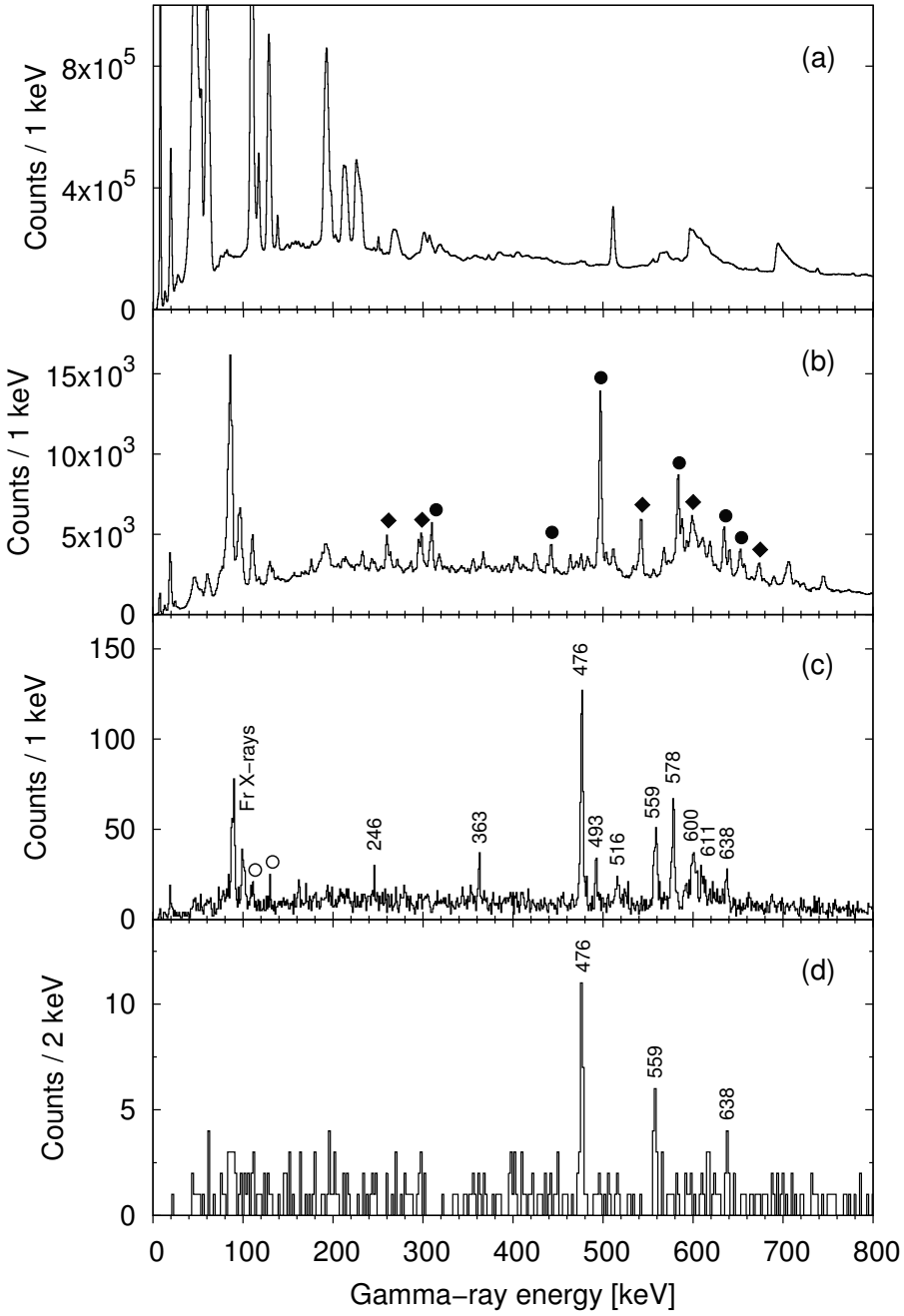

Figure 3.11: Energy spectra of gamma-ray transitions detected with the JUROGAM array from the ^{40}Ar + ^{169}Tm reaction used to produce the nucleus ^{203}Fr. (a) Raw (BGO-vetoed) gamma-ray data obtained without the requirement of a recoil implantation in the DSSD. (b) Recoil-gated gamma rays. Peaks belonging to the dominant reaction channels ^{203}Rn [Newman01] and ^{204}Rn [Dobson02] are marked with circles and diamonds, respectively. (c) Gamma rays tagged with the ^{203}Fr ground-state alpha decay. Peaks belonging to the contaminating recoils from the ^{169}Tm [Baglin08] target are indicated with open circles. (d) Gamma rays in coincidence with the 476-, 559- or 638-keV transitions.

with the 476-, 559- or 638-keV transition in panel (c). These three transitions build a cascade. Due to poor statistics no extra transitions can be observed in coincidence with the three transitions, and therefore the cascade cannot be continued to higher spin. It is, however, worth noting that some prominent transitions belonging to ^{203}Fr are not in coincidence with these three transitions, therefore belonging to a separate structure. The level scheme resulting from the analysis is presented in section 4.2.

The JUROGAM array can be divided into six separate rings with respect to the beam direction. Four of these rings are situated pairwise symmetrically around the axis perpendicular to the beam direction and adding the events from these rings together, a net amount of four rings is used. This annular structure enables the study of angular distributions of the gamma rays. The relative efficiency curve for each ring is determined using source data and the intensities of the studied gamma-ray peaks are normalised between rings using these curves. The normalised intensities for each transition are plotted with respect to the ring angle and equation (2.13) is fitted to the data points. The multipolarity of the transition is assigned based on the fit. In the present work, the angular distributions were extracted in the case of ^{205}Fr. For the other nuclei the statistics of the gamma-ray transitions were too low for such an analysis.

Chapter 4

Summary of experimental results

The experimental results obtained during the thesis studies are summarized in this chapter. Three publications have stemmed from the present work and more information concerning the results to be presented can be found in the publications attached as appendices A–C.

4.1 The odd-mass astatine nuclei ^{197}At and ^{199}At

Results from the studies of the nucleus ^{197}At have previously been reported by Andgren *et al.* [Andgren08]. A further analysis of the data presented in their study was made in the present study in order to further investigate prompt gamma-ray transitions associated with the ^{197}At recoils. Those recoils were examined where the alpha particle had escaped the DSSD leaving only a partial energy deposit. By tagging with these recoil-alpha chains, together with those ^{197}At recoil-alpha chains where the ground-state alpha-decay events were detected with a full energy deposit, the prompt gamma-ray statistics of ^{197}At were nearly doubled. The resulting level scheme of ^{197}At, constructed based on gamma-ray coincidence, energy sum and intensity relations, is presented in figure 4.1. It should be noted, however, that there remain gamma-ray transitions presented in the work by Andgren *et al.* that could not be placed in the level scheme in their work nor in the present work.

Andgren *et al.* assigned a cascade on top of the $9/2^-$ ground state, that in ^{197}At originates from the odd proton on the $h_{9/2}$ orbital. The results from the present study support this assignment, and an unfavoured signature partner belonging to this band has, furthermore, been tentatively assigned. Low statistics did not allow for gamma-gamma coincidence studies to be performed for the transitions forming this signature, and the assignment is thus based entirely on energy-sum and intensity arguments. This band is indicated as Band 1 in figure 4.1, with the tentative unfavoured signature

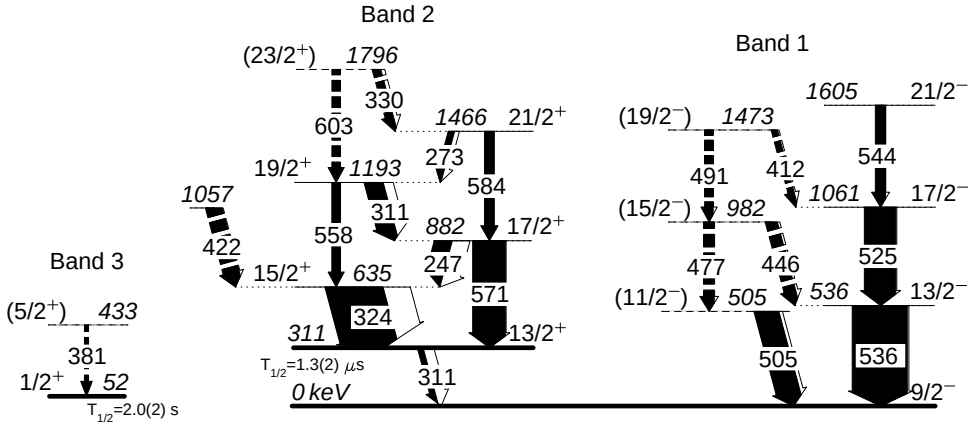

Figure 4.1: The level scheme of ^{197}At. The thickness of an arrow represents the intensity of the transition, with the black area indicating the relative gamma-ray intensity and the white area the corresponding conversion-electron intensity. Transitions and resulting levels that are tentatively assigned are indicated with a dashed line. The tentative unfavoured signature partner in Band 1 is assigned based on energy-sum and intensity arguments. The energy levels of isomeric states and the ground state are indicated by a thicker line. Note that the intensity of the 311-keV $M2$ transition deexciting the $13/2^+$ isomer is not to scale.

partner indicated with dashed arrows. The ground state can be expected to be of a transitional nature, with spherical components, however, still dominating, as the signature splitting of this band is quite high. Andgren *et al.* did in fact suggest a near-spherical shape for the $9/2^-$ ground state in ^{197}At, based on their total Routhian surface (TRS) calculations. The near-spherical nature of the ground state is further supported by its favoured alpha decay [Coenen86] to the near-spherical ground state in ^{193}Bi [Nieminen04].

The 311-keV transition in ^{197}At was first observed by Smith *et al.* [Smith99] and assigned a $M2$ character. The transition was later observed by Andgren *et al.*, and they confirmed that it represents the single-step deexcitation of the $13/2^+$ isomer to the $9/2^-$ ground state [Andgren08]. The half-life of 1.3(2) μs obtained by Andgren *et al.* differs from the value of 5.5(14) μs reported by Smith *et al.*. Andgren *et al.* obtained a strength of 0.086(13) W.u. for the transition, which is comparable with the value of 0.182(22) W.u. [Kondev07a] for a similar $M2$ transition observed in ^{201}At. Consequently they interpreted that the $13/2^+$ state originates from the odd proton excited to the $i_{13/2}$ orbital. The 324-keV transition, previously assigned by Smith *et al.* to depopulate an $11/2^-$ state to the $9/2^-$ ground state, was now assigned by Andgren *et al.* to populate the $13/2^+$ isomer. This assignment was made possible by isolating the prompt gamma-ray transitions associated with the $13/2^+$ isomer through tagging with the electrons from the internal conversion of the 311-keV $M2$ transition. Andgren *et al.*, moreover, presented TRS calculations predicting a deformation parameter of $\beta_2 = -0.2$, indicating an oblate deformation for the $13/2^+$ isomer. The present study

expands the start of the rotational band, presented in reference [Andgren08], to a spin and parity of $(23/2^+)$, and introduces the unfavoured signature partner. The strong coupling of this band supports the results from the TRS calculations predicting an oblate deformation for the $13/2^+$ isomer. Consequently the state can be assigned to originate from the odd proton on the $13/2^+[606]$ Nilsson orbital (see figure 2.1). Furthermore, the present study supports the results obtained by Andgren *et al.* on the isomeric properties obtained for the $13/2^+$ state. The rotational band is indicated as Band 2 in figure 4.1.

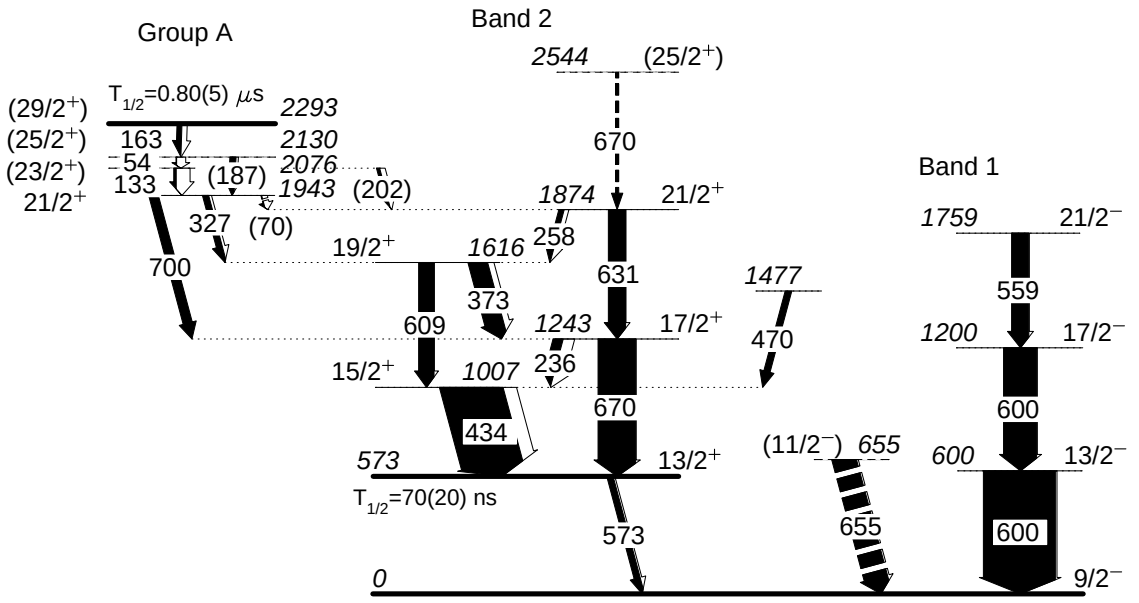

Figure 4.2: The level scheme of ^{199}At. The intensities of the 54-, 70-, 133-, 163-, 187-, 202- and 573-keV transitions are not to scale.

The level scheme obtained for ^{199}At is shown in figure 4.2. Investigations of the excited states of this nucleus were previously reported in three separate studies. Męczyński *et al.* [Męczyński98] presented a strongly coupled rotational band on top of the ground state. Styczeń *et al.* [Styczeń99] observed the same rotational band but placed it on the $13/2^+$ isomer. They did not, however, observe the decay of the isomer to the ground state. They presented, furthermore, a cascade of transitions to the ground state with a branch feeding the $13/2^+$ isomer. The assignments of the multipolarities of the most prominent transitions were supported by angular distributions of the gamma rays. Lastly Lach *et al.* [Lach00] observed the deexcitation of the $13/2^+$ isomer as a single-step transition, with an energy of 573 keV and a half-life of 580(130) ns, to the $9/2^-$ ground state. The present work combines both prompt and delayed spectroscopy of ^{199}At. Moreover, the amount of data that was collected for the 573-keV transition in the present work is increased by over ten-fold as compared with that presented by Lach *et al.*

Band 1 in figure 4.2 presents the cascade of gamma-ray transitions directly feeding the ground state. The ordering of these transition differs from that reported by Styczeń *et al.* and no link between the two $I = 13/2$ states has been observed. A non-yrast $(11/2^-)$ state, with a level energy in accordance with systematics, has tentatively been assigned to feed the $9/2^-$ ground state by a 655-keV transition. All negative-parity states are suggested to originate from the coupling of the odd $h_{9/2}$ proton to the low-lying positive-parity states in the ^{198}Po core. Furthermore, the $11/2^-$ state is suggested to belong to the same multiplet as the $13/2^-$ state. The ground state in ^{199}At was suggested by Andgren *et al.* [Andgren08], based on their TRS-calculations, to be near-spherical with a similar but slightly smaller deformation as in ^{197}At. The present work supports this suggestion, as no clear signature partner has been found for the cascade denoted as Band 1. Suggested configurations for relevant states in ^{199}At are presented in table 4.1.

The present study reports the $13/2^+$ isomer at the same level energy of 573 keV as reported by Lach *et al.*. The internal K-conversion coefficient of 0.19(4) obtained in the present study further supports the assignment of a $M2$ character for the 573-keV transition, confirming the spin and parity of $13/2^+$ of the isomer. However, a significantly shorter half-life of 70(20) ns for the $13/2^+$ isomer was obtained in the present study. This half-life results in a transition strength of 0.16(5) W.u., which is comparable to the value of 0.086(13) W.u. [Andgren08] for the $M2$ transition depopulating the $13/2^+$ state to the $9/2^-$ ground state in ^{197}At. The rotational band built on top of this isomer is indicated as Band 2 in figure 4.2. The results from the present study support the assignment of this band made by Styczeń *et al.*, with a slight difference on the depopulation of the yrare $21/2^+$ state. The gamma-ray transitions in this band were, furthermore, observed both with the JUROGAM array and the GREAT spectrometer in the present work, indicating that a higher-lying isomer feeds this band.

Table 4.1: The proposed configurations for relevant states in ^{199}At.

	E_{state} (keV)	Configuration
$9/2^-$	0	$\pi h_{9/2} \otimes 0^+$
$11/2^-$	655	$\pi h_{9/2} \otimes 2^+$
$13/2^-$	600	$\pi h_{9/2} \otimes 2^+$
$17/2^-$	1200	$\pi h_{9/2} \otimes 4^+$
$21/2^-$	1759	$\pi h_{9/2} \otimes 6^+$
$13/2^+$	573	$\pi i_{13/2}$
$21/2^+$	1943	$\pi h_{9/2} \otimes 7^-$
$(23/2^+)$	2076	$\pi h_{9/2} \otimes 8^-$
$(25/2^+)$	2130	$\pi h_{9/2} \otimes 9^-$
$(29/2^+)$	2293	$\pi (h_{9/2})^2 i_{13/2}$
$1/2^+$	∼240	$\pi (s_{1/2})^{-1}$
$7/2^-$	∼150	$\pi f_{7/2}$

By studying the distribution of time differences of the implantation of the ^{199}At recoil and the detection of the 163-keV transition, depopulating the higher-lying isomer, with the GREAT planar detector a half-life of 0.80(5) μs was obtained for the higher-lying isomer. This result could explain the longer half-life of the $13/2^+$ isomer obtained by Lach *et al.* The higher-lying isomer has been assigned a spin and parity of $(29/2^+)$ and it is suggested to originate from the maximum projection of the $(\pi(h_{9/2})^2 i_{13/2})$ coupling between the three valence protons. In the polonium isotone ^{198}Po, a similar 11^- $(\pi h_{9/2} i_{13/2})$ isomer was earlier identified at an excitation energy of 2565 keV [Lach94]. The isomer deexcites through the group of states indicated in figure 4.2 as Group A to states in Band 2. The $(25/2^+)$, $(23/2^+)$ and $21/2^+$ states in Group A can be interpreted as the $I_{\mathrm{MAX}} - 1$ states of the odd $h_{9/2}$ proton coupled to the 9^-, 8^- and 7^- states having possible neutron configurations of $(\nu(f_{5/2})^{-1}(i_{13/2})^{-1})$, $(\nu(p_{3/2})^{-1}(i_{13/2})^{-1})$ and $(\nu(p_{3/2})^{-1}(i_{13/2})^{-1})$, respectively, of the polonium core. This major configuration difference between the $(29/2^+)$ and the $(25/2^+)$ state results in the former becoming isomeric. A more detailed description of the analysis of the higher-lying isomer is presented in appendix A.

The $1/2^+$ state in ^{199}At has been observed for the first time in the present work. It was produced through the alpha decay of the $1/2^+$ state in the parent nucleus ^{203}Fr, and its properties will therefore be discussed in the following section together with the results obtained for ^{203}Fr.

4.2 The odd-mass francium nuclei ^{203}Fr and ^{205}Fr

The level scheme of ^{203}Fr is presented in figure 4.3. A cascade of transitions directly feeding the ground state was observed, recall figures 3.11(c) and 3.11(d), and it is indicated as Band 1 in figure 4.3. The ordering of the transitions in Band 1 was made based on coincidence relations and the relative intensities of the transitions. Each of the transitions were assigned an $E2$ multipolarity based on systematics in this region. The $13/2^-$, $17/2^-$ and $(21/2^-)$ states are suggested to originate from the odd $h_{9/2}$ proton coupled to the ^{202}Rn core, in a similar manner as in the case of the nucleus ^{199}At that has the ^{198}Po nucleus as a core.

The deexcitation of a fast isomer, with a transition energy of 426 keV, was observed in the present study with the GREAT clover detector when tagging with the ground-state alpha decay of ^{203}Fr. The gamma-ray and conversion-electron spectra extracted from this transition have been presented in figure 3.8. From the corresponding conversion-electron data collected with the PIN array, a $K/(L + M + ...)$ ratio of 3.3(4) was obtained in agreement with the value of 3.1(3) for a $M2$ transition as extracted using the BrIcc database [Kibédi08]. The half-life of 0.37(5) μs (see figure 3.8) results in a transition strength of 0.10(2) W.u. This strength is comparable with corresponding

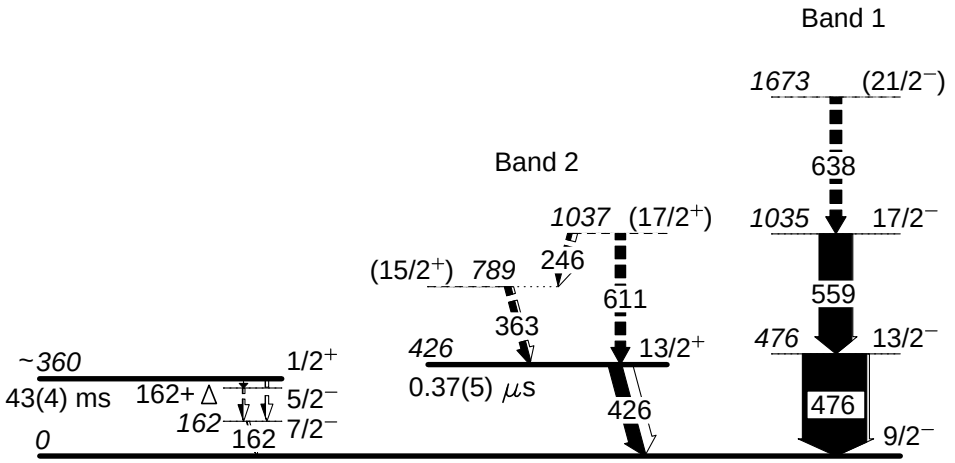

Figure 4.3: The level scheme of ^{203}Fr. Note that the intensities of the transitions depopulating the $1/2^+$ isomer are not to scale. Δ ~175 keV, see text and figure 4.4 for details on the decay scheme of the $1/2^+$ isomer.

values for $M2$ transitions deexciting the $13/2^+$ isomer to the $9/2^-$ ground state in ^{197}At and ^{199}At. The isomer has consequently been assigned a spin and parity of $13/2^+$. Although the $13/2^+$ state is yrast, the feeding through it is surprisingly low. This can be seen when comparing the relative intensity of the transitions proceeding to the $13/2^+$ state with the corresponding transitions in ^{197}At and ^{199}At, see figures 4.1 and 4.2, respectively. The reason for this anomaly is unclear, but the most likely origin is a higher-lying fast isomer that favours the feeding to the negative-parity states instead of the states above the $13/2^+$ isomer. The start of a rotational band, indicated as Band 2 in figure 4.3, was tentatively placed on top of the $13/2^+$ isomer based on energy-sum arguments and systematics in this region.

Previously only the $1/2^+$ state was known in ^{203}Fr alongside the $9/2^-$ ground state. Uusitalo *et al.* [Uusitalo05] reported the alpha decay of the $1/2^+$ state with an alpha-particle energy of 7227(8) keV and a half-life of 60^{+30}_{-20} ms. The level energy of the state remained undetermined as the decay of the corresponding $1/2^+$ state in the daughter nucleus ^{199}At was not observed. Uusitalo *et al.* suggested, however, that there exists an internal-transition branch that deexcites the $1/2^+$ isomer to the $9/2^-$ ground state in ^{203}Fr. This suggestion was based on the high reduced alpha-emission width of 208 keV [Uusitalo05] obtained for the alpha decay of the $1/2^+$ state in ^{203}Fr. This internal transition branch has been observed in the present study. Furthermore, the alpha decay reported by Uusitalo *et al.* has been observed with five-fold statistics. The results are presented in the decay scheme in figure 4.4. The alpha-particle energy of 7246(5) keV obtained in the present work from the decay of the $1/2^+$ isomer in ^{203}Fr is slightly higher than the previously reported value, however, the half-life of 43(4) ms is consistent with that reported by Uusitalo *et al.* A branching ratio of 20(4) % was

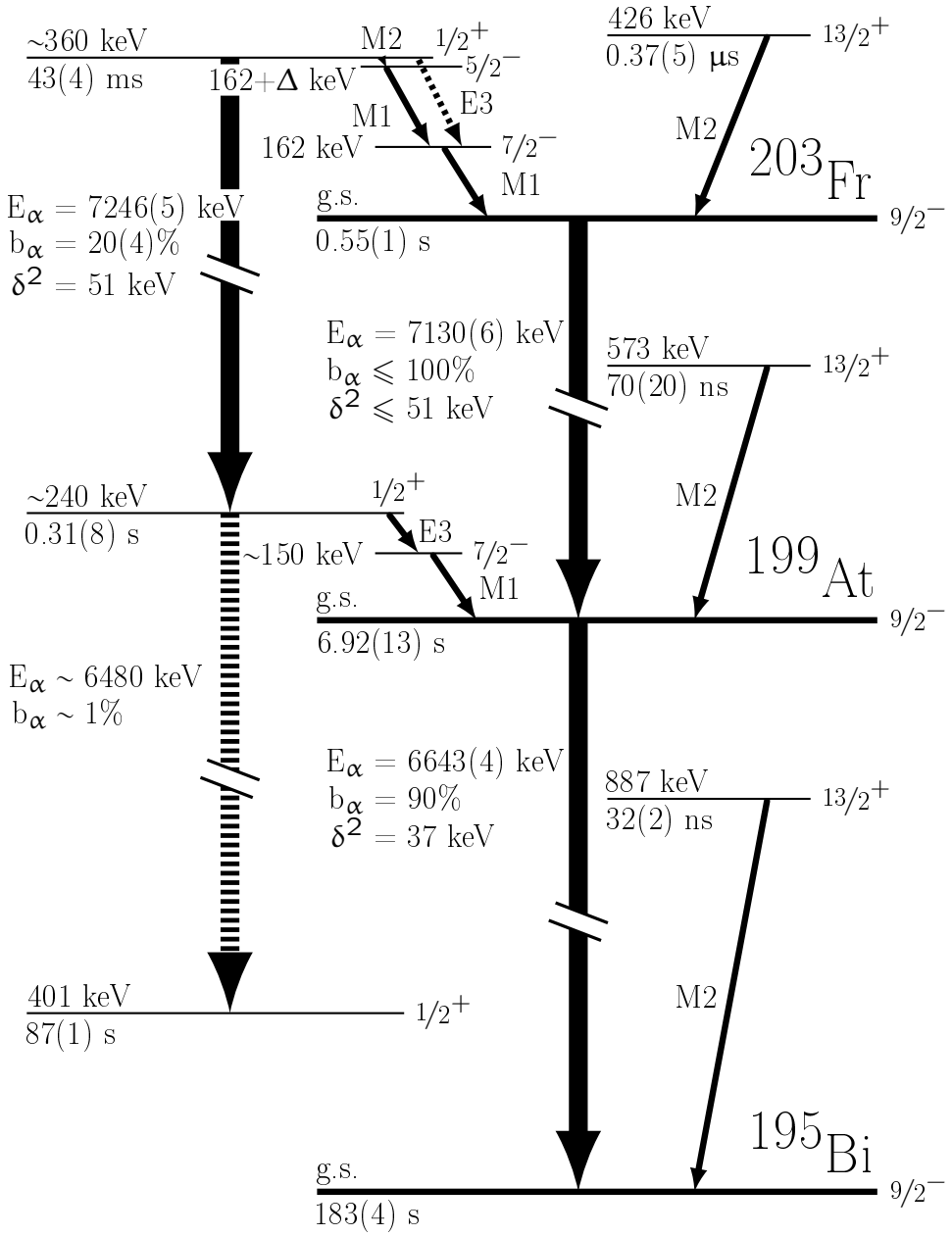

Figure 4.4: The decay scheme of the low-lying isomeric states and the $9/2^-$ ground state in ^{203}Fr, ^{199}At and ^{195}Bi. For the bismuth data see references [Lönnroth86, Zhou99, Pai12], for the data for the ground-state alpha decay of ^{199}At references [De Witte05, Singh07] and for the ground state alpha decay of ^{203}Fr references [Uusitalo05, Kondev05]. The alpha decay of the $1/2^+$ state in ^{199}At is presented with a dashed line as the decay has not been observed. $\Delta \sim 175$ keV, see text for details.

obtained in the present study for the alpha decay of the $1/2^+$ state by comparing alpha-particle yields with the conversion electron yields from the internal transition branch. Consequently a reduced alpha-emission width of 51 keV was extracted for this decay using the method developed by Rasmussen [Rasmussen59], resulting in a hindrance factor of 1.1 as compared with the ground-state alpha decay of ^{202}Rn [Zhu08]. This is a sign of a favoured alpha decay between states of equal spin and parity. In the recent work by Kalaninová *et al.* [Kalaninová13] systematics of reduced alpha-decay widths for neutron-deficient francium nuclei are presented, and the result from the present study coincides well with these systematics. The internal transition branch will be discussed in the following.

The energy spectrum of conversion-electrons from the internal transition branch of the $1/2^+$ isomer in ^{203}Fr was shown in figure 3.10(a). Based on the structure of the spectrum, it is suggested to present a three-step cascade with a ∼20-keV $M2$ transition followed by a ∼175-keV $M1$ transition and a 162-keV $M1$ transition to the $9/2^-$ ground state. A significant competing branch, with a branching ratio possibly as high as 70 %, consisting of an $E3$ transition followed by the 162-keV $M1$ transition is suggested as well, based on the properties of the electron spectrum. Such a possible branch is further supported by the non-observation of the ∼175-keV $M1$ transition with the GREAT clover and planar detector. A transition strength of $\sim 0.8 \times 10^{-4}$ W.u. was obtained for the $M2$ transition based on the 43(4)-ms half-life and by assuming no competing $E3$ transition. This result is comparable with the value of $2.5(6) \times 10^{-4}$ W.u. [Kondev04] obtained for a similar transition in ^{205}Bi. The electron spectrum of the corresponding internal transition branch in the daughter nucleus ^{199}At was shown in figure 3.10(b). The branch is suggested to consist solely of a ∼90-keV $E3$ transition followed by a ∼150-keV $M1$ transition to the $9/2^-$ ground state. A half-life of 0.31(8) s was obtained for the $1/2^+$ state, leading to a transition strength of ∼0.09 W.u. for the $E3$ transition. This value is comparable with the values obtained for similar transitions in ^{191}Bi and ^{195}At [Nyman13]. The alpha decay of the $1/2^+$ state in ^{199}At was not observed in the present study. However, by assuming a similar alpha-emission width as for the ground-state alpha decay, a branching ratio of approximately 1% was estimated for this possible branch. Clearly this alpha-decay branch cannot compete with the internal transition branch proceeding to the $9/2^-$ ground state. Low statistics, combined with high internal-conversion coefficients of the transitions, did not allow for all of the gamma-ray transitions from the cascades deexciting the $1/2^+$ states in figure 4.4 to be observed, and only the 162-keV transition in ^{203}Fr was detected. The non-observation of the gamma-ray transitions, together with the low statistics of the conversion-electron data, has led to the decision of leaving the level energies as approximate estimates. In addition the level energy of the $5/2^-$ state in ^{203}Fr has a $\Delta \sim 175$ keV as the gamma rays from the transition depopulating the state were not observed.

The interpretations of the structure of the electron cascades from the $1/2^+$ state in

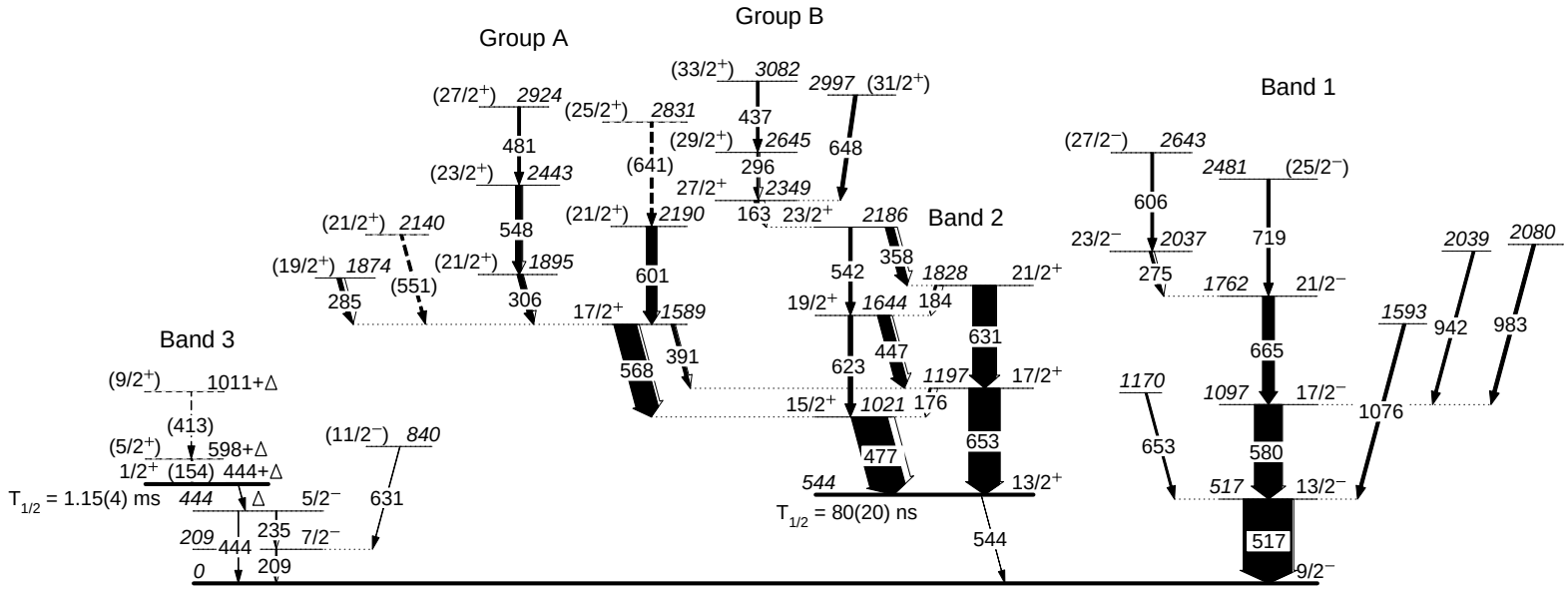

Figure 4.5: The level scheme of ^{205}Fr. The intensity of the 544-keV transition and of the transitions deexciting the $1/2^+$ isomer are not to scale. $\Delta = 165(5)$ keV, see text for details.

^{203}Fr and ^{199}At are supported by GEANT4 [Agostinelli03, Allison06] simulations. The simulations, performed by K. Hauschild [Hauschild13], were to generate conversion-electron spectra from a cascade with the properties suggested in the present work, together with other feasible decay scenarios. For the results of the simulations, and a comparison to the experimental data see appendix C.

Excited states associated with ^{205}Fr are presented in figure 4.5. The prompt gamma-ray transitions from the present study can be divided into two groups based on coincidence relations. The strongest of these transitions, a 517-keV transition, was placed to proceed to the $9/2^-$ ground state and Band 1 was built further based on coincidence relations. The multipolarities for the most prominent transitions were assigned based on the angular distributions of the gamma rays from the transitions. The $13/2^+$ isomer was observed in ^{205}Fr through its deexcitation that was assigned as a single-step transition with a $M2$ character to the $9/2^-$ ground state. This transition with a gamma-ray energy of 544 keV, was observed with the GREAT clover detector and the corresponding conversion electrons were detected with the PIN array. An internal K-conversion coefficient of 0.25(10) was obtained, suggesting that the transition is indeed of $M2$ character. The half-life of the $13/2^+$ isomer was estimated by investigating the yield of the isomer through a comparison of the intensity of the two transitions feeding it in JUROGAM and the intensity of the 544-keV transition. By considering the time of flight of close to 800 ns of the ^{205}Fr recoils through RITU, a half-life of 80(20) ns was obtained for the isomer. Hence only the tail of the isomeric activity was observed with the GREAT spectrometer. A transition strength of 0.17(4) W.u. was obtained for the transition, which coincides well with the results for similar $M2$ transitions observed in ^{197}At, ^{199}At and ^{203}Fr. Band 2 was placed on top of the $13/2^+$ isomer based on systematics in this region and on the fact that the strongest transitions in this band were not observed in coincidence with the 517-keV transition.

The conversion electrons from the deexcitation of an isomer to the $9/2^-$ ground state in ^{205}Fr were observed with the DSSD. The structure of this electron spectrum is quite similar to that of the neighbouring odd-mass nucleus ^{203}Fr, representing a three-step cascade, and it is interpreted as consisting of a 165-keV $M2$ transition followed by a 235-keV $M1$ transition and a 209-keV $M1$ transition to the $9/2^-$ ground state. The gamma rays from these two $M1$ transitions were observed with the planar and clover detector in coincidence with the conversion electrons, but the $M2$ transition was only observed indirectly through the effects of its internal conversion on the structure of the electron spectrum. Therefore the level energy of the $1/2^+$ state has been left as uncertain. A 444-keV $E2$ transition was observed to proceed in parallel with the two $M1$ transitions when requiring an electron-gamma coincidence and a branching ratio of 35(10) % was obtained for this transition. This observation supports the existence of a $M2$ transition depopulating the $1/2^+$ isomer. A half-life of 1.15(4) ms was obtained for the isomer, resulting in a transition strength of $3.5(2)\times10^{-4}$ W.u., assuming a 100 % $M2$ branching. Consequently the isomer was assigned a spin and parity of $1/2^+$.

The transition strength is, furthermore, comparable with the estimate obtained for the corresponding transition from the $1/2^+$ state in ^{203}Fr. Similarly as in ^{203}Fr, a significant competing $E3$ branch from the $1/2^+$ state to the $7/2^-$ state is suggested to exist in ^{205}Fr with a branching ratio of 5–40 %. The setup was, however, not sensitive enough to resolve this possible $E3$ branch. The suggestion of the structure of the cascade from the $1/2^+$ state is further supported by GEANT4 [Agostinelli03, Allison06] simulations of electron spectra performed by K. Hauschild [Hauschild12]. See appendix B for further details on the simulations and for a comparison to the experimental data. As the 165(5)-keV $M2$ transition was not directly observed, the level energy of the $1/2^+$ state is indicated by a value 444 keV+Δ, where $\Delta = 165(5)$ keV, in figure 4.5.

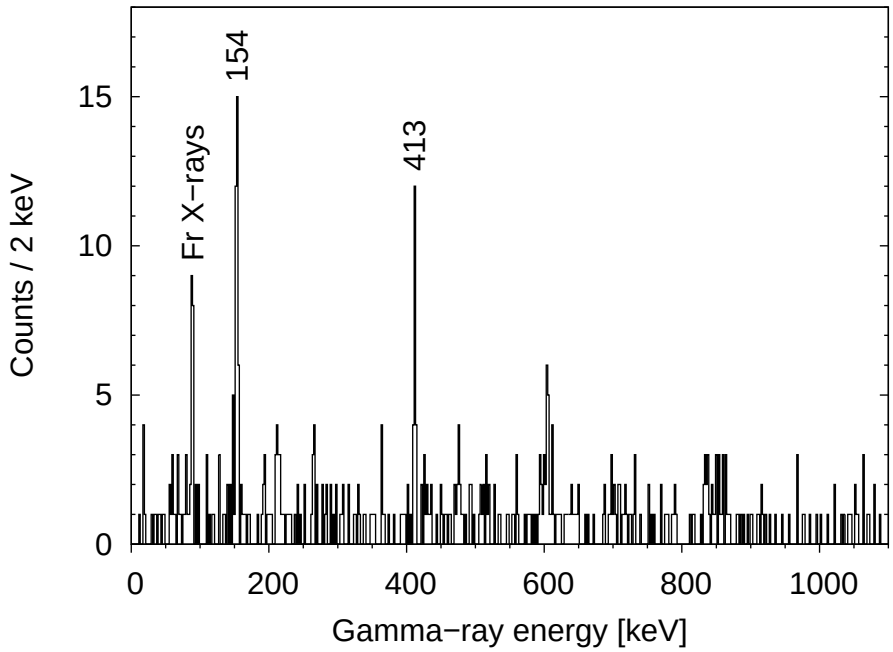

Figure 4.6: Energy spectrum of prompt gamma-ray transitions detected with the JUROGAM array and tagged with the transitions deexciting the $1/2^+$ isomer in ^{205}Fr. Note the broad peaks close to 600 and 840 keV that could originate from the $(n, n'\gamma)$ reaction in the detector material.

Figure 4.6 presents prompt gamma-ray transitions detected with the JUROGAM array and tagged with the events deexciting the $1/2^+$ isomer in ^{205}Fr. Two prominent peaks, with energies of 154 and 413 keV, emerge from the spectrum. The low intensity of the X-ray peaks suggests that both of the transitions could have an $E2$ character. A weak coincidence was observed between the transitions, and the 154-keV transition was placed lower in the level scheme due to its higher intensity, with an $E2$ character. The assignments are highly tentative.

The proposed configurations for relevant states in ^{205}Fr are presented in table 4.2. The low-lying negative-parity states originate from proton configurations similar to

Table 4.2: The proposed configurations for relevant states in ^{205}Fr.

	E_{state} (keV)	Configuration
$9/2^-$	0	$\pi h_{9/2} \otimes 0^+$
$13/2^-$	517	$\pi h_{9/2} \otimes 2^+$
$17/2^-$	1097	$\pi h_{9/2} \otimes 4^+$
$21/2^-$	1762	$\pi h_{9/2} \otimes 6^+$
$23/2^-$	2037	$\pi (h_{9/2})^2 f_{7/2}$
$(25/2^-)$	2481	$\pi (h_{9/2})^5$ or $\pi (h_{9/2})^3 \otimes 2^+$
$(27/2^-)$	2643	$\pi (h_{9/2})^4 f_{7/2}$ or $\pi (h_{9/2})^2 f_{7/2} \otimes 2^+$
$13/2^+$	544	$\pi i_{13/2}$
$17/2^+$	1589	$\pi h_{9/2} \otimes 5^-$
$23/2^+$	2186	$\pi h_{9/2} \otimes 7^-$
$27/2^+$	2349	$\pi h_{9/2} \otimes 10^-$
$(29/2^+)$	2645	$\pi h_{9/2} \otimes 11^-$
$1/2^+$	444+Δ	$\pi (s_{1/2})^{-1}$
$7/2^-$	209	$\pi f_{7/2}$
$5/2^-$	444	$\pi h_{9/2} \otimes 2^+$

those of the ^{204}Rn [Dobson02] isotone, here used as the core. In these cases all valence protons lie on the $h_{9/2}$ orbital. However, to produce the higher-lying states a contribution from the proton $f_{7/2}$ orbital can be expected as well. The positive-parity states, indicated in figure 4.5 as Group A, feeding into Band 2 could originate from the odd $h_{9/2}$ proton coupled to the negative-parity states in the ^{204}Rn core. Of these core states the 5^-, 6^- and 7^- states are suggested to originate from the coupling of the last neutron hole pair. The configurations of the 5^- and 7^- states are suggested to be $(\nu(f_{5/2})^{-1}(i_{13/2})^{-1}; \nu(p_{3/2})^{-1}(i_{13/2})^{-1})$ and $(\nu(f_{5/2})^{-1}(i_{13/2})^{-1}; \nu(p_{3/2})^{-1}(i_{13/2})^{-1}; \nu(p_{1/2})^{-1}(i_{13/2})^{-1})$, respectively, and the 6^- state could originate from either of the two suggested configurations. These states are observed in the isotone ^{200}Pb [Kondev07b], and they can be expected to exist in ^{204}Rn. However, a full set of the negative-parity core states presented in table 4.2 has not yet been observed in ^{204}Rn [Dobson02]. The $27/2^+$ and $(29/2^+)$ states, in Group B feeding the $23/2^+$ state, presumably a part of Band 2, can represent the I_{MAX} state from the coupling of the odd $h_{9/2}$ proton to the 10^- ($\pi f_{7/2} i_{13/2}$) and 11^- ($\pi h_{9/2} i_{13/2}$) states [Horn81] in the ^{204}Rn radon core. Finally the $5/2^-$ state depopulating the $1/2^+$ isomer is suggested to belong to the same multiplet as the $13/2^-$ state, and the $7/2^-$ state to originate from the odd proton on the $f_{7/2}$ orbital. Similar configurations as presented in table 4.2 are suggested for the states observed in ^{203}Fr as well. Lastly it is worth noting that the spin and parity of $9/2^-$ of the ground state in ^{203}Fr has not yet been measured and it is still based on systematics in this region. Therefore the ground-state assignments are strictly speaking still tentative in this nucleus [Kondev05]. However, in the present work this is left

as a note and the appropriate brackets have been omitted merely for convenience. A very recent laser-spectroscopic measurement has been performed by Voss *et al.* for the neutron-deficient francium isotopes ^{204}Fr, ^{205}Fr and ^{206}Fr. They report that the ground state in ^{205}Fr indeed has a spin of $9/2$ [Voss13].

4.3 The odd-odd francium nuclei ^{204}Fr and ^{206}Fr

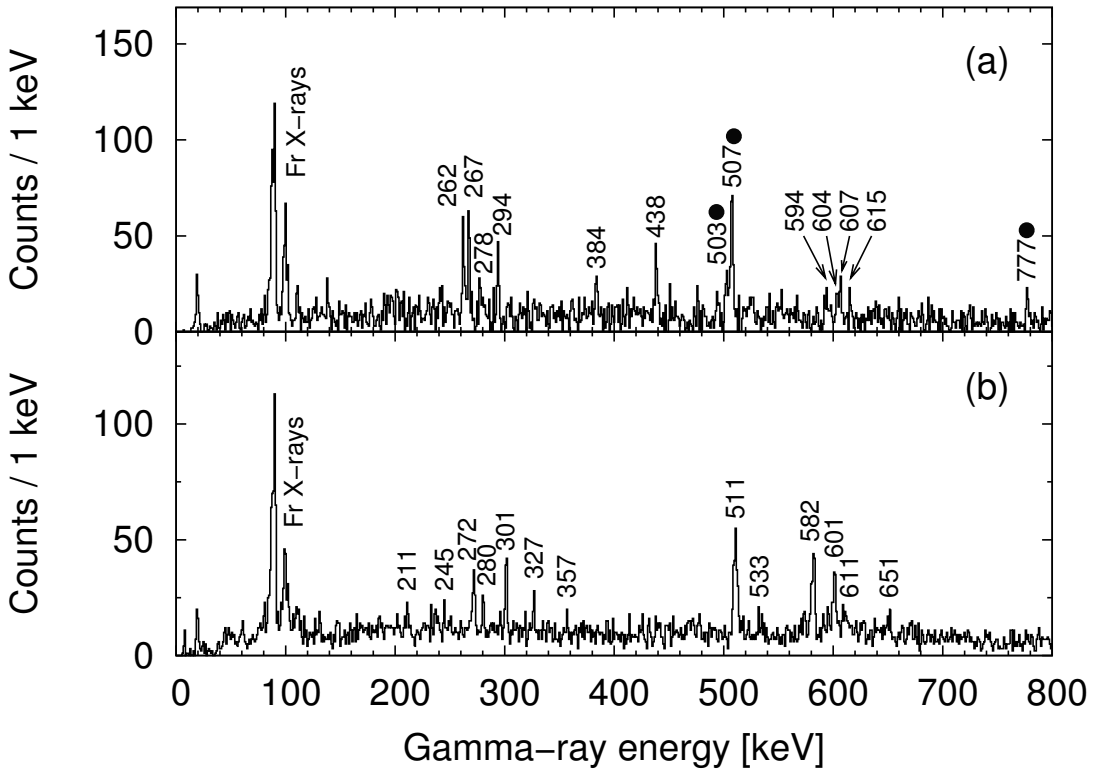

Figure 4.7: Energy spectra of prompt gamma-ray transitions tagged with (a) the 7^+ and $(2^+, 3^+)$ states in ^{206}Fr and (b) the 3^+, 7^+ and 10^- states in ^{204}Fr. Panel (a) includes gamma-ray transitions assigned to ^{205}Fr by Hartley *et al.* [Hartley08]. These transitions are indicated by filled circles.

The odd-odd nuclei ^{204}Fr and ^{206}Fr were side products in the present study, and no extensive spectroscopic investigations could be performed for these nuclei. In the following, prompt gamma-ray spectra associated with these nuclei are presented together with measured half-lives of the alpha-decaying states in ^{204}Fr.

The 275-keV $E3$ transition from the 10^- to the 7^+ state in ^{204}Fr has now been observed for the first time, see figure 3.9(b). This observation is in agreement with the decay scheme reported by Huyse *et al.* [Huyse92] for ^{204}Fr. By tagging with the alpha decay from the 7^+ state and studying the distribution of time differences between the

recoil implantation and the detection of the subsequent 275-keV electron, a half-life of 1.65(15) s was obtained for the 10^- state. This result is slightly higher that the value of ∼1 s reported by Huyse *et al.* Furthermore, by studying the distribution of time differences between the detection of the 275-keV electron and the subsequent alpha decay from the 7^+ state, a half-life of 2.6(3) s was obtained for the 7^+ state. This value is in full agreement with the corresponding value of 2.6(3) s reported by Huyse *et al.*

Figure 4.7(a) presents the energy spectrum of prompt gamma-ray transitions detected with the JUROGAM array when tagging with the alpha decay of the 7^+ and (2^+, 3^+) states in ^{206}Fr [Huyse92], and figure 4.7(b) when tagging with the alpha decay of the 3^+, 7^+ and 10^- states in ^{204}Fr [Huyse92], respectively. In both cases the lack of statistics together with overlapping alpha-particle energies prevented the division of the gamma-ray transitions between the alpha-decaying states. In ^{204}Fr the alpha-particle energy from the decay of the 7^+ state does not overlap with the alpha-particle energies from the decays of the 3^+ and 10^- states, that in turn have overlapping alpha-particle energies. There exists, however, the internal transition branch between the 10^- and 7^+ states, discussed earlier. This branch caused the observation of the same prompt gamma-ray transitions when tagging with the three different alpha decays. Consequently figure 4.7(b) includes transitions tagged with all three alpha decays in ^{204}Fr.

Excited states of the nucleus ^{205}Fr were previously reported in a study by Hartley *et al.* [Hartley08]. They presented a level scheme with states up to a spin and parity of ($21/2^-$) at a level energy of approximately 1.6 MeV. The level scheme obtained in the present study, see figure 4.5, does not agree with the results presented by Hartley *et al.* Instead the present results suggest that the gamma-ray transitions that they had analysed in fact belong to the neighbouring nucleus ^{206}Fr. This claim is based on the fact that the transitions reported by Hartley *et al.* to belong to ^{205}Fr are visible among the transitions associated with ^{206}Fr in figure 4.7(a). This figure does further include a number of the transitions assigned to ^{206}Fr by Hartley *et al.*, and a possible reason for them not being in coincidence with the ones marked with filled circles could be that the latter ones proceed to a different alpha-decaying state.

Chapter 5

Discussion

Systematics of the low-lying negative-parity states in the neutron-deficient odd-mass francium and astatine nuclei are presented in figure 5.1. Panel (a) presents the states in the astatine nuclei compared with yrast positive-parity states in their polonium isotones and panel (b) depicts the corresponding states as in the left panel now as a comparison between the francium nuclei and their radon isotones. In both panels the positive-parity states at the neutron shell closure are formed by the coupling of the last two valence protons in the $h_{9/2}$ orbital. This coupling gains a maximum spin and parity of 8^+. The negative-parity states in the astatine nuclei are formed by the odd $h_{9/2}$ proton coupled to the polonium core, resulting in a maximum spin and parity of $21/2^-$. The $23/2^-$ state in the astatine nuclei originates from a $(h_{9/2})^2 f_{7/2}$ configuration. In the francium nuclei the negative-parity states are formed similarly as in the astatine nuclei, with a coupling to the radon core. In both panels the excited states of the astatine and francium nuclei have been normalized to the $9/2^-$ ground state.

When moving away from the neutron shell closure, a sudden drop in the level energy of the 2^+ state can be seen for the polonium and radon nuclei, obediently followed by the astatine and francium nuclei, respectively. This drop originates from the opening of the first neutron orbital below the $N = 126$ shell closure. When moving further away from the neutron shell closure collectivity gradually increases as the number of neutron holes increases. In both polonium and radon nuclei the level energies of the 2^+ and 4^+ state indicate that in this region the two states have a vibrational character, whereas the 6^+ and 8^+ states in the polonium nuclei originate from the coupling between the two valence protons [Maj90]. In an earlier study [Zemel83] Zemel and Dobes had used the IBA + two-quasiparticle model to reproduce level systematics for neutron deficient polonium and radon nuclei. They observed that the 2^+ state is best described by collective behaviour, whereas the 6^+ and 8^+ states have a quasi-particle character. The 4^+ state, with a more irregular behaviour, could only be explained by a mixture of both collective and quasi-particle properties, with the quasi-particle

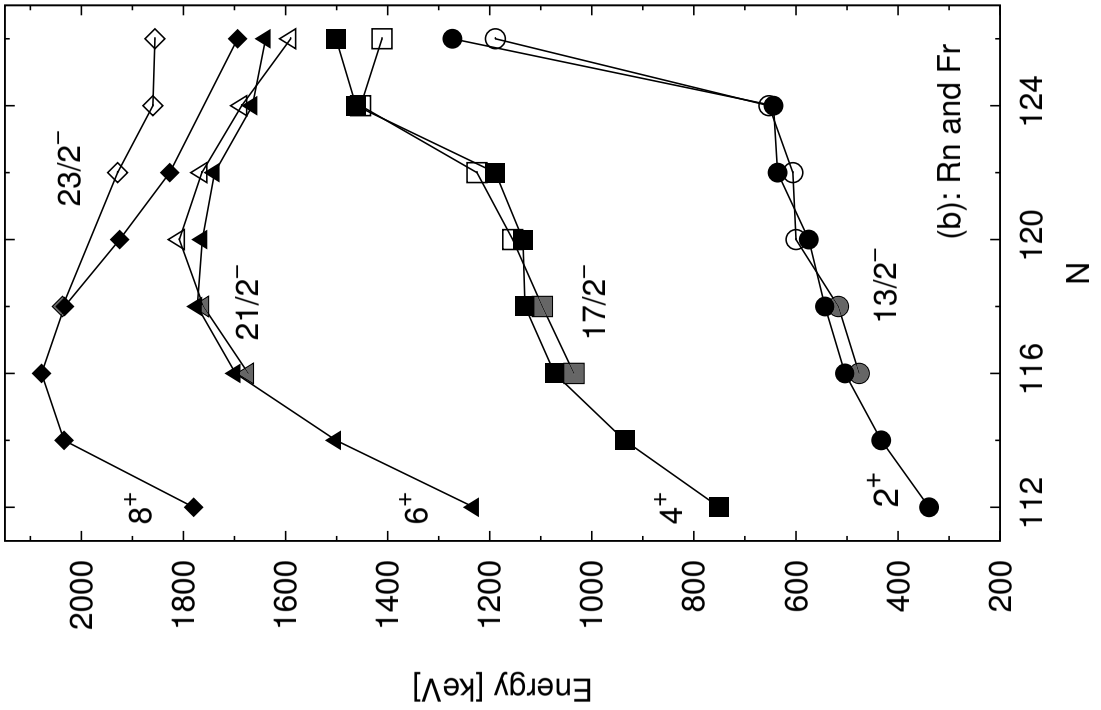
Energy [keV]
N
(b): Rn and Fr
8+
6+
4+
2+
21/2−
17/2−
13/2−
23/2−

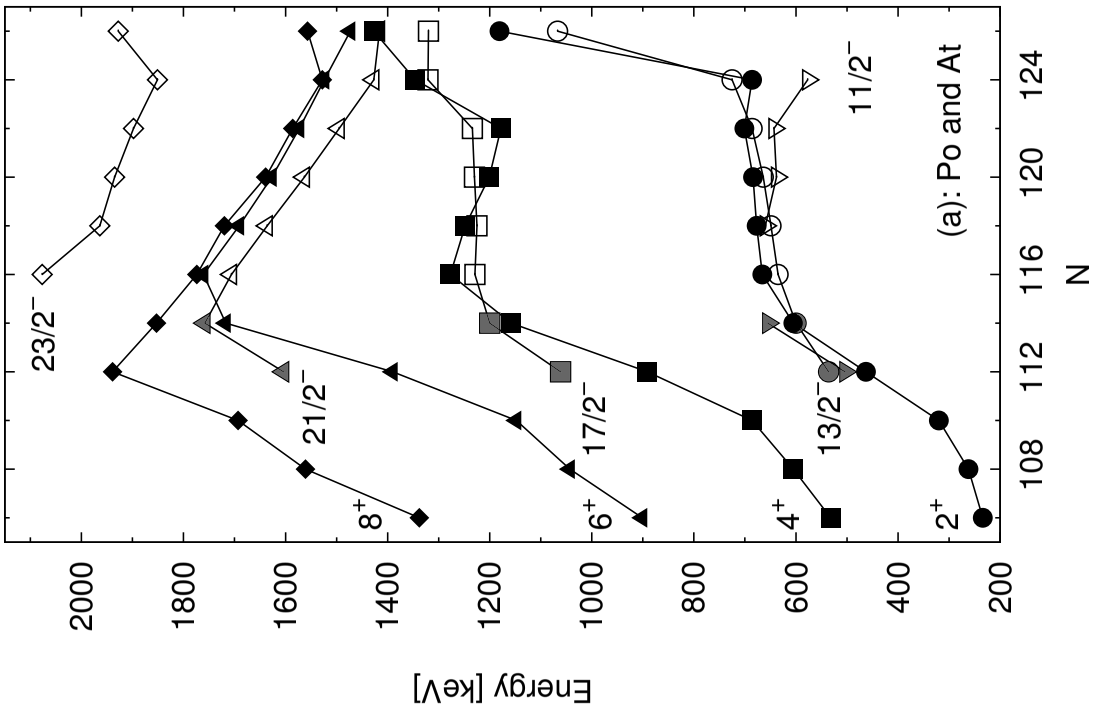
Energy [keV]
N
(a): Po and At
8+
6+
4+
2+
21/2−
17/2−
13/2−
11/2−
23/2−

properties including contributions of both proton and neutron type. The very similar trend of the level energies for the astatine and francium nuclei as compared with their polonium and radon isotones, respectively, is clearly visible. This similarity is a sign of a weak coupling between the $h_{9/2}$ proton and the underlying core, indicating the role of a spectator for the odd proton. At $N = 114$ a sudden bend downward in the level energies of the polonium nuclei can be seen in figure 5.1(a). This bend is associated with the onset of the oblate intruder configuration [Oros99, Julin01]. Further, at $N = 108$, a second bend downward can be seen pronounced for the 6^+ and 8^+ states in the polonium nuclei. This bend, in turn, originates from the onset of the prolate intruder configuration [Oros99, Julin01]. The first bend downward, describing the strengthening of the coupling of the $h_{9/2}/f_{7/2}$ proton to the polonium core, can already be observed for the $21/2^-$ state in ^{197}At and possibly in the lower-lying states of this nucleus, although with a softer effect on the level energy. This observation is supported by the assignment in the present study of a tentative unfavoured signature partner in the ground state band of ^{197}At. Searching for effects of the oblate intruder configuration in the systematics of radon isotopes in panel (b) is less satisfying as the neutron-deficient radon nuclei are not as well-known as the corresponding polonium nuclei. A steady increase in collectivity can be seen when moving away from the neutron shell closure, and the first effects from the oblate intruder configuration are visible in ^{198}Rn [Taylor99] at $N = 112$, slightly pronounced for the 8^+ state. Due to the similarity of the level energies between the polonium and radon nuclei, the radon nuclei are assumed to be affected by the same intruder mechanism as the polonium nuclei [Dobson02]. The neutron-deficient odd-mass francium nuclei are even less studied than their radon isotones, with ^{203}Fr being the lightest nucleus studied to date with known excited states, promptly feeding the ground state. No clear signs of the strengthening of the coupling of the $h_{9/2}/f_{7/2}$ proton to the radon core have been observed yet in the neutron-deficient francium nuclei and the ground state is still dominated by spherical structures. This observation for ^{205}Fr is further consistent with the recent results from laser-spectroscopic studies by Voss *et al.* [Voss13] reporting that the ground state remains spherical in the odd-mass francium nuclei down to ^{205}Fr.

Level energy systematics of the intruder $1/2^+$ state in neutron-deficient odd-mass bis-

Figure 5.1 ***(preceding page)*****:** Systematics of low-lying negative-parity states feeding the ground state in odd-mass neutron deficient (a) astatine nuclei compared with the yrast positive-parity states in their polonium isotones and (b) francium nuclei compared with yrast positive-parity states in their radon isotones, as a function of neutron number. The polonium and radon isotopes are indicated with filled symbols and the astatine and francium isotopes with open symbols. The lines connect yrast states without specifying the configuration of the states. For the polonium data see references [Baxter90, Fant90, Maj90, Bernstein95, Poletti97, Helariutta99, Browne03, Wiseman07], the data of the heavier astatine nuclei references [Bergström70, Sjoreen76, Sjoreen81, Dybdal83, Davie84], the radon data references [Horn81, Taylor99, Dobson02, Poletti05, Dracoulis09b] and for the data on the heavier francium nuclei references [Byrne86, Hartley08, Dracoulis09a]. The data points indicated in grey are from the present work.

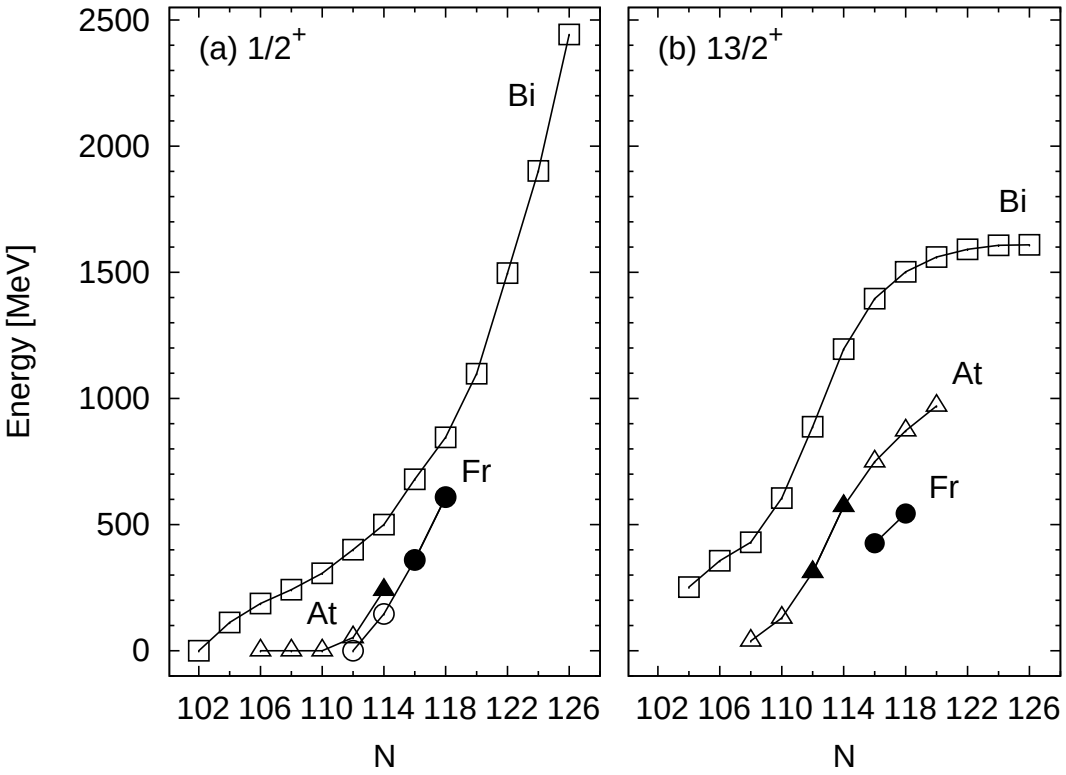

Figure 5.2: Systematics of (a) the intruder $1/2^+$ state and (b) the isomeric $13/2^+$ state in neutron-deficient odd-mass bismuth (squares), astatine (triangles) and francium (circles) nuclei as a function of neutron number. For the bismuth data see references [Alpsten69, Lönnroth82, Lönnroth86, Chapuran86, Braga86, Coenen86, Firestone96, Andreyev01, Hürstel02, Kettunen03a, Kettunen03b, Andreyev04a, Nieminen04], the astatine data the present work and references [Dybdal83, Davie84, Coenen86, Kettunen03b, Kettunen03a, Andgren08, Nyman13] and for the francium data the present work and references [Uusitalo05, Kalaninová13, Uusitalo13]. The nuclei studied in this thesis are denoted by filled symbols.

muth, astatine and francium nuclei are presented in figure 5.2(a). The state originates from a $1p-1h$ excitation across the $Z = 82$ shell closure, creating a proton hole on the $s_{1/2}$ orbital. This mechanism is similar to that of the oblate intruder configuration discussed above, and due to this similarity, the $1/2^+$ state is interpreted as being intrinsically of oblate structure. This state is known throughout the odd-mass bismuth isotopes, and it becomes the ground state in ^{185}Bi [Andreyev04a], where the configuration has changed as originating from a $3p-3h$ excitation. This configuration has a proton hole on the $s_{1/2}$ orbital and it resembles the $4p-4h$ excitation discussed above introducing a prolate shape. If the excited oblate intruder 0^+ states in lead and polonium nuclei in figure 1.2 are compared, the slope exhibited by the polonium nuclei is steeper than that in the lead nuclei. There is, furthermore, a similarity between the slope of the oblate intruder 0^+ state in the lead nuclei in figure 1.2 and the $1/2^+$ state in the bismuth nuclei shown in figure 1.2 and 5.2. The $1/2^+$ state is only known in the

lightest odd-mass astatine isotopes and it already becomes the ground state in ^{195}At introducing oblate ground-state deformation. This state has now been observed in ^{199}At for the first time and with this assignment the upward-sloping trend in astatine nuclei in figure 5.2 starts to resemble that of the polonium intruder 0^+ state in figure 1.2. Consequently, by following the upward trend when moving towards the neutron shell closure, the level energy of the $1/2^+$ state in for instance ^{201}At could be expected to exceed 450 keV. In the francium nuclei the $1/2^+$ state has been observed in ^{203}Fr and ^{205}Fr at a quite high excitation energy. Together with the level energy of 146 keV in ^{201}Fr, reported by Uusitalo *et al.* [Uusitalo05], the level energies in francium nuclei follow a trend where the $1/2^+$ state may become the ground state already in ^{199}Fr as Uusitalo *et al.* predict. Indeed two very recent studies [Kalaninová13, Uusitalo13] report that this is the case. Hence the $1/2^+$ state reaches the ground state considerably earlier in astatine and francium nuclei than it does in bismuth nuclei. Furthermore, the data points for the francium nuclei lie quite close to those of the astatine nuclei as compared with the bismuth systematics. The excited oblate 0^+ state has not yet been observed in the neutron-deficient radon nuclei. However, with the similarities visible in the behaviour of the $1/2^+$ state between the astatine and francium nuclei in figure 5.2, it becomes tempting to suggest that the excited oblate 0^+ state in radon nuclei may behave very similarly as the corresponding state in the polonium isotones.

When considering the states belonging to the structure built on the $1/2^+$ state in ^{205}Fr, presented in figure 4.5, a peculiarity can be observed in the level energies of the $(9/2^+)$ state and the $(5/2^+)$ state if the 154-keV transition has an $E2$ character. When normalizing to the underlying level energy of the $1/2^+$ state, a level-energy ratio of close to 3.7 is obtained which clearly exceeds that of the rigid rotor limit of 3.33. In this case a possibility could for instance be that the transitions observed do not form a structure built on the $1/2^+$ state, but that the 154-keV $E2$ transition feeds the $1/2^+$ state from another structure. This scenario could possibly resemble that of the $13/2^+$ $(13/2^+[606])$ state in ^{189}Bi [Hürstel04], where the oblate $13/2^+$ state is fed through an $E2$ transition by a prolate band based on the rotation-aligned $1/2^+[660]$ configuration. If the transition would be of $E1$ character, the states preceding it would be of negative parity. In this case the $1/2^+$ state would be bypassed to the states below it, however, the 154-keV $E1$ transition could ensure a moderate population of the $1/2^+$ state. I this case the structure could involve an $f_{7/2}$ or $h_{9/2}$ proton. A similar situation as observed in ^{205}Fr could be the case in ^{197}At [Andgren08], where a 381-keV transition with an $E2$ character, was set to proceed to the $1/2^+$ state. Andgren *et al.* presented a gamma-ray spectrum tagged with the alpha decay from the $1/2^+$ state. The 381-keV transition was the most prominent one in that spectrum, but there were also two weak transitions with energies of 134 and 181 keV visible in the spectrum. The astatine X-ray peaks were, furthermore, not observed, indicating that the low-energy transitions were possibly not of $M1$ character. The gamma-ray statistics are certainly low, but a similar scenario as in ^{205}Fr could perhaps be possible. This discussion together with the assignments in ^{205}Fr are, however, highly speculative and a further investigation

is certainly needed to shed more light on the properties of the structure built on the $1/2^+$ state.

Figure 5.2(b) presents the isomeric $13/2^+$ state in a similar systematic way as the $1/2^+$ state is presented in figure 5.2(a). The $13/2^+$ state originates from the odd proton excited to the $i_{13/2}$ orbital. It is known throughout the odd-mass bismuth isotopes. The level energy stays quite constant when moving away from the neutron shell closure, but starts to drop close to $N = 114$. This downward-sloping trend follows quite smoothly that of the oblate 0^+ state in the lead isotones (see figure 1.2). The similarity suggests that the coupling of the $i_{13/2}$ proton to the oblate intruder configuration in lead could be the origin of the deformation of the $13/2^+$ state, as suggested by Nieminen *et al.* [Nieminen04]. A kink in the energy systematics is visible at $N = 106$ close to the neutron mid-shell. This kink could in turn originate from the coupling of the $i_{13/2}$ proton to the prolate intruder configuration. Such a coupling would result in the $13/2^+$ state already having a prolate shape in ^{187}Bi. The decoupled band observed to feed this state in ^{187}Bi [Hürstel04] is suggested by Hürstel *et al.* to be built on the $13/2^+$ state. This would indicate that the $13/2^+$ state has a prolate deformation. Hürstel *et al.*, however, point out that it cannot be excluded that the decoupled band would be built on another, non-yrast, $13/2^+$ state that instead would have a prolate deformation, as is the case in ^{189}Bi [Hürstel04]. Similarly, a coupling mechanism could be suggested for the systematic behaviour in the astatine nuclei where the downward-sloping trend of level energies follows the downward intrusion of the oblate 0^+ state in the polonium isotones, although the downward slope is softer than in the bismuth nuclei, see figure 5.2(b). This coupling of the $i_{13/2}$ proton to the oblate intruder configuration in the polonium core is further supported by for example the observation of a strongly coupled rotational band reported to be built on top of the $13/2^+$ state in ^{197}At and ^{199}At, indicating oblate deformation for this state. The $13/2^+$ states in the francium nuclei are not yet well-known, with the first identifications in the present work. Furthermore, no excited 0^+ states have yet been observed in the corresponding radon nuclei that could serve as a comparison. The observation of a strongly coupled rotational band in ^{205}Fr and the start of one in ^{203}Fr, together with these systematics do, however, point towards an oblate deformation for the $13/2^+$ state in these two nuclei. The deformed character of the $13/2^+$ state in these two nuclei would then originate from a coupling to the oblate intruder configuration in the radon core.

Experimental $B(M1)/B(E2)$ values for the rotational band built on the $13/2^+$ state extracted for the nuclei in the present study, together with the values for the corresponding band in ^{193}Bi [Nieminen04] are presented in figure 5.3. Theoretical estimates of the $B(M1)/B(E2)$ values, using the Dönau-Frauendorf model [Dönau82, Dönau87], have been made based on the assumption that the band head stems from the spherical $\pi i_{13/2}$ configuration. The prediction is represented by a dashed line. The results represent the ^{197}At data quite reasonably, and ^{193}Bi very well, but the data for ^{199}At

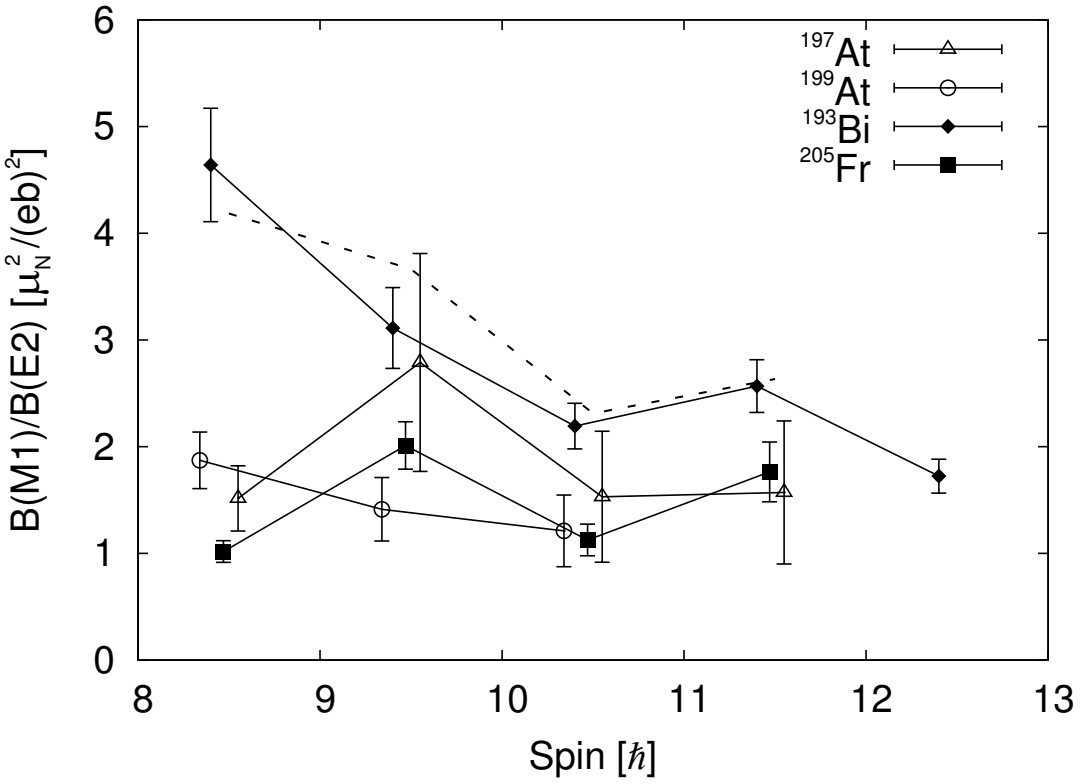

Figure 5.3: Experimental $B(M1)/B(E2)$ values from the strongly coupled rotational band built on top of the $13/2^+$ state in the nuclei ^{197}At, ^{199}At and ^{205}Fr in comparison with the $\pi i_{13/2}$ band in ^{193}Bi [Nieminen04]. The dashed line presents a theoretical estimate based on the model presented by Dönau and Frauendorf [Dönau82, Dönau87] calculated for ^{197}At. Oblate deformation is assumed with a deformation parameter of $\beta_2 = -0.2$ [Andgren08]. The single-particle g-factor used is 1.181 for an $i_{13/2}$ proton, estimated from the Schmidt values (see for instance [Blatt52]) and using an attenuation of 0.6 for the proton spin g-factor. The band-head spin has been set as the Ω-value, the signature splitting $\Delta e'$ is roughly estimated as 60 keV and the aligned angular momentum i_0 is set as 0.5. The experimental values have been shifted slightly on the horizontal axis for visual purposes.

and ^{205}Fr fall clearly below the estimate. The rotational properties may not yet be well-developed, and a deformation parameter estimate of -0.2 is possibly an overestimation for these two nuclei. Nevertheless the data points of the latter nuclei agree quite well with those of ^{197}At, of which the band-head of the rotational band is established as $13/2^+$ based on tagging with the transition depopulating the $13/2^+$ isomer to the $9/2^-$ ground state. A similar estimate using the other feasible scenario of the proton on the $h_{9/2}$ orbital would fall clearly below the experimental data points. This supports the placing of the rotational bands on top of the oblate $13/2^+$ state, rather than on the $9/2^-$ ground state, for each of the nuclei. Consequently each of the bands in figure 5.3 can be assigned as originating from the odd proton on the $13/2^+[606]$ Nilsson orbital. Furthermore, the structure built on the $13/2^+$ state in ^{203}Fr could have a similar origin based on systematics.

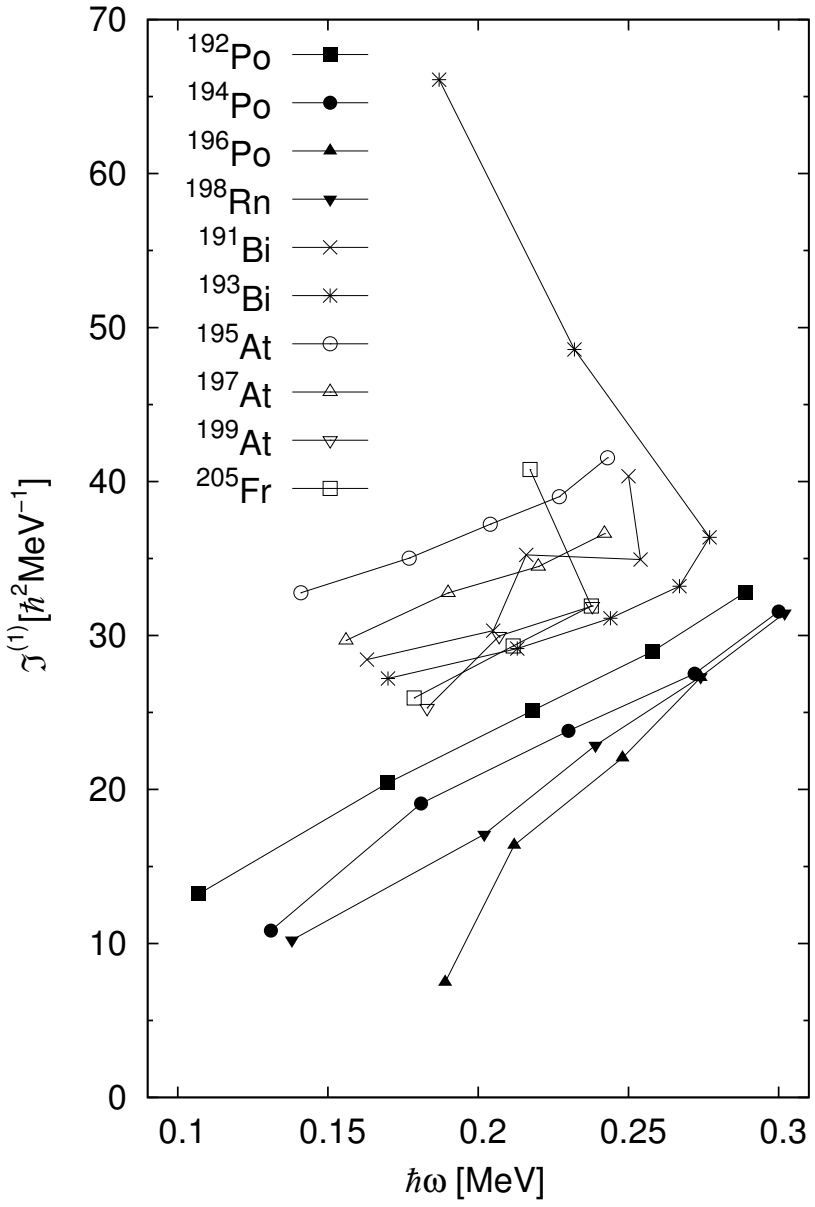

Figure 5.4: Experimental kinematic moments of inertia $\mathscr{J}^{(1)}$ as a function of rotational frequency of the $i_{13/2}$ band in the nuclei ^{197}At, ^{199}At and ^{205}Fr studied in the present work compared with the corresponding $i_{13/2}$ bands in neighbouring odd-mass nuclei and yrast lines in neighbouring oblate deformed even-mass nuclei. The bismuth data are taken from references [Nieminen04, Nyman09], the polonium data from references [Bernstein95, Helariutta99], the astatine data from the present work and [Nyman13], the radon data from [Taylor99] and the francium data from the present work.

Plots of experimental kinematic moments of inertia $\mathscr{I}^{(1)}$ of the $i_{13/2}$ band are presented in figure 5.4 for the nuclei ^{197}At, ^{199}At and ^{205}Fr in the present study. Similar plots for the $i_{13/2}$ band in neighbouring odd-mass nuclei and the yrast line for neighbouring even-mass nuclei have been added for comparison. For the even-mass nuclei the ground states include components of oblate structure (see figure 5.1) and therefore the yrast lines are assumed to display properties of an oblate rotor. For all nuclei in figure 5.4, an up-sloping behaviour of the moments of inertia can be observed, which is typical for a rotor having properties that are soft against rotation. The plots of the moments of inertia are situated in the figure in two groups of which the group consisting of the odd-mass nuclei lies higher in $\mathscr{I}^{(1)}$. This shift in the moment of inertia can be interpreted by a significant contribution of the unpaired proton on the moment of inertia of the whole nucleus. Furthermore, inside the groups the nuclei are suggested to have similar rotational properties. Hence the nucleus ^{198}Rn, situated at the point where the deformation in radon isotopes sets in (see figure 5.1), can possibly already have similar properties of an oblate rotor as the polonium nuclei. Between isotopes of the same element, a higher moment of inertia can be observed for the lighter isotopes. An explanation for this can be that when moving towards the mid-shell, the nuclei become more deformed and therefore better rotors. For instance in ^{192}Po the oblate intruder configuration has reached the ground state [Helariutta99] and smoother rotational properties can therefore be assumed than in the heavier polonium isotopes, resulting in higher moments of inertia. In the higher-$\mathscr{I}^{(1)}$ group consisting of odd-Z nuclei, the gradual rise in $\mathscr{I}^{(1)}$ when moving from ^{199}At to ^{197}At and further to ^{195}At, is clearly visible in figure 5.4. This change is supported by the increase in oblate deformation between ^{197}At and ^{195}At as predicted by TRS calculations [Andgren08] and by the fact that the rotational band observed built on the $13/2^+$ state in ^{195}At [Nyman13] has a stronger coupling than the one observed in the present work for ^{197}At. TRS calculations were not available for the present study, to predict the deformation of the $13/2^+$ state in ^{199}At. However, the coupling of the rotational band in this nucleus is weaker than for the corresponding band in ^{197}At and the moments of inertia for ^{199}At have analogously lower values as well. Nevertheless the values for ^{199}At settle in the region for the oblate deformed odd-mass nuclei, and consequently, the deformations may qualitatively be similar. A corresponding rise in moment of inertia as in the astatine nuclei can be observed between ^{193}Bi and ^{191}Bi as well. The values for ^{205}Fr lie quite low in $\mathscr{I}^{(1)}$, when comparing with the lighter odd-mass nuclei. The reason for this could possibly lie in the $13/2^+$ band in ^{205}Fr still being of a transitional nature. Indeed in figure 4.5 a signature splitting, that is larger than in the other three nuclei studied in this thesis, is observed for this band. The high-spin point in ^{205}Fr deviates from the slowly rising trend of the moment of inertia. A possible explanation for this could be that the $23/2^+$ state is no longer a part of the rotational structure. This deviation in moment of inertia is very abrupt and does not resemble that of the backbending in ^{193}Bi, which has been attributed to the alignment of an $i_{13/2}$ neutron pair [Nieminen04]. It is finally worth noting that all of the moments of inertia in figure 5.4 lie, however, still quite far away from the rigid rotor value (see for instance

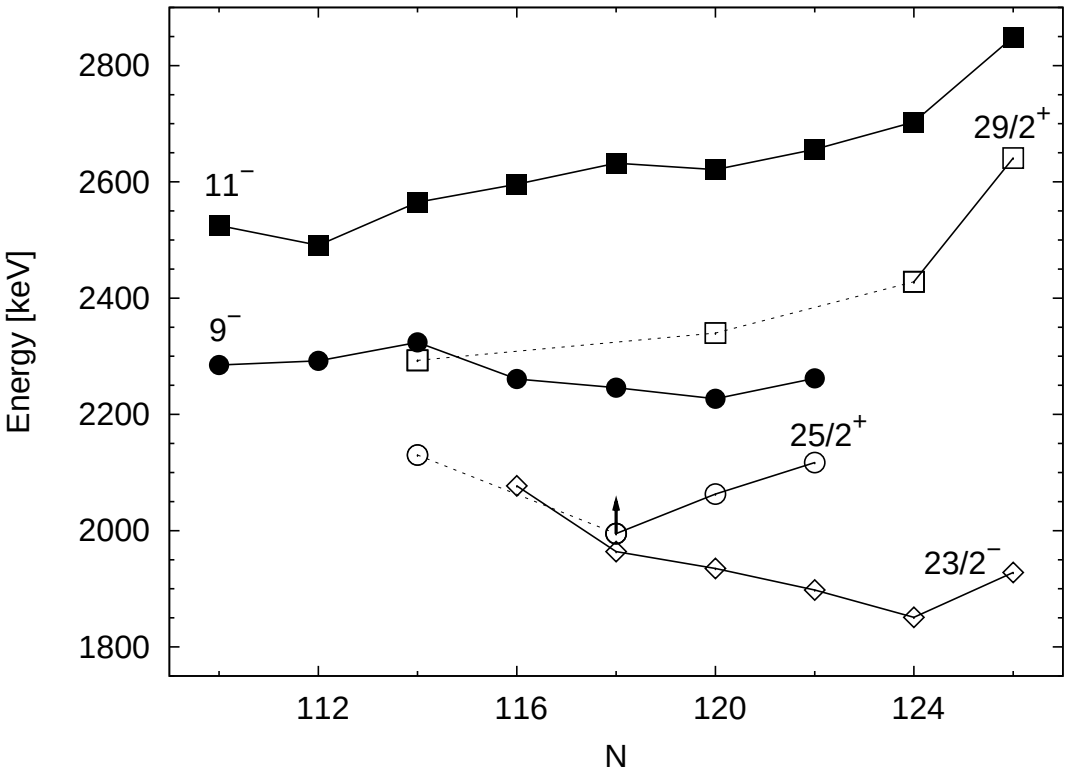

Figure 5.5: Level energies of the $29/2^+$, $25/2^+$ and $23/2^-$ states in the odd-mass astatine nuclei, denoted by open symbols, compared with those of the 11^- and 9^- states in their polonium isotones, denoted by filled symbols. ^{199}At has a neutron number of 114. The data point indicated with an arrow is floating in the level scheme, and has been lifted 30 keV in the figure for visual purposes. For the polonium data see the studies [Baxter90, Fant90, Maj90, Bernstein95, Poletti97, Helariutta99, Browne03] and for the heavier astatine data references [Bergström70, Sjoreen76, Sjoreen81, Dybdal83, Davie84].

[Krane88]) of close to 100 $\hbar^2$/MeV.

The $(29/2^+)$ isomer observed in ^{199}At deserves further inspection. Level-energy systematics of the $23/2^-$ $(\pi(h_{9/2})^2 f_{7/2})$, $25/2^+$ and the $29/2^+$ states in the neutron-deficient odd-mass astatine nuclei are presented in figure 5.5. The states are compared with the 9^- $(\nu(f_{5/2})^{-1}(i_{13/2})^{-1})$ and $11^-(\pi h_{9/2} i_{13/2})$ states in the polonium isotones. The $29/2^+$ state and the $25/2^+$ state are not as well-known in the astatine nuclei as the 11^- and the 9^- state are known in their polonium isotones. A similar trend is, however, visible supporting our configuration assignment for the $(29/2^+)$ and the $(25/2^+)$ state in ^{199}At, see table 4.1. The $23/2^-$ state rises steadily in energy when moving away from the neutron shell closure, while the positive-parity states are expected to stay rather constant in energy with decreasing neutron number. This rising trend of the $23/2^-$ state will make the feeding of the $29/2^+$ isomer to it increasingly unfavoured and the $29/2^+$ state will start to feed the $i_{13/2}$ band through positive-

parity states, such as the $25/2^+$ state. In ^{205}At, with $N = 120$, the $29/2^+$ isomer feeds the $23/2^-$ state through an $E3$ transition and the $25/2^+$ state through an $E2$ transition [Davie84]. In ^{199}At this $E3$ branch is no longer observed as the $23/2^-$ state has presumably risen too high for a feeding to it to be favourable. Unfortunately such a state, that could confirm this suggestion, has not yet been observed in ^{199}At. The $25/2^+$ state has also been reported to be isomeric in the heavier astatine nuclei [Sjoreen81, Dybdal83, Davie84], feeding the $23/2^-$ state through an $E1$ transition. However, its possible isomeric nature in ^{199}At could not be resolved in the present study. The corresponding states in the neutron deficient radon and francium nuclei are less well-known than in the polonium and astatine nuclei. A similar feeding pattern between the higher-lying states in the francium nuclei, as discussed above could, however, serve to explain the yield anomaly between the $13/2^+$ and the $13/2^-$ state observed in ^{203}Fr.

Chapter 6

Summary and outlook

The present study investigates the evolution of low-lying states in the neutron deficient astatine and francium nuclei by concentrating on the four nuclei ^{197}At, ^{199}At, ^{203}Fr and ^{205}Fr. The studies have been performed through prompt and delayed spectroscopy using the recoil-decay tagging technique. The results suggest that the ground states in ^{197}At and ^{199}At, having I^{π}=$9/2^{-}$, are still dominated by spherical structures. The coupling of the $h_{9/2}/f_{7/2}$ proton to the polonium core is, however, suggested to increase in ^{197}At as the unfavoured signature partner in the ground-state band has been observed. Similar investigations have been performed for the francium nuclei with the result that in both ^{203}Fr and ^{205}Fr the ground state is still dominated by spherical structures. No strengthening of the coupling of the $h_{9/2}/f_{7/2}$ proton to the radon core has, moreover, been observed.

The isomeric $1/2^{+}$ ($\pi(s_{1/2})^{-1}$) state has been identified for the first time in ^{199}At and in ^{205}Fr through the internal transition branch to the $9/2^{-}$ ground state. While the state was previously known in ^{203}Fr [Uusitalo05], the level energy of the state has now been established through the internal transition branch deexciting the state to the $9/2^{-}$ ground state, together with the confirmed alpha-decay branch to the $1/2^{+}$ state in ^{199}At. The systematics of this state show a striking similarity between the neutron-deficient astatine and francium nuclei. A corresponding similarity in the behaviour of the intruder oblate 0^{+} state is consequently suggested to exist between neutron-deficient polonium and radon nuclei.

The properties of the isomeric $13/2^{+}$ ($\pi i_{13/2}$) state have been investigated in ^{197}At and ^{199}At. A rotational band is observed to be built on this state in both nuclei, and consequently oblate deformation is suggested resulting in the state originating from a $13/2^{+}$[606] configuration where the odd proton is coupled to the oblate intruder configuration in the polonium core. The $13/2^{+}$ state has, furthermore, been observed for the first time in the neutron-deficient francium nuclei. In ^{205}Fr a strongly coupled rotational band is observed to be built on this state and in ^{203}Fr the start of a band is

assigned based on systematics. In both cases oblate deformation is suggested based on systematics and the state is suggested to originate from the coupling of the $13/2^+[606]$ proton to the oblate intruder configuration in the radon core. Consequently the present study suggests that the proton-intruder picture prevails up to the francium nuclei five protons away from the $Z = 82$ shell closure.

A higher-lying $(29/2^+)$ $(\pi h_{9/2} i_{13/2})$ isomer has been observed in ^{199}At and the existence of one, with a feeding to the negative-parity states, is suggested to be the cause for the surprisingly low yield of the isomeric $13/2^+$ state in ^{203}Fr.

There still remain a number of open questions that certainly deserve continued investigations in the four nuclei studied. The possible rotational properties of the $1/2^+$ state in all four nuclei are still unknown or highly speculative. The results for ^{203}Fr call, furthermore, for a study with improved statistics, as the properties of the $1/2^+$ state could not be determined with a satisfying precision. The isomeric $13/2^+$ state likewise needs a deeper investigation in this nucleus with higher statistics to observe a possible rotational band built on the state. Moreover, spectroscopy with the aim to observe states at higher spin in ^{203}Fr needs to be pursued, in order to confirm or dismiss the prediction of the existence of a higher-lying positive-parity isomer with a deexcitation pattern favouring a feeding to the negative-parity states in this nucleus. Furthermore, in ^{197}At the unfavoured signature partner in the ground-state band still needs confirmation.

Alongside the present work other studies of neutron-deficient astatine and francium nuclei have been carried out. A study of the properties of ^{195}At [Nyman13] has been accepted for publication in Phys. Rev. C and two studies on the properties of ground-state and low-lying states in very neutron-deficient francium nuclei have been published very recently [Kalaninová13, Uusitalo13]. A new study on prompt and delayed spectroscopy of ^{199}At and ^{201}At is ongoing and to be published, and interesting results are already appearing. There is also an experiment in preparation to perform prompt and delayed spectroscopy on the proton-unbound nucleus ^{201}Fr. This study, if successful, will increase our knowledge on the evolution of low-lying states in francium nuclei further to lighter nuclei. Moreover, this nucleus will, in fact, be the lightest one that can be reached in in-beam measurements with the equipment available to date. Interesting results could also be obtained for the heavier nucleus ^{207}Fr that is now the least well-known of the francium nuclei with in-beam studies performed. Although the ground state is expected to be spherical in this nucleus, a search for the $13/2^+$ and $1/2^+$ state could provide interesting information. At the moment, however, a large part of the properties of the low-lying states in the neutron-deficient francium nuclei rely heavily on systematics of odd-mass nuclei in this region. For instance predictions based on TRS calculations would be very valuable when studying the nature of low-lying states in the francium nuclei. Such calculations are still lacking. Moreover, the measurement of the spins of the low-lying states of the very neutron-deficient francium and astatine nuclei would be very important as for example the ground-state spins

for some of the nuclei in the present study are still tentative.

The systematics of low-lying states in nuclei in the region above lead are still far from complete and further investigations are crucial to form a picture on how these states evolve when moving from the neutron shell closure towards the neutron mid-shell. It could, furthermore, be interesting to investigate if the intruder picture still prevails when moving even further away from the proton shell closure towards nuclei heavier than francium. Continued nuclear-spectroscopy studies in this region from bismuth to higher-Z nuclei become increasingly important, as these nuclei gradually become available for laser-spectroscopy studies. Recently extensive studies have been performed for polonium nuclei, and further investigations into heavier nuclei are highly anticipated as these two independent methods will serve to complement each other.

Bibliography

[Agostinelli03] S. Agostinelli, J. Allison, K. Amako, J. Apostolakis, H. Araujo, P. Arce, M. Asai, D. Axen, S. Banerjee, G. Barrand *et al.*, *GEANT4 simulation toolkit*, Nucl. Instrum. Meth. A **506**, 250 (2003).

[Alburger57] D. E. Alburger, *Encyclopedia of physics, Nuclear Reactions III* (Editor S. Flügge. Springer-Verlag, Berlin, 1957).

[Allison06] J. Allison, K. Amako, J. Apostolakis, H. Araujo, P. Arce Dubois, M. Asai, G. Barrand, R. Capra, S. Chauvie, R. Chytracek *et al.*, *GEANT4 developments and applications*, IEEE T. Nucl. Sci. **53**, 270 (2006).

[Alpsten69] M. Alpsten and G. Astner, *Positive-parity states in some odd-mass bismuth isotopes*, Nucl. Phys. A **134**, 407 (1969).

[Andgren08] K. Andgren, U. Jakobsson, B. Cederwall, J. Uusitalo, T. Bäck, S. J. Freeman, P. T. Greenlees, B. Hadinia, A. Hugues, A. Johnson, P. M. Jones, D. T. Joss, S. Juutinen, R. Julin, S. Ketelhut, A. Khaplanov, M. Leino, M. Nyman, R. D. Page, P. Rahkila, M. Sandzelius, P. Sapple, J. Sarén, C. Scholey, J. Simpson, J. Sorri, J. Thomson and R. Wyss, *γ-ray spectroscopy of ^{197}At*, Phys. Rev. C **78**, 044328 (2008).

[Andreyev99] A. N. Andreyev, D. Ackermann, P. Cagarda, J. Gerl, F. Heβberger, S. Hofmann, M. Huyse, A. Keenan, H. Kettunen, A. Kleinböhl, A. Lavrentiev, M. Leino, B. Lommel, M. Matos, G. Münzenberg, C. Moore, C. D. O'Leary, R. D. Page, S. Reshitko, S. Saro, C. Schlegel, H. Schaffner, M. Taylor, P. Van Duppen, L. Weissman and R. Wyss, *Alpha decay of the new isotopes $^{188,189}Po$*, Eur. Phys. J. A **6**, 381 (1999).

[Andreyev00] A. Andreyev, M. Huyse, P. Van Duppen, L. Weissman, D. Ackermann, J. Gerl, F. Heβberger, S. Hofmann, A. Kleinböhl, G. Münzenberg, S. Reshitko, C. Schlegel, H. Schaffner, P. Cagarda, M. Matos, S. Saro, A. Keenan, C. Moore, C. D. O'Leary, R. D. Page, M. Taylor, H. Kettunen, M. Leino, A. Lavrentiev, R. Wyss and K. Heyde,

A triplet of differently shaped spin-zero states in the atomic nucleus ^{186}Pb, Nature **405**, 430 (2000).

[Andreyev01] A. N. Andreyev, D. Ackermann, P. Cagarda, J. Gerl, F. P. Heβberger, S. Hofmann, M. Huyse, A. Keenan, H. Kettunen, A. Kleinböhl, A. Lavrentiev, M. Leino, B. Lommel, M. Matos, G. Münzenberg, C. J. Moore, C. D. O'Leary, R. D. Page, S. Reshitko, S. Saro, C. Schlegel, H. Schaffner, M. J. Taylor, P. Van Duppen, L. Weissman and R. Wyss, *New microsecond isomers in* $^{189,190}Bi$, Eur. Phys. J. A **10**, 129 (2001).

[Andreyev04a] A. N. Andreyev, D. Ackermann, F. P. Heβberger, K. Heyde, S. Hofmann, M. Huyse, D. Karlgren, I. Kojouharov, B. Kindler, B. Lommel, G. Münzenberg, R. D. Page, K. Van de Vel, P. Van Duppen, W. B. Walters and R. Wyss, *Shape-changing particle decays of* ^{185}Bi *and structure of the lightest odd-mass Bi isotopes*, Phys. Rev. C **69**, 054308 (2004).

[Andreyev04b] A. N. Andreyev, P. A. Butler, R. D. Page, D. E. Appelbe, G. D. Jones, D. T. Joss, R.-D. Herzberg, P. H. Regan, J. Simpson and R. Wadsworth, *GEANT Monte Carlo simulations for the GREAT spectrometer*, Nucl. Instrum. Meth. A **533**, 422 (2004).

[Andreyev06a] A. N. Andreyev, S. Antalic, D. Ackermann, S. Franchoo, F. P. Heβberger, S. Hofmann, M. Huyse, I. Kojouharov, B. Kindler, P. Kuusiniemi, S. R. Lesher, B. Lommel, R. Mann, G. Münzenberg, K. Nishio, R. D. Page, J. J. Ressler, B. Streicher, S. Saro, B. Sulignano, P. V. Duppen, D. Wiseman and R. Wyss, *α-decay of the new isotope* ^{187}Po*: Probing prolate structures beyond the neutron mid-shell at* $N = 104$, Phys. Rev. C **73**, 044324 (2006).

[Andreyev06b] A. N. Andreyev, S. Antalic, M. Huyse, P. V. Duppen, D. Ackermann, L. Bianco, D. M. Cullen, I. G. Darby, S. Franchoo, S. Heinz, F. P. Heβberger, S. Hofmann, I. Kojouharov, B. Kindler, A.-P. Leppänen, B. Lommel, R. Mann, G. Münzenberg, J. Pakarinen, R. D. Page, J. J. Ressler, S. Saro, B. Streicher, B. Sulignano, J. Thomson and R. Wyss, *α decay of the new isotopes* $^{193,194}Rn$, Phys. Rev. C **74**, 064303 (2006).

[Baglin08] C. M. Baglin, *Nuclear data sheets for* $A = 169$, Nucl. Data Sheets **109**, 2033 (2008).

[Baxter90] A. M. Baxter, A. P. Byrne, G. D. Dracoulis, R. A. Bark, F. Riess, A. E. Stuchbery, M. C. Kruse and A. R. Poletti, *Spectroscopy of high-spin states of* ^{206}Po, Nucl. Phys. A **515**, 493 (1990).

[Beausang92] C. Beausang, S. Forbes, P. Fallon, P. Nolan, P. Twin, J. Mo, J. Lisle, M. Bentley, J. Simpson, F. Beck, D. Curien, G. deFrance, G. Duchêne and D. Popescu, *Measurements on prototype Ge and BGO detectors for the Eurogam array*, Nucl. Instrum. Meth. A **313**, 37 (1992).

[Bergström70] I. Bergström, B. Fant, C. J. Herrlander, K. Wikström and J. Blomqvist, *Evidence for an Isomeric $29/2^+$ Level in ^{211}At*, Physica Scripta **1**, 243 (1970).

[Bernstein95] L. A. Bernstein, J. A. Cizewski, H.-Q. Jin, W. Younes, R. G. Henry, L. P. Farris, A. Charos, M. P. Carpenter, R. V. F. Janssens, T. L. Khoo, T. Lauritsen, I. G. Bearden, D. Ye, J. A. Becker, E. A. Henry, M. J. Brinkman, J. R. Hughes, A. Kuhnert, T. F. Wang, M. A. Stoyer, R. M. Diamond, F. S. Stephens, M. A. Deleplanque, A. O. Macchiavelli, I. Y. Lee, B. Cederwall, J. R. B. Oliveira, J. Burde, P. Fallon, C. Duyar, J. E. Draper, E. Rubel and D. T. Vo, *Onset of collectivity in neutron deficient $^{196,198}Po$*, Phys. Rev. C **52**, 621 (1995).

[Bijnens98] N. Bijnens, P. Decrock, S. Franchoo, M. Gaelens, M. Huyse, H.-Y. Hwang, I. Reusen, J. Szerypo, J. von Schwarzenberg, G. Vancraeynest, P. Van Duppen and J. Wauters, *Study of $^{200,202}Po$ through β^+ and electron-capture decay and the manifestation of shape coexistence in the lighter Po isotopes*, Phys. Rev. C **58**, 754 (1998).

[Blatt52] J. M. Blatt and V. F. Weisskopf, *Theoretical nuclear physics* (John Wiley and Sons, New York, 1952).

[Bohr53] A. Bohr and B. R. Mottelson, *Collective and individual-particle aspects of nuclear structure*, Kong. Dansk. Vidensk. **27**, 1 (1953).

[Bohr75] A. Bohr and B. R. Mottelson, *Nuclear structure, volume II* (Benjamin, New York, 1975).

[Braga86] R. A. Braga, P. B. P.B. Semmes, W. R. Western and R. W. Fink, *Decay of mass-separated ^{201m}Po and ^{201g}Po*, Nucl. Phys. A **459**, 359 (1986).

[Browne03] E. Browne, *Nuclear Data Sheets for $A = 210$*, Nucl. Data Sheets **99**, 649 (2003).

[Bucurescu94] D. Bucurescu, G. Căta-Danil, M. Ivaşcu, L. Stroe and C. A. Ur, *Global systematics of unique parity quasibands in odd-A collective nuclei*, Phys. Rev. C **49**, R1759 (1994).

BIBLIOGRAPHY

[Byrne86] A. P. Byrne, G. D. Dracoulis, C. Fahlander, H. Hübel, A. R. Poletti, A. E. Stuchbery, J. Gerl, R. F. Davie and S. J. Poletti, *Spectroscopy of high-spin states in* $^{211,212,213}Fr$, Nucl. Phys. A **448**, 137 (1986).

[Casten00] R. F. Casten, *Nuclear structure from a simple perspective*, second edition (Oxford science publications, 2000).

[Chapuran86] T. Chapuran, K. Dybdal, D. B. Fossan, T. Lönnroth, W. F. Piel, D. Horn and E. K. Warburton, *High-spin γ-ray spectroscopy in* ^{197}Bi, Phys. Rev. C **33**, 130 (1986).

[Cocolios11] T. E. Cocolios, W. Dexters, M. D. Seliverstov, A. N. Andreyev, S. Antalic, A. E. Barzakh, B. Bastin, J. Büscher, I. G. Darby, D. V. Fedorov, V. N. Fedosseyev, K. T. Flanagan, S. Franchoo, S. Fritzsche, G. Huber, M. Huyse, M. Keupers, U. Köster, Y. Kudryavtsev, E. Mané, B. A. Marsh, P. L. Molkanov, R. D. Page, A. M. Sjødin, I. Stefan, J. Van de Walle, P. Van Duppen, M. Venhart, S. G. Zemlyanoy, M. Bender and P.-H. Heenen, *Early Onset of Ground State Deformation in Neutron Deficient Polonium Isotopes*, Phys. Rev. Lett. **106**, 052503 (2011).

[Coenen86] E. Coenen, K. Deneffe, M. Huyse, P. Van Duppen and J. Wood, *First identification of a $1/2^+$ intruder state in the* ^{197}At *isotope*, Z. Phys. A **324**, 485 (1986).

[Davie84] R. F. Davie, A. R. Poletti, G. D. Dracoulis, A. P. Byrne and C. Fahlander, *Isomers and high-spin states in* ^{205}At, Nucl. Phys. A **430**, 454 (1984).

[De Witte05] H. De Witte, A. N. Andreyev, S. Dean, S. Franchoo, M. Huyse, O. Ivanov, U. Köster, W. Kurcewicz, J. Kurpeta, A. Plochocki, K. Van de Vel, J. Van de Walle and P. Van Duppen, *Alpha-decay of neutron-deficient* ^{200}Fr *and heavier neighbours*, Eur. Phys. J. A **23**, 243 (2005).

[De Witte07] H. De Witte, A. N. Andreyev, N. Barré, M. Bender, T. E. Cocolios, S. Dean, D. Fedorov, V. N. Fedoseyev, L. M. Fraile, S. Franchoo, V. Hellemans, P. H. Heenen, K. Heyde, G. Huber, M. Huyse, H. Jeppessen, U. Köster, P. Kunz, S. R. Lesher, B. A. Marsh, I. Mukha, B. Roussière, J. Sauvage, M. Seliverstov, I. Stefanescu, E. Tengborn, K. Van de Vel, J. Van de Walle, P. Van Duppen and Y. Volkov, *Nuclear Charge Radii of Neutron-Deficient Lead Isotopes Beyond $N = 104$ Midshell Investigated by In-Source Laser Spectroscopy*, Phys. Rev. Lett. **98**, 112502 (2007).

[deGroot68] S. R. deGroot, H. A. Tolhoek and W. J. Huiskamp, *Orientation of nuclei at low temperatures* (Editor K. Siegbahn. North-Holland, Amsterdam, 1968).

[deVoigt83] M. J. A. de Voigt, J. Dudek and Z. Szymański, *High-spin phenomena in atomic nuclei*, Rev. Mod. Phys. **55**, 949 (1983).

[Diamond66] R. M. Diamond, E. Matthias, J. O. Newton and F. S. Stephens, *Nuclear alignment in heavy-ion reactions*, Phys. Rev. Lett. **16**, 1205 (1966).

[Dobson02] D. J. Dobson, S. J. Freeman, P. T. Greenlees, A. N. Qadir, S. Juutinen, J. L. Durell, T. Enqvist, P. Jones, R. Julin, A. Keenan, H. Kettunen, P. Kuusiniemi, M. Leino, P. Nieminen, P. Rahkila, S. D. Robinson, J. Uusitalo and B. J. Varley, *Low-lying structure of light radon isotopes*, Phys. Rev. C **66**, 064321 (2002).

[Dönau82] F. Dönau and S. Frauendorf, *Magnetic moments as a probe for rotational alignment*, Nucl. Sci. R. **4**, 143 (1982).

[Dönau87] F. Dönau, *Electromagnetic radiation of rotating nuclei*, Nucl. Phys. A **471**, 469 (1987).

[Dracoulis09a] G. D. Dracoulis, P. M. Davidson, G. J. Lane, A. P. Byrne, T. Kibédi, P. Nieminen, H. Watanabe and A. N. Wilson, *Spectroscopy and high-spin structure of* ^{209}Fr, Phys. Rev. C **79**, 054313 (2009).

[Dracoulis09b] G. D. Dracoulis, G. J. Lane, A. P. Byrne, P. M. Davidson, T. Kibédi, P. H. Nieminen, H. Watanabe, A. N. Wilson, H. L. Liu and F. R. Xu, *Structure of the* $N = 126$ *nuclide* ^{212}Rn*: Valence and core excited configurations*, Phys. Rev. C **80**, 054320 (2009).

[Dybdal83] K. Dybdal, T. Chapuran, D. B. Fossan, W. F. Piel, D. Horn and E. K. Warburton, *High-spin states in* $^{201,203}At$ *and the systematic behavior of* $Z = 85$ *isotopes*, Phys. Rev. C **28**, 1171 (1983).

[Erler12] J. Erler, N. Birge, M. Kortelainen, W. Nazarewicz, E. Olsen, A. M. Perhac and M. Stoitsov, *The limits of the nuclear landscape*, Nature **486**, 509 (2012).

[Fant90] B. Fant, T. Weckström and A. Källberg, *The high-spin structure of* ^{202}Po *and* ^{204}Po *and systematical features of the even polonium isotopes*, Phys. Scripta **41**, 652 (1990).

[Firestone96] R. B. Firestone, *Table of isotopes*, eight edition (Editor V. S. Shirley, publisher Wiley interscience, 1996).

BIBLIOGRAPHY

[Fröbrich96] P. Fröbrich and R. Lipperheide, *Theory of nuclear reactions* (Oxford Science Publications, New York, 1996).

[Gamow28] G. Gamow, *Zur Quantentheorie des Atomkernes*, Z. Phys. **51**, 204 (1928).

[Geiger11] H. Geiger and J. M. Nuttall, *LVII. The ranges of the α particles from various radioactive substances and a relation between range and period of transformation*, Phil. Mag. S. **22**, 613 (1911).

[Grahn06] T. Grahn, A. Dewald, O. Möller, R. Julin, C. W. Beausang, S. Christen, I. G. Darby, S. Eeckhaudt, P. T. Greenlees, A. Görgen, K. Helariutta, J. Jolie, P. Jones, S. Juutinen, H. Kettunen, T. Kröll, R. Krücken, Y. L. Coz, M. Leino, A.-P. Leppänen, P. Maierbeck, D. A. Meyer, B. Melon, P. Nieminen, M. Nyman, R. D. Page, J. Pakarinen, P. Petkov, P. Rahkila, B. Saha, M. Sandzelius, J. Sarén, C. Scholey and J. Uusitalo, *Collectivity and Configuration Mixing in $^{186,188}Pb$ and ^{194}Po*, Phys. Rev. Lett. **97**, 062501 (2006).

[Grodzins62] L. Grodzins, *The uniform behaviour of electric quadrupole transition probabilities from first 2+ states in even-even nuclei*, Phys. Lett. **2**, 88 (1962).

[Gurney28] R. W. Gurney and E. U. Condon, *Wave mechanics and radioactive disintegration*, Nature **122**, 439 (1928).

[Hartley08] D. J. Hartley, E. P. Seyfried, W. Reviol, D. G. Sarantites, C. J. Chiara, O. L. Pechenaya, K. Hauschild, A. Lopez-Martens, M. P. Carpenter, R. V. F. Janssens, D. Seweryniak and S. Zhu, *Possible shears bands in ^{204}At and ^{206}Fr, and identification of excited states in $^{205,207}Fr$*, Phys. Rev. C **78**, 054319 (2008).

[Hauschild12] K. Hauschild (2012), private communication.

[Hauschild13] K. Hauschild (2013), private communication.

[Haxel49] O. Haxel, J. H. D. Jensen and H. E. Suess, *On the "Magic Numbers" in Nuclear Structure*, Phys. Rev. **75**, 1766 (1949).

[Helariutta99] K. Helariutta, J. Cocks, T. Enqvist, P. Greenlees, P. Jones, R. Julin, S. Juutinen, P. Jämsen, H. Kankaanpää, H. Kettunen, P. Kuusiniemi, M. Leino, M. Muikku, M. Piiparinen, P. Rahkila, A. Savelius, W. Trzaska, S. Törmänen, J. Uusitalo, R. Allatt, P. Butler, R. Page and M. Kapusta,
Gamma-ray spectroscopy of $^{192-195}Po$,
Eur. Phys. J. A **6**, 289 (1999).

[Heyde89] K. Heyde, C. De Coster, J. Ryckebusch and M. Waroquier, *Equivalence of the spherical and deformed shell-model approach to intruder states*, Phys. Lett. B **218**, 287 (1989).

[Heyde11] K. Heyde and J. L. Wood, *Shape coexistence in atomic nuclei*, Rev. Mod. Phys. **83**, 1467 (2011).

[Horn81] D. Horn, C. Baktash and C. J. Lister, *Spectroscopy of* $^{204,206,208}Rn$ *and the systematic behavior of* $Z = 86$ *isotopes*, Phys. Rev. C **24**, 2136 (1981).

[Hürstel02] A. Hürstel, M. Rejmund, E. Bouchez, P. T. Greenlees, K. Hauschild, S. Juutinen, H. Kettunen, W. Korten, Y. Le Coz, P. Nieminen, C. Theisen, A. N. Andreyev, F. Becker, T. Enqvist, P. M. Jones, R. Julin, H. Kankaanpää, A. Keenan, P. Kuusiniemi, M. Leino, A.-P. Leppänen, M. Muikku, J. Pakarinen, P. Rahkila and J. Uusitalo, *Isomeric states in proton-unbound* $^{187,189}Bi$ *isotopes*, Eur. Phys. J. A **15**, 329 (2002).

[Hürstel04] A. Hürstel, Y. Coz, E. Bouchez, A. Chatillon, A. Görgen, P. T. Greenlees, K. Hauschild, S. Juutinen, H. Kettunen, W. Korten, P. Nieminen, M. Rejmund, C. Theisen, J. Wilson, A. N. Andreyev, F. Becker, T. Enqvist, P. M. Jones, R. Julin, H. Kankaanpää, A. Keenan, P. Kuusiniemi, M. Leino, A.-P. Leppänen, M. Muikku, J. Pakarinen, P. Rahkila and J. Uusitalo, *Prolate deformation in the* $^{187,189}Bi$ *isotopes*, Eur. Phys. J. A **21**, 365 (2004).

[Huyse92] M. Huyse, P. Decrock, P. Dendooven, G. Reusen, P. Van Duppen and J. Wauters, *Isomers in three doubly odd Fr-At-Bi* α*-decay chains*, Phys. Rev. C **46**, 1209 (1992).

[Igo58] G. Igo, *Optical Model Potential at the Nuclear Surface for the Elastic Scattering of Alpha Particles*, Phys. Rev. Lett. **1**, 72 (1958).

[Inglis54] D. R. Inglis, *Particle Derivation of Nuclear Rotation Properties Associated with a Surface Wave*, Phys. Rev. **96**, 1059 (1954).

[Jones02] G. D. Jones, *Detection of long-lived isomers in super-heavy elements*, Nucl. Instrum. Meth. A **488**, 471 (2002).

[Julin01] R. Julin, K. Helariutta and M. Muikku, *Intruder states in very neutron-deficient Hg, Pb and Po nuclei*, J. Phys. G: Nucl. Partic. **27**, R109 (2001).

[Kalaninová13] Z. Kalaninová, A. N. Andreyev, S. Antalic, F. P. Heβberger, D. Ackermann, B. Andel, M. C. Drummond, S. Hofmann, M. Huyse,

B. Kindler, J. F. W. Lane, V. Liberati, B. Lommel, R. D. Page, E. Rapisarda, K. Sandhu, v. Šáro, A. Thornthwaite and P. Van Duppen, *α decay of the very neutron-deficient isotopes $^{197-199}Fr$*, Phys. Rev. C **87**, 044335 (2013).

[Kantele86] J. Kantele, M. Luontama, W. Trzaska, R. Julin, A. Passoja and K. Heyde, *E0 transitions in $^{202,204}Pb$ and intruder-state systematics of even-even lead isotopes*, Phys. Lett. B **171**, 151 (1986).

[Kantele95] J. Kantele, *Handbook of nuclear spectrometry* (Academic press, London, 1995).

[Kettunen01] H. Kettunen, J. Uusitalo, M. Leino, P. Jones, K. Eskola, P. T. Greenlees, K. Helariutta, R. Julin, S. Juutinen, H. Kankaanpää, P. Kuusiniemi, M. Muikku, P. Nieminen and P. Rahkila, *α decay studies of the nuclides ^{195}Rn and ^{196}Rn*, Phys. Rev. C **63**, 044315 (2001).

[Kettunen03a] H. Kettunen, T. Enqvist, T. Grahn, P. Greenlees, P. Jones, R. Julin, S. Juutinen, A. Keenan, P. Kuusiniemi, M. Leino, A.-P. Leppänen, P. Nieminen, J. Pakarinen, P. Rahkila and J. Uusitalo, *Alpha-decay studies of the new isotopes ^{191}At and ^{193}At*, Eur. Phys. J. A **17**, 537 (2003).

[Kettunen03b] H. Kettunen, T. Enqvist, M. Leino, K. Eskola, P. Greenlees, K. Helariutta, P. Jones, R. Julin, S. Juutinen, H. Kankaanpää, H. Koivisto, P. Kuusiniemi, M. Muikku, P. Nieminen, P. Rahkila and J. Uusitalo, *Investigations into the alpha-decay of ^{195}At*, Eur. Phys. J. A **16**, 457 (2003).

[Kibédi08] T. Kibédi, T. W. Burrows, M. B. Trzhaskovskaya, P. M. Davidson and C. W. Nestor Jr., *Evaluation of theoretical conversion coefficients using BrIcc*, Nucl. Instrum. Meth. A **589**, 202 (2008).

[Kondev04] F. G. Kondev, *Nuclear Data Sheets for $A = 205$*, Nucl. Data Sheets **101**, 521 (2004).

[Kondev05] F. G. Kondev, *Nuclear Data Sheets for $A = 203$*, Nucl. Data Sheets **105**, 1 (2005).

[Kondev07a] F. G. Kondev, *Nuclear Data Sheets for $A = 201$*, Nucl. Data Sheets **108**, 365 (2007).

[Kondev07b] F. G. Kondev and S. Lalkovski, *Nuclear Data Sheets for $A = 200$*, Nucl. Data Sheets **108**, 1471 (2007).

[Krane88] K. S. Krane, *Introductory nuclear physics* (John Wiley and Sons, 1988).

[Lach94] M. Lach, M. Waring, D. Alber, D. B. Fossan, H. Grawe, H. Kluge, K. H. Maier, M. Schramm and R. Schubart, *Spectroscopy of* $^{198,199}Po$, Z. Phys. A **350**, 207 (1994).

[Lach00] M. Lach, P. Bednarczyk, P. T. Greenlees, K. Helariutta, P. Jones, R. Julin, S. Juutinen, H. Kankaanpää, H. Kettunen, P. Kuusiniemi, M. Leino, W. Meczyński, M. Muikku, P. Nieminen, P. Rahkila, J. Styczeń and J. Uusitalo, *Identification of the* $13/2^+$ *isomer in* ^{199}At, Eur. Phys. J. A **9**, 307 (2000).

[Larabee84] A. J. Larabee, L. H. Courtney, S. Frauendorf, L. L. Riedinger, J. C. Waddington, M. P. Fewell, N. R. Johnson, I. Y. Lee and F. K. McGowan, *Shape effects in* $h_{\frac{11}{2}}$ *and* $g_{\frac{7}{2}}$ *bands in* ^{159}Tm, Phys. Rev. C **29**, 1934 (1984).

[Lazarus01] I. H. Lazarus, D. E. Appelbe, P. A. Butler, P. J. Coleman-Smith, J. R. Cresswell, S. J. Freeman, R. D. Herzberg, I. Hibbert, D. T. Joss, S. C. Letts, R. D. Page, V. F. E. Pucknell, P. H. Regan, J. Sampson, J. Simpson, J. Thornhill and R. Wadsworth, *The GREAT triggerless total data readout method*, IEEE T. Nucl. Sci. **48**, 567 (2001).

[Le Coz99] Y. Le Coz, F. Becker, H. Kankaanpää, W. Korten, E. Mergel, P. A. Butler, J. F. C. Cocks, O. Dorvaux, D. Hawcroft, K. Helariutta, R.-D. Herzberg, M. Houry, H. Hübel, P. Jones, R. Julin, S. Juutinen, H. Kettunen, P. Kuusiniemi, M. Leino, R. Lucas, M. Muikku, P. Nieminen, P. Rahkila, D. Rossbach, A. Savelius and C. Theisen, *Evidence of Multiple Shape-Coexistence in* ^{188}Pb, EPJ direct **A3**, 1 (1999).

[Leino95] M. Leino, J. Äystö, T. Enqvist, P. Heikkinen, A. Jokinen, M. Nurmia, A. Ostrowski, W. H. Trzaska, J. Uusitalo, K. Eskola, P. Armbruster and V. Ninov, *Gas-filled recoil separator for studies of heavy elements*, Nucl. Instrum. Meth. B **99**, 653 (1995).

[Lönnroth82] T. Lönnroth, *In-beam studies of* $^{203,205}Bi$ *and shell-model features of odd-a bismuth isotopes*, Z. Phys. A **307**, 175 (1982).

[Lönnroth86] T. Lönnroth, C. W. Beausang, D. B. Fossan, L. Hildingsson, W. F. Piel, M. A. Quader, S. Vajda, T. Chapuran and E. K. Warburton, *Excited states in neutron-deficient* ^{195}Bi, Phys. Rev. C **33**, 1641 (1986).

[Magill06] J. Magill, G. Pfennig and J. Galy, *Karlsruher nuklidkarte, 7. edition* (European Commission - Joint Research Centre - Institute for Transuranium Elements, 2006).

[Maj90] A. Maj, H. Grawe, H. Kluge, A. Kuhnert, K. H. Maier, J. Recht, N. Roy, H. Hübel and M. Guttormsen, *Levels, lifetimes and g-factors in* ^{198}Po *and* ^{200}Po, Nucl. Phys. A **509**, 413 (1990).

[Mayer49] M. G. Mayer, *On Closed Shells in Nuclei. II*, Phys. Rev. **75**, 1969 (1949).

[Męczyński98] W. Męczyński, P. Bednarczyk, R. Chapman, S. Courtin, J. Gręboszi, F. Hannachi, P. Jones, J. Kownacki, M. Lach, A. Lopez-Martens, K. Maier, J. Merdinger, D. Middleton, M. Palacz, M. Smith, K. Spohr, N. Schulz, M. Zięblińskii and J. Styczeń, *Gamma-spectroscopy of the* ^{199}At *nucleus with the Recoil Filter Detector*, Eur. Phys. J. A **3**, 311 (1998).

[Morinaga56] H. Morinaga, *Interpretation of Some of the Excited States of* $4n$ *Self-Conjugate Nuclei*, Phys. Rev. **101**, 254 (1956).

[Newman01] H. Newman, J. R. Novak, C. W. Beausang, C. J. Barton, M. A. Caprio, R. F. Casten, J. R. Cooper, A. A. Hecht, R. Krücken, N. Pietralla, A. Wolf, N. V. Zamfir, J. Zhang, K. E. Zyromski, I. Birriel and J. Saladin, *High-spin states in* ^{203}Rn, Phys. Rev. C **64**, 027304 (2001).

[Nieminen04] P. Nieminen, S. Juutinen, A. N. Andreyev, J. F. C. Cocks, O. Dorvaux, K. Eskola, P. T. Greenlees, K. Hauschild, K. Helariutta, M. Huyse, P. M. Jones, R. Julin, H. Kankaanpää, H. Kettunen, P. Kuusiniemi, Y. L. Coz, M. Leino, T. Lönnroth, M. Muikku, P. Rahkila, A. Savelius, J. Uusitalo, N. Amzal, N. J. Hammond, C. Scholey and R. Wyss, γ*-ray spectroscopy of* $^{191,193}Bi$, Phys. Rev. C **69**, 064326 (2004).

[Nilsson55] S. G. Nilsson, *Binding states of individual nucleons in strongly deformed nuclei*, Kong. Dansk. Vidensk. **29**, 1 (1955).

[Nilsson95] S. G. Nilsson and I. Ragnarsson, *Shapes and shells in nuclear structure* (Cambridge university press, Cambridge, 1995).

[nndc13] nndc (2013), national Nuclear Data Center, information extracted from the Chart of Nuclides database, http://www.nndc.bnl.gov/chart/. Date: 3.9.2013.

[Nyman09] M. Nyman, *Shape coexistence in light bismuth and astatine isotopes: An in-beam and decay-spectroscopic study,*, Ph.D. thesis, JYFL research report 12/2009, University of Jyväskylä (2009).

[Nyman13] M. Nyman, S. Juutinen, I. Darby, S. Eeckhaudt, T. Grahn, P. T. Greenlees, U. Jakobsson, P. Jones, R. Julin, S. Ketelhut, H. Kettunen, M. Leino, P. Nieminen, P. Peura, P. Rahkila, J. Sarén, C. Scholey, J. Sorri, J. Uusitalo and T. Enqvist, *γ-ray and decay spectroscopy of $^{194,195,196}At$*, Phys. Rev. C (2013), accepted for publication.

[Oros99] A. M. Oros, K. Heyde, C. De Coster, B. Decroix, R. Wyss, B. R. Barrett and P. Navratil, *Shape coexistence in the light Po isotopes*, Nucl. Phys. A **645**, 107 (1999).

[Paar79] V. Paar, *A parabolic rule for the energy dependence on $x = I(I+1)$ for proton-neutron multiplets in odd-odd nuclei*, Nucl. Phys. A **331**, 16 (1979).

[Page03] R. D. Page, A. N. Andreyev, D. E. Appelbe, P. A. Butler, S. J. Freeman, P. T. Greenlees, R.-D. Herzberg, D. G. Jenkins, G. D. Jones, P. Jones, D. T. Joss, R. Julin, H. Kettunen, M. Leino, P. Rahkila, P. H. Regan, J. Simpson, J. Uusitalo, S. M. Vincent and R. Wadsworth, *The GREAT spectrometer*, Nucl. Instrum. Meth. B **204**, 634 (2003).

[Pai12] H. Pai, G. Mukherjee, R. Raut, S. K. Basu, A. Goswami, S. Chanda, T. Bhattacharjee, S. Bhattacharyya, C. Bhattacharya, S. Bhattacharya, S. R. Banerjee, S. Kundu, K. Banerjee, A. Dey, T. K. Rana, J. K. Meena, D. Gupta, S. Mukhopadhyay, S. Bhattacharya, S. Bhattacharya, S. Ganguly, R. Kshetri and M. K. Pradhan, *Onset of deformation at $N = 112$ in Bi nuclei*, Phys. Rev. C **85**, 064317 (2012).

[Pakarinen05] J. Pakarinen, *Probing non-yrast structures of ^{186}Pb in a RDT measurement employing the JUROGAM Array*, Ph.D. thesis, JYFL research report 4/2005, University of Jyväskylä (2005).

[Paul95] E. S. Paul, P. J. Woods, T. Davinson, R. D. Page, P. J. Sellin, C. W. Beausang, R. M. Clark, R. A. Cunningham, S. A. Forbes, D. B. Fossan, A. Gizon, J. Gizon, K. Hauschild, I. M. Hibbert, A. N. James, D. R. LaFosse, I. Lazarus, H. Schnare, J. Simpson, R. Wadsworth and M. P. Waring, *In-beam γ-ray spectroscopy above ^{100}Sn using the new technique of recoil decay tagging*, Phys. Rev. C **51**, 78 (1995).

[Perlman57] I. Perlman and J. O. Rasmussen, *Encyclopedia of physics, Nuclear Reactions III* (Editor S. Flügge. Springer-Verlag, Berlin, 1957).

[Poletti97] A. Poletti, G. Dracoulis, A. Byrne, A. Stuchbery, B. Fabricius, T. Kibèdi and P. Davidson, *Core-excited states and the yrast line in ^{208}Po*, Nucl. Phys. A **615**, 95 (1997).

[Poletti05] A. R. Poletti, A. P. Byrne, G. D. Dracoulis, T. Kibédi and P. M. Davidson, *High spin states in ^{210}Rn approaching the region of 3-particle-hole neutron excitations*, Nucl. Phys. A **756**, 83 (2005).

[Radford95a] D. Radford, *Background subtraction from in-beam HPGe coincidence data sets*, Nucl. Instrum. Meth. A **361**, 306 (1995).

[Radford95b] D. Radford, *ESCL8R and LEVIT8R: Software for interactive graphical analysis of HPGe coincidence data sets*, Nucl. Instrum. Meth. A **361**, 297 (1995).

[Rahkila08] P. Rahkila, *Grain - A Java data analysis system for Total Data Readout*, Nucl. Instrum. Meth. A **595**, 637 (2008).

[Rainwater50] J. Rainwater, *Nuclear Energy Level Argument for a Spheroidal Nuclear Model*, Phys. Rev. **79**, 432 (1950).

[Rasmussen59] J. O. Rasmussen, *Alpha-Decay Barrier Penetrabilities with an Exponential Nuclear Potential: Even-Even Nuclei*, Phys. Rev. **113**, 1593 (1959).

[Rossi Alvarez93] C. Rossi Alvarez, *The GASP array*, Nuclear Physics News **3**, 10 (1993).

[Schmidt84] K.-H. Schmidt, C.-C. Sahm, K. Pielenz and H.-G. Clerc, *Some remarks on the error analysis in the case of poor statistics*, Z. Phys. A **316**, 19 (1984).

[Schmidt86] K.-H. Schmidt, R. S. Simon, J.-G. Keller, F. P. Heβberger, G. Münzenberg, B. Quint, H.-G. Clerc, W. Schwab, U. Gollerthan and C.-C. Sahm, *Gamma-Spectroscopic investigations in the radiative fusion reaction ^{90}Zr + ^{90}Zr*, Phys. Lett. B **168**, 39 (1986).

[Schmidt00] K.-H. Schmidt, *A new test for random events of an exponential distribution*, Eur. Phys. J. A **8**, 141 (2000).

[Seliverstov13] M. D. Seliverstov, T. E. Cocolios, W. Dexters, A. N. Andreyev, S. Antalic, A. E. Barzakh, B. Bastin, J. Büscher, I. G. Darby, D. V. Fedorov, V. N. Fedoseyev, K. T. Flanagan, S. Franchoo, S. Fritzsche, G. Huber, M. Huyse, M. Keupers, U. Köster,

Y. Kudryavtsev, B. A. Marsh, P. L. Molkanov, R. D. Page, A. M. Sjødin, I. Stefan, J. Van de Walle, P. Van Duppen, M. Venhart and S. G. Zemlyanoy, *Charge radii of odd-A* $^{191-211}$*Po isotopes*, Phys. Lett. B **719**, 362 (2013).

[Simon86] R. S. Simon, K.-H. Schmidt, F. P. Heβberger, S. Hlavac, M. Honusek, G. Münzenberg, H.-G. Clerc, U. Gollerthan and W. Schwab, *Evidence for nuclear shape coexistence in* ^{180}*Hg*, Z. Phys. A **325**, 197 (1986).

[Singh07] B. Singh, *Nuclear Data Sheets for* $A = 199$, Nucl. Data Sheets **108**, 79 (2007).

[Sjoreen76] T. P. Sjoreen, G. Schatz, S. K. Bhattacherjee, B. A. Brown, D. B. Fossan and P. M. S. Lesser, *High-spin states and neutron-hole influence in* ^{209}*At*, Phys. Rev. C **14**, 1023 (1976).

[Sjoreen81] T. P. Sjoreen, U. Garg and D. B. Fossan, *High-spin states in* ^{207}*At*, Phys. Rev. C **23**, 272 (1981).

[Smith99] M. B. Smith, R. Chapman, J. F. C. Cocks, O. Dorvaux, K. Helariutta, P. M. Jones, R. Julin, S. Juutinen, H. Kankaanpää, H. Kettunen, P. Kuusiniemi, Y. Le Coz, M. Leino, D. J. Middleton, M. Muikku, P. Nieminen, P. Rahkila, A. Savelius and K.-M. Spohr, *First observation of excited states in* ^{197}*At: the onset of deformation in neutron-deficient astatine nuclei*, Eur. Phys. J. A **5**, 43 (1999).

[Spiegel09] M. R. Spiegel, S. Lipschutz and J. Liu, *Mathematical handbook of formulas and tables, third edition* (McGraw-Hill, 2009).

[Stephens75] F. S. Stephens, *Coriolis effects and rotation alignment in nuclei*, Rev. Mod. Phys. **47**, 43 (1975).

[Styczeń99] J. Styczeń, W. Męczyński, M. Lach, P. Bednarczyk, R. Chapman, S. Courtin, J. Grębosz, F. Hannachi, P. M. Jones, J. Kownacki, A. Lopez-Martens, K. H. Maier, J. C. Merdinger, D. Middleton, M. Palacz, N. Schulz, M. B. Smith, K.-M. Spohr, M. Wolińska and M. Zięblíński, *First observation of excited states in* ^{199}*At with the recoil filter detector*, AIP Conf. Proc., Experimental nuclear physics in Europe: Facing the next millennium **495**, 255 (1999).

[Suhonen07] J. Suhonen, *From nucleons to nucleus* (Springer-Verlag, Berlin, 2007).

[Taylor99] R. B. E. Taylor, S. J. Freeman, J. L. Durell, M. J. Leddy, S. D. Robinson, B. J. Varley, J. F. C. Cocks, K. Helariutta, P. Jones,

R. Julin, S. Juutinen, H. Kankaanpää, A. Kanto, H. Kettunen, P. Kuusiniemi, M. Leino, M. Muikku, P. Rahkila, A. Savelius and P. T. Greenlees, *γ decay of excited states in ^{198}Rn identified using correlated radioactive decay*, Phys. Rev. C **59**, 673 (1999).

[Uusitalo05] J. Uusitalo, M. Leino, T. Enqvist, K. Eskola, T. Grahn, P. T. Greenlees, P. Jones, R. Julin, S. Juutinen, A. Keenan, H. Kettunen, H. Koivisto, P. Kuusiniemi, A.-P. Leppänen, P. Nieminen, J. Pakarinen, P. Rahkila and C. Scholey, *α decay studies of very neutron-deficient francium and radium isotopes*, Phys. Rev. C **71**, 024306 (2005).

[Uusitalo13] J. Uusitalo, J. Sarén, S. Juutinen, M. Leino, S. Eeckhaudt, T. Grahn, P. T. Greenlees, U. Jakobsson, P. Jones, R. Julin, S. Ketelhut, A.-P. Leppänen, M. Nyman, J. Pakarinen, P. Rahkila, C. Scholey, A. Semchenkov, J. Sorri, A. Steer and M. Venhart, *α-decay studies of the francium isotopes ^{198}Fr and ^{199}Fr*, Phys. Rev. C **87**, 064304 (2013).

[Van de Vel03] K. Van de Vel, A. N. Andreyev, R. D. Page, H. Kettunen, P. T. Greenlees, P. Jones, R. Julin, S. Juutinen, H. Kankaanpää, A. Keenan, P. Kuusiniemi, M. Leino, M. Muikku, P. Nieminen, P. Rahkila, J. Uusitalo, K. Eskola, A. Hürstel, M. Huyse, Y. Le Coz, M. B. Smith, P. Van Duppen and R. Wyss,
In-beam γ-ray spectroscopy of ^{190}Po: First observation of a low-lying prolate band in Po isotopes,
Eur. Phys. J. A **17**, 167 (2003).

[Van de Vel05] K. Van de Vel, A. N. Andreyev, D. Ackermann, H. J. Boardman, P. Cagarda, J. Gerl, F. P. Heβberger, S. Hofmann, M. Huyse, D. Karlgren, I. Kojouharov, M. Leino, B. Lommel, G. Münzenberg, C. Moore, R. D. Page, S. Saro, P. Van Duppen and R. Wyss, *Prolate structures in ^{189}Po and ^{185}Pb*, Eur. Phys. J. A **24**, 57 (2005).

[Van Duppen84] P. Van Duppen, E. Coenen, K. Deneffe, M. Huyse, K. Heyde and P. Van Isacker, *Observation of Low-Lying $J^\pi = 0^+$ States in the Single-Closed-Shell Nuclei $^{192-198}$Pb*, Phys. Rev. Lett. **52**, 1974 (1984).

[Van Duppen87] P. Van Duppen, E. Coenen, K. Deneffe, M. Huyse and J. L. Wood, *β^+/electron-capture decay of ^{192,194,196,198,200}Bi: Experimental evidence for low lying 0^+ states*, Phys. Rev. C **35**, 1861 (1987).

[Van Duppen00] P. Van Duppen and M. Huyse, *Shape coexistence around the Z= 82 closed shell probed by α-decay*, Hyperfine Interact. **129**, 149 (2000).

[Voss13] A. Voss, M. R. Pearson, J. Billowes, F. Buchinger, B. Cheal, J. E. Crawford, A. A. Kwiatkowski, C. D. P. Levy and O. Shelbaya, *First Use of High-Frequency Intensity Modulation of Narrow-Linewidth Laser Light and Its Application in Determination of* $^{206,205,204}Fr$ *Ground-State Properties*, Phys. Rev. Lett. **111**, 122501 (2013).

[Walker99] P. Walker and G. Dracoulis, *Energy traps in atomic nuclei*, Nature **399**, 35 (1999).

[Weisskopf51] V. F. Weisskopf, *Radiative Transition Probabilities in Nuclei*, Phys. Rev. **83**, 1073 (1951).

[Wiseman07] D. R. Wiseman, A. N. Andreyev, R. D. Page, M. B. Smith, I. G. Darby, S. Eeckhaudt, T. Grahn, P. T. Greenlees, P. Jones, R. Julin, S. Juutinen, H. Kettunen, M. Leino, A.-P. Leppänen, M. Nyman, J. Pakarinen, P. Rahkila, M. Sandzelius, J. Sarén, C. Scholey and J. Uusitalo, *In-beam gamma-ray spectroscopy of* $^{190,197}Po$, Eur. Phys. J. A **34**, 275 (2007).

[Yamazaki67] T. Yamazaki, *Tables of coefficients for angular distribution of gamma rays from aligned nuclei*, Nucl. Data Sheets, Section A **3**, 1 (1967).

[Zemel83] A. Zemel and J. Dobes, *Low-spin states in even Po and Rn isotopes and the interplay between collective and quasiparticle configurations*, Phys. Rev. C **27**, 2311 (1983).

[Zhou99] C. Zhou, *Nuclear Data Sheets for* $A = 195$, Nucl. Data Sheets **86**, 645 (1999).

[Zhu08] S. Zhu and F. G. Kondev, *Nuclear Data Sheets for* $A = 202$, Nucl. Data Sheets **109**, 699 (2008).

Appendix A

Prompt and delayed spectroscopy of ^{199}At

PHYSICAL REVIEW C **82**, 044302 (2010)

Prompt and delayed spectroscopy of ^{199}At

U. Jakobsson,[1,*] J. Uusitalo,[1] S. Juutinen,[1] M. Leino,[1] P. Nieminen,[1] K. Andgren,[2] B. Cederwall,[2] P. T. Greenlees,[1] B. Hadinia,[2,†] P. Jones,[1] R. Julin,[1] S. Ketelhut,[1] A. Khaplanov,[2] M. Nyman,[1,‡] P. Peura,[1] P. Rahkila,[1] P. Ruotsalainen,[1] M. Sandzelius,[1] J. Sarén,[1] C. Scholey,[1] and J. Sorri[1]

[1]*Department of Physics, University of Jyväskylä, P.O. Box 35, FI-40014 Jyväskylä, Finland*

[2]*Department of Physics, Royal Institute of Technology, SE-10691 Stockholm, Sweden*

(Received 2 July 2010; published 6 October 2010)

The neutron-deficient nucleus ^{199}At has been studied through γ-ray and electron spectroscopy, using the recoil-decay tagging technique. Two experiments were conducted, using a gas-filled recoil separator with a focal-plane spectrometer alone and together with a germanium-detector array at the target position. The resulting level scheme for ^{199}At includes a new isomer with a half-life of 0.80(5) μs and a spin and parity of $(29/2^+)$. The $13/2^+$ isomer, which de-excites via an $M2$ transition to the $9/2^-$ ground state, was measured to have a half-life of 70(20) ns. Our earlier version of the level scheme for ^{197}At has been updated as well.

DOI: 10.1103/PhysRevC.82.044302 PACS number(s): 23.20.Lv, 23.35.+g, 27.80.+w, 29.30.Kv

I. INTRODUCTION

The neutron-deficient nuclei in the light lead region exhibit a variety of different shapes. These coexisting configurations involve an excitation of one or more pairs of protons across the $Z = 82$ shell gap, interacting with an increasing number of valence neutrons as the $82 \leqslant N \leqslant 126$ shell becomes depleted [1,2]. The low-lying yrast states in even-mass polonium nuclei, for instance, show a transition from spherical structures toward oblate-deformed and onward to prolate-deformed collective bands when approaching the $N = 104$ mid-shell (see, for example, [3,4] and references therein). Similar behavior could be expected in the odd-mass astatine nuclei, as they have only one proton more than their polonium isotones.

The low-lying states of the neutron-deficient astatine nuclei down to $A = 201$ have been found to be dominated by spherical structures [5–10]. However, a recent in-beam γ-ray spectroscopic study, supported with theoretical total Routhian surface (TRS) calculations, showed evidence of shape coexistence in ^{197}At [11]. The $9/2^-$ ground state is predicted to be nearly spherical, with $\beta_2 \approx 0.1$, in agreement with the observed vibrational level pattern. In contrast, the single-proton $13/2^+$ state, known throughout the odd-mass astatine isotopes down to $A = 193$ (excluding ^{195}At), was observed at an excitation energy of 311 keV and predicted to have an oblate deformation with $\beta_2 \approx 0.2$ in ^{197}At. This conclusion is supported by the observation of the beginning of a strongly coupled band built on this state.

Earlier results for ^{199}At are somewhat varying. Męczyński *et al.* [12] presented a strongly coupled rotational band on top of the $9/2^-$ ground state. Styczeń *et al.* [13], however, placed it on top of the $13/2^+$ isomer, which was suggested to have an excitation energy of 466 keV and a half-life of the order of 1 μs. The isomeric decay itself was not detected. In a later study, Lach *et al.* [14] observed a delayed 573-keV γ-ray transition showing a half-life of 580(130) ns. They assigned it as the single-step de-excitation of the $13/2^+$ isomer to the $9/2^-$ ground state.

The present work aims to resolve the discrepancies among the previous results for ^{199}At and to investigate more thoroughly the shape competition in ^{199}At. In addition, an updated level scheme for ^{197}At is presented, based on an independent analysis of the data used in Ref. [11].

II. EXPERIMENTAL DETAILS

The measurements were conducted in the Accelerator Laboratory at the Department of Physics of the University of Jyväskylä (JYFL), Finland. The nucleus ^{199}At was produced in two different fusion-evaporation reactions, ^{150}Sm(^{52}Cr, $p2n$)^{199}At and ^{120}Sn(^{82}Kr, $p2n$)^{199}At, where the main goal was an in-beam study of ^{199}Rn [15]. In the first reaction, the beam of ^{52}Cr, provided by the K-130 cyclotron, was accelerated to an energy of 231 MeV with an average beam current of 17 particle-nA (pnA) (80 h irradiation time). The target consisted of two foils of ^{150}Sm with a total thickness of 500 μg/cm^2. The targets were evaporated on a 10 μg/cm^2 thick carbon backing foil and an additional carbon reset foil, with a thickness of 42 μg/cm^2, was used behind the stacked target. The target material included contamination by small amounts of more abundant heavier samarium isotopes. This resulted in a high population of ^{202}Rn, which has a half-life and α decay energy similar to those of ^{199}At. For the second reaction a beam of ^{82}Kr, with an energy of 355 MeV and an average intensity of 10 pnA (60 h irradiation time), was used to bombard a self-supporting ^{120}Sn target. The target had a thickness of 500 μg/cm^2, and a 42 μg/cm^2 thick carbon reset foil was used. In these two reactions, ^{199}At was populated with cross sections of approximately 10 and 15 μb, respectively.

The JUROGAM Ge-detector array was used to detect prompt γ rays at the target position. The array consisted of 43 Compton-suppressed high-purity germanium (HPGe) detectors of EUROGAM Phase1 [16] and GASP type [17].

*ulrika.jakobsson@jyu.fi

†Current address: Department of Physics, University of Guelph, Guelph, Ontario N1G2W1, Canada.

‡Current address: Laboratory of Radiochemistry, University of Helsinki, P.O. Box 55, FI-00014 Helsinki, Finland.

The recoiling fusion-evaporation products were separated from beam particles and other unwanted reaction products by the gas-filled recoil separator RITU [18] and transported to the GREAT spectrometer [19]. When arriving in GREAT, the recoils passed through a multiwire proportional counter (MWPC) and were finally implanted into a 300-μm-thick double-sided silicon strip detector (DSSD), which has 4800 pixels in total. A planar and a clover germanium detector were used to detect delayed γ rays close to the DSSD, and a silicon PIN detector array, situated upstream from the DSSD, was used for measuring conversion electrons. All data channels were recorded synchronously using the triggerless total data readout (TDR) [20] data acquisition system, which gives each event an absolute time stamp with a time resolution of 10 ns.

An additional third measurement, using only RITU and GREAT, was conducted to improve the quality of the previously obtained focal-plane data. An ^{40}Ar beam, with an energy of 200 MeV, was used to bombard a self-supporting ^{165}Ho target with a thickness of 340 μg/cm^2. A carbon reset foil with a thickness of 70 μg/cm^2 was used behind the target. The nucleus ^{199}At was produced in the $6n$ fusion-evaporation channel with a cross section of approximately 0.7 mb. Alongside ^{199}At, the polonium isotopes ^{198}Po, ^{199}Po, and ^{200}Po were relatively strongly populated through pxn fusion-evaporation channels. A beam current of 6 pnA was chosen to obtain clean γ-ray spectra, reducing random correlations caused by the contaminating polonium isotopes. A higher beam current of 40 pnA was used to collect γ-γ coincidences. The total irradiation time was 30 h. Two clover HPGe detectors [21] were added to the focal-plane setup alongside the GREAT clover detector for an improved high-energy γ-ray detection efficiency.

The nucleus ^{197}At was produced in a separate experiment. The ^{118}Sn(^{82}Kr, $p2n$)^{197}At reaction was used with a beam energy of 362 MeV and a target thickness of 500 μg/cm^2. A description of the experimental details for the ^{197}At measurement is presented in the work by Andgren *et al.* [11].

III. RESULTS

A. ^{199}At

The data were analyzed using the recoil-decay tagging (RDT) technique [22] and processed using the GRAIN [23] and RADWARE [24,25] software packages. The recoiling fusion-evaporation products were selected by their time of flight between the MWPC and the DSSD and their energy loss in the MWPC. Furthermore, the different isotopes were identified by linking the recoils with their subsequent α decays in the DSSD, using spatial and temporal correlations. The α-decay branch of approximately 90% [26] and half-life of 6.92 s [27] for the $9/2^-$ ground state allowed for an effective identification of the ^{199}At recoils, using a maximum correlation time of 21 s between the detection of a recoil and its subsequent α decay. The α-particle energy spectrum obtained from the ^{82}Kr + ^{120}Sn reaction is shown in Fig. 1. Prompt and delayed γ rays belonging to ^{199}At were identified based on their time correlation with the α-tagged recoil observed in the DSSD. For the prompt γ rays detected in the JUROGAM detector array, this time gate was set by taking into account the flight time of approximately 600 ns of the recoils through RITU.

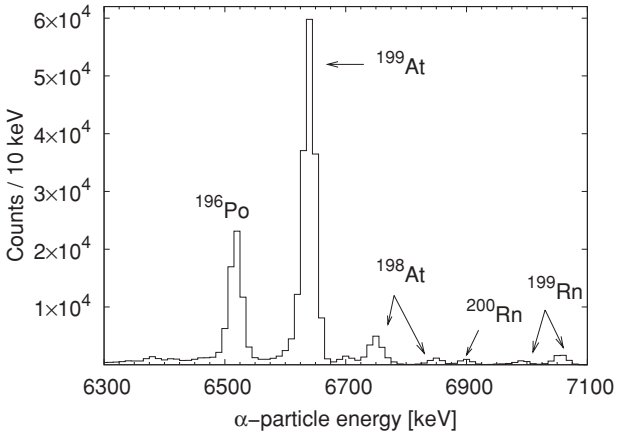

FIG. 1. The α-particle energy spectrum obtained using the ^{82}Kr + ^{120}Sn reaction. A maximum correlation time of 21 s was set between the implantation of the recoil and its subsequent α decay.

The measured prompt data from the ^{150}Sm(^{52}Cr, $p2n$)^{199}At and ^{120}Sn(^{82}Kr, $p2n$)^{199}At reactions were summed to gain statistics for a γ-γ coincidence analysis. A spectrum of prompt γ rays tagged with the α decay of ^{199}At is shown in Fig. 2(a). Figure 2(b) presents the energy spectrum of the coincident γ rays obtained by setting an energy gate on the 600-keV γ-ray peak, which is the strongest γ-ray peak in the spectrum of Fig. 2(a). The gated spectrum confirms the doublet nature of the 600-keV peak, as reported by Styczeń *et al.* [13]. In the present work the 600-keV transitions were placed lowest in a cascade on top of the ground state, according to the high intensity of the doublet peak, at variance with the previous work. By examining γ-γ coincidences, the 559-keV transition was identified to precede this doublet. The 92-keV γ-ray transition reported in Ref. [13] was not observed. The intensity division between the transitions in the 600-keV doublet was made by comparing the intensity

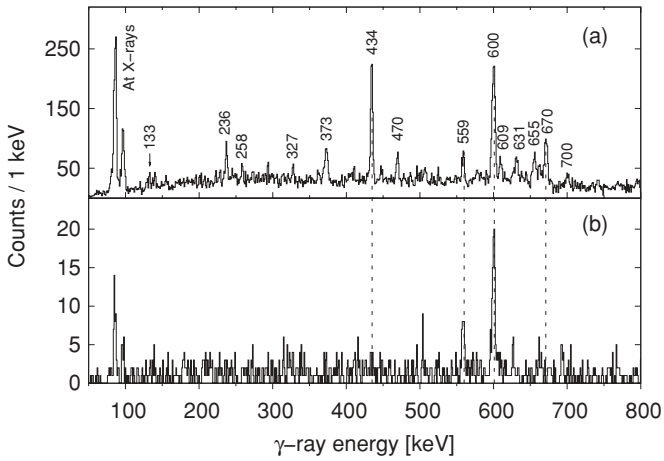

FIG. 2. (a) Spectrum of singles prompt γ rays tagged with the α decay of ^{199}At, collected from the ^{120}Sn(^{82}Kr, $p2n$)^{199}At reaction. (b) Spectrum of γ rays in coincidence with the 600-keV doublet, obtained from the ^{150}Sm(^{52}Cr, $p2n$)^{199}At and ^{120}Sn(^{82}Kr, $p2n$)^{199}At reactions. The dashed lines are inserted to guide the eye for some relevant coincidence-anticoincidence relations.

TABLE I. The γ-ray energies and relative intensities for transitions assigned to ^{199}At.

E_γ (keV)	I_γ (%) delayed	I_γ (%) prompt	I_i^π	I_f^π	E_γ (keV)	I_γ (%) delayed	I_γ (%) prompt	I_i^π	I_f^π
53.8(3)	6(2)	–	$(25/2^+)$	$(23/2^+)$	572.9(1)	100(11)	–	$13/2^+$	$9/2^-$
(70(1))[a]	–	–	$21/2^+$	$21/2^+$	(597.3(6))	15(6)	–	–	–
133.1(5)	16(2)	5(1)	$(23/2^+)$	$21/2^+$	600.0(10)[b]	–	53(3)	$17/2^-$	$13/2^-$
162.9(2)	56(2)	–	$(29/2^+)$	$(25/2^+)$	600.0(10)[b]	–	118(3)	$13/2^-$	$9/2^-$
(187.3(3))	9(2)	–	$(25/2^+)$	$21/2^+$	610.0(3)[c]	18(5)	25(5)	$19/2^+$	$15/2^+$
(202(1))[a]	–	–	$(23/2^+)$	$21/2^+$	631.0(3)	33(7)	28(4)	$21/2^+$	$17/2^+$
236.3(6)	15(3)	16(2)	$17/2^+$	$15/2^+$	655.3(2)	–	39(3)	$(11/2^-)$	$9/2^-$
258.5(3)	10(3)	8(2)	$21/2^+$	$19/2^+$	(662.5(3))	–	24(3)	–	–
327.0(4)	21(5)	10(2)	$21/2^+$	$19/2^+$	670.1(3)[b]	38(6)	61(4)	$17/2^+$	$13/2^+$
372.4(5)	16(5)	31(2)	$19/2^+$	$17/2^+$	670.1(3)[b]	–	–	$(25/2^+)$	$21/2^+$
434.0(2)	44(7)	100(4)	$15/2^+$	$13/2^+$	699.9(3)	49(8)	15(2)	$21/2^+$	$17/2^+$
469.6(2)	–	20(2)	–	$15/2^+$	(795.2(3))	–	14(2)	–	–
558.5(2)	–	28(3)	$21/2^-$	$17/2^-$					

[a]The transition has been tentatively identified (see Fig. 5 and text for details).
[b]The peak is a doublet.
[c]The peak includes events from the 611.2-keV transition in ^{200}Po [28].

of the 600-keV peak in the singles spectrum and the gated spectrum [Fig. 2(b)]. The 655-keV transition [see Fig. 2(a)] was not in coincidence with any strong transition assigned to ^{199}At. It is assumed to depopulate the expected $11/2^-$ state to the ground state. These levels are indicated as the newly assigned Band 1 in the level scheme shown in Fig. 4. The properties of the γ-ray transitions assigned to ^{199}At are listed in Table I.

The delayed γ-ray energy spectra in Fig. 3 are collected from α-tagged events detected in the clover detectors, with a 5-μs correlation time gate. It is evident that several γ-ray transitions (236, 373, 434, 609, and 670 keV) in the singles spectrum of Fig. 2(a) were also detected at the focal plane

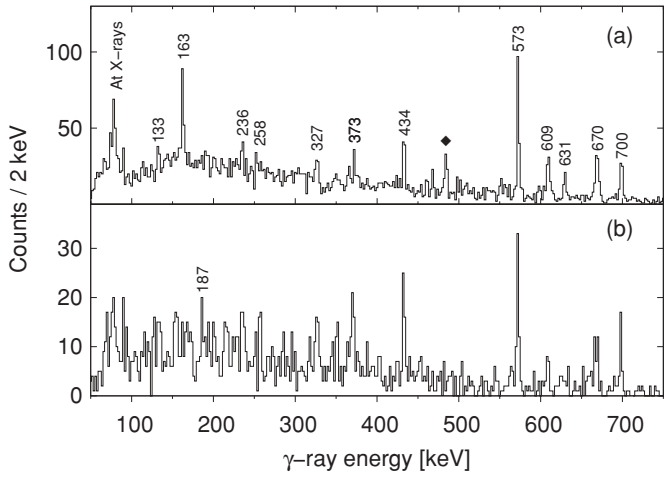

FIG. 3. Delayed γ rays tagged with the ^{199}At α decay, detected in the clover detectors. (a) Spectrum of delayed singles γ rays obtained with lower beam intensity. (b) Spectrum of γ rays in coincidence with the 163-keV transition detected in the planar detector. The 484-keV peak, denoted by a diamond, belongs to ^{200}Po. The data are obtained from the ^{165}Ho(^{40}Ar,6n)^{199}At reaction; a maximum correlation time of 5 μs was set between the recoil and its isomeric decay.

[Fig. 3(a)], indicating the existence of a new high-lying isomer in ^{199}At. These transitions belong to the previously reported level structure [13], placed to feed the expected $13/2^+$ isomer. This study focused on prompt γ-ray spectroscopy, and no high-lying isomer was reported.

Lach *et al.* [14] placed the $13/2^+$ isomer at an excitation energy of 573 keV. At the same time, they noted that the level energies suggested by Styczeń *et al.* [13] have to be revised. In the present work, the 573-keV γ ray is the most intense delayed transition assigned to ^{199}At [see Fig. 3(a)]. Additionally, the 573-keV transition is the only transition that shows two components in the recoil-γ time-difference spectrum. These observations support the assignment made by Lach *et al.* [14]. A 466-keV transition, suggested by Styczeń *et al.* [13], was not observed. Their suggestion that the half-life of the isomer was on the order of a microsecond and that the excitation energy was 466 keV was based on systematics. The properties of the isomeric states in ^{199}At, as well as results from the conversion electron measurements, will be discussed in the following.

The present results, utilizing γ-γ coincidence studies and energy-sum arguments, largely support the previously reported level structure of the $i_{13/2}$ band based on the $13/2^+$ state [13] (Band 2 in Fig. 4). However, γ-γ coincidences support the placement of a previously unknown 631-keV transition to precede the 670-keV transition, establishing a new level at 1874 keV. The relative intensity of the previously reported 700-keV transition is distinctly weaker in Fig. 2(a) than in Fig. 3(a), indicating that it lies closer to the higher lying isomer and is not part of Band 2. Furthermore, a new level at an energy of 2544 keV was tentatively established.

The delayed 133- and 163-keV transitions visible in Fig. 3(a) do not belong to Band 2 and are thus candidates for transitions in the de-excitation path of the indicated higher lying isomer. The energy spectrum of γ rays gated by the 163-keV transition, presented in Fig. 3(b), shows mostly the

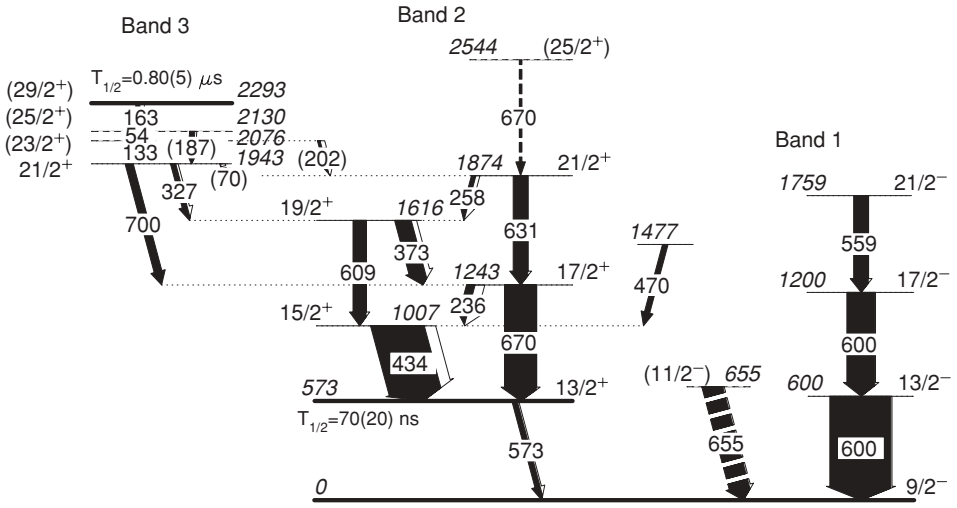

FIG. 4. The proposed level scheme of ^{199}At. The intensities of the 54-, 70-, 133-, 163-, 187-, 202-, and 573-keV transitions below the isomeric states are not to scale.

same transitions as those in Fig. 3(a). Thus, it is likely that the majority of the decay intensity of the isomer proceeds via the 163-keV transition. Although the 163-keV transition is clearly visible in Fig. 3(a) it is not seen in Fig. 2(a), suggesting its placement directly below the isomeric state. In contrast, the 133-keV transition is weakly visible in the α-tagged spectrum of prompt γ rays [Fig. 2(a)], excluding it from being the transitions that depopulates the isomer itself. The suggested de-excitation path of the isomer is shown in the level scheme of Fig. 4, indicated as Band 3.

Figure 5 displays a delayed γ-ray spectrum from the planar detector up to 5 μs after the detection of the ^{199}At recoils. In addition to the 133- and 163-keV transitions, lines at energies of 54, 70, 187, 202, 236, 258, and 327 keV are also observed. The very weak 187-keV transition is in coincidence with the 163-keV transition [see Fig. 3(b)] and, based on

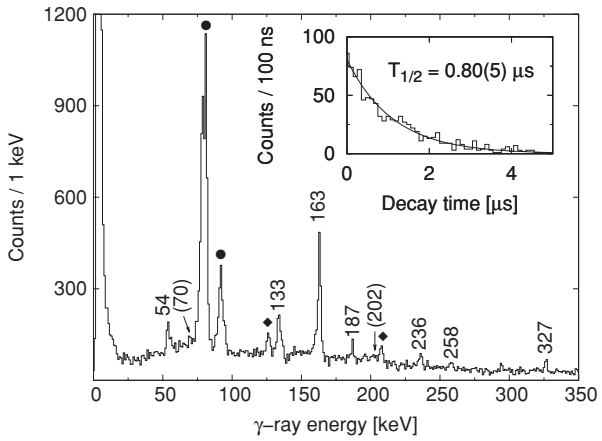

FIG. 5. A spectrum of delayed γ-ray transitions detected in the planar detector within 5 μs after the detection of the ^{199}At recoil in the DSSSD, obtained with lower beam intensity. The inset presents the time distribution between the implantation of a ^{199}At recoil and the observation of the 163-keV γ ray. The filled circles denote the astatine x-ray peaks and the diamonds denote peaks belonging to the polonium isotopes. A spectrum acquired within the time interval of 5–10 μs has been subtracted. The data are obtained from the ^{165}Ho(^{40}Ar,6n)^{199}At reaction.

energy sum arguments, is tentatively placed to proceed in parallel with the 54- and 133-keV transitions. The 631- and 258-keV transitions show weak coincidences with the delayed 163-keV transition [Fig. 3(b)], implying a connection from the high-lying isomer to the $21/2^+$ level at 1874 keV. Weak 70- and 202-keV transitions were tentatively identified (see Fig. 5). They are possibly connecting transitions from states in Band 3 to the $21/2^+$ state in Band 2, allowing the 631- and 258-keV transitions to be detected at the focal plane. Owing to a lack of statistics, the ordering of the transitions in Band 3 remains tentative.

The total internal conversion coefficient of the intense 163-keV transition was estimated by comparing its γ-ray intensity to the total intensity of the 573-keV transition. The resulting value close to 1 indicates an $E2$ multipolarity for the 163-keV transition. By assuming the 133- and 54-keV transitions are in a cascade with the 163-keV transition, with minimal side feeding, an $M1$ multipolarity for both transitions was evaluated. These multipolarities suggest a spin-parity of $29/2^+$ for the isomeric state at 2293 keV. By fitting the time difference between the implantation of the ^{199}At recoil in the DSSD and the detection of the 163-keV transition in the planar detector, a half-life of 0.80(5) μs was determined for the $29/2^+$ isomer (see Fig. 5).

Previously, a half-life of 580(130) ns [14] had been assigned for the $13/2^+$ state. To obtain the half-life of the $13/2^+$ isomer, time differences of transitions in the recoil-gated data below and above the $13/2^+$ state were measured. An energy versus time difference matrix, gated on the 163-keV transition detected in the planar detector, was constructed. The energies of the subsequent transitions, detected in the clover detectors or PIN detector array, were plotted against the time difference with the 163-keV transition. An example of the procedure, using the 474(2)-keV K-conversion electron peak of the 573-keV transition, is shown in Fig. 6. The decay curve was fitted from a point after the drop of the prompt time component. Here the remaining prompt component in the time spectrum originates mainly from the background underneath the peak designated as being due to K conversion. The background component originating from random correlations between the detection of the recoil and the decay event was neglected in

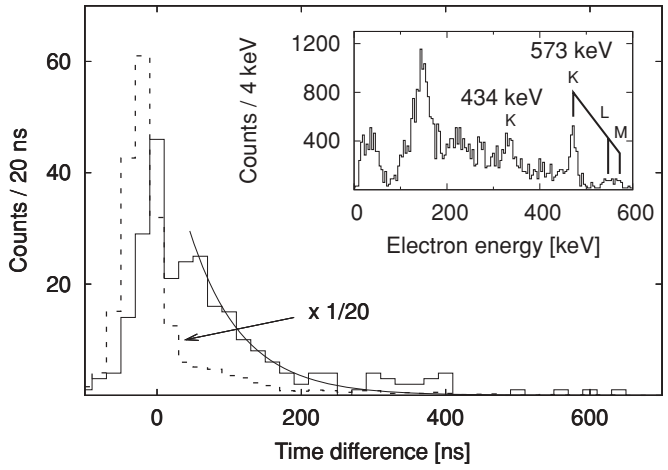

FIG. 6. Time-difference spectrum between the 163-keV γ-ray transition observed in the planar detector and the K-conversion peak of the 573-keV transition observed in the PIN-detector array. The solid line presents the decay curve fitted from 60 ns on. The dashed line, with the intensity compressed by a factor of 20, shows the total projection of the time spectrum for comparison. The inset presents the delayed conversion electron spectrum tagged with the ^{199}At α decay. The K-, L-, and M-conversion peaks of the 573-keV transition are marked in the spectrum together with the K-conversion peak of the 434-keV transition. The data are obtained from the ^{165}Ho(^{40}Ar,$6n$)^{199}At reaction.

this study. A half-life of 70(20) ns was obtained for the $13/2^+$ state, corresponding to a single-particle transition strength of 0.16(5) W.u. for an $M2$ transition. This result is comparable with corresponding values of an $M2$ transition in neighboring odd-mass astatine nuclei, 0.086(2) W.u. for ^{197}At [11] and 0.182(22) W.u. for ^{201}At [29].

Additionally, a comparison between the 573-keV γ and K-conversion electron peak intensities [in Fig. 3(a) and the inset of Fig. 6] gives a K-conversion coefficient of 0.19(4) for the 573-keV transition, which supports an $M2$ multipolarity as well. The 434-keV $M1$ transition has been used for normalization.

B. ^{197}At

An independent analysis of the ^{197}At data of Andgren *et al.* [11] has been performed, allowing for additional γ-ray transitions to be assigned to the level scheme. The prompt γ-ray spectrum is shown in Fig. 7. The strongly coupled

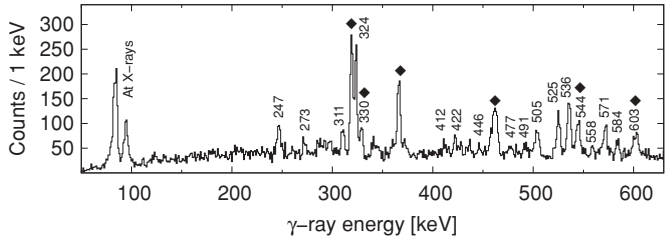

FIG. 7. A prompt γ-ray spectrum tagged with the α decay of ^{197}At, including escaped α particles. Peaks containing events from the contaminating ^{194}Po are denoted with diamonds.

rotational band on top of the $13/2^+$ isomer is extended by two new states with level energies of 1193 and 1796 keV. The latter of these states is denoted as tentative owing to a lack of γ-γ coincidence data.

Some γ-ray transitions evident in Fig. 7 are not associated with the $13/2^+$ isomer, although they clearly belong to ^{197}At. The 505-keV transition is not in coincidence with any of the strong transitions in Band 2 nor with the 536-keV γ-ray transition. It is therefore assigned to depopulate the $11/2^-$ state. The placements of the new 412-, 446-, 477-, and 491-keV γ-ray transitions are based on energy sums and intensity arguments. The extended level scheme for ^{197}At is shown in Fig. 8.

IV. DISCUSSION

Figure 9 presents energy systematics of negative-parity levels in odd-mass astatine and corresponding yrast levels in polonium isotones. The polonium isotopes with $114 \leqslant N \leqslant 124$ have been interpreted to have a vibrational character. Below $N = 114$ the drop in the level energies, particularly visible for the 6^+ and 4^+ states, has been interpreted to be caused by a 2p-2h excitation across the proton shell gap, enhancing the effect of the oblate component in the wave functions [30]. A similar drop, though more gentle for the lower lying states, can be seen for the astatine nuclei in ^{199}At. Because of the resemblance of the energy levels between the corresponding isotones, the states in the astatine nuclei can be interpreted as the odd $h_{9/2}$ proton weakly coupled to the polonium core.

The growing deviation of corresponding states between the isotones around $N = 112$ in Fig. 9 may indicate a strengthening of the coupling between the odd proton and the core. An $11/2^-$ state is assigned tentatively for both ^{197}At and ^{199}At. The energy of this state in ^{199}At is higher than that of the $13/2^-$ state, as can be expected based on the systematics of heavier astatine nuclei (see [5] and references therein). In ^{197}At our candidate for the $11/2^-$ state is below the $13/2^-$ state. This observation further supports the suggestion of a strengthening of the coupling between the mixed configuration of the $h_{9/2}/f_{7/2}$ proton and the polonium core. A similar behavior has been observed earlier in the odd-mass bismuth isotopes (see [33] and references therein). The suggested configuration for each state is shown in Table II.

The excitation energy of the $13/2^+$ state decreases, with decreasing neutron number, and becomes yrast in ^{199}At. A similar decrease for the $13/2^+$ level is seen for example in the odd-mass bismuth isotopes, when approaching the neutron mid-shell. This is interpreted as an effect brought on by a coupling of the $i_{13/2}$ proton to an increasing number of valence neutron holes. This interaction is less repulsive for a proton in the $i_{13/2}$ shell than in the $h_{9/2}$ shell, thus bringing the $13/2^+$ state down in energy [34].

The $13/2^+$ isomer in ^{197}At is interpreted as being oblate deformed [11]. The level spacing in the $i_{13/2}$ band decreases when moving from ^{199}At to ^{197}At. It can also be noted that the signature splitting is larger for ^{199}At in comparison with the corresponding band in ^{197}At. Figure 10 depicts the $B(M1)/B(E2)$ values for the $i_{13/2}$ band of ^{197}At and ^{199}At

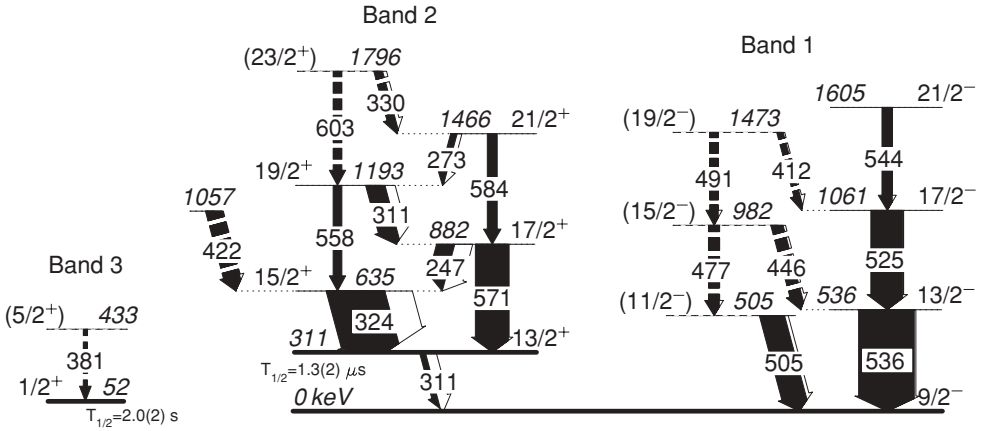

FIG. 8. The level scheme of ^{197}At. The intensity of the isomeric 311-keV transition is not to scale.

compared to the ^{193}Bi nucleus. A theoretical estimate was calculated using the Dönau-Frauendorf model [35,36]. The $B(M1)/B(E2)$ values for ^{199}At are lower than one would expect for a collectively behaving nucleus. This may be caused by a stronger contribution of the spherical components in the wave functions in ^{199}At than in ^{197}At, resulting in a weaker deformation for the states in ^{199}At. The values for ^{197}At and ^{199}At are, nonetheless, of comparable magnitude with those of the $i_{13/2}$ band in ^{193}Bi.

Plots of experimental kinematic moments of inertia $\mathscr{I}^{(1)}$ for the $i_{13/2}$ band in ^{197}At and ^{199}At show similar linear behavior as bands in neighboring oblate deformed nuclei (see Fig. 11). This, together with the observed strongly coupled character of the band, supports the interpretation of oblate structure for the $i_{13/2}$ band in ^{197}At and in ^{199}At.

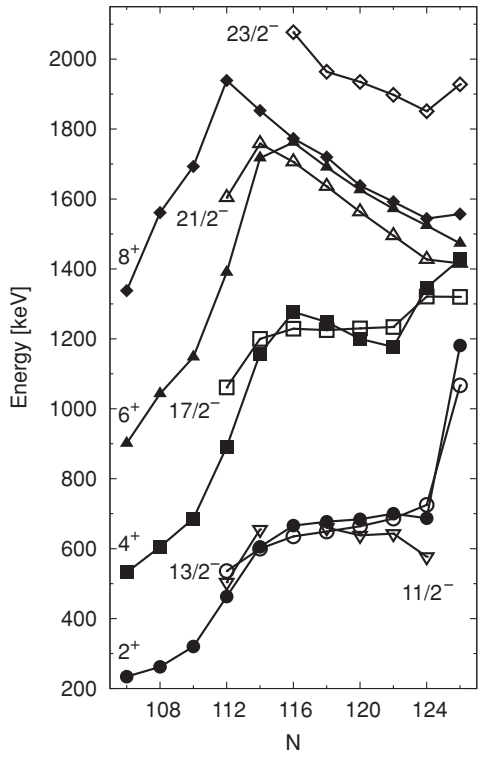

FIG. 9. Level energies of negative-parity states in odd-mass astatine nuclei compared with the yrast states in their even-mass polonium isotones. ^{199}At has a neutron number of 114. For the polonium data, denoted by closed symbols, see the studies [3,31,32] and references therein. The data for the heavier astatine nuclei are taken from the studies [5,7–10].

The $29/2^+$ isomer and the subsequent states in Band 3 of ^{199}At (see Fig. 4) need a more detailed examination. In the polonium isotone ^{198}Po, an 11^- $\pi(h_{9/2}i_{13/2})$ isomer has been identified at an excitation energy of 2565 keV [38]. The following states have also been identified: 9^- $\nu(f_{5/2}^{-1}i_{13/2}^{-1})$, 8^- $\nu(p_{3/2}^{-1}i_{13/2}^{-1})$, and 7^- $\nu(p_{3/2}^{-1}i_{13/2}^{-1})$. The 11^- isomer populates the 9^- state through an $E2$ transition. The $29/2^+$ isomer in ^{199}At is assumed to originate from the odd proton in the $i_{13/2}$ shell coupled to the maximally aligned $h_{9/2}$ proton pair. However, the subsequent $25/2^+$, $23/2^+$, and $21/2^+$ states can be interpreted as the $J_{\max-1}$ states of the odd $h_{9/2}$ proton coupled to the 9^-, 8^-, and 7^- neutron states of the polonium core just discussed. This major configuration difference between the states results in the $29/2^+$ state becoming isomeric. Figure 12 shows a comparison of the level energies of the yrast $29/2^+$ and $25/2^+$ states with the 11^- and 9^- states of the proposed polonium isotone core. Although the states are not well known throughout the astatine nuclei, a similarity between the curves is clearly visible.

The energy of the $23/2^-$ $\pi(h_{9/2}^2 f_{7/2})$ state increases steadily when approaching the neutron mid-shell (see Fig. 12). However, if the energies of the yrast $29/2^+$ and $25/2^+$ states indeed continue to follow the 11^- and 9^- states, respectively,

TABLE II. The proposed configurations for some of the states in ^{199}At.

	E_{state} (keV)	Configuration
$9/2^-$	0	$\lvert\pi h_{9/2} \otimes {}^{198}\text{Po}_{\,0^+}\rangle$
$11/2^-$	655	$\lvert\pi h_{9/2} \otimes {}^{198}\text{Po}_{\,2^+}\rangle$
$13/2^-$	600	$\lvert\pi h_{9/2} \otimes {}^{198}\text{Po}_{\,2^+}\rangle$
$17/2^-$	1200	$\lvert\pi h_{9/2} \otimes {}^{198}\text{Po}_{\,4^+}\rangle$
$21/2^-$	1759	$\lvert\pi h_{9/2} \otimes {}^{198}\text{Po}_{\,6^+}\rangle$
$13/2^+$	573	$\lvert(\pi h_{9/2})^2_{0^+} \otimes \pi i_{13/2}\rangle$
$21/2^+$	1943	$\lvert\pi h_{9/2} \otimes {}^{198}\text{Po}_{\,7^-}\rangle$
$23/2^+$	2076	$\lvert\pi h_{9/2} \otimes {}^{198}\text{Po}_{\,8^-}\rangle$
$25/2^+$	2130	$\lvert\pi h_{9/2} \otimes {}^{198}\text{Po}_{\,9^-}\rangle$
$29/2^+$	2293	$\lvert(\pi h_{9/2})^2 \otimes \pi i_{13/2}\rangle_{J_{\max}}$

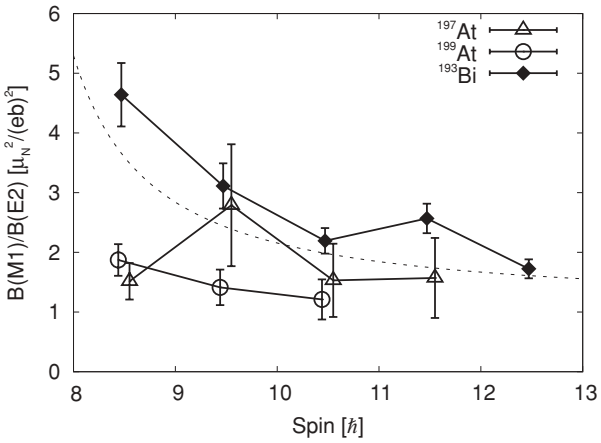

FIG. 10. $B(M1)/B(E2)$ values of the $i_{13/2}$ band in comparison with theory and the corresponding band in ^{193}Bi [33]. The theoretical estimate, denoted by the dashed line, was calculated using the Dönau-Frauendorf model [35,36], assuming $\beta_2 = -0.2$ and $K = 13/2$. The datasets have been shifted slightly along the spin axis for visual purposes.

they are expected to stay rather constant with decreasing neutron number. This results in the $29/2^+$ isomer favoring a feeding to the positive-parity states rather than to the $23/2^-$ state. In ^{205}At, the $29/2^+$ isomer feeds the $23/2^-$ state through an $E3$ transition [10]. However, there is also an $E2$ branch between the $29/2^+$ and $25/2^+$ states in this nucleus. Whereas the single-particle transition strength for this 163-keV $E2$ transition is 0.044 W.u. in ^{199}At, the transition is even more retarded in ^{205}At with a strength of 0.00018 W.u. The $23/2^-$ state is also fed by an $E1$ transition from the $25/2^+$ isomer in the heavier astatine nuclei. The level energy of the $23/2^-$ state, however, rises steadily with decreasing neutron number, making the feeding to it from both the $25/2^+$ and the $29/2^+$ isomer increasingly unfavored.

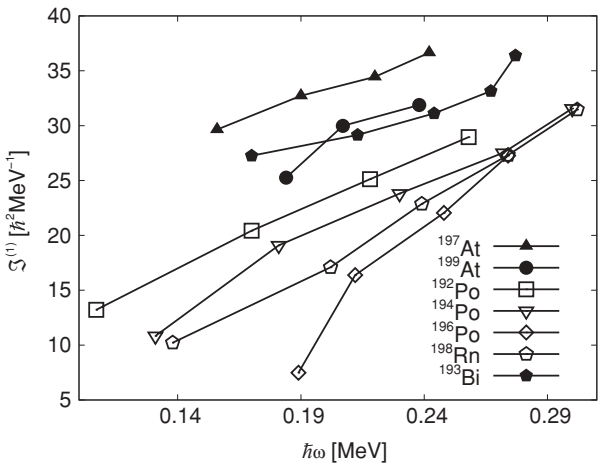

FIG. 11. Experimental kinematic moments of inertia of the rotational band feeding the $13/2^+$ isomer ^{197}At and in ^{199}At in the studied astatine nuclei compared with neighboring oblate deformed nuclei [3,31,33,37]. High-spin data, which exhibit a back bend, have been omitted for ^{193}Bi, for purposes of low-spin comparison.

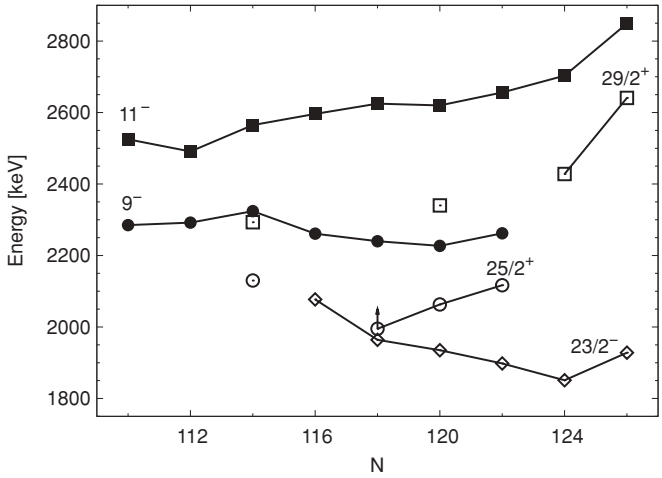

FIG. 12. Level energies of the $29/2^+$, $25/2^+$, and $23/2^-$ states in the odd-mass astatine nuclei, denoted by open symbols, compared with the 11^- and 9^- states in their polonium isotones, denoted by closed symbols. ^{199}At has a neutron number of 114. The data point indicated with an arrow is floating in the level scheme and has been lifted 30 keV in the figure for visual purposes. For the polonium data see the studies [3,31,32] and references therein.

An alternative scheme for the depopulation of the $29/2^+$ isomer is that it decays through the 54-keV $M1$ transition to a $27/2^+$ state, followed by the 133-keV $M1$ and 163-keV $E2$ transitions. This would indicate a strong retardation of 1×10^5 compared to the Weisskopf estimate for the 54-keV $M1$ transition. Similarly hindered $M1$ transitions have been found in the decay of the 10^- $\pi(f_{7/2}i_{13/2})$ isomer in the ^{204,206,208}Rn isotopes [39]. In this case, the subsequent $27/2^+$ and $25/2^+$ states in ^{199}At would be interpreted as the $J_{\max}$ and $J_{\max-1}$ states from the $h_{9/2}$ proton coupled to the 9^- polonium core. A similar pair of states has been reported by Mabala *et al.* in ^{197}Bi [40], which is moreover an isotone to ^{199}At, and by Lönnroth *et al.* [34] in the α-decay daughter ^{195}Bi. In this scheme, the transition between the $25/2^+$ state and the $21/2^+$ state is believed to mimic a core transition between the 9^- and the 7^- states in ^{198}Po. The $25/2^+$ state is reported to be isomeric in the heavier astatine isotopes, with a half-life of some tens of nanoseconds. However, its possible isomeric nature could not be resolved in this study.

V. CONCLUSIONS

The present study clarifies some ambiguities related to the previous results for ^{199}At. We present a strongly coupled rotational band on top of the $13/2^+$ isomer and a series of transitions to the $9/2^-$ ground state. The transitions observed feeding the ground state point to a vibrational structure in ^{199}At. The $11/2^-$ state is above the $13/2^-$ state in energy in ^{199}At, but it drops below the $13/2^-$ state in ^{197}At, as being part of the nonfavored signature partner in the ground-state band. This indicates a strengthening of the coupling between the odd $h_{9/2}/f_{7/2}$ proton and the rotating polonium core. The strongly coupled character of the $i_{13/2}$ band is a sign of collective behavior in both ^{197}At and ^{199}At. The coupling is, however, weaker in ^{199}At, showing a sign of the nucleus

being of transitional nature between spherical structures and the oblate deformed ^{197}At. A $29/2^+$ isomer has been identified to feed the $i_{13/2}$ band through states originated from the odd proton coupled to a neutron pair. The configuration for this isomer is suggested to be $\pi(h_{9/2}^2 i_{13/2})$.

ACKNOWLEDGMENTS

This work has been supported through EURONS (European Commission Contract No. RII3-CT-2004-506065) and by the Academy of Finland under the Finnish Centre of Excellence Programme 2006-2011 (Nuclear and Accelerator Based Physics Contract No. 213503). The authors would also like to thank the UK/France (STFC/IN2P3) detector Loan Pool and GAMMAPOOL European Spectroscopy Resource for the loan of the detectors for JUROGAM and GSI for the loan of the VEGA detectors. Support has also been provided by the UK Engineering and Physical Sciences Research Council. U.J. acknowledges support from the Finnish Academy of Science and Letters (the Vilho, Yrjö, and Kalle Väisälä Foundation), P.N. acknowledges support from the Academy of Finland (Contract No. 121110).

[1] K. Heyde, P. Van Isacker, M. Waroquier, J. L. Wood, and R. A. Meyer, Phys. Rep. **102**, 291 (1983).
[2] J. L. Wood, K. Heyde, W. Nazarewicz, M. Huyse, and P. Van Duppen, Phys. Rep. **215**, 101 (1992).
[3] K. Helariutta *et al.*, Eur. Phys. J. A **6**, 289 (1999).
[4] K. Van de Vel *et al.*, Eur. Phys. J. A **17**, 167 (2003).
[5] K. Dybdal, T. Chapuran, D. B. Fossan, W. F. Piel Jr., D. Horn, and E. K. Warburton, Phys. Rev. C **28**, 1171 (1983).
[6] T. P. Sjoreen, D. B. Fossan, U. Garg, A. Neskakis, A. R. Poletti, and E. K. Warburton, Phys. Rev. C **25**, 889 (1982).
[7] T. P. Sjoreen, U. Garg, and D. B. Fossan, Phys. Rev. C **23**, 272 (1981).
[8] T. P. Sjoreen, G. Schatz, S. K. Bhattacherjee, B. A. Brown, D. B. Fossan, and P. M. S. Lesser, Phys. Rev. C **14**, 1023 (1976).
[9] I. Bergström, B. Fant, C. J. Herrlander, K. Wikström, and J. Blomqvist, Phys. Scr. **1**, 243 (1970).
[10] R. F. Davie, A. R. Poletti, G. D. Dracoulis, A. P. Byrne, and C. Fahlander, Nucl. Phys. A **430**, 454 (1984).
[11] K. Andgren *et al.*, Phys. Rev. C **78**, 044328 (2008).
[12] W. Męczyński *et al.*, Eur. Phys. J. A **3**, 311 (1998).
[13] J. Styczeń *et al.*, AIP Conf. Proc. **495**, 255 (1999).
[14] M. Lach *et al.*, Eur. Phys. J. A **9**, 307 (2000).
[15] K. Andgren *et al.*, Phys. Rev. C **77**, 054303 (2008).
[16] C. W. Beausang *et al.*, Nucl. Instrum. Methods Phys. Res. A **313**, 37 (1992).
[17] C. Rossi Alvarez, Nucl. Phys. News **3**, 10 (1993).
[18] M. Leino *et al.*, Nucl. Instrum. Methods Phys. Res. B **99**, 653 (1995).
[19] R. D. Page *et al.*, Nucl. Instrum. Methods Phys. Res. B **204**, 634 (2003).
[20] I. H. Lazarus *et al.*, IEEE Trans. Nucl. Sci. **48**, 567 (2001).
[21] P. J. Nolan, F. A. Beck, and D. B. Fossan, Annu. Rev. Nucl. Part. Sci. **44**, 561 (1994).
[22] E. S. Paul *et al.*, Phys. Rev. C **51**, 78 (1995).
[23] P. Rahkila, Nucl. Instrum. Methods Phys. Res. A **595**, 637 (2008).
[24] D. C. Radford, Nucl. Instrum. Methods Phys. Res. A **361**, 297 (1995).
[25] D. C. Radford, Nucl. Instrum. Methods Phys. Res. A **361**, 306 (1995).
[26] B. Singh, Nucl. Data Sheets **108**, 79 (2007).
[27] H. De Witte *et al.*, Eur. Phys. J. A **23**, 243 (2005).
[28] T. Weckström, B. Fant, T. Lönnroth, V. Rahkonen, A. Källberg, and C.-J. Herrlander, Z. Phys. A **321**, 231 (1985).
[29] F. G. Kondev, Nucl. Data Sheets **108**, 365 (2007).
[30] A. M. Oros, K. Heyde, C. De Coster, B. Decroix, R. Wyss, B. R. Barrett, and P. Navratil, Nucl. Phys. A **645**, 107 (1999).
[31] L. A. Bernstein *et al.*, Phys. Rev. C **52**, 621 (1995).
[32] D. R. Wiseman *et al.*, Eur. Phys. J. A **34**, 275 (2007).
[33] P. Nieminen *et al.*, Phys. Rev. C **69**, 064326 (2004).
[34] T. Lönnroth, C. W. Beausang, D. B. Fossan, L. Hildingsson, W. F. Piel Jr., M. A. Quader, S. Vajda, T. Chapuran, and E. K. Warburton, Phys. Rev. C **33**, 1641 (1986).
[35] F. Dönau and S. Frauendorf, in *Proceedings of the Conference on High Angular Momentum Properties of Nuclei, Oak Ridge, Tennessee, USA, 1982*, edited by N. R. Johnson (Harwood, New York, 1983), p. 143.
[36] F. Dönau, Nucl. Phys. A **471**, 469 (1987).
[37] R. B. E. Taylor *et al.*, Phys. Rev. C **59**, 673 (1999).
[38] M. Lach *et al.*, Z. Phys. A **350**, 207 (1994).
[39] D. Horn, C. Baktash, and C. J. Lister, Phys. Rev. C **24**, 2136 (1981).
[40] G. K. Mabala *et al.*, Eur. Phys. J. A **25**, 49 (2005).

Appendix B

Recoil-decay tagging study of ^{205}Fr

PHYSICAL REVIEW C **85**, 014309 (2012)

Recoil-decay tagging study of ^{205}Fr

U. Jakobsson,[1,*] J. Uusitalo,[1] S. Juutinen,[1] M. Leino,[1] T. Enqvist,[2] P. T. Greenlees,[1] K. Hauschild,[1,3] P. Jones,[1,†] R. Julin,[1] S. Ketelhut,[1,‡] P. Kuusiniemi,[2] M. Nyman,[1] P. Peura,[1] P. Rahkila,[1] P. Ruotsalainen,[1] J. Sarén,[1] C. Scholey,[1] and J. Sorri[1]

[1]*Department of Physics, University of Jyväskylä, P. O. Box 35, FI-40014 Jyväskylä, Finland*

[2]*Oulu Southern Institute and Department of Physics, University of Oulu, FI-90041 Oulu, Finland*

[3]*CSNSM, IN2P3-CNRS, F-91405 Orsay Campus, France*

(Received 1 October 2011; published 12 January 2012)

The nucleus ^{205}Fr has been studied through γ-ray and electron spectroscopy using the recoil-decay tagging technique. The resulting level scheme presents a spherical structure built on the $9/2^-$ ground state and a rotational structure on top of a short-lived isomer. The isomer, with a spin and parity of $13/2^+$ and a half-life of 80(20) ns, de-excites by an $M2$ transition directly to the $9/2^-$ ground state. Another, longer-lived, isomer, with a half-life of 1.15(4) ms, has also been found and assigned a spin and parity of $1/2^+$. Transitions populating and de-exciting this isomer have been observed as well.

DOI: 10.1103/PhysRevC.85.014309 PACS number(s): 23.20.Lv, 23.35.+g, 27.80.+w, 29.30.Kv

I. INTRODUCTION

Shape coexistence has been studied throughout neutron-deficient nuclei in the lead region. A competition among spherical, oblate, and prolate shapes has been reported to exist in nuclei up to $Z = 84$ (see Ref. [1] and references therein). The gradual transition between spherical and deformed shapes is believed to be caused by the increasing number of neutron holes, when approaching the neutron mid-shell, coupling to the particle-hole excitations across the proton shell gap. This interaction is attractive and, thus, brings the resulting nuclear states down in energy and increases the collective behavior. The major challenge in studying these proton drip-line nuclei is the decreasing production yield due to the increase of fission.

An onset of oblate ground-state deformation, associated with the 2p-2h excitation across the proton shell gap, has been reported to occur in even-mass polonium nuclei around $N \leqslant 114$ [2–4]. Low-lying excited states in neutron-deficient radon nuclei have been studied down to ^{198}Rn [5–10]. An increase in collectivity for these states, caused by the increasing number of neutron-hole pairs is reported, showing signs of contributions from the 2p-2h excitation. α-decay properties obtained for ^{193}Rn [11] and ^{196}Rn [12] suggest an onset of oblate ground-state deformation in ^{196}Rn and, further, of prolate deformation in ^{193}Rn. The chain of corresponding neutron-deficient odd-mass francium nuclei is less well known than the radon isotopes, with ^{205}Fr being the lightest isotope with in-beam studies reported to date [13–15]. No onset of deformation has been observed in these nuclei.

The $1/2^+$ state, created by exciting a proton from the $s_{1/2}$ shell across the proton shell gap, is well known throughout the odd-mass bismuth nuclei. The state is highly nonyrast in ^{199}Bi and ^{201}Bi [16]. It comes down in energy with decreasing neutron number and becomes the ground state in ^{185}Bi [17]. Interesting features have been observed related to this state throughout the isotopic chain, such as very slow $M4$ transitions to the $9/2^-$ ground state [16]. In the astatine nuclei the state is first observed in ^{197}At [18], decaying by α emission, and it becomes the ground state in ^{195}At [19]. Uusitalo *et al.* [20] have observed the $1/2^+$ state in ^{203}Fr and ^{201}Fr through α-decay studies. In ^{201}Fr the level lies at 146 keV, but in ^{203}Fr the level energy has not yet been established, as the corresponding state in the α-decay daughter ^{199}At has also not been observed. The $1/2^+$ state is expected to become the ground state in ^{199}Fr, leading to oblate ground-state deformation [20].

Another state, characteristic of this region, is the $13/2^+$ state based on the odd proton excited to the $i_{13/2}$ shell. Throughout the odd-mass bismuth and astatine nuclei this state is better known than the $1/2^+$ state. For instance, when approaching the neutron mid-shell, the $13/2^+$ state first becomes isomeric in ^{201}At [21], yrast in ^{199}At, and α decaying in ^{193}At [22]. In ^{199}At and ^{197}At rotational bands have been observed to be built on the $13/2^+$ state, with an estimated deformation parameter of $\beta_2 = -0.2$ in ^{197}At [18]. The $13/2^+$ state has not yet been observed in the odd-mass francium nuclei with $A < 213$.

The nucleus ^{205}Fr has previously been reported by Hartley *et al.* [15], presenting a level scheme with tentative spin and parity assignments constructed up to nearly $10\hbar$ with a level energy of 1736 keV. The transitions were associated with a francium nucleus based on the x rays visible in the coincidence data and, further, with the nucleus ^{205}Fr by total γ-ray fold distributions and cross-bombardment. The assignment of this structure was supported by its similarity with the structure of the one assigned for ^{207}Fr [15].

The present work investigates the possible shape coexistence in ^{205}Fr. Isomeric states generated by the $i_{13/2}$ and the intruding $s_{1/2}$ orbitals are presented, with excited states built on these isomers. Transitions to the ground state are also presented. The present work disagrees entirely with the previous study presented by Hartley *et al.* on the excited states in ^{205}Fr. This disagreement will be discussed as well.

*ulrika.jakobsson@jyu.fi

†Present address: iThemba Laboratory for Accelerator Based Sciences, P. O. Box 722, 7129 Somerset West, South Africa.

‡Present address: TRIUMF, Westbrook Mall, Vancouver, British Columbia, V6T 2A3 Canada.

II. EXPERIMENTAL DETAILS

The measurements were conducted in the Accelerator Laboratory at the Department of Physics of the University of Jyväskylä (JYFL), Finland. The nucleus ^{205}Fr was produced in the fusion-evaporation reaction ^{169}Tm(^{40}Ar, $4n$)^{205}Fr. The ^{40}Ar ion beam, provided by the K-130 cyclotron, was accelerated to an energy of 180 MeV with an average beam current of 14 particle-nA (pnA), during an irradiation time of 60 h. The self-supporting ^{169}Tm target had a thickness of 410 μg/cm^2, and a 50-μg/cm^2-thick carbon reset foil was used behind the target. The ^{205}Fr isotopes were produced with a cross section of 1.3 mb. The rate of detected fusion-evaporation products was estimated to be 27 Hz.

The JUROGAM Ge-detector array was used to detect prompt γ rays at the target position. The array consisted of 43 Compton-suppressed high-purity germanium (HPGe) detectors of EUROGAM phase one [23] and GASP [24] type. The recoiling fusion-evaporation products were separated from beam particles and other unwanted reaction products by the gas-filled recoil separator RITU [25] and transported to the GREAT spectrometer [26] at its focal plane. When arriving in GREAT, the recoils passed through a multiwire proportional counter (MWPC) and were finally implanted into a 300-μm-thick double-sided silicon strip detector (DSSD), which has 4800 pixels in total. The horizontal strips of the DSSD were set to measure α-decay energies and the vertical strips to measure conversion-electron energies, by adjusting the gain ranges of the amplifiers. A clover and a planar germanium detector were used to detect delayed γ rays close to the DSSD, and a silicon PIN-detector array, situated upstream in a box arrangement at the edges of the DSSD, was used for detecting conversion electrons. The PIN detectors and the vertical strips of the DSSD were calibrated using a ^{133}Ba source. All data channels were recorded synchronously using the triggerless total data readout (TDR) [27] data acquisition system, which gives each event an absolute time stamp with a time resolution of 10 ns.

III. RESULTS

The measurement data were analyzed using the recoil-decay tagging (RDT) technique [28] and processed using the GRAIN [29] and RADWARE [30,31] software packages. The recoiling fusion-evaporation products were selected by their time of flight between the MWPC and the DSSD and their energy loss in the MWPC. Furthermore, the different isotopes were identified by linking the recoils with their subsequent α decays in the DSSD, using spatial and temporal correlations. The α-decay branch of $\geqslant$98.5% [32] and half-life of 3.80(3) s [33] for the $9/2^-$ ground state allowed for an effective identification of the ^{205}Fr recoils using a maximum correlation time of 12 s between the recoil and its subsequent α decay. The MWPC-vetoed α-particle energy spectrum obtained from the ^{40}Ar + ^{169}Tm reaction is shown in Fig. 1. Prompt and delayed γ rays belonging to ^{205}Fr were identified based on their time correlation with the α-tagged recoil observed in the DSSD.

The delayed γ-ray and electron spectra in Fig. 2 are collected from recoil-correlated events detected in the GREAT clover detector and the PIN-detector array, respectively. The 440-keV peak in the electron spectrum represents the K-shell conversion of the 544-keV isomeric transition. An internal K-shell conversion coefficient of 0.25(10) can be obtained by comparing the intensities of the peaks in the two spectra (simulated efficiencies were used for the PIN-detector array; see Ref. [34]). This result suggests an $M2$ multipolarity for the isomeric transition [35]. The half-life of the isomer could not be directly determined, due to poor statistics. Based on the feeding of the isomer detected in the JUROGAM array, the number of events detected in the GREAT clover detector and the flight time of the recoil through RITU, a value of 80(20) ns can be estimated for the half-life of the isomer. The estimates assume roughly equal efficiencies for the JUROGAM array and the GREAT clover detector

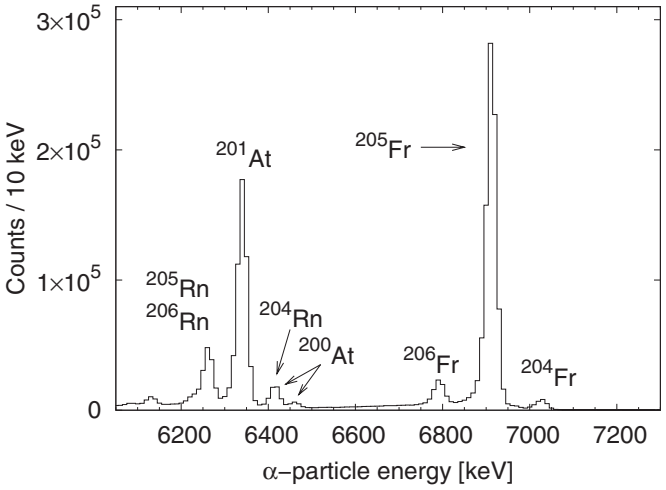

FIG. 1. The MWPC-vetoed α-particle energy spectrum obtained using the ^{40}Ar + ^{169}Tm reaction.

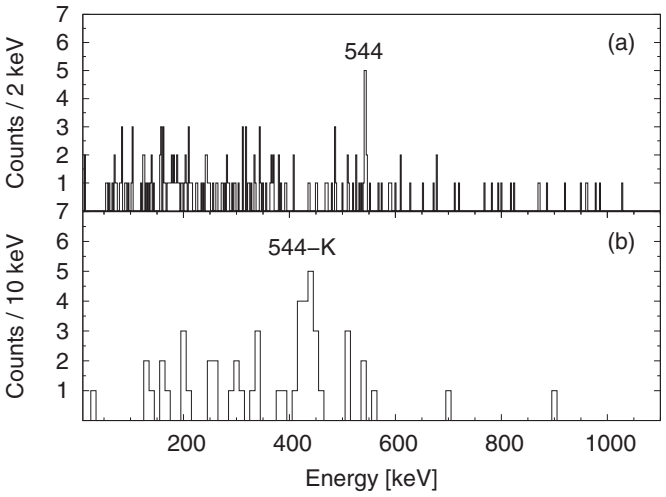

FIG. 2. (a) The spectrum of the delayed γ rays detected in the GREAT clover detector, associated with a recoil implantation in the DSSD. (b) The corresponding conversion electrons detected in the PIN-detector array. A correlation time of 100 ns was used between the recoil implantation and the isomeric decay to get optimal visibility of the peaks.

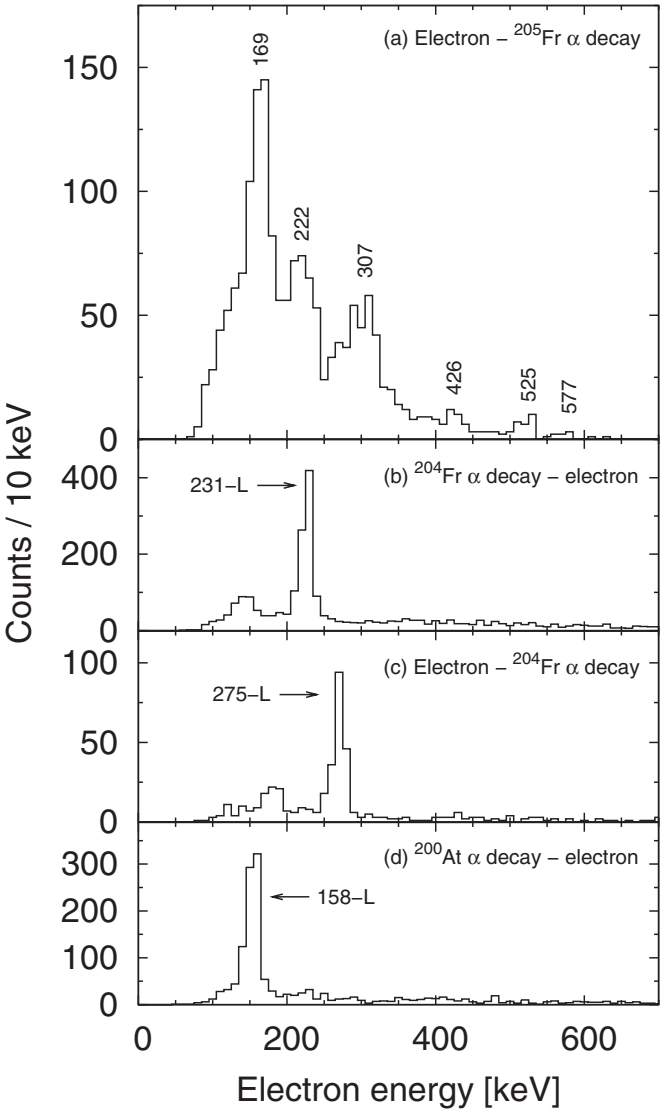

FIG. 3. Energy spectra of electrons detected in the horizontal strips of the DSSD. (a) The spectrum obtained by tagging with the ^{205}Fr α decay, using a correlation time of 8 ms between the recoil and the isomeric decay. The spectrum consists of events from a cascade of electrons. [(b)–(d)] The conversion-electron spectra obtained by tagging with the α decays of ^{204}Fr and ^{200}At [38], using a correlation time of 5 s between the α decay and the subsequent electron in panel (b), 3 s between the recoil implantation and the electron in panel (c), and 5 s between the α decay and the subsequent electron in panel (d). See text for further details.

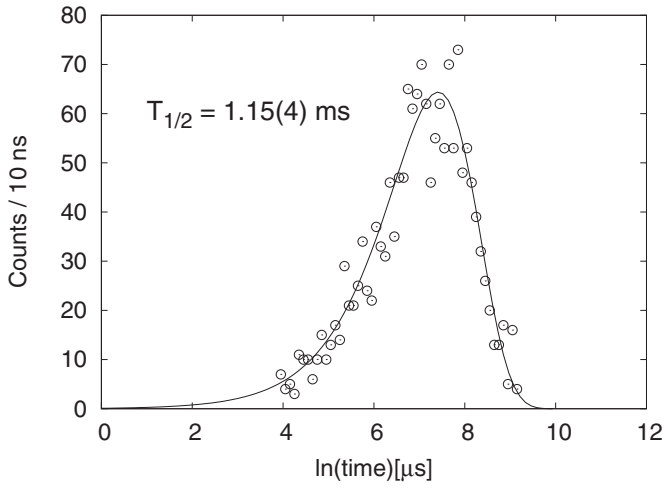

FIG. 4. Time distribution between ^{205}Fr recoil implantation and the subsequent de-excitation of the $1/2^+$ isomer detected in the PIN-detector array. See Ref. [40] for method details. A time window between 50 μs and 8 ms was used, with the lower limit set to eliminate noise effects.

[34]. Based on the results obtained, a transition strength of 0.17(4) W.u. was determined for this $M2$ transition. This value is comparable with those obtained for $M2$ transitions depopulating the $13/2^+$ isomer directly to the $9/2^-$ ground state in odd-mass astatine nuclei. For example, the values 0.182(22) W.u. for ^{201}At [36], 0.16(5) W.u. for ^{199}At [37], and 0.086(13) W.u. for ^{197}At [18] have been reported. Based on these observations the spin and parity of the fast isomer is assigned to be $13/2^+$.

Another, longer-living, isomeric state was also observed by studying ^{205}Fr α-tagged delayed electrons and γ-ray transitions detected in the GREAT DSSD and the planar and clover detectors, respectively. A correlation time of 8 ms was used between the implantation of the ^{205}Fr recoil and the detection of the isomeric decay. Figure 3(a) presents the ^{205}Fr α-tagged electrons with internal-conversion electron spectra [Figs. 3(b)–3(d)] related to the α decays of ^{204}Fr and the daughter nucleus ^{200}At [38,39]; see Fig. 1. Figure 3(b) presents the 231-keV $E3$ transition from the 10^- state in ^{200}At following the 7013-keV α decay of ^{204}Fr, Fig. 3(c) the 275-keV $E3$ transition from the 10^- state in ^{204}Fr preceding the 6969-keV α decay (this transition is now observed, while previous results obtained the transition energy from the difference of the α-decay energies), and Fig. 3(d) the 158-keV $M3$ transition from the 6^+ state in ^{196}Bi following the 6411-keV α decay of ^{200}At. The spectra in Figs. 3(b) and 3(d) provide a means for internal calibration of the spectrum in Fig. 3(a). It is worth noting that since the FWHM is close to 12 keV for the obtained electron peaks, the L- and higher shell conversion electrons will not be separated, and a sum peak representing all these events should situate roughly 12–13 keV below the corresponding transition energy. In this special case, the internal conversion takes place inside the DSSD. Therefore, the energy deposited by the Auger electrons and low-energy x rays, released in the internal conversion process, sum up with the energy deposit of the conversion electron, giving an additional $\sim$10 keV to the total energy deposit. As a result, the electron peak representing emission from the $L + M$ (+higher) shells is found close to 2–3 keV below the corresponding transition energy. This effect is also confirmed in simulations performed for the cases presented above.

Figure 4 presents the time difference between the recoil implantation and the electrons in Fig. 3(a). Using the logarithmic-time method [40] a half-life of 1.15(4) ms was obtained for the isomeric decay. Based on the half-life the assumption can be made that the longer living isomer is actually the $1/2^+$ isomer. Figure 5 depicts the spectrum of delayed

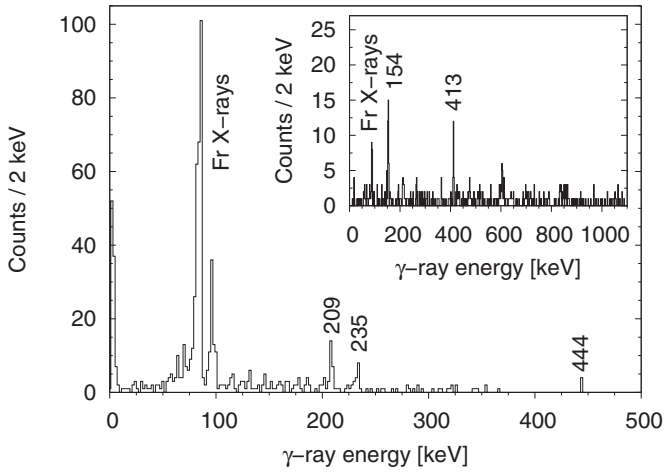

FIG. 5. Spectrum of delayed γ rays tagged with the ^{205}Fr α decay, detected in the GREAT planar and clover detector, in coincidence with electrons associated with the 1.15(4)-ms isomer. (Inset) The spectrum of prompt γ rays detected in the JUROGAM array and associated with the isomeric decay. A correlation time of 8 ms was used between the recoil implantation and the isomeric decay. Note the broad peaks close to 600 and 840 keV originated from the $(n, n'\gamma)$ reaction in the detector material.

γ rays obtained from the GREAT planar and clover detector tagged with the isomeric electrons in Fig. 3(a). Two γ-ray transitions with energies of 209 and 235 keV are clearly visible together with a weaker 444-keV peak. To understand the complicated structure of the electron spectrum in Fig. 3(a), the 209- and 235-keV transitions need to be in a cascade with an additional highly converted ($M2$ or $E3$) transition depopulating the 1.15(4)-ms isomer. This observation is supported by the presence of an intense 169-keV peak in Fig. 3(a). If the electrons generating the 169-keV peak originated from K-shell conversion, a corresponding γ-ray peak should be visible in Fig. 5; however, no such peak has been observed. The 444-keV transition energy equals the sum of the 209- and 235-keV transition energies, and, therefore, the transition is set to proceed alongside the 209- and 235-keV transitions. Based on similar cases in the odd-mass bismuth isotopes [41], we propose that the 1.15(4)-ms isomer de-excites to the $9/2^-$ ground state via a cascade consisting of an $M2$ transition and two $M1$ transitions with energies of 209 and 235 keV, respectively. The 209-keV transition is also observed in the prompt γ-ray data; therefore, it is set to populate the ground state. The suggested structure of the cascade is presented in Band 3 of Fig. 6.

GEANT4 [42] simulations were performed to reproduce the conversion-electron and γ-ray spectrum of the de-excitation of the $1/2^+$ state with the decay characteristics discussed above; see Fig. 7. As a test, the simulations reproduced the calibration spectra in Figs. 3(b)–3(d) successfully. The results from the simulations support our interpretation of the de-excitation path of the $1/2^+$ isomer, with a transition energy of 165(5) keV for the depopulating $M2$ transition and a 35(10)% branching ratio for the 444-keV $E2$ transition. Figure 7(a) presents the scenario discussed above. As a comparison, the above-discussed scenario, without the parallel $E2$ transition, was simulated; see Fig. 7(b). In this scenario, 169-keV peak is clearly not as enhanced as in Figs. 7(a) and 3(a). To verify these results, spectra were generated for a scenario where the $1/2^+$ state is assumed to de-excite by a 235-keV $E3$ transition (100% branching) to the $7/2^-$ state. This result, presented in Fig. 7(c), clearly does not resemble the experimental results. A transition strength of $3.5(2)\times10^{-4}$ W.u. was obtained for the 165-keV $M2$ transition, by assuming a 100% branching ratio. This result agrees well with the value of $9.96(14)\times10^{-4}$ W.u. for the corresponding transition in ^{205}Bi [41]. There is a possibility for a ~400-keV $E3$ transition to occur between the $1/2^+$ state and the $7/2^-$ state (see Fig. 6). With a transition strength as for similar transitions in neutron-deficient odd-mass thallium [36,43], bismuth [44], and astatine [44] nuclei, a branching ratio of 5–40% can be estimated for this competing transition. However, the setup was not sensitive enough to resolve the possible $E3$ branch.

Figure 8(a) presents the energy spectrum of prompt γ rays associated with any fusion-evaporation recoil detected in the DSSD. It is evident in the figure that the dominant fusion-evaporation products are ^{205}Fr (peaks denoted by circles) and

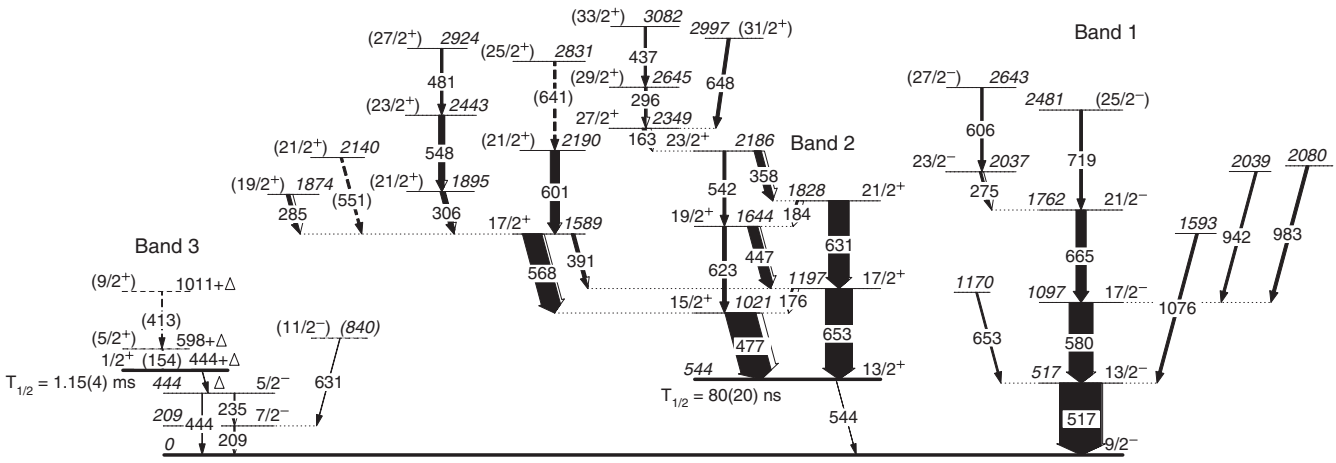

FIG. 6. The proposed level scheme. The intensity of the 544-keV isomeric transition and transitions associated with the $1/2^+$ isomer are not to scale. $\Delta = 165(5)$ keV; see text for details.

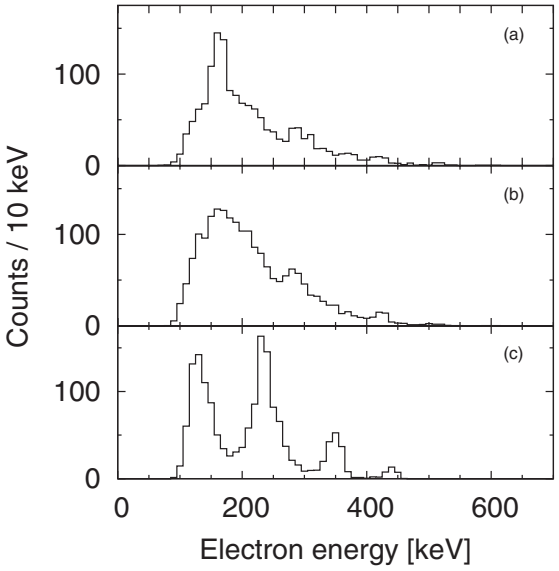

FIG. 7. Simulated electron spectra for three different scenarios in the de-excitation of the $1/2^+$ isomer. (a) The scenario of a 165(5)-keV $M2$ transition followed by a 235-keV and a 209-keV $M1$ transition, with a 35(10)% branching to a parallel 444-keV $E2$ transition. (b) The same scenario without the parallel $E2$ transition. (c) A scenario with the isomer depopulated by a 235-keV $E3$ transition followed by a 209-keV $M1$ transition. See text for further details.

^{205}Rn (peaks denoted by diamonds). The events belonging to ^{205}Rn are eliminated when tagging with the ^{205}Fr α decay, as shown in Fig. 8(b). Events from the Coulomb-excited ^{169}Tm target ions still leak through despite α-decay tagging. The strongest of these peaks are denoted by open circles. The fusion-evaporation reaction also produces neutrons which excite the germanium nuclei in the HPGe detector material. The resulting γ rays cannot be completely filtered out, and, thus, two broad peaks close to 600 and 840 keV [47,48] are visible in Fig. 8 (and in the inset of Fig. 5).

Angular-distribution measurements were performed for a number of strong γ-ray transitions. The prompt γ-ray data were sorted according to the four detector rings (at angles of 158°, 134°, 108°, and 94° with respect to the beam direction) of the JUROGAM array. The relative-efficiency corrected data for each transition were studied relative to the detector angle. Legendre polynomials according to the method presented in the work by Yamazaki [49] were fitted to the data to obtain the value of the A_2 coefficient. The A_4 coefficient was set to zero as the aim was to distinguish between the possible stretched dipole and stretched $E2$ character of the transition and not to consider quadrupole mixing. The obtained values for the Legendre polynomial A_2 coefficient, where the procedure was possible, are presented in Table I, with a negative value usually presenting a stretched dipole transition and a positive value a stretched $E2$ transition. The level scheme resulting from the analysis is presented in Fig. 6 and further details for each transition are presented in Table I.

Figure 8(c) presents the spectrum of coincident γ rays obtained by setting an energy gate on the 517-keV peak, which is the strongest of the γ-ray transitions associated with the

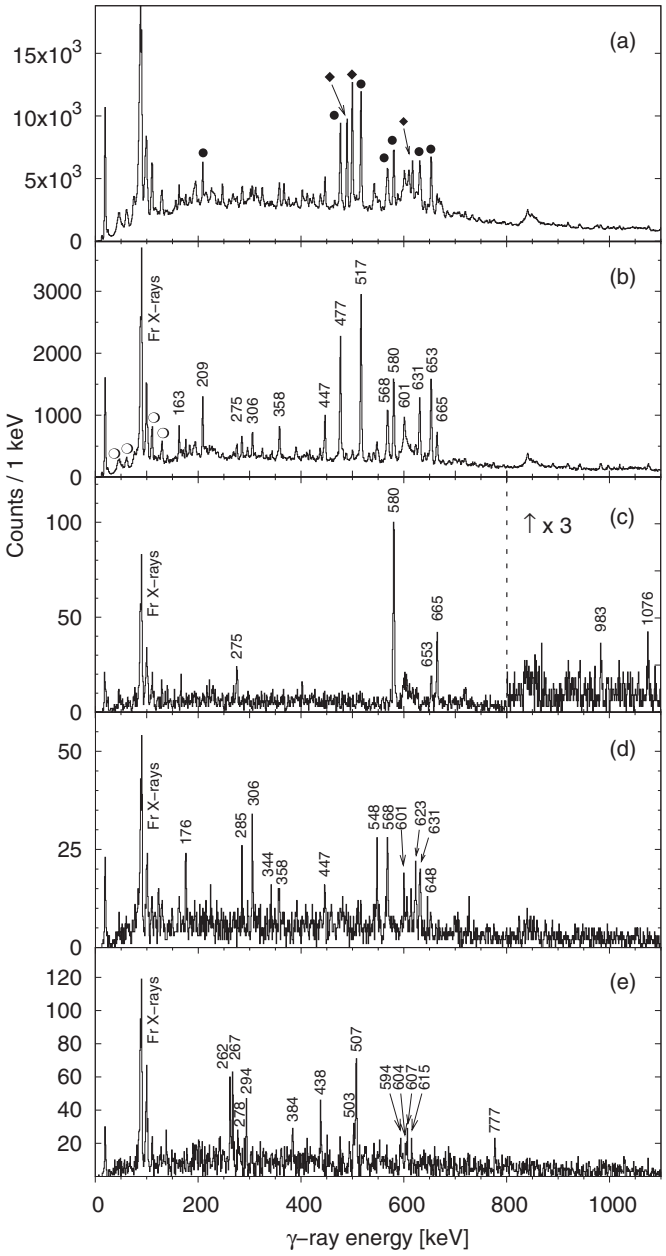

FIG. 8. (a) Spectrum of singles prompt γ rays obtained by requiring a recoil implantation in the DSSD. Peaks belonging to ^{205}Fr are indicated by circles and those belonging to ^{205}Rn [45] by diamonds. (b) Spectrum of singles prompt γ rays tagged with the α decay of ^{205}Fr. Transitions belonging to ^{169}Tm [46] are indicated by open circles. [(c) and (d)] Spectra of transitions in coincidence with the 517- and the 477-keV transition, respectively. The two spectra include γ rays tagged with escaped α particles. The intensity scale of the high-energy end of panel (c) has been expanded threefold. (e) Spectrum of prompt singles γ rays tagged with the α decay of ^{206}Fr. Note the broad peaks close to 600 and 840 keV, visible in each panel, originated from the $(n, n'\gamma)$ reaction in the detector material.

^{205}Fr recoils. The spectrum shows strong transitions at 580 and 665 keV. All three transitions have positive A_2 values (see Table I) and are, thus, assigned an $E2$ multipolarity. This sequence of transitions is placed on top of the $9/2^-$ ground state, and it forms a regular level pattern up to a $21/2^-$ state

TABLE I. The energies and relative γ-ray intensities of transitions assigned to ^{205}Fr. Results for A_2 coefficients from angular-distribution measurements are included where they could be obtained. The transitions associated with Band 3 are placed separately at the bottom of the table.

E_γ (keV)	I_γ(%)	I_i^π	I_f^π	A_2	E_γ (keV)	I_γ(%)	I_i^π	I_f^π	A_2
140.2(1)	3.8(6)				568.5(1)	45(2)	$17/2^+$	$15/2^+$	−0.28(16)
162.9(1)	9.5(5)	$27/2^+$	$23/2^+$	0.23(9)	580.5(1)	56(2)	$17/2^-$	$13/2^-$	0.28(4)
166.8(2)	3.5(5)				601.3(1)	21(2)	$(21/2^+)$	$17/2^+$	
170.9(2)	1.9(4)				605.8(3)	5.6(11)	$(27/2^-)$	$23/2^-$	
175.8(1)	4.2(4)	$17/2^+$	$15/2^+$		623.5(2)	8.8(9)	$19/2^+$	$15/2^+$	
183.6(2)	4.8(6)	$21/2^+$	$19/2^+$		630.9(1)[a]	48(2)	$21/2^+$	$17/2^+$	0.24(3)
191.2(3)	3.7(6)				640.9(2)	5.8(9)	$(25/2^+)$	$(21/2^+)$	
194.5(2)	6.3(6)				648.2(2)	7.3(9)	$(31/2^+)$	$27/2^+$	
275.3(1)	5.4(5)	$23/2^-$	$21/2^-$	−0.51(13)	653.2(1)[a]	63(2)	$17/2^+$	$13/2^+$	0.21(5)
285.0(1)	8.7(5)	$(19/2^+)$	$17/2^+$		664.6(1)	24(1)	$21/2^-$	$17/2^-$	0.29(7)
296.0(2)	3.7(5)	$(29/2^+)$	$27/2^+$		675.7(5)	3.5(10)			
305.6(1)	11(1)	$(21/2^+)$	$17/2^+$		688.4(5)	3.5(8)			
324.9(2)	3.5(5)				697.2(4)	5.2(11)			
343.6(2)	2.4(4)				701.4(3)	4.9(11)			
358.2(6)	17(1)	$23/2^+$	$21/2^+$	−0.29(11)	707.6(3)	5.5(10)			
390.6(1)	6.4(5)	$17/2^+$	$17/2^+$		714.2(4)	3.8(8)			
411.4(2)	3.4(5)				719.2(2)	6.5(8)	$(25/2^-)$	$21/2^-$	
417.0(2)	3.3(5)				774.6(2)	3.7(6)			
437.3(1)	5.1(5)	$(33/2^+)$	$(29/2^+)$	0.43(17)	840.8(3)	7(4)			
446.6(1)	24(1)	$19/2^+$	$17/2^+$		848.3(6)	7.0(15)			
472.4(2)	4.1(6)				857.6(8)	4.0(15)			
476.6(2)	72(2)	$15/2^+$	$13/2^+$	−0.17(4)	890.3(3)	3.7(7)			
481.2(2)	5.6(6)	$(27/2^+)$	$(23/2^+)$		919.1(2)	5.5(7)			
516.8(2)	100(2)	$13/2^-$	$9/2^-$	0.25(1)	942.4(2)	5.5(7)	—	$17/2^-$	
532.4(2)	6.0(8)				983.2(2)	7.1(7)	—	$17/2^-$	
541.4(2)	6.8(10)	$23/2^+$	$19/2^+$	0.6(3)	997.7(3)	4.5(7)			
544(1)[b]		$13/2^+$	$9/2^-$		1020.0(4)	3.0(7)			
547.5(1)	13(2)	$(23/2^+)$	$(21/2^+)$	−0.48(4)	1076.0(2)	6.5(8)	—	$13/2^-$	
550.6(3)	5.4(9)	$(21/2^+)$	$17/2^+$						
154.3(5)		$(5/2^+)$	$1/2^+$		235(1)		$5/2^-$	$7/2^-$	
165(5)[c]		$1/2^+$	$5/2^-$		413.1(5)		$(9/2^+)$	$(5/2^+)$	
209(1)[d]	19(1)	$7/2^-$	$9/2^-$		444(2)		$5/2^-$	$9/2^-$	

[a]The peak is a doublet.
[b]The transition is isomeric.
[c]The γ ray was not observed, see text for details.
[d]The transition is also visible in Fig. 8(b).

(see Band 1 in Fig. 6). A 275-keV stretched dipole (presumably of $M1$ multipolarity) transition is in coincidence with each of these transitions and is, therefore, assigned to depopulate a $23/2^-$ state. Figure 8(c) shows a 653-keV transition in clear coincidence with the 517-keV transition but not with the other transitions in Band 1. Therefore, it is set to precede the 517-keV transition. It is evident that the 653-keV peak must be a doublet by comparing its intensity with the intensity of the 580-keV transition between Figs. 8(b) and 8(c). A 606-keV transition was observed to populate the $23/2^-$ state. High-energy transitions (with energies of 719, 942, 983, and 1076 keV) were observed in coincidence with the low-lying ground-state band transitions.

It is evident that some of the most intense peaks in Fig. 8(b) are not visible in Fig. 8(c), implying that the transitions in Fig. 8(b) can be divided into two dominating structures. Figures 8(c) and 8(d) indicate that the intense 477-keV transition in Fig. 8(b) is not in coincidence with the 517-keV transition or with any of the other transitions in Band 1. This $M1$ transition is assumed to populate the $13/2^+$ state. Coincidence and energy relations produce a strongly coupled band, up to a spin and parity of $23/2^+$, including γ-ray transitions with energies of 176, 184, 358, 447, 477, 542, 623, 631, and 653 keV. Angular distribution measurements support the multipolarity assignments for several of these transitions. This sequence is indicated as Band 2 in Fig. 6.

Figure 6 presents several transitions feeding into Band 2, of which the most intense is the 568-keV transition. It is also one of the most intense peaks in Fig. 8(d) produced by setting a gate on the 477-keV transition. It is not in coincidence with the other transitions in Band 2 and is, therefore, set to populate the $15/2^+$ state. Results from angular-distribution measurements

provide a stretched dipole character for the transition, and it is, thus, placed to depopulate a $17/2^+$ state. A weaker 391-keV transition can be assigned to depopulate this state to the $17/2^+$ state in Band 2. A γ-ray peak at 601-keV is the strongest peak visible in the spectrum gated on the 568-keV transition.

A 163-keV $E2$ transition is clearly visible when setting an energy gate on the 358-keV transition. This transition is, furthermore, in coincidence with the 447-, 631-, and 653-keV transitions. The transition is placed to depopulate a $27/2^+$ state to the $23/2^+$ state in Band 2. Similarly, the rest of the transitions in these cascades are placed based on coincidence studies.

The inset of Fig. 5 presents prompt γ rays associated with the $1/2^+$ isomer. Lack of statistics did not allow for an adequate γ-γ coincidence analysis, although some weak evidence for coincidences between the 154- and 413-keV transitions was found. The ordering of the transitions is purely based on their intensities. The strength of the x-ray peak suggests an $E2$ multipolarity for the 154-keV transition. There is, however, a weak γ-ray peak close to an energy of 200 keV. If a considerable amount of the x-ray intensity originates from the internal conversion of this peak, the total internal conversion coefficient of the 154-keV transition will be lower and the multipolarity could approach the value of an $E1$ transition. The spin and parity assignments of the states remain, therefore, tentative.

The γ-ray transitions reported by Hartley *et al.* [15] were not observed in the present work among the transitions associated with ^{205}Fr. In the previous work RDT-type tagging methods were not used; instead, the identification of the studied isotopes relied on excitation-function analysis. We have found that the γ-ray transitions identified in the previous study actually belong to the neighboring isotope ^{206}Fr as shown in Fig. 8(e), where observed transitions include the 503-, 507-, and 777-keV transitions previously reported as belonging to ^{205}Fr. The 384-keV transition reported by Hartley *et al.* to belong to ^{206}Fr is clearly visible in this spectrum, with the 262-, 267-, 278-, and 294-keV transitions reported as part of the shears band. Furthermore, the 438-keV transition and the group of transitions close to 600-keV have not been previously reported. There are three α-decaying states in ^{206}Fr [38]; unfortunately, the lack of statistics in the present work and the overlap of the α-decay energies prevent us from associating the above-mentioned γ-ray transitions with the corresponding α-decaying state.

IV. DISCUSSION

The level scheme obtained for ^{205}Fr, shown in Fig. 6, presents separate positive-parity and negative-parity structures. This scheme differs from what has earlier been found for heavier francium nuclei [13,14], where the positive-parity states de-excite toward the ground state through high-lying negative-parity states. The origin of this change is in the lowering of the $13/2^+$ state, which de-excites to the ground state. A similar transformation has been observed in the odd-mass astatine nuclei when comparing ^{199}At [37] with

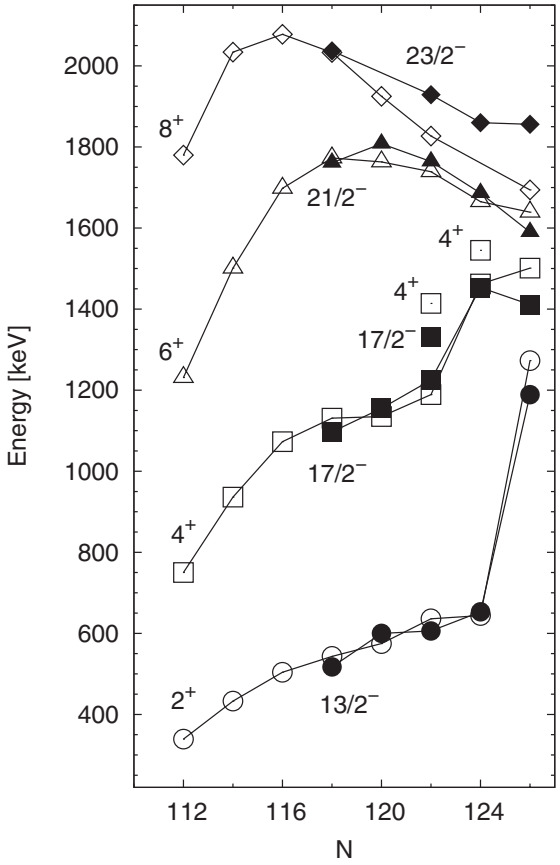

FIG. 9. Level energies of negative-parity states in odd-mass francium nuclei compared with yrast and near-yrast positive-parity states in their even-mass radon isotones. ^{205}Fr has a neutron number of 118. For the radon data, denoted by open symbols, see the studies in Refs. [5,8–10,51]. The data for the heavier francium nuclei are taken from the studies in Refs. [13–15]. The lines connect yrast states without specifying the configuration of the states.

heavier astatine isotopes (see Refs. [21,50] and references therein).

Figure 9 presents energy systematics of negative-parity states in odd-mass francium nuclei compared with yrast levels in their radon isotones. The increasing number of valence neutron holes lowers the level energies when moving away from the closed neutron shell. The first sign of the effect is visible in the drastic drop of the 2^+ state in ^{210}Rn, caused by the opening of the first neutron shell. While the corresponding state in ^{212}Rn is still purely a $(\pi h_{9/2})^4$ state, the neutron holes generate components in the wave function of the 2^+ state bringing the state down in energy. This scheme is followed by the francium isotones, with a clear analogy visible for the $13/2^-$ state. The same effect appears in the radon 4^+ states at ^{208}Rn, where both the proton state and the yrast neutron state have been observed. The nonyrast proton state is still known in ^{206}Rn, but as the neutron states decrease in energy, the proton state is nonyrast and is not observed in the lighter even-mass radon isotopes. Again, the $17/2^-$ states in the francium isotones show a similar behavior with a change between proton and neutron-hole configuration in ^{209}Fr. Although collectivity increases with each new neutron

hole, the level spacing between the 2^+ and 4^+ states in the radon nuclei indicates that no sign of the proton intruder configuration, visible in ^{198}Rn [10], is yet to be expected this far from the neutron mid-shell in the francium nuclei. Further up in energy, the 6^+ states show signs of neutron-hole configurations in ^{202}Rn, where a down bend in the energy curve is visible. Francium systematics do not reach this far yet, and the $21/2^-$ state in ^{205}Fr could still originate from the $(\pi h_{9/2})^3$ configuration. Furthermore, the $23/2^-$ state could originate from the $(\pi h_{9/2})^2 f_{7/2}$ configuration.

Band 1 includes states feeding into the cascade mentioned above. A $(25/2^-)$ state has been observed at a level energy of 2481 keV and can be interpreted as originating from the maximum alignment of the five $h_{9/2}$ protons. This state is expected to lie approximately 750 keV above the $21/2^-$ state in odd-mass francium nuclei [13]. It has not been observed in ^{213}Fr and ^{211}Fr [14], but it has been observed in ^{209}Fr [13] at a level energy of 2559 keV (that is 795 keV above the $21/2^-$ state). The level-energy difference of 719 keV between the $(25/2^-)$ and $21/2^-$ states in ^{205}Fr agrees well, therefore, with these observations. The $(27/2^-)$ state in ^{205}Fr, at a level energy of 2643 keV, is observed to de-excite to the $23/2^-$ state discussed earlier. It is interpreted as originating from the $\pi(h_{9/2})^4 f_{7/2}$ [or the $\pi(h_{9/2})^2 f_{7/2} \otimes 2^+$] configuration. Similar states have earlier been observed in ^{209}Fr and in ^{213}Fr at level energies of 2599 and 2740 keV, respectively.

Strongly coupled bands have been observed on top of the $13/2^+$ state in ^{197}At and ^{199}At, indicating an oblate deformation for the $13/2^+$ state [37]. A similar, but slightly weaker, coupling is observed for the band built on top of the $13/2^+$ state in the present work (Band 2), indicating that the $13/2^+$ state in ^{205}Fr originates from the odd proton in the $13/2^+$[606] Nilsson state. Plots of kinematic moments of inertia $\mathcal{J}^{(1)}$, extracted from the level energies, for Band 2 in ^{205}Fr compared with similar bands in neighboring nuclei are presented in Fig. 10. The result for ^{205}Fr follows the same, quite linear, behavior as the other nuclei, with collective characteristics similar to those of ^{199}At. The high-spin point, with a $\mathcal{J}^{(1)}$ value close to 40 $\hbar^2$ MeV^{-1}, shows a clear deviation from the smooth behavior. This deviation may suggest that the $23/2^+$ state is no longer part of the structure of Band 2.

A group of positive-parity states, identified in the odd-mass bismuth ($A > 191$), astatine ($A > 199$), and francium ($A > 209$) nuclei, are formed by coupling the odd $h_{9/2}$ proton to the negative-parity states of the corresponding even-even core nucleus. For example, the negative-parity states 5^- $[(\nu f_{5/2})^{-1}(\nu i_{13/2})^{-1};(\nu p_{3/2})^{-1}(\nu i_{13/2})^{-1}]$ at 1909 keV, 7^- $[(\nu f_{5/2})^{-1}(\nu i_{13/2})^{-1};(\nu p_{3/2})^{-1}(\nu i_{13/2})^{-1};(\nu p_{1/2})^{-1}(\nu i_{13/2})^{-1}]$ at 2154 keV, 9^- $[(\nu f_{5/2})^{-1}(\nu i_{13/2})^{-1}]$ at 2183 keV, and 6^- (similar configuration as the 5^- or 7^- state) at 2257 keV in ^{200}Pb [53], which is the isotone of ^{205}Fr, are formed by the valence neutron pairs. It is worth noting that these core states are very stable in level energy against changing neutron number; see, for instance, the studies (and references therein) for systematics in lead [54] and polonium [55] nuclei. Similar negative-parity states are expected to exist in ^{204}Rn, although a complete set of them has not yet been observed [9]. When these states are coupled to the odd $h_{9/2}$ proton, the favored J_{MAX}-1 $17/2^+$, $21/2^+$, $25/2^+$, and $19/2^+$ states are formed. Additionally, a 10^- $(f_{7/2}i_{13/2})$ state is present in the ^{204}Rn isotone at 2462 keV [9]. Coupling the odd $h_{9/2}$ proton to this 10^- state yields the J_{MAX} state $29/2^+$. Similarly, the 11^- $(h_{9/2}i_{13/2})$ state in ^{204}Rn at 2597 keV yields a J_{MAX} state $29/2^+$ in ^{205}Fr when coupled with the odd $h_{9/2}$ proton.

Positive-parity states based on the configurations discussed above can be associated with levels in ^{205}Fr observed in the present work. The $17/2^+$ state at 1589 keV is interpreted to have the configuration $\pi h_{9/2} \otimes 5^-$. A $17/2^+$ state lies at 1748 keV in the isotone ^{201}Bi. Further, in the isotone ^{203}At, two $17/2^+$ states have been observed at level energies of 1633 and 1696 keV, respectively. Both states have an $E2$ branch to the $13/2^+$ state and an $M1$ branch to the $15/2^+$ state. In ^{205}Fr the $17/2^+$ state feeds the $15/2^+$ state in Band 2. The $(21/2^+)$ (at 1895 keV) and $(19/2^+)$ (at 1874 keV) states are interpreted to have the configurations $\pi h_{9/2} \otimes 7^-$ or $\pi h_{9/2} \otimes 6^-$. Similarly, the $23/2^+$ state at 2186 keV could have the configuration $\pi h_{9/2} \otimes 7^-$ with maximum alignment, although the transition to the $21/2^+$ state is missing. The $27/2^+$ state at 2349 keV is suggested to have the configuration $\pi h_{9/2} \otimes 10^-$. There is no good candidate for the $25/2^+$ state ($\pi h_{9/2} \otimes 9^-$). If it is isomeric as in ^{209}Fr [13], it will remain unobserved in RDT experiments such as the present one. Finally, the $(29/2^+)$ J_{MAX} state at 2645 keV could originate from the $\pi h_{9/2} \otimes 11^-$ configuration.

The $1/2^+$ state has been identified and assigned as originating from a proton-hole in the $s_{1/2}$ shell. The corresponding state has been observed in odd-mass bismuth isotopes. In ^{205}Bi this $1/2^+$ state de-excites by a hindered $M2$ transition to a $5/2^-$ state [41]. In ^{203}Bi a competing $E3$ transition to a $7/2^-$ state has additionally been observed [41]. In ^{201}Bi and ^{199}Bi these two states lie above the $1/2^+$ state, and the $1/2^+$ state (with a half-life of tens of minutes) decays mainly by electron capture but also de-excites by a strongly hindered $M4$ transition to the $9/2^-$ ground state. In the present work, the $5/2^-$ state is assigned to belong to the $\pi h_{9/2} \otimes 2^+$ multiplet as in the isotopes ^{199}Bi to ^{205}Bi, but, unlike in the bismuth nuclei, the $7/2^-$ level

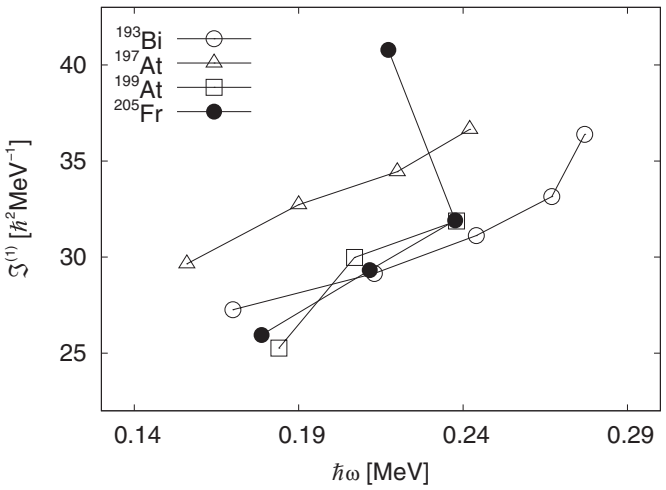

FIG. 10. Experimental kinematic moments of inertia of the rotational band feeding the $13/2^+$ isomer in ^{205}Fr compared with neighboring oblate deformed nuclei. The data for the astatine nuclei are taken from Ref. [37] and the bismuth data from Ref. [52].

TABLE II. The proposed configurations for some of the states in ^{205}Fr.

	E_{state} (keV)	Configuration
$9/2^-$	0	$\pi h_{9/2} \otimes 0^+$
$13/2^-$	517	$\pi h_{9/2} \otimes 2^+$
$17/2^-$	1097	$\pi h_{9/2} \otimes 4^+$
$21/2^-$	1762	$\pi h_{9/2} \otimes 6^+$
$23/2^-$	2037	$\pi (h_{9/2})^2 f_{7/2}$
$25/2^-$	2481	$\pi (h_{9/2})^5_{\text{MAX}}$ or $\pi (h_{9/2})^3 \otimes 2^+$
$27/2^-$	2643	$\pi (h_{9/2})^4 f_{7/2}$ or $\pi (h_{9/2})^2 f_{7/2} \otimes 2^+$
$13/2^+$	544	$\pi i_{13/2}$
$17/2^+$	1589	$\pi h_{9/2} \otimes 5^-$
$23/2^+$	2186	$\pi h_{9/2} \otimes 7^-$
$27/2^+$	2349	$\pi h_{9/2} \otimes 10^-$
$29/2^+$	2645	$\pi h_{9/2} \otimes 11^-$
$1/2^+$	$444 + \Delta$	$\pi (s_{1/2})^{-1}$
$7/2^-$	209	$\pi f_{7/2}$
$5/2^-$	444	$\pi h_{9/2} \otimes 2^+$

lies further away from the $5/2^-$ state, which indicates that it is not part of the multiplet. It is, therefore, assumed to originate from the odd proton on the $f_{7/2}$ shell as in the lighter bismuth and astatine nuclei [19,22]. Similarly to the behavior in the bismuth nuclei, the $1/2^+$ state in ^{205}Fr continues the rising trend in level energy when approaching the closed neutron shell. This is a characteristic feature of the intruder states involving proton excitations across the $Z = 82$ shell gap.

Finally, no additional higher-spin isomers, as reported in the heavier odd-mass francium nuclei, were observed in the present study. If such isomers exist in ^{205}Fr, they would need to be as fast as to decay inside the RITU separator but as slow as not to be seen by the JUROGAM array (Table II).

V. CONCLUSIONS

The nucleus ^{205}Fr has been studied using both in-beam γ-ray and delayed γ-ray and electron spectroscopy. We present results of the de-excitation of the $13/2^+$ isomer, with a weakly deformed band built on top of the isomer. A series of transitions to the $9/2^-$ ground state have also been observed. This result indicates that the ground-state band is still dominated by spherical structures in ^{205}Fr and pushes the onset of ground-state deformation in francium nuclei further toward the neutron mid-shell. Using highly selective electron-γ coincidence methods, the $1/2^+$ isomer was observed and it continues the tendency of a rising level energy, when approaching the closed neutron shell, as expected when comparing with odd-mass bismuth isotopes. The systematic study of the odd-mass francium isotopes would highly benefit from a deeper examination of the properties of ^{207}Fr. Certainly a continued, although challenging, search toward the proton drip line in both radon and francium nuclei would present data of high interest.

ACKNOWLEDGMENTS

This work has been supported through EURONS (European Commission contract no. RII3-CT-2004-506065) and by the Academy of Finland under the Finnish Centre of Excellence Programme 2006-2011 (Nuclear and Accelerator Based Physics contract no. 213503). The authors also thank the UK/France (STFC/IN2P3) detector Loan Pool and GAMMAPOOL European Spectroscopy Resource for the loan of the detectors for the JUROGAM array. Support has also been provided by the UK Engineering and Physical Sciences Research Council. U.J. acknowledges support from the Finnish Academy of Science and Letters; Vilho, Yrjö and Kalle Väisälä Foundation.

[1] R. Julin, K. Helariutta, and M. Muikku, J. Phys. G **27**, R109 (2001).
[2] A. M. Oros, K. Heyde, C. De Coster, B. Decroix, R. Wyss, B. R. Barrett, and P. Navratil, Nucl. Phys. A **645**, 107 (1999).
[3] K. Helariutta *et al.*, Eur. Phys. J. A **6**, 289 (1999).
[4] T. E. Cocolios *et al.*, Phys. Rev. Lett. **106**, 052503 (2011).
[5] G. D. Dracoulis, G. J. Lane, A. P. Byrne, P. M. Davidson, T. Kibédi, P. H. Nieminen, H. Watanabe, A. N. Wilson, H. L. Liu, and F. R. Xu, Phys. Rev. C **80**, 054320 (2009).
[6] A. R. Poletti, A. P. Byrne, G. D. Dracoulis, T. Kibédi, and P. M. Davidson, Nucl. Phys. A **756**, 83 (2005).
[7] W. J. Triggs, A. R. Poletti, G. D. Dracoulis, C. Fahlander, and A. P. Byrne, Nucl. Phys. A **395**, 274 (1983).
[8] D. Horn, C. Baktash, and C. J. Lister, Phys. Rev. C **24**, 2136 (1981).
[9] D. J. Dobson *et al.*, Phys. Rev. C **66**, 064321 (2002).
[10] R. B. E. Taylor *et al.*, Phys. Rev. C **59**, 673 (1999).
[11] A. N. Andreyev *et al.*, Phys. Rev. C **74**, 064303 (2006).
[12] H. Kettunen *et al.*, Phys. Rev. C **63**, 044315 (2001).
[13] G. D. Dracoulis, P. M. Davidson, G. J. Lane, A. P. Byrne, T. Kibédi, P. Nieminen, H. Watanabe, and A. N. Wilson, Phys. Rev. C **79**, 054313 (2009).
[14] A. P. Byrne, G. D. Dracoulis, C. Fahlander, H. Hubel, A. R. Poletti, A. E. Stuchbery, J. Gerl, R. F. Davie, and S. J. Poletti, Nucl. Phys. A **448**, 137 (1986).
[15] D. J. Hartley *et al.*, Phys. Rev. C **78**, 054319 (2008).
[16] R. A. Braga, W. R. Western, J. L. Wood, R. W. Fink, R. Stone, C. R. Bingham, and L. L. Riedinger, Nucl. Phys. A **349**, 61 (1980).
[17] A. N. Andreyev *et al.*, Phys. Rev. C **69**, 054308 (2004).
[18] K. Andgren *et al.*, Phys. Rev. C **78**, 044328 (2008).
[19] H. Kettunen *et al.*, Eur. Phys. J. A **16**, 457 (2003).
[20] J. Uusitalo *et al.*, Phys. Rev. C **71**, 024306 (2005).
[21] K. Dybdal, T. Chapuran, D. B. Fossan, W. F. Piel Jr., D. Horn, and E. K. Warburton, Phys. Rev. C **28**, 1171 (1983).
[22] H. Kettunen *et al.*, Eur. Phys. J. A **17**, 537 (2003).
[23] C. W. Beausang *et al.*, Nucl. Instrum. Methods A **313**, 37 (1992).
[24] C. Rossi Alvarez, Nucl. Phys. News **3**, 10 (1993).
[25] M. Leino *et al.*, Nucl. Instrum. Methods B **99**, 653 (1995).
[26] R. D. Page *et al.*, Nucl. Instrum. Methods B **204**, 634 (2003).
[27] I. H. Lazarus *et al.*, IEEE Trans. Nucl. Sci. **48**, 567 (2001).
[28] E. S. Paul *et al.*, Phys. Rev. C **51**, 78 (1995).
[29] P. Rahkila, Nucl. Instrum. Methods A **595**, 637 (2008).
[30] D. C. Radford, Nucl. Instrum. Methods A **361**, 297 (1995).

[31] D. C. Radford, Nucl. Instrum. Methods A **361**, 306 (1995).
[32] A. Y. Deo *et al.*, Phys. Rev. C **81**, 024322 (2010).
[33] H. De Witte *et al.*, Eur. Phys. J. A **23**, 243 (2005).
[34] A. N. Andreyev *et al.*, Nucl. Instrum. Methods A **533**, 422 (2004).
[35] T. Kibédi, T. W. Burrows, M. B. Trzhaskovskaya, P. M. Davidson, and C. W. Nestor Jr., Nucl. Instrum. Methods A **589**, 202 (2008).
[36] F. G. Kondev, Nucl. Data Sheets **108**, 365 (2007).
[37] U. Jakobsson *et al.*, Phys. Rev. C **82**, 044302 (2010).
[38] M. Huyse, P. Decrock, P. Dendooven, G. Reusen, P. Van Duppen, and J. Wauters, Phys. Rev. C **46**, 1209 (1992).
[39] P. Van Duppen, E. Coenen, K. Deneffe, M. Huyse, and J. L. Wood, Phys. Rev. C **35**, 1861 (1987).
[40] K.-H. Schmidt, Eur. Phys. J. A **8**, 141 (2000).
[41] T. Lönnroth, Z. Phys. A **307**, 175 (1982).
[42] S. Agostinelli *et al.*, Nucl. Instrum. Methods A **506**, 250 (2003).
[43] B. Singh, Nucl. Data Sheets **108**, 79 (2007).
[44] M. Nyman *et al.* (submitted to Phys. Rev. C).
[45] J. R. Novak *et al.*, Phys. Rev. C **59**, R2989 (1999).
[46] C. M. Baglin, Nucl. Data Sheets **109**, 2033 (2008).
[47] B. Singh and A. Farhan, Nucl. Data Sheets **107**, 1923 (2006).
[48] D. Abriola and A. A. Sonzogni, Nucl. Data Sheets **111**, 1 (2010).
[49] T. Yamazaki, Nucl. Data, Sect. A **3**, 1 (1967).
[50] R. F. Davie, A. R. Poletti, G. D. Dracoulis, A. P. Byrne, and C. Fahlander, Nucl. Phys. A **430**, 454 (1984).
[51] A. R. Poletti, T. P. Sjoreen, D. B. Fossan, U. Garg, A. Neskakis, and E. K. Warburton, Phys. Rev. C **20**, 1768 (1979).
[52] P. Nieminen *et al.*, Phys. Rev. C **69**, 064326 (2004).
[53] F. G. Kondev and S. Lalkovski, Nucl. Data Sheets **108**, 1471 (2007).
[54] B. Fant, T. Weckström, H. C. Jain, L. O. Norlin, K.-G. Rensfelt, P. Carle, and U. Rosengård, Nucl. Phys. A **475**, 338 (1987).
[55] N. Bijnens *et al.*, Phys. Rev. C **58**, 754 (1998).

Appendix C

Spectroscopy of the proton drip-line nucleus ^{203}Fr

Spectroscopy of the proton drip-line nucleus ^{203}Fr

U. Jakobsson,[1,*] S. Juutinen,[1] J. Uusitalo,[1] M. Leino,[1] K. Auranen,[1] T. Enqvist,[2] P. T. Greenlees,[1] K. Hauschild,[3] P. Jones,[1,†] R. Julin,[1] S. Ketelhut,[1,‡] P. Kuusiniemi,[2] M. Nyman,[1,§] P. Peura,[1] P. Rahkila,[1] P. Ruotsalainen,[1] J. Sarén,[1] C. Scholey,[1] and J. Sorri[1]

[1]*Department of Physics, University of Jyväskylä, P.O. Box 35, FI-40014, Jyväskylä, Finland*

[2]*Oulu Southern Institute and Department of Physics, University of Oulu, Finland*

[3]*CSNSM, IN2P3-CNRS, F-91405 Orsay Campus, France*

(Received 21 January 2013; revised manuscript received 12 February 2013; published 17 May 2013)

The nucleus ^{203}Fr has been studied through γ-ray and electron spectroscopy, using the recoil-decay tagging technique. A $13/2^+$ state, with a half-life of 0.37(5) μs, has been observed in ^{203}Fr. Both the α-decay branch and the internal de-excitation of the $1/2^+$ isomer in ^{203}Fr have been studied. Furthermore, the corresponding $1/2^+$ state, with a half-life of 0.31(8) s, has been found in ^{199}At. In addition, transitions feeding the $9/2^-$ ground state of ^{203}Fr have been identified. The observed level pattern suggests that the ground state is still spherical.

DOI: 10.1103/PhysRevC.87.054320 PACS number(s): 23.20.Lv, 23.35.+g, 27.80.+w, 29.30.Kv

I. INTRODUCTION

Coexisting spherical, oblate and prolate shapes have been found to exist in neutron-deficient nuclei around lead up to $Z = 84$ (see Ref. [1] and references therein). The transition from spherical to deformed shapes, when approaching the neutron midshell, is believed to be caused by the increasing number of neutron holes coupled to the particle-hole excitations across the proton shell gap.

An onset of oblate ground-state deformation, associated with the 2p-2h excitation across the proton shell gap, has been reported to occur in even-mass polonium nuclei with $N \leqslant 114$ [2–4]. Low-lying excited states in neutron-deficient even-even radon nuclei have been studied down to ^{198}Rn [5–10]. An increase in collectivity for these states, caused by the increasing number of neutron-hole pairs has been observed, and contributions from the 2p-2h excitation have been suggested as well. α-decay properties obtained for ^{196}Rn [11] suggest an onset of oblate ground-state deformation in ^{196}Rn. The chain of neutron-deficient odd-mass francium nuclei is less well known than the radon isotopes, with ^{205}Fr being the lightest isotope with in-beam studies reported to date [12–15]. No onset of ground-state deformation has been observed in these nuclei, although we reported an increase of collectivity for the states feeding the ground state in ^{205}Fr [15].

Similarly to the 2p-2h excitation in even-even lead nuclei, the $1/2^+$ state, well known throughout the neutron-deficient odd-mass bismuth nuclei, is also associated with the intruder mechanism. The state comes down in energy with decreasing neutron number and becomes the ground state in ^{185}Bi [16]. Interesting features have been observed related to this state, such as very slow $M4$ transitions to the $9/2^-$ ground state [17]. In astatine nuclei the $1/2^+$ state is first observed in ^{197}At [18], decaying by α-particle emission, and becoming the ground state in ^{195}At [19]. Uusitalo *et al.* have previously observed the corresponding $1/2^+$ state in ^{203}Fr and ^{201}Fr through α-decay studies [20]. In ^{201}Fr the level lies at 146 keV, but in ^{203}Fr the level energy has not been established, as the corresponding state in the α-decay daughter ^{199}At has not yet been observed. The $1/2^+$ state, presumed to be oblate, is expected to become the ground state in ^{199}Fr [20].

Another state, characteristic of this region, is the $13/2^+$ state based on the odd proton excited to the $i_{13/2}$ orbital. Throughout the neutron-deficient odd-mass bismuth and astatine nuclei this state is better known than the $1/2^+$ state. For instance, when approaching the neutron midshell, the $13/2^+$ state becomes isomeric in ^{201}At [21], yrast in ^{199}At [22] and α decaying in ^{193}At [23]. In ^{199}At, ^{197}At [22], and ^{195}At [24] rotational bands, consistent with oblate deformation, have been observed to be built on top of the $13/2^+$ state. Among the odd-mass francium nuclei with $A < 213$, the $13/2^+$ state has so far only been observed in ^{205}Fr [15]. It is still non-yrast with a weakly deformed rotational band built on top of the isomer.

The present work investigates the possibility of shape coexistence in ^{203}Fr. Isomeric states involving the $\pi i_{13/2}$ and the $\pi s_{1/2}$ orbitals, respectively, are presented. An observation of the $1/2^+$ state in the α-decay daughter ^{199}At is reported as well. Prompt γ-ray transitions to the $9/2^-$ ground state have been observed and a level scheme for ^{203}Fr is presented. Additionally, a number of γ-ray transitions associated with the neighboring nucleus ^{204}Fr are presented.

II. EXPERIMENT

The experiment was performed at the Accelerator Laboratory at the Department of Physics of the University of Jyväskylä (JYFL), Finland. The ^{203}Fr nuclei were produced in the fusion-evaporation reaction ^{169}Tm(^{40}Ar, $6n$)^{203}Fr. The ^{40}Ar beam, provided by the K-130 cyclotron, was accelerated

*ulrika.jakobsson@jyu.fi

†Present address: iThemba Laboratory for Accelerator Based Sciences, P. O. Box 722, 7129 Somerset West, South Africa.

‡Present address: TRIUMF, Westbrook Mall, Vancouver, BC, V6T 2A3, Canada.

§Present address: European Commission, Joint Research Centre, Institute for Reference Materials and Measurements (IRMM), Retieseweg 111, B-2440 Geel, Belgium.

to an energy of 205 MeV with an average beam current of 13 particle-nA (pnA), during an irradiation time of 68 h in total. The self-supporting ^{169}Tm target had a thickness of 410 μg/cm^2. The ^{203}Fr nuclei were produced with a cross section of 4 μb.

The JUROGAM Ge-detector array was used to detect prompt γ rays at the target position. The array consisted of 43 Compton-suppressed high-purity germanium (HPGe) detectors of EUROGAM phase one [25] and GASP [26] type. The recoiling fusion-evaporation products were separated from beam particles and other unwanted reaction products by the gas-filled recoil separator RITU [27] and transported to the GREAT spectrometer [28] at its focal plane. When arriving in GREAT, the recoils passed through a multiwire proportional counter (MWPC) and were finally implanted into a 300-μm-thick double-sided silicon strip detector (DSSD), which has 4800 pixels in total. The horizontal strips of the DSSD were set to measure α-particle energies and the vertical strips to measure conversion-electron energies, by adjusting the gain ranges of the amplifiers. A clover germanium and a planar germanium detector close to the DSSD were used to detect delayed γ rays, and a silicon PIN-detector array, situated upstream in a box arrangement at the edges of the DSSD, was used for detecting conversion electrons. The PIN detectors and the vertical strips of the DSSD were calibrated using a ^{133}Ba source. All data channels were recorded synchronously using the triggerless total data readout (TDR) [29] data acquisition system, which gives each event an absolute time stamp with a time resolution of 10 ns.

III. RESULTS

The recoil-decay tagging (RDT) technique [30–32] was used in the experiment and the measurement data were processed using the GRAIN [33] and RADWARE [34,35] software packages. The recoiling fusion-evaporation products were selected by their time of flight between the MWPC and the DSSD and their energy loss in the MWPC. Furthermore, the different isotopes were identified by linking the recoils with their subsequent α decays in the DSSD, using spatial and temporal correlations. An α-decay branch close to 100% and a half-life of 0.55(1) s for the $9/2^-$ ground state [36] allowed for an effective identification of the ^{203}Fr recoils. A maximum correlation time of 1.5 s was used between the implantation of the recoil and its subsequent α decay. The energy spectrum of MWPC-vetoed α particles obtained from the ^{40}Ar + ^{169}Tm reaction is shown in Fig. 1. Conversion electrons and γ rays belonging to ^{203}Fr were identified based on their time correlation with the α-tagged recoil observed in the DSSD.

The energy spectra of delayed γ rays and electrons shown in Fig. 2 represent events detected with the GREAT clover detector and the PIN-detector array, respectively, tagged with the ^{203}Fr ground-state α decay. A peak with an energy of 426(1) keV is pronounced in the γ-ray spectrum. The two peaks in the electron spectrum represent the internal K- and $L + M + \ldots$-conversion peaks of this 426-keV γ-ray transition, respectively. The extracted $K/(L + M + \ldots)$ ratio of 3.3(4) indicates that the transition is of $M2$ character.

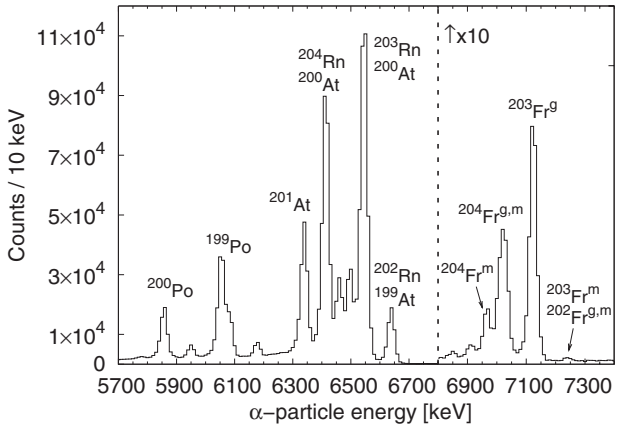

FIG. 1. Energy spectrum of MWPC-vetoed α particles obtained from the ^{40}Ar + ^{169}Tm reaction. For the α-particle energies of the francium nuclei, see, for example, Refs. [20,47].

The corresponding theoretical value is 3.1(3) as extracted from Ref. [37]. This value differs significantly from the corresponding values of 4.2(6) and 1.6(1) extracted for $M1$ and $E2$ transitions, respectively. By studying the time differences between the implantation of the ^{203}Fr recoil and the detection of the subsequent electrons (see inset of Fig. 2), a half-life of 0.37(5) μs was obtained, resulting in a transition strength of 0.10(2) W.u. for the $M2$ transition. The result is comparable with known values of $M2$ transitions depopulating the $13/2^+$ states directly to the $9/2^-$ ground states in neighboring odd-mass nuclei (for example 0.17(4) W.u. in ^{205}Fr [15], 0.182(22) W.u. in ^{201}At [38], 0.16(5) W.u. in ^{199}At [22], and 0.086(13) W.u. in ^{197}At [39]). Based on these observations the spin and parity of the isomer were assigned as $13/2^+$.

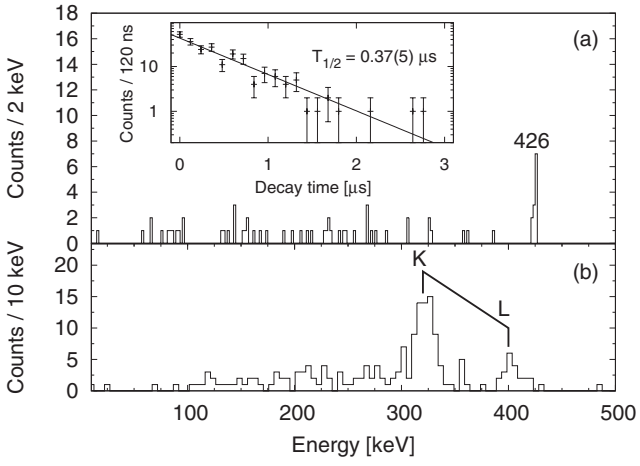

FIG. 2. Energy spectrum of delayed (a) γ rays detected with the GREAT clover detector and (b) conversion electrons detected with the GREAT PIN-detector array, tagged with the ^{203}Fr ground-state α decay. A maximum correlation time of 1.2 μs was set between the recoil implantation and the detection of an isomeric transition. The inset presents the distribution of time differences between the recoil implantation and the detection of the electron with the PIN-detector array. The half-life was obtained through a least squares fit to the data.

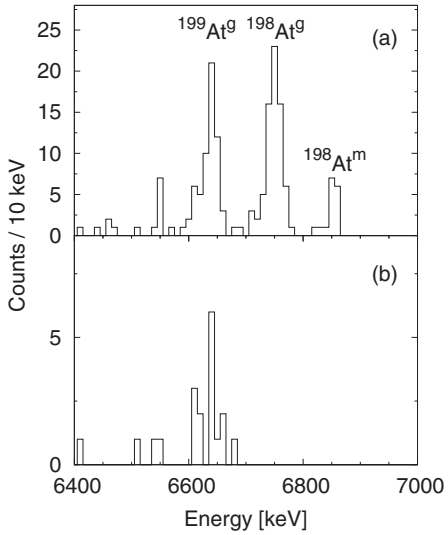

FIG. 3. (a) Energy spectrum of α particles from the decay of the daughter astatine nuclei following the α decay of the francium nuclei in Fig. 1 with the energy of ~7240 keV. (b) Energy spectrum of the α particles in (a) including the requirement of a conversion electron temporally between the two α decays in the same pixel of the DSSD. The ^{198}At events are filtered out. A maximum correlation time of 21 s has been used between the recoil implantation and the α decay of the daughter astatine nucleus.

Eight events from the α decay of the $1/2^+$ state in ^{203}Fr to the $1/2^+$ state in the daughter nucleus ^{199}At, with an α-particle energy of 7227(8) keV, have been reported by Uusitalo *et al.* [20]. Figure 3(a) presents the energy spectrum of the events from the α decay of the daughter astatine nuclei following the α decay of the parent francium nuclei in Fig. 1 with an energy of ~7240 keV. These events include the ones from the α decay of the $1/2^+$ isomer with the energy reported by Uusitalo *et al.* Three peaks are clearly visible, one of which represents the ground-state α decay of ^{199}At. The two other peaks originate from the α decays of ^{198}At following the α decays of the 3^+ ground state and the isomeric 10^- state, with the α-particle energies of 7241(8) keV and 7235(8) keV, respectively, in ^{202}Fr [20]. The half-life of the $1/2^+$ isomer was extracted by requiring the ground-state α decay of ^{199}At subsequent to the α decay of the isomer in ^{203}Fr. Using the maximum-likelihood method [40] for the time between the recoil implantation and the isomeric α decay, a half-life of 41^{+5}_{-4} ms was obtained. This value agrees well with the result of 60^{+30}_{-20} ms reported by Uusitalo *et al.* [20]. As the $1/2^+$ state in ^{203}Fr probably decays to the corresponding $1/2^+$ state in ^{199}At, and events from the $9/2^-$ ground-state α decay of ^{199}At are visible in Fig. 3(a), there must be an internal deexcitation branch depopulating the $1/2^+$ state in ^{199}At to the $9/2^-$ ground state. This branch will be discussed in detail later on in this section, but at this point it is justified to assume that there will be internal conversion contributing to the depopulation of the $1/2^+$ isomer to the $9/2^-$ ground state in ^{199}At, as the $1/2^+$ state will lie relatively low in energy. Figure 3(b) presents the energy spectrum of the events from the daughter α decays as in Fig. 3(a) but with a conversion electron required temporally between the two α decays in the same pixel of the DSSD. The events from the two

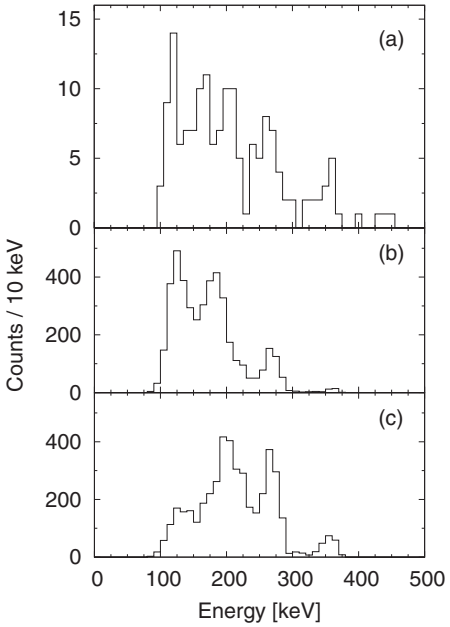

FIG. 4. (a) Energy spectrum of electrons detected in the DSSD temporally between the implantation of the ^{203}Fr recoil and the subsequent $9/2^-$ ground-state α decay. A correlation time of 150 ms was used between the recoil implantation and the conversion electron. (b) Energy spectrum of electrons from a GEANT4 simulation performed based on our interpretation of a three-step deexcitation and (c) for comparison a two-step deexcitation. See text for details.

decay chains of ^{202}Fr are filtered out, indicating that if there are any conversion electrons to be observed associated with the α decays of ^{202}Fr, they are below the detection threshold of the GREAT DSSD. Based on this observation, from the α decays in the peak consisting of events from ^{203}Fr and ^{202}Fr in Fig. 1, only the ones were chosen with a subsequent conversion electron observed. This α-electron pair gave a slight increase in statistics compared to using the α-α pair. From these events, an α-particle energy of 7246(5) keV was extracted for the decay of the $1/2^+$ state in ^{203}Fr.

Figure 4(a) presents the energy spectrum of the electrons detected in the DSSD, temporally between the implantation of the ^{203}Fr recoil and the subsequent $9/2^-$ ground-state α decay. The structure of the electron spectrum strongly resembles that obtained for the neighboring nucleus ^{205}Fr, associated with the depopulation of the $1/2^+$ isomer by an $M2$ transition to a $5/2^-$ state followed by a cascade consisting of two $M1$ transitions, one to a $7/2^-$ state followed by one to the $9/2^-$ ground state (see Ref. [15]). The FWHM is approximately 12 keV for the electron peaks in Fig. 4(a). Therefore the L- and higher-shell conversion electrons will not be separated, and a sum peak representing all these events should situate roughly 12–13 keV below the corresponding transition energy. In this special case, however, the internal conversion takes place inside the DSSD. Therefore, the energy deposited by the Auger electrons and low-energy x rays, released in the internal conversion process, sums up with the energy deposit of the conversion electron, giving an additional ~10 keV to the total energy deposit. As a result, the electron peak representing emission from the L + M (+ higher) shells is found close to

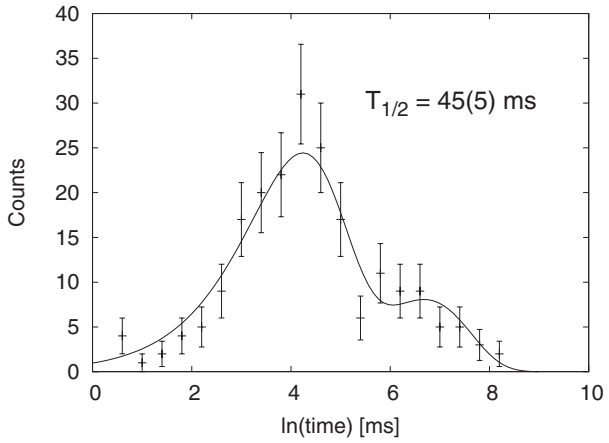

FIG. 5. Distribution of time differences between the implantation of the ^{203}Fr recoil in the DSSD and the subsequent electron detected in the same pixel before the $9/2^-$ ground-state α decay. Note the component consisting of random correlations on the right-hand side of the studied activity. See Ref. [48] for details on the method of using a logarithmic time scale.

2–3 keV below the corresponding transition energy. See our previous work on ^{205}Fr for a more detailed description on the analysis methods related to the electron spectra [15]. The distribution of time differences, see Fig. 5, obtained between the implantation of the ^{203}Fr recoil and the detection of the subsequent electrons, produces a half-life of 45(5) ms for the isomer. This value is in agreement with the value of 41^{+5}_{-4} ms obtained from the α-decay branch of the $1/2^+$ isomer, confirming that the electrons in Fig. 4(a) indeed originate from the branch that depopulates the $1/2^+$ isomer to the $9/2^-$ ground state. The half-life of the $1/2^+$ state is furthermore obtained as the weighted average 43(4) ms. Figure 6 presents the energy spectrum of γ rays detected with the GREAT clover and planar detector, and observed in coincidence with the electrons in Fig. 4(a). A 162-keV γ-ray peak is weakly visible alongside the francium x-ray peaks. Assuming this transition is, similarly as in ^{205}Fr, one of the $M1$ transitions, the structure

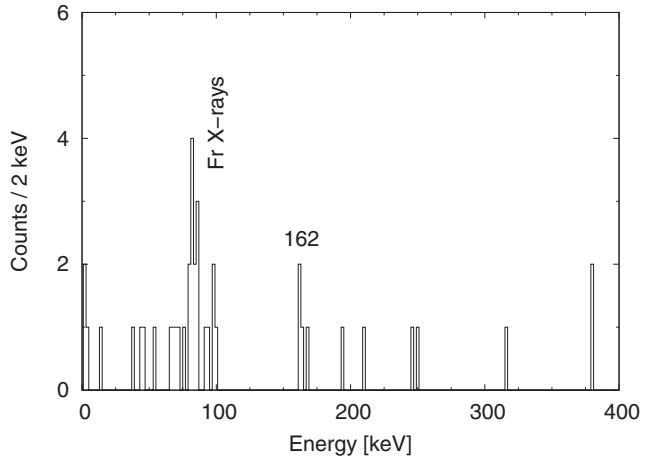

FIG. 6. Energy spectrum of γ rays detected with the GREAT clover detector and planar detector, and in coincidence with the electrons in Fig. 4(a).

of the electron spectrum can be explained as originating from a ∼20-keV $M2$ transition from the $1/2^+$ state followed by a cascade of a ∼175-keV $M1$ transition and the 162-keV transition. The 162-keV transition is visible in the prompt data and thus it is set to proceed to the $9/2^-$ ground state.

An energy spectrum of electrons, from the above-presented scenario, simulated using the GEANT4 package [41,42] is shown in Fig. 4(b). The similar shape of Fig. 4(b) and Fig. 4(a) supports our interpretation of the electron spectrum as representing a three-step cascade. To further confirm this interpretation, a simulation was made [see Fig. 4(c)], representing the alternative feasible scenario, where the $1/2^+$ isomer is depopulated solely by an $E3$ transition followed by the 162-keV transition to the $9/2^-$ ground state. Comparing the electron spectra from the two simulated scenarios with that in Fig. 4(a), it is likely that the electron spectrum in Fig. 4(a) actually results from the depopulation of the $1/2^+$ isomer being a combination of both scenarios. The fact that a γ-ray peak representing the ∼175-keV transition is not visible in Fig. 6 may additionally support the interpretation of a competing $E3$ transition depopulating the $1/2^+$ state to the $7/2^-$ state. Furthermore, while the 360-keV electron peak, representing the sum of the L + M + . . .-conversions of the transitions, is visible in all three spectra, it is less evident in Fig. 4(b). This could as well indicate the existence of a possible competing $E3$ branch in Fig. 4(a). Assuming a similar strength for this transition as in neighboring odd-mass nuclei [24,38,43] the $E3$ branch could be as high as 70%. Although the branching ratio cannot be determined to an acceptable precision due to low statistics, we suggest that the $E3$ branch is significant. Based on the α-particle and conversion-electron yields, a branching ratio of 20(4)% for the α decay of the $1/2^+$ isomer was obtained. Additionally, a reduced α-emission width of 51 keV was extracted for this decay using the method developed by Rasmussen [44], resulting in a hindrance factor of 1.1 as compared with the ground-state α decay of ^{202}Rn [45]. This is a sign of a favored α decay between states of equal spin and parity. Furthermore, a transition strength of $\sim 0.8 \times 10^{-4}$ W.u. was obtained for the ∼20-keV $M2$ transition assuming no competing $E3$ branch from the $1/2^+$ isomer. This result is in agreement with the strength of $3.5(2)\times 10^{-4}$ W.u. reported for the corresponding $M2$ transition in ^{205}Fr [15]. Moreover, the uncertainty of the branching ratio of the competing $E3$ transition does not affect the transition strength of the $M2$ transition to such an extent that it would create inconsistency with the assignment of an $M2$ multipolarity. Figure 7 presents a detailed view of the decay scheme. As the ∼175-keV γ-ray transition was not observed, the level energy of the $5/2^-$ state is set as tentative.

Figure 8(a) presents the energy spectrum of electrons following the α decay of the $1/2^+$ isomer of ^{203}Fr in the same DSSD pixel, and therefore representing the deexcitation of the $1/2^+$ state to the $9/2^-$ ground state in the daughter nucleus ^{199}At. The structure of the spectrum clearly differs from the one in Fig. 4(a) as there is a smaller number of peaks visible. Based on this observation, the assumption can be made that the depopulating cascade consists of less transitions than in ^{203}Fr, consisting for example of an $E3$ transition to a $7/2^-$ state followed by an $M1$ transition to the $9/2^-$ ground state.

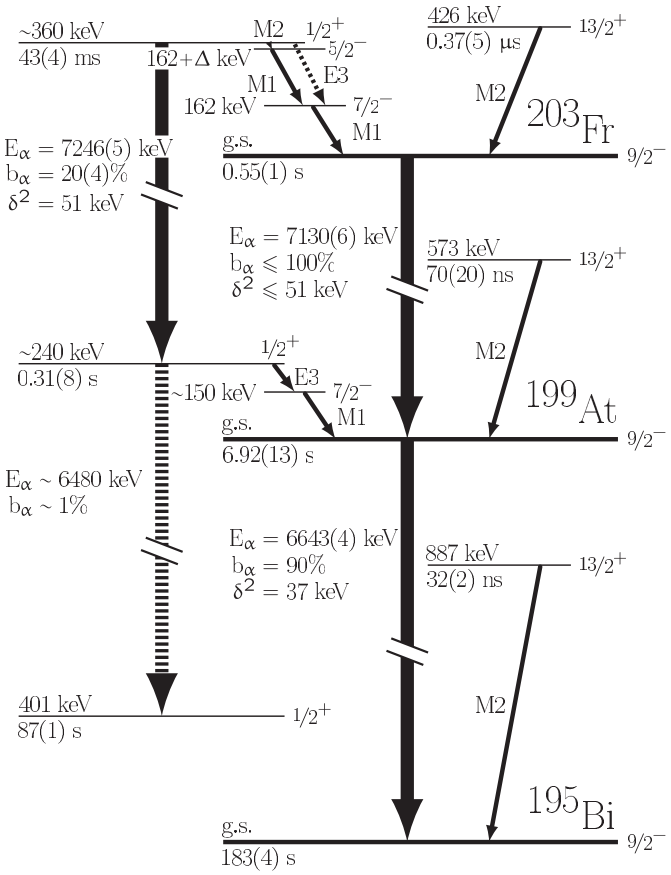

FIG. 7. The decay schemes of the $1/2^+$ state in ^{203}Fr and ^{199}At. For the ^{195}Bi data, see Refs. [51–53], for the ^{199}At data see the present work and Refs. [22,43,54] and for the ground-state α decay of ^{203}Fr see Refs. [20,36]. The α decay of the $1/2^+$ state in ^{199}At is presented with a dashed line as it has not been observed. $\Delta \sim 175$ keV, see text for details.

Figure 9 presents the distribution of time differences between the α decay of the $1/2^+$ state in ^{203}Fr and the subsequent electrons. A half-life of 0.31(8) s was obtained. Although no γ-ray transitions were seen in coincidence with the electrons in Fig. 8, both the astatine K- (four events) and L- (one event) x-ray peaks were observed with the GREAT clover and planar detector, indicating that one of the transitions in the cascade depopulating the $1/2^+$ isomer has to be above the energy threshold to produce a K-conversion electron. To understand the structure of the electron spectrum, the 150-keV peak may represent the L conversion of one of the two proposed transitions, and the 240-keV peak the sum of the L conversions of the two transitions. Based on these observations, the energy of the other transition would be ~90 keV. Furthermore, the intensity ratio of the two electron peaks in Fig. 8(a) supports our interpretation of the ~90-keV transition being of $E3$ character. Consequently, the ~150-keV transition would be of $M1$ character. Figure 8(b) presents an energy spectrum from a GEANT4 simulation of electrons from a cascade consisting of a 90-keV $E3$ and a 150-keV $M1$ transition. In Fig. 8(c) these transitions are in reversed order, i.e. a 150-keV $E3$ transition depopulating the $1/2^+$ isomer. Comparing the peak intensities in the two simulated spectra, it is evident that the

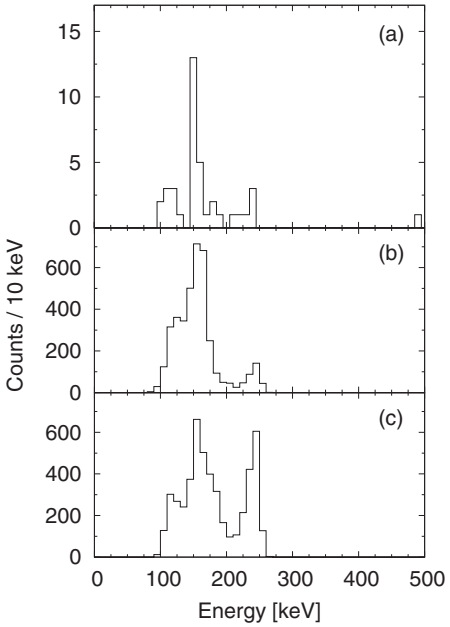

FIG. 8. (a) Energy spectrum of electrons detected in the DSSD following the α decay of the $1/2^+$ state in ^{203}Fr. A correlation time of 900 ms was used between the α decay and the subsequent electron. (b) Energy spectrum of electrons from a GEANT4 simulation performed based on our interpretation of a 90-keV $E3$ transition followed by a 150-keV $M1$ transition to the $9/2^-$ ground state. For comparison, an energy spectrum simulated for the reversed scenario, in which a 150-keV $E3$ transition is followed by a 90-keV $M1$ transition to the ground state, is shown in (c). See text for details.

results from the simulations support our interpretation of the cascade. A transition strength of ~0.09 W.u. was derived for the ~90-keV $E3$ transition, which is comparable with the strengths extracted for the corresponding transitions in ^{191}Bi and ^{195}At [24], respectively.

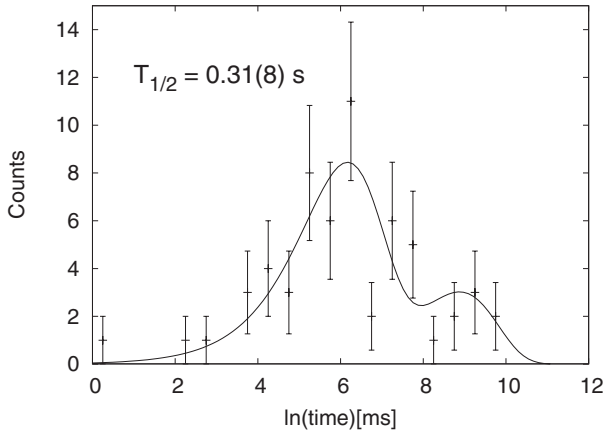

FIG. 9. Distribution of time differences between the α decay of the $1/2^+$ state in ^{203}Fr to the $1/2^+$ state in ^{199}At in the DSSD, and the subsequent electron detected in the same pixel. A maximum correlation time of 150 ms was used between the recoil implantation and the α decay. Note the component consisting of random correlations on the right-hand side of the studied activity. See Ref. [48] for details on the method of using a logarithmic time scale.

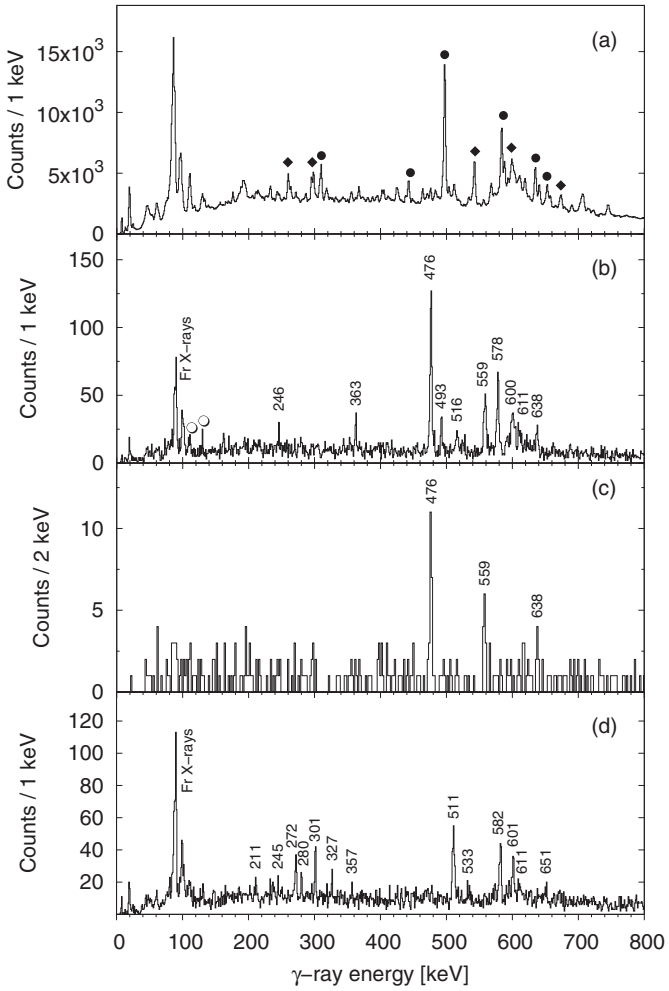

FIG. 10. Energy spectrum of prompt γ rays from the ^{40}Ar + ^{169}Tm reaction, detected with the JUROGAM array. (a) γ rays associated with any recoil detected in the GREAT DSSD. Peaks belonging to the dominant reaction channels ^{203}Rn and ^{204}Rn are marked with circles and diamonds, respectively. (b) γ rays tagged with the ^{203}Fr ground-state α decay. Peaks belonging to the contaminating ^{169}Tm [55] recoils are indicated by circles. (c) γ rays in the sum gate on the 476-, 559-, and 638-keV transitions. (d) γ rays associated with ^{204}Fr.

It is now worth noting that the level energies of the $1/2^+$ state in ^{203}Fr and ^{199}At fit well with the extracted α-particle energy from the decay of the $1/2^+$ state in ^{203}Fr, see Fig. 7. Additionally, by assuming a similar reduced width for the α decay of the $1/2^+$ state in ^{199}At as for the $9/2^-$ ground state, a branching ratio of $\sim$1% is predicted for the α decay. No events were observed from the α decay of the $1/2^+$ state in ^{199}At in the present data, as can be expected with such a low branching ratio combined with the low yield.

Figure 10(a) presents the energy spectrum of prompt γ rays detected with the JUROGAM array and associated with any fusion-evaporation recoil from the ^{40}Ar + ^{169}Tm reaction, detected in the GREAT DSSD. The strongest peaks belong to ^{203}Rn [46] and ^{204}Rn [9]. Prompt γ rays tagged with the ^{203}Fr ground-state α decay are presented in Fig. 10(b). The radon isotopes dominant in Fig. 10(a) are effectively filtered out. However, events from the Coulomb-excited ^{169}Tm target, indicated with open circles, still remain. The amount of statistics did only allow for a limited γ-γ coincidence analysis. However, three transitions with energies of 476-, 559-, and 638-keV were observed to be in coincidence. An energy spectrum of γ rays in coincidence with these three transitions is presented in Fig. 10(c). The transitions were sequenced according to the coincidence analysis and their intensities, with the 476-keV transition set as the lowest one, and each assigned an $E2$ multipolarity based on systematics in this region. The total population of the $13/2^+$ isomer was estimated by studying the yield of the depopulating $M2$ transition. This yield was then compared with the total intensity of the 476-keV transition. It was found that the total intensity of the 476-keV transition was too high for it to populate the $13/2^+$ state (and hence for the cascade to be built on top of this state) or the $1/2^+$ state. Therefore the cascade is assigned to be built on the $9/2^-$ ground state. Statistics did not allow for tagging with the electromagnetic transitions or α decays depopulating the $1/2^+$ or the $13/2^+$ isomers. The 246-, 363-, and 611-keV transitions are placed on the $13/2^+$ isomer based on intensity and energy sum relations, and in accordance with systematics. The 578-keV transition, prominent in Fig. 10(b) could not be associated with any of the other transitions in Fig. 10(b) and therefore remains unassigned. It could populate a higher-lying isomer or it could directly populate the $9/2^-$ ground state. The γ-ray transitions associated with ^{203}Fr [see Fig. 10(b)] are listed in Table I. See Fig. 11 for the level scheme.

α decays of the 3^+, 7^+, and 10^- states in ^{204}Fr [47] were observed in the experiment (see Fig. 1). The α-particle energies of 7013(5) keV and 7031(5) keV of the decays from the 10^- and 3^+ states, respectively, overlap, but the α-particle energy of 6969(5) keV from the decay of the 7^+ state is clearly distinguishable. The 10^- state is furthermore depopulated by a 275-keV $E3$ transition to the 7^+ state [15,47]. Using

TABLE I. The energies and relative intensities of prompt γ-ray transitions assigned to ^{203}Fr.

E_γ(keV)	I_γ(%)	I_i^π	I_f^π
161.9(4)	7(2)	$7/2^-$	$9/2^-$
245.5(4)[a]	7(2)	$(17/2^+)$	$(15/2^+)$
279.0(5)	6(2)		
344.2(6)	5(2)		
362.5(3)[a]	13(3)	$(15/2^+)$	$13/2^+$
367.8(3)	3(2)		
476.4(1)	100(6)	$13/2^-$	$9/2^-$
481.1(6)	7(3)		
492.5(3)	19(3)		
516.0(5)	13(4)		
558.6(2)	51(5)	$17/2^-$	$13/2^-$
578.1(2)	60(6)		
600.0(7)	24(9)		
603.5(9)	18(7)		
611.1(5)[a]	16(5)	$(17/2^+)$	$13/2^+$
637.7(3)[a]	18(4)	$(21/2^-)$	$17/2^-$

[a]The assignment of the γ-ray transition in the level scheme is tentative.

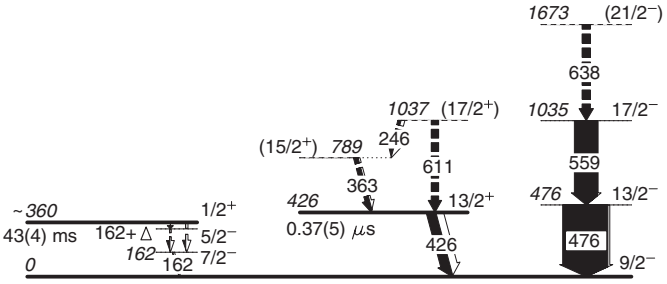

FIG. 11. The ^{203}Fr level scheme. Note that the intensities of the γ-ray transitions depopulating the $1/2^+$ isomer are not in scale. $\Delta \sim 175$ keV, see text and Fig. 7 for details. The black part of an arrow represents the γ-ray intensity of the transition and the white part the corresponding conversion-electron intensity.

the α decay of the 7^+ state for tagging, and requiring this 275-keV conversion electron temporally between the recoil implantation in the DSSD and the α decay in the same pixel, the half-lives of the 7^+ state and the 10^- state could be determined. By measuring the time differences between the conversion electron and the subsequent α decay a half-life of 2.6(3) s was obtained for the 7^+ state. This result is in full agreement with the half-life of 2.6(3) s reported by Huyse *et al.* [47]. Furthermore, by measuring the time differences between the recoil implantation and the subsequent conversion electron, a half-life of 1.65(15) s was obtained for the 10^- state. This result is slightly higher than that of approximately 1 s reported by Huyse *et al.* The method developed by Schmidt [48] was used to obtain the half-lives. Figure 10(d) presents the energy spectrum of prompt γ rays detected with the JUROGAM array and tagged with the α decays of the three states in ^{204}Fr. Statistics did not allow for an assignment of the transitions between the states.

IV. DISCUSSION

Both the $1/2^+$ state, based on a proton hole in the $s_{1/2}$ orbital, and the $13/2^+$ state, based on the odd proton in the $i_{13/2}$ orbital, are well known in the light odd-mass bismuth nuclei, see Fig. 12. The $13/2^+$ state lies quite constant in energy close to the $N = 126$ neutron shell closure, but comes down in energy when moving further toward the midshell. In the astatine nuclei the $13/2^+$ state is consistently lower in energy, but the down-sloping behavior is similar as in the bismuth nuclei. Furthermore, the state in the francium nuclei lies even lower in energy although no conclusions can yet be made of the systematics. In the astatine nuclei the proton-intruder $1/2^+$ state is only known in the lightest isotopes, and it becomes the ground state already in ^{195}At [19]. Based on systematics, it can be expected that the $1/2^+$ state becomes the ground state in ^{199}Fr as Uusitalo *et al.* [20] predict. The $7/2^-$ states observed in ^{203}Fr and ^{199}At are both suggested to originate from the odd proton in the $f_{7/2}$ orbital similarly as in ^{205}Fr [15]. This suggestion is reasonable, since the alternative $7/2^-$ state, originating from the $\pi h_{9/2} \otimes 2^+$ multiplet, should lie closer to the $13/2^-$ state. The level energy of the $5/2^-$ state remains tentative.

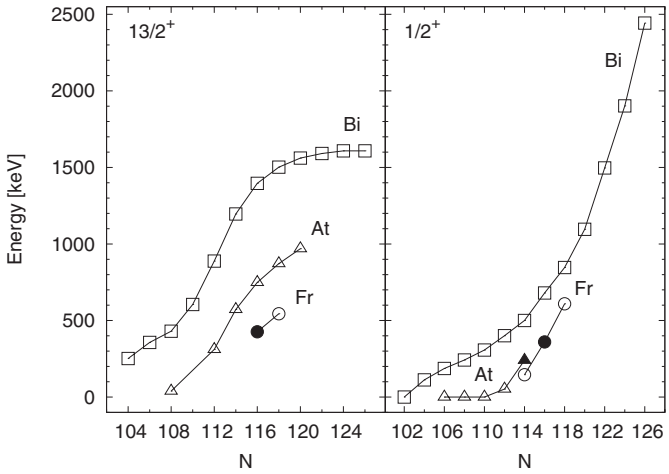

FIG. 12. Systematics of the $13/2^+$ state (left panel) and the $1/2^+$ state (right panel) in neutron-deficient odd-mass bismuth (squares), astatine (triangles), and francium (circles) nuclei. For the bismuth data see Refs. [16,56] and references therein, for the astatine data Refs. [18,19,21–23,39,49] and for the francium data Refs. [15,20]. ^{203}Fr has neutron number 116. The data points obtained from the present study are indicated with filled symbols.

The beginning of a possible rotational band was tentatively placed on top of the $13/2^+$ isomer. Comparing Fig. 10(b) with corresponding γ-ray spectra from neighboring odd-mass nuclei [15,22], it is evident that prominent γ-ray peaks, representing $M1$ transitions between the signature partners, a typical feature for a strongly coupled rotational band, are missing from Fig. 10(b). Furthermore, the intensity of the francium x-ray peaks relative to the intensity of the peak representing the γ-ray transition from the $13/2^-$ state to the $9/2^-$ ground state is significantly lower than in these neighboring odd-mass nuclei. The population of the $13/2^+$ state compared to the population of the ground state through the $13/2^-$ state state was estimated, and it is much lower in ^{203}Fr compared with these neighboring nuclei, see Table II. As the $13/2^+$ state becomes yrast in ^{203}Fr, it would be justified to expect that the population of this state would be relatively higher compared with the corresponding state in ^{205}Fr. Instead the population of the $13/2^+$ state is lower in ^{203}Fr than in ^{205}Fr. Furthermore, in ^{203}Fr the $13/2^+$ state is less populated in comparison with the ground-state population through the $13/2^-$ state. The most probable reason for this peculiarity is that there exists a higher-lying positive-parity

TABLE II. The population of the ground state through the $13/2^-$ state in ^{203}Fr and neighboring odd-mass nuclei as compared with the yield of the two γ-ray transitions populating directly the $13/2^+$ state. The number of ground-state α decays is used for normalization. The data are taken from our previous studies of the nuclei ^{197}At, ^{199}At [22], and ^{205}Fr [15].

Nucleus	^{197}At	^{199}At	^{203}Fr	^{205}Fr
$13/2^-$ vs g.s. α (%)	19 [a]	24 [a]	26	17
$13/2^+$ vs g.s. α (%)	26	28	10	24

[a]The yield of the $11/2^-$ state has been added.

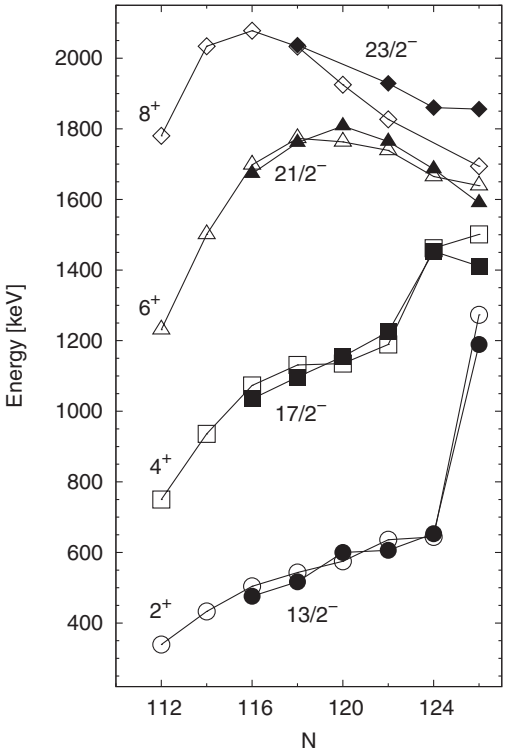

FIG. 13. Level energies of low-lying negative-parity states in neutron-deficient odd-mass francium nuclei (filled symbols) compared with yrast positive-parity states in their even-mass radon isotones (open symbols). ^{203}Fr has neutron number 116. For the radon data see Refs. [5,6,8–10]. The data for the heavier francium nuclei are taken from Refs. [12–15]. The lines connect yrast states without specifying the configuration of the states.

isomer feeding the negative-parity states via, e.g., an $E1$ transition. This isomer would be as fast as to decay inside RITU and none of the subsequent γ-ray transitions would be observed at the focal plane. A fast high-lying isomer has previously been observed in ^{209}Fr [13] with a spin and parity of $25/2^+$ ($\pi h_{9/2} \otimes \nu f_{5/2}^{-1} i_{13/2}^{-1}$) deexciting via an $E1$ transition to the $23/2^-$ ($\pi f_{7/2}$) state. This scenario could be the case in ^{203}Fr as well. Furthermore, similar fast $25/2^+$ isomers have been observed in light odd-mass astatine nuclei [21,49,50]. Such an isomer is not, however, reported in ^{205}Fr [15]. Unfortunately neither of the above-mentioned states have been observed in the present study, and therefore only speculations can be made concerning the curious weakness of the population of the $13/2^+$ state.

Figure 13 presents energy systematics of low-lying negative-parity states in neutron-deficient odd-mass francium nuclei compared with yrast positive-parity states in their radon isotones. The level energies of the states in ^{203}Fr fit well with systematics, showing an increase in collectivity when compared with the neighbor ^{205}Fr. No significant drops in the level energies, which would indicate an onset of ground-state deformation, can however yet be established. Based on these observations, the $13/2^-$, $17/2^-$, and $(21/2^-)$ states are assumed to originate from the odd $h_{9/2}$ proton coupled to the 2^+, 4^+, and 6^+ states, respectively, of the ^{202}Rn core.

V. CONCLUSION

The isomeric $13/2^+$ ($\pi i_{13/2}$) state was observed in ^{203}Fr. The beginning of a possible rotational band on top of this isomer was tentatively established, but a curious lack in population of the isomer was observed. There could, for example, be a high-lying positive-parity isomer feeding the negative-parity states instead of the $13/2^+$ state. The nature of this isomer could not be established. A ground-state feeding branch and the previously known α-decay branch from the deexcitation of the $1/2^+$ ($\pi s_{1/2}^{-1}$) state in ^{203}Fr were observed. The $1/2^+$ state in the α-decay daughter nucleus ^{199}At was observed as well. The level energies of this state both in ^{203}Fr and ^{199}At follow consistently the systematic behavior of the $1/2^+$ state observed in the odd-mass francium and astatine nuclei. A prompt γ-ray cascade was established on top of the the $9/2^-$ ground state. The structure of this cascade indicates that the dominance of the spherical structures in the ground state still prevails, as expected from the behavior of the neutron-deficient radon nuclei. Therefore the onset of oblate ground-state deformation is still pushed forward toward the neutron midshell. Continued studies toward the neutron midshell and ^{201}Fr could reveal interesting data as the ground state in ^{203}Fr is still spherical, while the ground state in ^{199}Fr is predicted to be oblate deformed. Moreover, a study, providing higher statistics than in the present work, is needed to further investigate the properties of the $13/2^+$ isomer in ^{203}Fr.

ACKNOWLEDGMENTS

This work has been supported through EURONS (European Commission Contract No. RII3-CT-2004-506065) and by the Academy of Finland under the Finnish Centre of Excellence Programme 2006-2011 (Nuclear and Accelerator Based Physics Contract No. 213503). The authors would also like to thank the UK/France (STFC/IN2P3) detector Loan Pool and GAMMAPOOL European Spectroscopy Resource for the loan of the detectors for the JUROGAM array. Support has also been provided by the UK Engineering and Physical Sciences Research Council. U.J. acknowledges support from the Finnish Academy of Science and Letters; Vilho, Yrjö, and Kalle Väisälä Foundation.

[1] R. Julin, K. Helariutta, and M. Muikku, J. Phys. G **27**, R109 (2001).
[2] A. M. Oros, K. Heyde, C. De Coster, B. Decroix, R. Wyss, B. R. Barrett, and P. Navratil, Nucl. Phys. A **645**, 107 (1999).
[3] K. Helariutta *et al.*, Eur. Phys. J. A **6**, 289 (1999).
[4] T. E. Cocolios *et al.*, Phys. Rev. Lett. **106**, 052503 (2011).
[5] G. D. Dracoulis, G. J. Lane, A. P. Byrne, P. M. Davidson, T. Kibédi, P. H. Nieminen, H. Watanabe, A. N. Wilson, H. L. Liu, and F. R. Xu, Phys. Rev. C **80**, 054320 (2009).

[6] A. R. Poletti, A. P. Byrne, G. D. Dracoulis, T. Kibédi, and P. M. Davidson, Nucl. Phys. A **756**, 83 (2005).
[7] W. J. Triggs, A. R. Poletti, G. D. Dracoulis, C. Fahlander, and A. P. Byrne, Nucl. Phys. A **395**, 274 (1983).
[8] D. Horn, C. Baktash, and C. J. Lister, Phys. Rev. C **24**, 2136 (1981).
[9] D. J. Dobson *et al.*, Phys. Rev. C **66**, 064321 (2002).
[10] R. B. E. Taylor *et al.*, Phys. Rev. C **59**, 673 (1999).
[11] H. Kettunen *et al.*, Phys. Rev. C **63**, 044315 (2001).
[12] A. P. Byrne, G. D. Dracoulis, C. Fahlander, H. Hübel, A. R. Poletti, A. E. Stuchbery, J. Gerl, R. F. Davie, and S. J. Poletti, Nucl. Phys. A **448**, 137 (1986).
[13] G. D. Dracoulis, P. M. Davidson, G. J. Lane, A. P. Byrne, T. Kibédi, P. Nieminen, H. Watanabe, and A. N. Wilson, Phys. Rev. C **79**, 054313 (2009).
[14] D. J. Hartley *et al.*, Phys. Rev. C **78**, 054319 (2008).
[15] U. Jakobsson *et al.*, Phys. Rev. C **85**, 014309 (2012).
[16] A. N. Andreyev *et al.*, Phys. Rev. C **69**, 054308 (2004).
[17] R. A. Braga, W. R. Western, J. L. Wood, R. W. Fink, R. Stone, C. R. Bingham, and L. L. Riedinger, Nucl. Phys. A **349**, 61 (1980).
[18] E. Coenen, K. Deneffe, M. Huyse, P. Van Duppen, and J. L. Wood, Z. Phys. A **324**, 485 (1986).
[19] H. Kettunen *et al.*, Eur. Phys. J. A **16**, 457 (2003).
[20] J. Uusitalo *et al.*, Phys. Rev. C **71**, 024306 (2005).
[21] K. Dybdal, T. Chapuran, D. B. Fossan, W. F. Piel, Jr., D. Horn, and E. K. Warburton, Phys. Rev. C **28**, 1171 (1983).
[22] U. Jakobsson *et al.*, Phys. Rev. C **82**, 044302 (2010).
[23] H. Kettunen *et al.*, Eur. Phys. J. A **17**, 537 (2003).
[24] M. Nyman *et al.* [Phys. Rev. C (to be published)].
[25] C. W. Beausang *et al.*, Nucl. Instrum. Methods Phys. Res. A **313**, 37 (1992).
[26] C. Rossi Alvarez, Nucl. Phys. News **3**, 10 (1993).
[27] M. Leino *et al.*, Nucl. Instrum. Methods Phys. Res. B **99**, 653 (1995).
[28] R. D. Page *et al.*, Nucl. Instrum. Methods Phys. Res. B **204**, 634 (2003).
[29] I. H. Lazarus *et al.*, IEEE Trans. Nucl. Sci. **48**, 567 (2001).
[30] K.-H. Schmidt *et al.*, Phys. Lett. B **168**, 39 (1986).
[31] R. S. Simon *et al.*, Z. Phys. A **325**, 197 (1986).
[32] E. S. Paul *et al.*, Phys. Rev. C **51**, 78 (1995).
[33] P. Rahkila, Nucl. Instrum. Methods Phys. Res. A **595**, 637 (2008).
[34] D. C. Radford, Nucl. Instrum. Methods Phys. Res. A **361**, 297 (1995).
[35] D. C. Radford, Nucl. Instrum. Methods Phys. Res. A **361**, 306 (1995).
[36] F. G. Kondev, Nucl. Data Sheets **105**, 1 (2005).
[37] T. Kibédi, T. W. Burrows, M. B. Trzhaskovskaya, P. M. Davidson, and C. W. Nestor, Jr., Nucl. Instrum. Methods Phys. Res. A **589**, 202 (2008).
[38] F. G. Kondev, Nucl. Data Sheets **108**, 365 (2007).
[39] K. Andgren *et al.*, Phys. Rev. C **78**, 044328 (2008).
[40] K.-H. Schmidt, C.-C. Sahm, K. Pielenz, and H.-G. Clerc, Z. Phys. A **316**, 19 (1984).
[41] S. Agostinelli *et al.*, Nucl. Instrum. Methods Phys. Res. A **506**, 250 (2003).
[42] J. Allison *et al.*, IEEE Trans. Nucl. Sci. **53**, 270 (2006).
[43] B. Singh, Nucl. Data Sheets **108**, 79 (2007).
[44] J. O. Rasmussen, Phys. Rev. **113**, 1593 (1959).
[45] S. Zhu and F. G. Kondev, Nucl. Data Sheets **109**, 699 (2008).
[46] H. Newman *et al.*, Phys. Rev. C **64**, 027304 (2001).
[47] M. Huyse, P. Decrock, P. Dendooven, G. Reusen, P. Van Duppen, and J. Wauters, Phys. Rev. C **46**, 1209 (1992).
[48] K.-H. Schmidt, Eur. Phys. J. A **8**, 141 (2000).
[49] R. F. Davie, A. R. Poletti, G. D. Dracoulis, A. P. Byrne, and C. Fahlander, Nucl. Phys. A **430**, 454 (1984).
[50] T. P. Sjoreen, U. Garg, and D. B. Fossan, Phys. Rev. C **23**, 272 (1981).
[51] Z. Chunmei, Nucl. Data Sheets **86**, 645 (1999).
[52] T. Lönnroth *et al.*, Phys. Rev. C **33**, 1641 (1986).
[53] H. Pai *et al.*, Phys. Rev. C **85**, 064317 (2012).
[54] H. De Witte *et al.*, Eur. Phys. J. A **23**, 243 (2005).
[55] C. M. Baglin, Nucl. Data Sheets **109**, 2033 (2008).
[56] P. Nieminen *et al.*, Phys. Rev. C **69**, 064326 (2004).